論文 / 著書情報
Article / Book Information

題目(和文)	自然信号および人工制御信号を用いた草津白根火山の電磁探査研究
Title(English)	Electromagnetic induction study of Kusatsu-Shirane volcano, Japan, using natural and controlled sources
著者(和文)	TSENGKuo-Hsuan
Author(English)	Kuo-Hsuan Tseng
出典(和文)	学位:博士(理学), 学位授与機関:東京工業大学, 報告番号:甲第11670号, 授与年月日:2020年12月31日, 学位の種別:課程博士, 審査員:小川 康雄,神田 径,中島 淳一,上野 雄一郎,中本 泰史
Citation(English)	Degree:Doctor (Science), Conferring organization: Tokyo Institute of Technology, Report number:甲第11670号, Conferred date:2020/12/31, Degree Type:Course doctor, Examiner:,,,,
学位種別(和文)	博士論文
Type(English)	Doctoral Thesis

Electromagnetic induction study of Kusatsu-Shirane volcano, Japan, using natural and controlled sources

(自然信号および人工制御信号を用いた草津白根火山の電磁探査研究)

Department of Earth and Planetary Sciences

Tokyo Institute of Technology

TSENG Kuo-Hsuan

ELECTROMAGNETIC INDUCTION STUDY OF KUSATSU-SHIRANE VOLCANO, JAPAN, USING NATURAL AND CONTROLLED SOURCES

by

TSENG Kuo-Hsuan

_____

APPROVED:

OGAWA, Yasuo, PhD
Thesis Director

KANDA, Wataru, PhD
Committee Member

NAKAJIMA, Junichi, PhD
Committee Member

UENO, Yuichiro, PhD
Committee Member

NAKAMOTO, Taishi, PhD
Committee Member

Dedication

This dissertation is dedicated to the memory of Liling Yeh. Although she was my inspiration to pursure my doctoral degree, she was unable to see my graduation. This is for her.

Abstract

The electromagnetic (EM) sounding is an efficient geophysical investigating method to provide distinct insight into the property of the volcanic hydrothermal system. Its sensitivity to the existence and connectivity of fluid leads to be extensively utilized in verifying the imaging features of a conductive anomaly. The time-lapse monitoring is one kind of its utilization for assessing and predicting the phreatic eruption in a volcano system. For obtaining a comprehensive image of the subsurface structures, both the natural and controlled source methods have pros and cons. The natural source method is accessible and does not need any artificial source current, but it is susceptible to cultural noises. On the other hand, the controlled-source method needs a source current but can be robust against noises. This study used both methods and investigated the three-dimensional structure of the Kusatsu-Shirane volcano and its temporal change during inactive and active periods.

First, the hydrothermal system below the Kusatsu-Shirane volcano, Japan, was investigated by the magnetotelluric (MT) method, which uses natural EM sources. An MT data set observed in a previous low activity period (2001-2005) of the volcano was inverted by a three-dimensional inversion code that can deal with the topography effect. The inverted model demonstrated (1) a shallow (100-800 meters deep from the surface) bell-shaped conductor which was interpreted as impermeable smectite clay cap; (2) a deep(900-2800 meters deep from the surface) conductor implying a brine reservoir; (3) a sub-vertical conductor that connecting the shallow and the deep conductors implying a fluid channel; (4) and a resistive gas-rich zone beneath the clay cap which is elongated along the past phreatic eruptions vents. The discovered features provided an

enhanced comprehension in interpreting the hydrothermal fluid path and the two-phase reservoir. Next, another set of MT data (in 2017-2018), which were acquired during the active period of the volcano, was inverted to investigate the temporal change due to volcanic activity. The data themselves show differences in the phase tensor plot. The results of the active period show the breakage of the conductive clay cap and underneath the Yumaga crater and decreased resistivity under the clay cap. These imply the invasion of fluid from the brine reservoir and breakage of the clay sealing.

For aiming more precise monitoring, an accurately controlled, routinely operated signal system for electromagnetic signal (EM-ACROSS) was developed. EM-ACROSS continuously transmits frequency comb signals (sets of superposed sinusoidal waves) with high accuracy and precision. In this experiment, two independent signals were transmitted respectively by the different grounded antenna for tensor EM fields. The frequency sets of the two transmitting antennae had sets of comb frequencies, which were slightly different between the antennas. This system provided vector source current at the transmitter and the vector electric field measurements at an observation site without interference, leading to the observation of a “source-current” to “electric-field” tensor response. As the source was precisely controlled, the receiver could get a high signal-to-noise ratio record by merely data stacking.

A forward modeling code was developed for EM-ACROSS by utilizing the finite element method with tetrahedral unstructured meshes. To compare the calculated electric fields in the forward modeling with those observed, we still needed to take care of the local distortion effect

due to near-surface inhomogeneities. In order to remove the local distortion effect in the observed electric field, a new tensor function was introduced, which dives out the distortion effect.

To evaluate the detectability of temporal change, two 3D resistivity models were prepared. One is a 3D inverted model which inverted from the 2001-2005 dataset, and the other is a 3D inverted model from the 2017-2018 dataset. For the respective two resistivity models, forward calculations were performed for EM-ACROSS, and the theoretical responses and observed EM-ACROSS responses (2017-2018) were compared by using the distortion-removed electric field tensors. The EM-ACROSS data (2018-2018) fit better with the 3D model response using the 2017-2018 MT data than to that using 2001-2015 MT data.

With the implication of time-lapse monitoring data, the hydrothermal system beneath Mt. Shirane could be changed within the 2014 volcanic activity. A serial change could be described as follows: (1) The supercritical fluid reservoir released overpressured fluid upward through the breached sealing zone; (2) The released overpressured flow through the fracture in the overlying mixed-layer clay structure that led the monitored microseismic activity; (3) The released fluid filled the two-phase reservoir in the mixed-layer clay structure and cause the thermal demagnetization, meanwhile, increases the liquid/gas ratio in the two-phase reservoir; (5) The filled two-phase reservoir released more gas upward to the surface through the expended crack in the clay cap, meanwhile, released more water upward to the Yugama crater lake. The path and time of releasing water upward to the Yugama can be indicated by the microseismic hypocenters

The conceptual model with credible spatial information for the temporal changes in the hydrothermal system beneath the Kusatsu-Shirane volcano is first demonstrated in this study. Credible spatial information is indicated by the change in the resistivity model. Moreover, the solution for the environmental noise issue and distortion effect with joint the passive and active EM sounding method that provided a new conception in future exploration and monitoring.

Acknowledgments

Throughout the writing of this dissertation I have received a great deal of support and assistance.

I would first like to thank my supervisor, Professor Yasuo Ogawa, whose expertise was invaluable in formulating the research questions and methodology. Your insightful feedback and guidance pushed me to sharpen my thinking and brought my work to a higher level.

I would like to acknowledge my labmates from Volcanic Fluid Research Center, Tokyo Institute of Technology for their wonderful collaboration in the fieldwork and seminar. I would particularly like to single out Dr. Yoshiya Usui at Earthquake Research Institute,The University of Tokyo, I want to thank you for your patient support of software utilization.

I would also like to thank Prof. Mineo Kumazawa, Dr. Takahiro Kunitomo and Dr. T. Grant Caldwell for their valuable guidance throughout my studies. You provided me with the tools that I needed to choose the right direction and successfully complete my dissertation.

In addition, I would like to thank my parents for their wise counsel and sympathetic ear. You are always there for me.

Table of Contents

List of Tables

List of Figures

Chapter 1. Introduction

In the assessment of predicting geological disaster or natural resource exploration, geophysical imaging of the subsurface structure is essential. Among the geophysical parameters, the electrical resistivity (or the reciprocal of electrical conductivity) is most sensitive to the existence and connectivity of fluids, which can be imaged by electromagnetic methods. Most of the fluid bearing crustal rocks are composite substances that are made up of a significant fraction of resistive host minerals and a minor fraction of conductive fluids. The bulk resistivities of such crustal materials are dominated by the existence and the connectivity of conductive fluids, although their fraction is minor. Thus, the electromagnetic methods are feasible for imaging the fluid distribution in the crust.

For saturated fluid, the conductivity and connectivity (i.e., the pore property as the filled fluid path in the structure) are the two most important factors that dominate the measured bulk conductivity (Stewart, 1982). In the shallow crust, the most common fluid with a higher electrical conductivity that dominates the measured bulk conductivity is sodium chloride (NaCl) concentrated, or in some cases, potassium chloride (KCl) concentrated water and bicarbonate salts (Nesbitt, 1993). The temperature and salinity influence the dissolution of chloride in the structure. The dissolved chloride can sharply increase the bulk conductivity and represent its influence in the temperature-salinity-conductivity relationship. These types of saline fluid have relatively higher electrical conductivity than most of the matrix material in the shallow crust (Palacky, 1988) that become the high potential for current flow. In the subsurface structure, the

path of current flow is controlled by the connected fluid bridge, which is related to the effective porosity. When the filled fluid is highly connected in the structure, the changing properties of the fluid (e.g., the volume fraction or the electrical conductivity of the fluid) intensely affect the bulk conductivity. Conversely, when the filled fluid is only slightly connected in the structure as isolated fluid pockets, the effect of changing properties of the fluid is relatively thimbleful. The relationship between the pore fluid content and the electrical resistivity of the rock has been described by an in-situ formula, which is widely known as Archie's Law (Archie, 1942):

$$\rho_b = a\,\rho_f\,\phi^{-m} \tag{1.1}$$

where ρ_b is the measured bulk resistivity of composed materials, ρ_f is the resistivity of the filling fluid, ϕ is the porosity of the matrix materials, and a and m are the material-related parameters.

The conventional Archie's Law has been further discussed with a variety of different models. For instance, the modified Archie's Law takes account of the volume factor within the different material phases (Glover et al., 2000). Another instance was a model discussing the relationship between the boundaries of bulk conductivity and fluid connectivity, which was called the Hashin-Shtrikman bounds (Hashin & Shtrikman, 1962). That model demonstrated that fluid connectivity in a fluid-filled geologic unit could further dominate the presented bulk conductivity in addition to the change of the conductivity of the saturated fluids. Waff (1974) introduced a model to demonstrate how the fluid connectivity changes the bulk electrical conductivity between the upper Hashin-Shtrikman bound (i.e., the relatively conductive liquid is fully connecting in a geologic unit, which is composed of relatively resistive matrix materials) and the

lower Hashin-Shtrikman bound (i.e., the relatively conductive liquid is fully isolated in a geologic unit, which is composed of relatively resistive matrix materials). In that model, the bulk conductivity of a fluid-filled material with a fully connected fluid bridge can be hundreds of times higher than the one with fully isolated fluid pockets.

In some specific cases, for example, a subsurface structure that is composed of clay minerals, the porosity can be quite low and with no fluid contents. In such an impermeable geologic unit, the current flow through the mineral sheets by the electrolyte exchange (Lévy et al., 2018) that the bulk conductivity is directly affected by the physical properties (e.g., temperature) and the composition of the minerals. This situation often exists in the geothermal field that the impermeable rock alteration products (e.g., smectite, smectite-illite, and mixed-layer clays) were predominant due to the increasing temperature (Gunderson et al., 2000). In the shallow unaltered zone, the bulk conductivity is controlled by the pore fluid conduction as most of the cases in the shallow crust. When the temperature increases with depth and the impermeable alteration products appear, the bulk conductivity then is controlled by the mineral conduction. In such "impermeable clay caps", the properties of the fluid in the geothermal field have less effect on the bulk conductivity until the impermeable clays transfer to porous clays composition such as chlorite (Schleicher et al., 2012). This alteration of bulk resistivity represents the change of the material composition of geologic units with the change of temperature in the subsurface structure (Flóvenz et al., 2012).

The factors mentioned above which dominate the measured bulk conductivity then could be sensitive indicators in the volcanic hydrothermal system: the subsurface structures with a high-temperature, conductive fluid, cumulated fracture zones, and high clay contained formations. The heat and/or fluid flux anomaly can be determined by the measured conductive anomaly. The high clay contained formations could be indicated by the relatively high conductivity. The cumulated fracture zones, which filled with the heated fluid, could intensely affect the bulk conductivity due to its high fluid connectivity. Therefore, the methods that can investigate the subsurface conductive anomaly are intensively available tools for the prospecting in the volcanic hydrothermal system. The electromagnetic (EM) sounding methods, among the standard geophysical investigating methods, are developed to measure the electrical conductivity of the earth materials and to obtain the subsurface structure information (e.g., Aizawa et al. 2011; Sasai et al. 2011). On account of the linked relationship between the temperature, conductivity, and fluid appearance, the EM sounding methods then are widely used with its sensitivity in the changes of pore fluids or the appearance of impermeable altered clay zones. Within the interpretation, the subsurface structures can be differentiated from electrical conductors (e.g., hydrothermal fluid, magma, smectite, and low-salinity flooding) and resistors (e.g., gas, igneous rock, and dry sand) due to bulk conductivity (Streich et al., 2010).

There are various types of EM sounding methods with their advantages and disadvantages. It generally can be separated into two categories: the passive EM sounding and the active EM sounding methods (Spies & Frischknecht, 1991), depending on the sources of the signal. A passive EM sounding method utilizes the signal from natural sources. Conversely, an active EM sounding method utilizes the signal from artificial sources. The passive EM sounding methods,

such as the magnetotelluric (MT) method, are well developed and widely applied in academic and industrial efforts. The observation area of a passive EM sounding method is highly adjustable due to the arrangement of instruments and utilizing signal frequencies (Nabighian & Macnae, 1991; Spies, 1989; Vozoff, 1991). That permits the practicality from a local observation to a regional-scale survey. The observing target can be deep regional crustal activities (e.g., Uyeshima, 2007) or the uppermost mantle (e.g., Meqbel et al., 2014) to the local magma plumbing system of a volcano (e.g., Aizawa et al., 2013a). With no consideration for the power supply of signal sources, the passive EM methods are cost-effective in a long-term operation for a year to decades. However, the variable strength of natural sources may cause uncertainty during the observation. Abdelfettah et al. (2018) demonstrated visible uncertainties in a long-term continuous MT monitoring due to the change of the geomagnetic field. Such effects reduce the stability in the operation that can be easily affected by the environmental noise. Another deficiency of the passive EM sounding method is the dead-band issue due to the deficiency of the natural signal in the specific frequency band (0.1-10 Hz) (Garcia & Jones, 2002). An effect of the dead-band was demonstrated by Aizawa et al. (2013b) with a high percentage (up to 90%) of outliers at dead-band values that cause large error bars of 50% to the dead-band data.

The signal uncertainty and dead-band issues can be solved in the active EM methods. The active EM methods, also known as controlled-source electromagnetic (CSEM) methods, have also been developed and employed with various procedures for different targets in past decades. The CSEM methods provide comparatively stable signals than using natural sources. Moreover, the controlled signal can provide frequencies coverage at dead-band. Utada et al. (2007) and Minami et al. (2018) demonstrated the addressed dead-band issue with small errors and low uncertainty

by utilizing a vertical-component magnetic field in CSEM volcano observation. However, there are lots of challenges in utilizing the CSEM methods, particularly in land-based observation. One challenge is the limited current transmission in the land-based CSEM survey because of the higher resistance of earth and the safety issue. According to Ohm's law, the penetrated current can be sharply reduced due to high resistance of the grounded soil then the system requires a heavy power load. Another challenge is the more robust response from air half-space due to its high resistivity, which masked the response from subsurface target more. That the observed data majorly responds to the features from the resistive air instead of to the subsurface anomaly (Løseth and Amundsen 2007; Løseth et al. 2010). Another challenge is the economic consideration of the sparser distribution, as well as its related number of immovable receivers and transmitters. Furthermore, the other challenge is the further complicated culture noise condition (Streich et al. 2011). Those challenges were discussed in Streich (2016) with their standard solutions, including correcting the airwave mask issue in the forward modeling, employing processing techniques for noise reduction, and increasing the source moment. Moreover, the noticeable environment changes (e.g., rainfall, frost, shallow groundwater table, dramatic seasonal weather) in some regions significantly affect the near-surface electric conductivity (Hayley et al. 2007; Wirianto et al. 2010). Likewise, the strength of the current transmission is affected by the environment condition. If the operation time is getting longer, such changes may cause data uncertainties and reduce the stability and repeatability of the result.

In both passive and active EM sounding methods, two significant problems should be solved for improving the credibility of observation results: one is the above-mentioned noise problem, and the other one is the galvanic distortion effect. The galvanic distortion effect is caused by the local

(e.g., few meters) conductive anomalies from the near-surface structures. When the current flow through the local anomalies, the measured electric field is affected even though the anomalies are relatively small structures (Constable, 2010). When the data is interpreting, the response of regional features (e.g., the existence of few kilometers structures) then could be masked by the response of local, near-surface inhomogeneities (Groom & Bailey, 1989). The solutions of the galvanic distortion effect have been well-developed and widely utilized in passive EM sounding methods, such as computing the model with utilizing a trade-off factor to controlled the distortion tensor and minimized its effect (Ledo et al., 1998; Usui, 2015), or utilizing the parameters from a distortionless tensor (Caldwell et al., 2004). However, there has not been a conventional solution in active EM sounding methods. The situation of the noise problem is similar. In passive EM sounding methods, if the natural signal is stable, there only the local culture noise should be considered as the problem during the observation. The solutions to reducing the effects of local culture noise have also been well-developed such as remote reference data (Gamble et al., 1979a,b). In the active EM sounding methods, the consideration becomes more complicated because the natural signal also becomes the noise and can be further stronger than the culture noise (Macnae et al., 1984). In such cases, the solutions utilized in the passive EM sounding methods are not as efficient. The details of those solutions will be further introduced and discussed in the following chapters with their features and limitations. Therefore, developing alternative solutions for the active EM sounding methods to solve those two major problems and utilizing them in the observation becomes the motivation of this study.

For such motivation, both the passive and active EM sounding methods are utilized in this article. Firstly, the well-developed MT method is utilized with conventional solutions for the

galvanic distortion effect and noise issues with obtaining a credible result. Secondly, a CSEM method with a newly developed system and methodologies is utilized to provide alternative solutions for solving those significant problems. Finally, the result from both the MT and CSEM methods are interpreted with their implications for improving the comprehension of the subsurface features of the volcanic hydrothermal system.

In the following chapters, a real case exploration will be introduced with the developed methodologies. In chapter 2, previous studies on Kusatsu-Shirane volcano were reviewed. In chapter 3, the magnetotelluric(MT) method was introduced, and then its applications to Kusatsu-Shirane volcano were described using unstructured finite element modeling. The obtained model and its potential time variation were described. In chapter 4, a signal system: EM-ACROSS (ElectroMagnetic- Actively Controlled Routinely Operated Signal System) was introduced with its hardware design and data processing scheme. A definition of a new tensor response function and numerical forward modeling for the three-dimensional structure were demonstrated with experimental data at Kusatsu-Shirane volcano. In chapter 5, joint interpretations of the observed results from both MT and EM-ACROSS methods will be discussed to comprehend the subsurface features of the volcanic hydrothermal system at Kusatsu-Shirane volcano from the time-lapse monitoring result.

Chapter 2. Geological setting

The electromagnetic investigation with either passive or active source has been widely utilized in academia and industry with various targets. In this study, both a passive method, MT method, and an active method, the CSEM method, are utilized in the hydrothermal fluid investigation at Kusatsu-Shirane volcano. This chapter introduces the background of Kusatsu-Shirane volcano as a geological setting.

Kusatsu-Shirane volcano is an active andesitic volcano situated north of the Kanto Plain (Figure 2.1). Kusatsu-Shirane volcano locates near the volcanic front (Obara & Sato, 1995) at Central Japan, where the Pacific plate and the Phillippine Sea plate are subducting beneath the North American plate (Uto & Tatsumi, 1996). The subducting oceanic crust leads to dehydration in the descending slab that generates magma as the source of volcanoes (Iwamori & Zhao, 2000; Wyss et al., 2001). Wada & He (2017) demonstrated a temperature distribution model along the surface of the Phillippine Sea slab and the Pacific plate, which presents a temperature up to 800° C in this region that leads to the heated hydrothermal system.

2.1. The Eruptive History of the Kusatsu-Shirane Volcano

The history of the eruption of Kusatsu-Shirane volcano was evidenced from analysing the layered beds of key tephra and intercalating loess soil in the surrounding region (Hayakawa & Yui, 1989) and from K–Ar dating method (Kaneko et al., 1991). The eruptive history of the

volcano can be divided into three major stages. The first stage started from Early to Middle Pleistocene (0.6~0.5 Ma), and the second stage started from Middle Pleistocene (0.5 Ma) and stopped with a dormant period for more than 100,000 years in the late Middle to Late Pleistocene (0.25 Ma). After that, the third stage of the eruption history in Late Pleistocene (started from 0.1 Ma) formed three pyroclastic cones, Mt.Shirane, Mt. Ainomine, and Mt. Motoshirane, on the summit of the volcano (Figure 2.2). The lava flows from the volcano were contemporaneously occurred during the eruption activity. Radially flew out from three pyroclastic cones to the east and to the south that formed the lava stratum around the summit of the volcano (e.g., Kagusa lava, 7ka and Sessyo lava, 3ka) (Uto et al., 1983). The third stage is continuing to the present due to the continuous phreatic eruptions and volcanic activities. The frequently occurred phreatic and magma eruptions are recorded in history. This series of eruptions in the past 14,000 years is the formation of three craters, Yugama, Mizugama, and Karegama craters, around the peak of Mt.Shirane. (Ohba et al., 2008) (Figure 2.2). The most recent phreatic eruptions of Mt. Shirane stared in 1805 (Tsuya, 1933) and stopped in 1982 (Takano & Watanuki, 1990). In this period, more than ten phreatic eruptions were recorded inside or surrounding Mt. Shirane. The most recent phreatic eruption was in 2018 at Mt. Motoshirane (Ogawa et al., 2018).

2.2. Previous Geophysical and Geochemical Studies

The feature of the hydrothermal system beneath three major craters has been intensively studied by geophysical and geochemical analysis. Those studies include the geochemical analysis of Yugama crater lake, the largest crater lake at the summit, and its surrounding region (Ohba et al., 1994, 2000, 2008, 2019; Sano et al., 1994; Takano et al.,1994); the seismicity analysis (Kumagai & Chouet, 1999; Kumagai et al., 2002; Nakano & Kumagai, 2005; Nakano et al., 2003);

magnetic total force monitoring (Takahashi & Fuji, 2014) and electromagnetic methods (Nurhasan et al., 2006; Ogawa et al., 2016). The geochemical analysis and seismicity analysis with long-term data directly present the temporal changing with time-variable of the volcanic hydrothermal system. The geochemical analysis provides the chemical content of related fluid from the volcano system, which clarifies the source of volcanic fluid and its temporal differences. The seismicity analysis directly provides a time-space relationship of the volcanic activity to aim for the spatial distribution of the small local activities such as the hydrothermal fluid flowing through the crack. The spatial-temporal distribution of the seismic hypocenters could demonstrate the location of volcanic activities events. By combing the results of electromagnetic observation with those sets of information, conductivity anomalies can be interpreted.

Ohba et al. (2008, 2019) demonstrated a conceptual model of the hydrothermal system beneath Yugama crater lake with its temporal changes by analyzing the chemical and isotopic composition of the lake water and the released fumarolic gases of Kusatsu-Shirane volcano. The geochemical concept model represents a crystallizing magma as a profound source of heat, which is sealed by hot plastic rock. The sealing zone could be composed of quartz, gypsum, alunite, or similar secondary hydrothermal minerals (Fournier, 1999; Kamineni, 1983; Takano & Watanuki, 1990). After the sealing zone breaching with the increased fluid pressure, the groundwater goes through the breached part and invades into the inner region and brings the magmatic content, such as re-dissolved material or HCl, to the shallow surface. With the crack of the sealing zone, the magmatic gases are also released upward. The heated water and magmatic gases then become a two-phase (liquid phase and vapor phase) hydrothermal reservoir beneath

the Yugama crater. Within the different periods of volcanic activity, the changes in chemical and isotopic composition denote the deep feature of the reservoir. For example, the composition of He and CO_2 increase during the high seismic activity period; on the contrary, CH_4 and N_2 increase within the low seismic activity period. The change of such compositions is due to the change of hydrothermal reservoir with an injection of magmatic gas from the deeper sealing magma reservoir. The geochemical study by Ohba et al. (2008) presents the data from 1949 to 2005. The data indicates the existence of three evolutions of the hydrothermal system: sealing zone establishment, hot rock-water interaction, and HCl extraction. A sketch in Figure 2.3 represents the purposed model, which is redrawn from the previous geochemical studies of Mt. Shirane.

The magma and hydrothermal fluid system are also studied by monitoring the long-period seismicity events. The sudden pressure disturbances within magma- or hydrothermal fluid-filled conduits and cracks can be characterized by this oscillating signature. Kumagai et al. (2002) verified a series of changes between cracks expand and collapse, and its drying process of the hydrothermal fluid contains in 1992-1993. Another long-period event study by Nakano & Kumagai (2005) with the observed data from 1988 to 1995 indicates the series of temporal variations is a repeated cycle caused by seasonally variable water supply. Another schematic view was represented by Nakano, et al. (2003) with indicating the depth of hydrothermal fluid contains crack zone at 300m depth beneath Yugama crater lake as a resonator of the acoustic signal. The sketch is redrawn in Figure 2.2. The recorded microseismic swarm beneath Mt. Shirane was described by Takahashi & Fuji (2014) and Nurhasan et al., (2006). The hypocenter of microseismic activities can straightforwardly indicate the location where hydrothermal fluid

flow through the cracks. A sketch in Figure 2.4 represents the purpose of the hydrothermal fluid-filled resonator beneath Mt. Shirane.

The subsurface electric conductive anomaly beneath Mt. Shirane is demonstrated by Nurhasan et al. (2006) and Ogawa et al. (2016) with modeling the MT data. Nurhasan et al. (2006) demonstrated a 2-D resistivity model with audio-frequency magnetotellurics (AMT) (a variant of the MT method by using the signals at higher-frequency for the shallower target) data. The 2-D model profile in the direction was N 85°W- N 95°E, located between Mt. Shirane and Mt. Motoshirane. The 2-D resistivity model revealed a shallow conductor to the east of Yugama crater lake and a thick conductor at a deeper part to the west of Yugama crater. In this model, the microseismic swarm hypocenters indicated the probability of a fluid path between the shallow and the deep conductor. The shallow conductor was interpreted as an impermeable caped rock, and the deep conductor was interpreted as the geothermal fluids. A 3-D resistivity model of Mt. Shirane was introduced by Ogawa et al. (2016). The primary feature, the existence of the two conductors, were accordant with the 2-D model by Nurhasan et al., (2006), but the shape of the shallow conductor was further comprehended. With 3-D modeling, the shallow conductor presented a bell-shape which satisfies the assumption of caped rock. Ogawa et al. (2016) additionally employed borehole data that indicated the composition of the caped rock is smectite, which has low permeability. A sketch in Figure 2.5 represents the purpose of the conductors and microseismic swarm that described by Nurhasan et al. (2006) and Ogawa et al. (2016).

Besides the resistivity model of Mt. Shirane, a geomagnetic analysis was described by Takahashi & Fuji (2014). In that study, total magnetic intensity changes were monitored and were modeled by magnetic dipole sources. The locations of the magnetic dipole source with demagnetization or magnetization characteristics were displayed during the active and inactive period, which indicate the high-temperature fluid reservoir location. Around Mizugama crater lake, two thermal-demagnetization sources were estimated at a depth of 400-600 m in different active periods. The sequent changes of the magnetic source indicate a cycle of the reservoir beneath Mt. Shirane is in a period of filling with or drying out of the hydrothermal fluid. The estimated locations of the sequentially changed reservoir coincided with the top of the seismicity swarm, which indicates the path of the hydrothermal fluid injection.

The previous geochemical and geophysical studies have provided partial comprehensions of the hydrothermal system beneath Mt. Shirane. The objective of the thesis is further imaging the hydrothermal system in three-dimensions and comprehending its potential temporal changes. This article will describe a new resistivity model from recently developed magnetotelluric modeling methods and a newly designed controlled-source electromagnetic method that utilizing an actively controlled, routinely operated signal system (ACROSS).

In chapter 3, a passive electromagnetic method (magnetotelluric method), which uses the natural source, will be introduced. The dense magnetotelluric data around the Yugama crater was inverted using a three-dimensional finite element modeling, including topography. The detail resistivity distribution and its temporal change during the recent active period were discussed.

In chapter 4, a new method with an improved system, ACROSS, will be introduced, starting from designing the hardware system and its application to Kusatsu-Shirane volcano. Then this article will discuss a data processing scheme and defining a new tensor response function with forwarding numerical modeling using an unstructured tetrahedral finite element method.

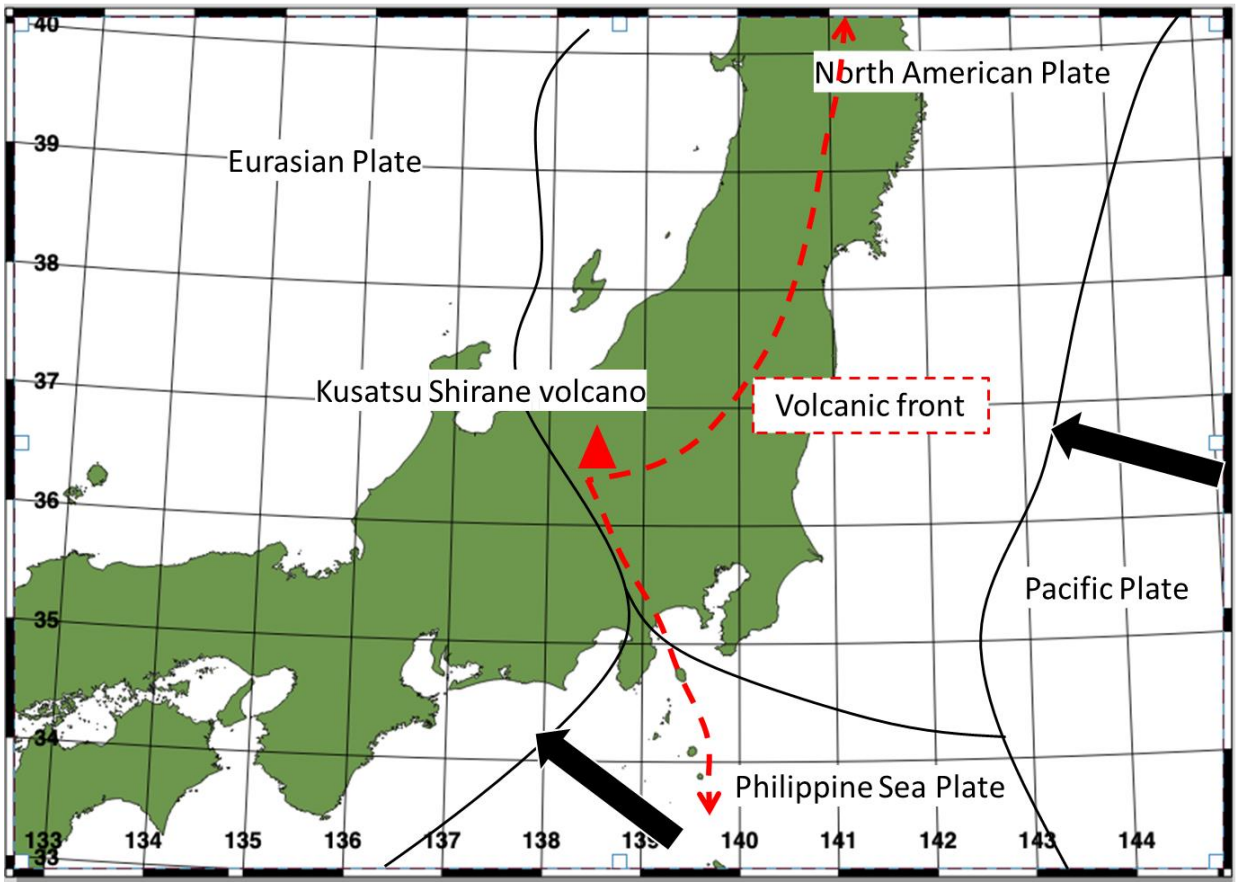

Figure 2.1

Schematic map of plate boundaries and volcanic front.

The black arrows represent the subduction direction at the plate boundaries.

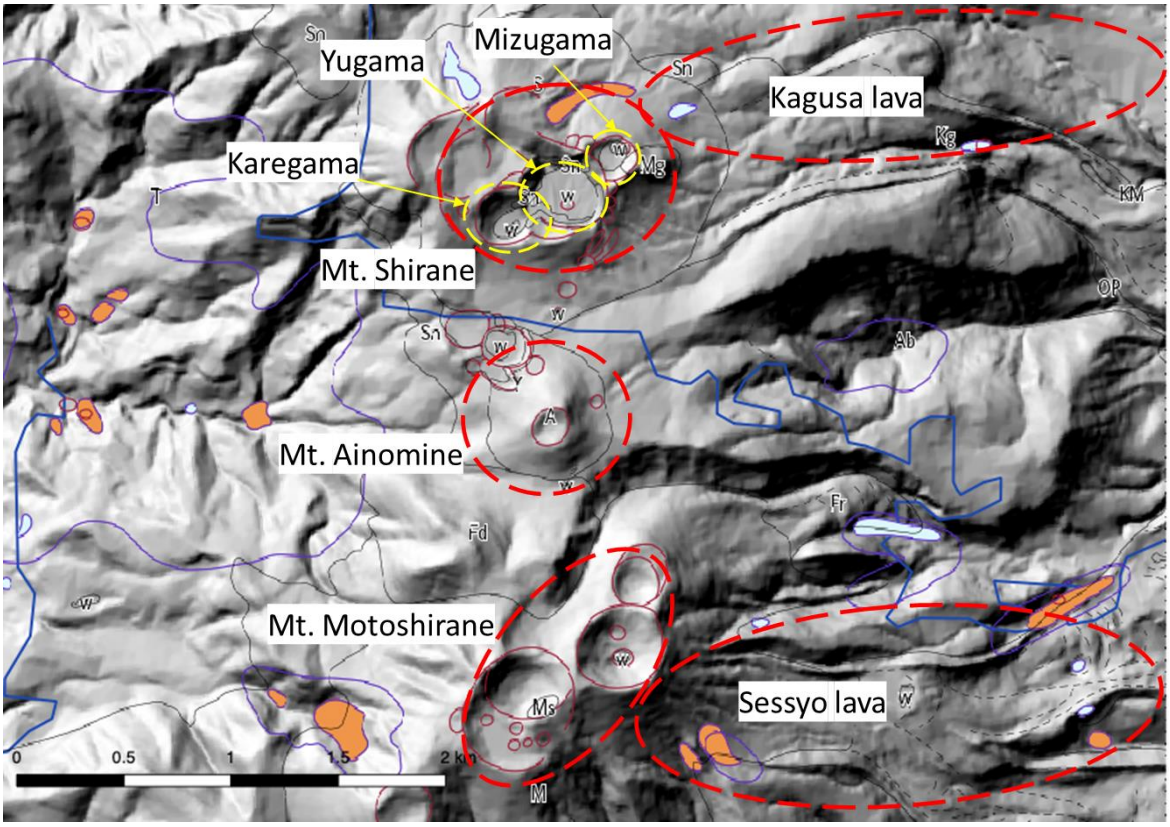

Figure 2.2

Shaded terrain map of the Kusatsu-Shirane volcano region.

The orange shapes represent the fumarole zones; the blue line represents the local highway; the purple line represents the sulfur alteration zones; the red circles represent the past eruption crater. The symbol “Sn” denotes the Shirane lava flow; the symbol “Fd” denotes the Futagoyama lava dome; the symbol “Ms” denotes the Motoshirane-Sancho lava flow; the symbol “Ab” denotes the Aoba lava flow.

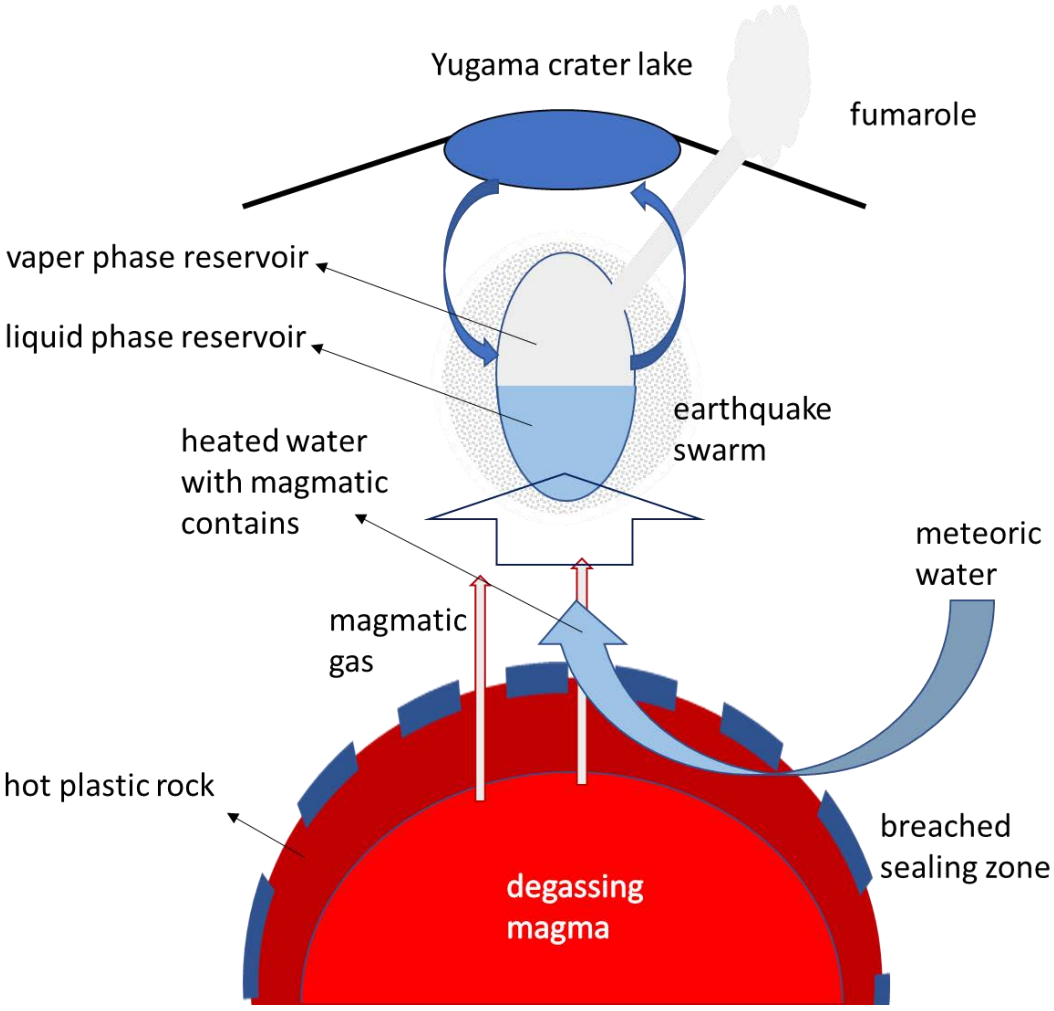

Figure 2.3

Sketch of the hydrothermal system beneath Yugama crater lake.

A sketch of the hydrothermal system beneath Yugama crater lake from the purpose in the previous studies of geochemical analysis of Mt. Shirane (Ohba et al., 2008; Ohba et al., 2019).

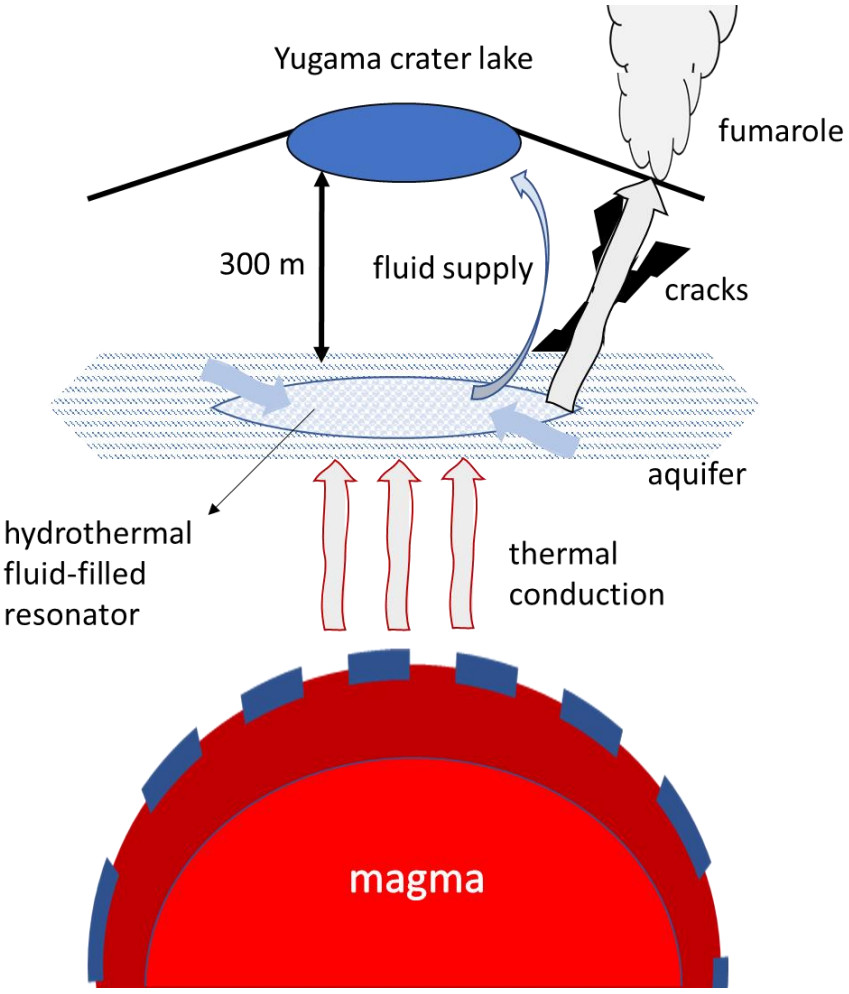

Figure 2.4

Sketch of the hydrothermal fluid-filled resonator beneath Yugama crater lake.

A sketch of the hydrothermal fluid-filled resonator beneath Yugama crater lake from the purpose in the previous studies of long-period events analysis of Mt. Shirane (Kumagai et al., 2002; Nakano, et al., 2003; Nakano & Kumagai, 2005).

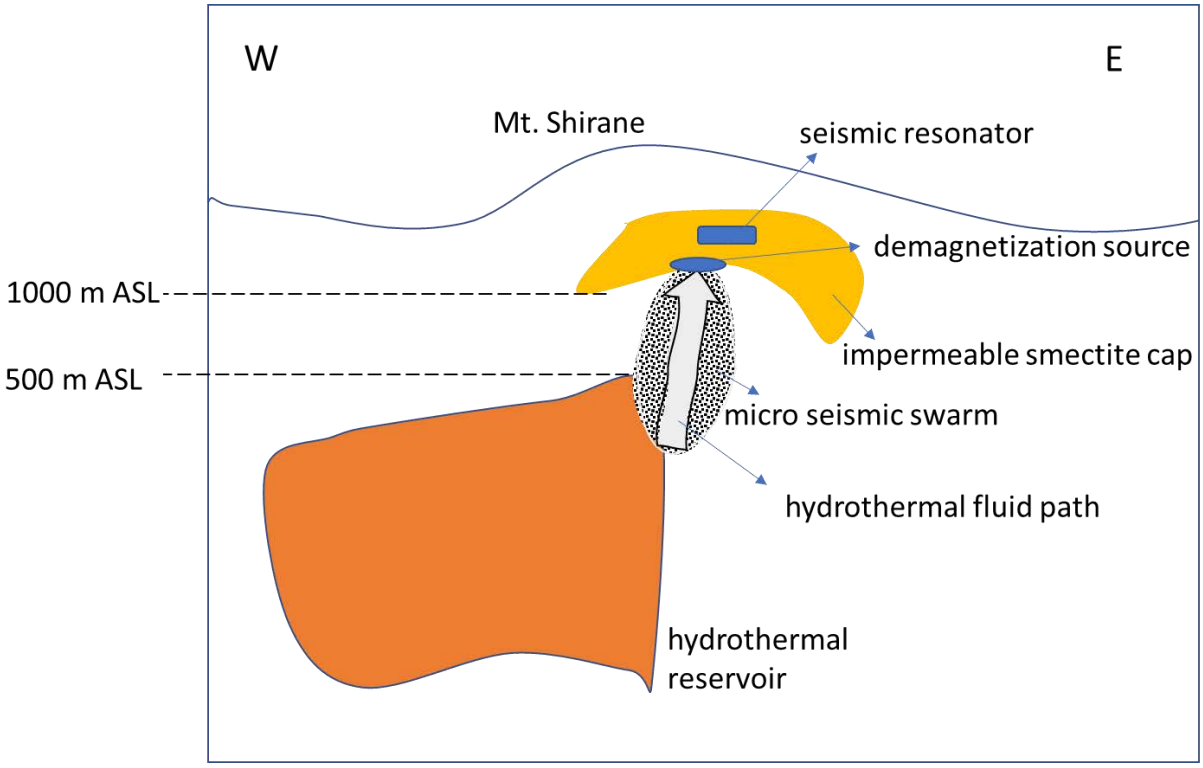

Figure 2.5

Sketch of the conductive structures beneath Mt. Shirane.

A sketch of the conductive structures beneath Mt. Shirane from the purpose in the previous studies of 2-D and 3-D MT inversed modeling (Nurhasan et al., 2006; Ogawa et al., 2016).

Chapter 3. Magnetotelluric Sounding Method

In this chapter, the theory of the magnetotelluric (MT) method is introduced firstly. Its application to an observation at Kusatsu-Shirane volcano and a three-dimensional model are demonstrated secondly. Then the interpretation will be shown lastly. The MT method was firstly introduced in the 1930s and thoroughly developed in the past decades. There are amounts of publications and textbooks that introduced this method. In this section, the description of the MT method and its fundamental theories are referenced to Chave & Jones (2012), Vozoff (1991), and Zhdanov & Keller (1994). The method is a passive electromagnetic method with utilizing the natural electromagnetic field originating from solar wind and globally propagated lightning activity. The solar wind affects the upper atmosphere of the earth and interacts with the geomagnetic field of Earth (Markson & Muir, 1980). This interaction produces long-period (>1s) electromagnetic signals and is utilized in the MT method. In contrast, the short-period (<11s) electromagnetic signals are produced by the lightning storm events while they propagating globally between the Earth's surface and the high conductive ionosphere. The essentials of the MT method is specifically developed according to the characteristics of electromagnetic waves from the natural signal. In this chapter, the fundamentals of the MT method will be briefly described first.

3.1 The Fundamentals of Magnetotelluric (MT) Method

The methodologies of electromagnetic investigation can be dissimilar depending on the conditions and gains of observation, such as the type of aimed target, the observation

environment, the source of electromagnetic signal. Nevertheless, they are relevant to the same fundamental theories: Maxwell's equations (Feynman et al., 1965):

$$\nabla \times \mathbf{E} = -\partial_t \mathbf{B} \quad (3.1)$$

$$\nabla \times \mathbf{H} = \mathbf{J} + \partial_t \mathbf{D} \quad (3.2)$$

$$\nabla \cdot \mathbf{B} = \mathbf{0} \quad (3.3)$$

$$\nabla \cdot \mathbf{D} = \rho_e \quad (3.4)$$

where **E** is the electric field, **B** is the magnetic induction**,** **H** is the magnetic field, **D** is the electric displacement, **J** is the current density, ε is the vacuum permittivity, and ρ_e is the electric charge density.

Where for external sources,

$$\mathbf{D} = \varepsilon \mathbf{E} \quad (3.5)$$

$$\mathbf{B} = \mu_0 \mathbf{H} \quad (3.6)$$

where μ_0 is the magnetic permeability for vacuum,

then Equation 3.2 and 3.4 become:

$$\nabla \times \mathbf{B} = \mu_0 \mathbf{J} + \frac{\partial_t \mathbf{E}}{c^2} \quad (3.7)$$

$$\nabla \cdot \mathbf{E} = \frac{\rho_e}{\varepsilon} \quad (3.8)$$

where *c* is the constant value of light speed.

Equation 3.7 is also known as Ampere's law. While the natural signals are penetrating and propagating through the Earth, the fluctuating magnetic field induces an electric current by following Ampere's law. The total electric current of the subsurface space can be determined by measuring the magnetic field fluctuation on the surface of the earth. With the measurement of the

electric field on the Earth surface, the electrical conductivity can be yielded with Maxwell's equation included Ohm's law:

$$\mathbf{J} = \sigma\mathbf{E} \tag{3.9}$$

where σ is the electrical conductivity.

Suppose the electromagnetic fields have a single angular frequency ω. The penetrated electromagnetic wave will transfer to heat and lose its energy. In a uniformly conducting medium, the electromagnetic wave decays to $1/e$ of its magnitude at the surface at a distance which is the familiar skin depth :

$$\delta(\omega) = \sqrt{\frac{2}{\omega\mu_0\sigma}} \tag{3.10a}$$

and can be simplified to

$$\delta(t) \cong 500\sqrt{\rho t} \tag{3.10b}$$

in SI units, where ω is the angular frequency, ρ is the medium resistivity and t is the period.

Therefore, the frequency-space relationship is determined as relevant information in the electromagnetic investigation (Figure 3.1). In the frequency domain, the electric field **E** and the magnetic field **B** can be further written as a time-frequency-space dependent formation:

$$\mathrm{A} = \mathrm{A}_0 e^{i\omega t} e^{-i\alpha z} e^{-\alpha z} \tag{3.11}$$

where A is one component (e.g., x, y, or z in a Cartesian coordinate system) of an electric or magnetic field and A_0 is its value on the surface, α is the reciprocal of the skin depth, z is the penetration depth.

Then $e^{i\omega t}$ becomes a term of sinusoidal time variation, $e^{-i\alpha z}$ becomes a sinusoidal depth variation and $e^{-\alpha z}$ becomes a term of exponential decay with depth (Nabighian & Macnae, 1991; Spies, 1989; Vozoff, 1991) for MT sounding.

With the time-frequency-space relationship, two assumptions were proposed by Cagniard (1953) in defining apparent resistivity for usual magnetotelluric signal (Madden & Nelson, 1964):

(1) the natural electromagnetic field from sources mentioned above is a plane wave propagating downward into the Earth, and
(2) the Earth is laterally uniform, which can be assumed as either a homogeneous half-space (Figure 3.2a) or one-dimensional (1-D) layered Earth (Figure 3.2b).

With two assumptions, Maxwell's equation then can be written with

$$\nabla \cdot \mathbf{E} = 0 \tag{3.12}$$

and

$$\nabla \cdot \mathbf{J} = 0 \tag{3.13}$$

that denotes no source current from the Earth. These assumptions permit a simple form for calculating the apparent resistivity:

$$\rho_a = \left(\frac{1}{\omega\mu}\right)\left|\frac{\mathbf{E}}{\mathbf{H}_\perp}\right|^2 \tag{3.14}$$

where ρ_a is the apparent resistivity, $\mathbf{H}_\perp$ is the magnetic field orthogonal component to the electric field.

Then the wave impedance for a 1-D case is defined as:

$$Z_{xy} = \frac{E_x}{H_y} \tag{3.15a}$$

$$Z_{yx} = -\frac{E_y}{H_x} \tag{3.15b}$$

When the Earth contains a lateral contact striking with a significantly longer length (longer than the skin depth in Equation 3.10a&b), the case becomes a two-dimensional (2-D) Earth (Figure 3.2c) assumption.

In 2-D assumption, it assumes all the fields parallel to the strike direction η (e.g., x-, y-, or z-direction in Cartesian coordinate) have zero variation, which means $\partial_\eta = 0$. The orthogonal electromagnetic fields in the 2-D case can be decoupled into a component that parallels to the strike in the electric field **E** and the magnetic field **B**. These two decoupled electromagnetic field are known as the transverse electric mode (TE-mode) and transverse magnetic mode (TM-mode) with **E**-polarization and **B**-polarization, respectively (Thiel, 2008). In an assumption of a model with an x-direction strike, the TE-mode can be described as:

$$\begin{cases} \dfrac{\partial E_x}{\partial x} = \dfrac{\partial B_x}{\partial t} = i\omega B_z \\ \dfrac{\partial E_x}{\partial z} = \dfrac{\partial B_y}{\partial t} = i\omega B_y \\ \dfrac{\partial B_y}{\partial y} - \dfrac{\partial B_y}{\partial z} = \mu_0 \sigma E_x \end{cases} \tag{3.16}$$

where the components of the electric field do not exist when they perpendicular to the strike, and the components of the magnetic field which perpendicular to the strike are produced by the components of the electric field which parallel to the strike. At the plane which perpendicular to the strike, the TM-mode occurs and the current flows through this polarization:

$$\begin{cases} \dfrac{\partial E_x}{\partial y} - \dfrac{\partial E_y}{\partial z} = i\omega B_x \\ \dfrac{\partial B_x}{\partial z} = -\mu_0 \sigma E_y \\ \dfrac{\partial B_x}{\partial y} = \mu_0 \sigma E_z \end{cases} \tag{3.17}$$

In 2-D case, H_x proportionally associates to E_x and E_y, and the H_y are, likewise, has associated with E_x and E_y. This relationship can be described by linear equations:

$$E_x = Z_{xx} H_x + Z_{xy} H_y \tag{3.18a}$$

$$E_y = Z_{yx} H_x + Z_{yy} H_y \tag{3.18b}$$

that the wave impedance becomes a 2-D tensor. The Equation 3.18a and 3.18b are also can be written in matrice format:

$$\begin{pmatrix} E_x \\ E_y \end{pmatrix} = \begin{pmatrix} Z_{xx} & Z_{xy} \\ Z_{yx} & Z_{yy} \end{pmatrix} \begin{pmatrix} H_x \\ H_y \end{pmatrix} \tag{3.19}$$

The impedance tensor can also be employed in the three-dimensional (3-D) case (Figure 3.2d). In 2-D case, the off-diagonal components $Z_{xx} = Z_{yy} = 0$ and $\left| Z_{xy} \right| \neq | Z_{yx} |$. The impedance tensor component Z_{xy} and Z_{yx} can be regarded as the impedance tensor of TM-mode Z_{TM} and TE-mode Z_{TE}, respectively. In 3-D cases, all the components of impedance tensor exist (Vozoff, 1991). Likewise, the apparent resistivity can also be determined by the impedance tensor:

$$\rho_{a,ij} = \frac{\mu_0}{2\pi\omega} \left| Z_{ij} \right|^2 \tag{3.20}$$

which is not a tensor. It is commonly used but not suitable for a function of rotation in MT impedance imaging properties. Besides representing the relationship between the horizontal electric field and magnetic field by impedance tensor, another relationship between the

horizontal magnetic field and the vertical magnetic field can also be represented by a linear equation:

$$H_z = T_{zx}H_x + T_{zy}H_y \tag{3.21}$$

which the T_{zx} and T_{zy} are called tipper vector (induction vector), which is a geomagnetic depth sounding transfer function. With interpreting the impedance tensor and the tipper vector of the data from a single site, the information about the depth-electrical conductivity relationship of subsurface structure can be obtained, and the existence of 1-D or 2-D structure can also be determined by plotting the apparent resistivity and phase tensor versus frequencies.

However, in the real case, the near-surface structure could exist as a local conductive anomaly, in which the electric field will change its amplitude and its direction without electromagnetic induction. It is called telluric distortion (Groom & Bailey, 1989). Thus, interpreting the magnetotelluric response by impedance tensor encounters a significant problem because the local distortion may not be represented on the regional scale. With considering this situation, a distortion matrix should be applied during interpreting the impedance tensor (Ledo et al., 1998):

$$\begin{pmatrix} E_{x-local} \\ E_{y-local} \end{pmatrix} = \begin{pmatrix} D_{xx} & D_{xy} \\ D_{yx} & D_{yy} \end{pmatrix} \begin{pmatrix} E_{x-regional} \\ E_{y-regional} \end{pmatrix} \tag{3.22}$$

where the D_{ij} are the real, frequency-independent galvanic distortion parameters for i- and j-components of the electric field which cause no inductive offset, $E_{i-local}$ is the i-component of the distorted local electric field and $E_{i-regional}$ is the i-component of the undistorted regional electric field. Note that near-surface anomaly will have no induction effect, and correspondingly, the tensor components of *D* are all real numbers.

In the distortion matrix, the galvanic deflection of the electric field is assumed as the source of distortion rather than the induction. Therefore, Equation 3.19 can be rewritten by combining Equation 3.22:

$$\begin{pmatrix} E_{x-regional} \\ E_{y-regional} \end{pmatrix} = \begin{pmatrix} Z_{xx-regional} & Z_{xy-regional} \\ Z_{yx-regional} & Z_{yy-regional} \end{pmatrix} \begin{pmatrix} H_{x-regional} \\ H_{y-regional} \end{pmatrix} \tag{3.23}$$

and

$$\begin{aligned} &\begin{pmatrix} D_{xx} & D_{xy} \\ D_{yx} & D_{yy} \end{pmatrix} \begin{pmatrix} E_{x-regional} \\ E_{y-regional} \end{pmatrix} \\ &= \begin{pmatrix} D_{xx} & D_{xy} \\ D_{yx} & D_{yy} \end{pmatrix} \begin{pmatrix} Z_{xx-regional} & Z_{xy-regional} \\ Z_{yx-regional} & Z_{yy-regional} \end{pmatrix} \begin{pmatrix} H_{x-regional} \\ H_{y-regional} \end{pmatrix} \\ &= \begin{pmatrix} D_{xx} & D_{xy} \\ D_{yx} & D_{yy} \end{pmatrix} \begin{pmatrix} Z_{xx-regional} & Z_{xy-regional} \\ Z_{yx-regional} & Z_{yy-regional} \end{pmatrix} \begin{pmatrix} H_{x} \\ H_{y} \end{pmatrix} \end{aligned} \tag{3.24}$$

then the relationship between the undistorted regional impedance tensor and the distorted local impedance tensor can be described by the following equation:

$$\begin{pmatrix} Z_{xx-local} & Z_{xy-local} \\ Z_{yx-local} & Z_{yy-local} \end{pmatrix} = \begin{pmatrix} D_{xx} & D_{xy} \\ D_{yx} & D_{yy} \end{pmatrix} \begin{pmatrix} Z_{xx-regional} & Z_{xy-regional} \\ Z_{yx-regional} & Z_{yy-regional} \end{pmatrix} \tag{3.25a}$$

or

$$\mathbf{Z}_{local} = \mathbf{D} \cdot \mathbf{Z}_{regional} \tag{3.25b}$$

In the modeling computation, the galvanic distortion matrix **D** can be controlled by a trade-off parameter to recover the regional features in the modeling result (e.g., Usui, 2015; Usui et al., 2017).

Another solution for solving the interpretation issues with the distorted local electric field is introduced by Caldwell et al. (2004), which is called the phase tensor method. For defining the phase tensor, the complex impedance tensor is divided into its real and imaginary part:

$$\mathbf{Z} = \begin{pmatrix} Z_{xx} & Z_{xy} \\ Z_{yx} & Z_{yy} \end{pmatrix} = \Re e \begin{pmatrix} Z_{xx} & Z_{xy} \\ Z_{yx} & Z_{yy} \end{pmatrix} + i\, \Im m \begin{pmatrix} Z_{xx} & Z_{xy} \\ Z_{yx} & Z_{yy} \end{pmatrix} = \mathbf{P} + i\mathbf{Q} \tag{3.26}$$

With substituting the impedance phase in Equation 3.25b by Equation 3.26, the phase tensor is defined as:

$$\mathbf{\Phi} = \begin{pmatrix} \Phi_{xx} & \Phi_{xy} \\ \Phi_{yx} & \Phi_{yy} \end{pmatrix} = \boldsymbol{P}_{local}{}^{-1} \cdot \boldsymbol{Q}_{local} = (\mathbf{D} \cdot \mathbf{P}_{regional})^{-1} \cdot \mathbf{D} \cdot \mathbf{Q}_{regional} \tag{3.27}$$

and it is evident that:

$$\begin{aligned} \mathbf{\Phi} = (\mathbf{D} \cdot \mathbf{P}_{regional})^{-1} \cdot \mathbf{D} \cdot \mathbf{Q}_{regional} &= \mathbf{P}_{regional}{}^{-1} \cdot \mathbf{D}^{-1} \cdot \mathbf{D} \cdot \mathbf{Q}_{regional} \\ &= \mathbf{P}_{regional}{}^{-1} \cdot \mathbf{Q}_{regional} = \mathbf{\Phi}_{regional} \end{aligned} \tag{3.28}$$

The phase tensor dives out the distortion matrix, and the locally determined phase tensor is identical with the regional phase tensor, which is equivalent to distortion independent. With interpreting the phase tensor instead of the impedance tensor in the data on a regional scale, the distortion issue can be removed that provides a superior result for the interpretation of the subsurface structure, rather than applying only the impedance tensor (Booker, 2012, 2014).

The phase tensor can moreover represent the space-frequency related features of subsurface structures. In a 1-D layered earth case, due to $Z_{xx} = Z_{yy} = 0$ and $Z_{xy} = -Z_{yx}$ from Equation 3.15a and 3.15b, then Equation 3.27 can be represented as:

$$\boldsymbol{\Phi} = \begin{pmatrix} 0 & P_{xy} \\ P_{yx} & 0 \end{pmatrix}^{-1} \cdot \begin{pmatrix} 0 & Q_{xy} \\ Q_{yx} & 0 \end{pmatrix} = \begin{pmatrix} 0 & P \\ -P & 0 \end{pmatrix}^{-1} \cdot \begin{pmatrix} 0 & Q \\ -Q & 0 \end{pmatrix}$$
$$= \begin{pmatrix} 0 & 1/P \\ -1/P & 0 \end{pmatrix} \cdot \begin{pmatrix} 0 & Q \\ -Q & 0 \end{pmatrix} = \begin{pmatrix} Q/P & 0 \\ 0 & Q/P \end{pmatrix} = \begin{pmatrix} \tan \emptyset & 0 \\ 0 & \tan \emptyset \end{pmatrix} \quad (3.29)$$

and in 2-D case:

$$\boldsymbol{\Phi} = \begin{pmatrix} \tan \emptyset_{xy} & 0 \\ 0 & \tan \emptyset_{yx} \end{pmatrix} \quad (3.30)$$

where $\emptyset$ is the phase angle of the complex impedance elements Z.

The $\tan \emptyset_{max}$ or $\tan \emptyset_{min}$ denote the strike of a 2-D structure, which is very functional for an interpretation of the data before modeling computation. There are many utilizations of the phase tensor that will be described in the following chapters with the real case study. In 3-D case, the phase tensor should be additionally parameterized with a unitary coordinate rotation operator vector:

$$\mathbf{R}(\theta) = \begin{pmatrix} \cos \theta & \sin \theta \\ -\sin \theta & \cos \theta \end{pmatrix} \quad (3.31)$$

which rotates the coordinate system in the right-hand sense. And then the phase tensor of 3-D cases is parameterized to:

$$\boldsymbol{\Phi} = \mathbf{R^{-1}}(\theta_{ellipse}) \begin{pmatrix} \Phi_{max} & 0 \\ 0 & \Phi_{min} \end{pmatrix} \mathbf{R}(\psi) \mathbf{R}(\theta_{ellipse}) \quad (3.32)$$

where the ψ is a normalized skew angle

$$\psi = \tan^{-1} \left(\frac{\Phi_{xy} - \Phi_{yx}}{\Phi_{xx} + \Phi_{yy}} \right) \quad (3.33)$$

and $\theta_{ellipse}$ is the direction of phase tensor ellipse, which represented by the angle of Φ_{max} (Booker, 2014).

The MT method has extensive utilization in geophysical prospecting due to the complete discussion of its features, which are far more than the content in this section. The data acquisition and observation method and its interpreting utilization will be further described in the following relative sections.

3.2 Benefit of the New Model and New Observation

The 2-D and 3-D electrical resistivity model in the previous studies (Nurhasan et al., 2006; Ogawa et al., 2016) have provided a comprehension of the underlying hydrothermal system beneath the Kusatsu-Shirane volcano. However, there are still benefit to computing a new model with the previously observed data, which has been utilized in the past (i.e., Nurhasan et al. (2006)). The first benefit is solving the distorted 3D structure in 2D inversion. There are some drawbacks in 2-D inversions that have been discussed in the previous researches with the comparison between the 2-D and 3-D inversed model. Uchida et al. (2002) demonstrated a probability of the undesirably generated distorted structure in the 2-D inversions when a 3-D structure is underlying the survey profile. Ledo (2005) discussed the sort of dimensional related distortion and introduced a solution of interpreting a 3-D structure by a 2-D inversed model. The solution improved the feasibility of the 2-D interpretation for 3-D data. Although the introduced method can provide a possibility for reasonable geological interpretation, nevertheless, due to the advance of computation conditions in the present, a 3-D modeling computation is more reasonable in recent days. With consideration for the enhancements of 3-D modeling (e.g., the improvement of illustration in complicated structures; the uniqueness of anisotropy; and a larger

range of interpreting solution) which has presented in the previous studies (Mogi & Nakama, 1993; Ogawa, 2002; Yamaya et al., 2009; Patro & Egbert, 2011), the 3-D modeling method becomes more practicable.

The second benefit of computing a new model is solving the topographic effect. The previous 3-D inversed modeling by Ogawa et al. (2016) has emphasized a possible location of the two-phase reservoir that can be jointly interpreted with the geomagnetic results from Takahashi & Fuji (2014) that provides a good comprehension. However, that represented model had not included the topography information that can be further improved. It should be noted that a steeply changing surface can occur the topographic responses in the modeling computation, which is called the topographic effect (Wannamaker et al., 1986). In the modeling computation, the earth is a relative conductor to the air. That some conductors will be generated in a flat-surface model (Usui, 2016) as spurious anomalies. Those spurious anomalies may give rise to distortions in the electromagnetic field, which should be solved in the computation to avoid misinterpreting comprehension (Ku et al., 1973). Therefore, modeling with topography is substantial, especially in the volcanoes region with steep surface conditions (Aizawa et al., 2005). Thus, recomputing a 3-D electrical resistivity model with topography information is necessary for the Kusatsu-Shirane volcano.

In addition to computing a new model with previously observed data, acquiring new MT data from the recent observation has its necessity for verifying the appearance of temporal changes of the hydrothermal system. The seismic activity monitoring data demonstrates frequent seismic

activity in 2014 (Figure 3.3) after the period of previously observed data (2001 to 2005) (Nurhasan et al., 2006; Ogawa et al., 2016). Besides the seismic activity data, geomagnetic monitoring data from JMA (2019) demonstrated the stopped magnetization event in 2012, which usually indicates the alteration of hydrothermal fluid features (Rikitake & Yokoyama, 1955).

With the consideration of those benefits, a new model with previously observed data (2001 to 2005) was computed in this study by a recently published 3-D inversed modeling algorithm. The result was compared with another model with newly observed data (2017 to 2018) afterward. The underlying electrical conductive structure beneath the Yugama crater will be anew examed with a joint interpretation for enhancing the comprehension of the local features in the following chapters.

3.3 MT DATA: the Acquisition, Processing, and Modeling

The MT/AMT surveys were conducted on the summit of Kusatsu-Shirane Volcano and surrounding regions. The previously observed MT data in this article was acquired from 2001 to 2005, which was introduced in the previous research articles (Nurhasan, 2006; Nurhasan et al., 2006; Ogawa et al., 2016). For verifying the temporal changes in the last decade, the additional data was observed in 2017 and 2018. The previously observed MT data consisted of 41 MT sites and 50 AMT sites; the newly observed data consisted of 10 MT sites and 1 AMT site (Figure 3.4). In both the previously observed data and the newly observed data, the measuring instruments were the Phoenix Geophysics designed satellite-synchronized data acquisition units: MTU-5 series electromagnetic field receiver. The MTU instruments individually measured two

horizontal components of the electric field, by two sets of the orthogonally grounded electrodes (2E) with a 40-times-40 meter-square area, and three components (two horizontal and one vertical) of the magnetic field (3H), by three induction coil sensors (Figure 3.5), which is commonly abbreviated to a 2E3H system. The instruments measured with 320-to-0.0001 Hz and 10k-to-0.1 Hz signals in MT and AMT surveys, respectively. The vertical electric component was not supposed to be measured due to the nature signal is a plane wave, and its normal component on the earth's surface is assumed to be zero. The full 2E3H components were measured in both the newly observed and the previously observed AMT data. For MT data, most of the sites only measured telluric fields, and magnetic fields were using at a specific reference location in the summit area. Due to the fundamentals of the galvanic distortion (Groom & Bailey, 1989), the electric field is firmly location-dependent, but the magnetic field is approximately regional. The difference in the location of telluric and magnetic fields was taken into account in the later numerical modeling. In this article, the fully measured 2E3H components were processed to the impedance tensor (Equation 3.19) and the tipper data (magnetic transfer function)(Equation 3.21).

The pre-processing flow from raw digitized electromagnetic filed to impedance tensor and tipper vector was processed in the data processing program “SSMT2000” from Phoenix Geophysics. The multi-coherency robust processing with remote reference data (Gamble et al., 1979a,b) was employed in the “SSMT2000” for reducing the local noise effects. Considering the efficient band of frequency for both MT and AMT data with the skin depth (Equation 3.10), the impedance tensor and tipper vector at 12 frequencies were utilized as the input parameters for modeling computation. The employed data frequencies were chosen from 280 Hz to 0.137 Hz,

exponentially. These frequencies were evenly placed on a logarithmic scale. The error floor was set to 5% of the geometric mean of off-diagonal components in the impedance tensor and 0.05 to the tipper vector. The previously observed data and the newly observed data were both applied with the above-mentioned process flow.

With the parameters from impedance tensor and the tipper vector, a 3-D inverse modeling program "FEMTIC" (Usui, 2015; Usui et al., 2017) was employed for computing the resistivity model. The initial model was composed of uniform earth with 100 ohm-meter resistivity, an air half-space with 1000 mega-ohm-meter resistivity, and a represented lake water with 0.2 ohm-meter resistivity for Yugama crater lake (Terada et al., 2018). For representing the topography features (e.g., Baba, 2005; Nam et al., 2007; Nam et al., 2008), the inversed modeling utilized unstructured tetrahedral elements with distance-related, gradually increasing volume (i.e., smaller volume toward the center and observation sites and larger away) by Delaunay refinement process (e.g., Usui et al. 2017; Yoshimura et al. 2018; Kanda et al., 2019). The computational domain was set to an 80 km (north-south direction) times 80 km (east-west direction) times 100 km (altitudinal direction) space with a defined Cartesian XY origin at the center of Yugama crater lake (N 36.6429°, E 138.5357°). In this study, the negative value of depth represents the height above mean sea level (ASL). The resistivity of the represented lake and air was fixed during the iterative computations. The horizontal electric fields were parallel with the ground surface to handle the topographic effects. The inversion program FEMTIC provided a minimizing objective function $\phi(\boldsymbol{m})$:

$$\phi(\boldsymbol{m}) = \phi_M(\boldsymbol{m}) + \alpha^2\phi_R(\boldsymbol{m}_\rho) + \beta^2\phi_D(\boldsymbol{m}_D) \tag{3.34}$$

for the model vector $\boldsymbol{m}$:

$$\boldsymbol{m} = \begin{bmatrix} \boldsymbol{m}_\rho \\ \boldsymbol{m}_D \end{bmatrix} \tag{3.35a}$$

and

$$\boldsymbol{m}_\rho = [\log \rho_1 \quad \log \rho_2 \quad \cdots \quad \log \rho_n]^T \tag{3.35b}$$

$$\boldsymbol{m}_D = \left[D'^{1}_{xx} \quad D'^{1}_{xy} \quad D'^{1}_{yx} \quad D'^{1}_{yy} \quad \cdots \quad D'^{n}_{xx} \quad D'^{n}_{xy} \quad D'^{n}_{yx} \quad D'^{n}_{yx} \right]^T \tag{3.35c}$$

where ρ_n is the resistivity parameter for the n-th mesh element; D'^{n}_{xx}, D'^{n}_{xy}, D'^{n}_{yx}, and D'^{n}_{yx} are the components of the deviation of the distortion matrix $\mathbf{D}'$ for the n-th mesh element.

The deviation of the distortion matrix $\mathbf{D}'$ is defined as:

$$\mathbf{D}' = \begin{bmatrix} D'_{xx} & D'_{xy} \\ D'_{yx} & D'_{yy} \end{bmatrix} = \begin{bmatrix} D_{xx} & D_{xy} \\ D_{yx} & D_{yy} \end{bmatrix} - \begin{bmatrix} 1 & 0 \\ 0 & 1 \end{bmatrix} = \mathbf{D} - \mathbf{I} \tag{3.36}$$

where $\mathbf{D}$ is the frequency-independent galvanic distortion matrix with four components D_{xx}, D_{xy}, D_{yx}, and D_{yy} in Equation 3.25a.

In Equation 3.34, $\phi_M(\boldsymbol{m})$ is the data misfit, $\phi_R(\boldsymbol{m}_\rho)$ is the model roughness, and $\phi_D(\boldsymbol{m}_D)$ is the strength of the galvanic distortion. The data misfit $\phi_M(\boldsymbol{m})$ is defined as:

$$\phi_M(\boldsymbol{m}) = \|\boldsymbol{W}\boldsymbol{d} - \boldsymbol{W}\boldsymbol{F}(\boldsymbol{m})\|^2 \tag{3.37}$$

where $\boldsymbol{W}$ is the diagonal matrix consisting of the reciprocal of the standard deviation of the observed data (i.e. observed data error); $\boldsymbol{d}$ is the real vector containing the real part and imaginary part of the components of the observed response functions; $\boldsymbol{F}(\boldsymbol{m})$ is the vector consisting of the real part and imaginary part of the forward calculating response functions.

The model roughness $\phi_R(\boldsymbol{m}_\rho)$ is defined as:

$$\phi_R(\boldsymbol{m}_\rho) = \|\boldsymbol{R}\,\boldsymbol{m}_\rho\|^2 \tag{3.38}$$

where $\boldsymbol{R}$ is the roughness matrix gives the difference of logarithmic resistivity value of the adjacent cells.

The strength of the galvanic distortion $\phi_D(\boldsymbol{m}_D)$ is defined as:

$$\phi_D(\boldsymbol{m}_D) = \sum_{i=1}^{n}\left(\left|D'^{i}_{xx}\right|^2 + \left|D'^{i}_{xy}\right|^2 + \left|D'^{i}_{yx}\right|^2 + \left|D'^{i}_{yy}\right|^2\right) \tag{3.39}$$

The model roughness $\phi_R(\boldsymbol{m}_\rho)$ gives a smoothness constraint for the stabilization of the inversion and controlled, meanwhile, the strength of the galvanic distortion $\phi_D(\boldsymbol{m}_D)$ regularized the distortion matrix to reduce the galvanic distortion effect. These two terms in the objective function $\phi(\boldsymbol{m})$ are controlled by two constant trade-off parameters α^2 and β^2, respectively.

In this article, a small value of $\boldsymbol{\beta^2}$=0.01 was chosen at first for the strength of galvanic distortion, in which the efficiency has been demonstrated in previous researches (e.g., Sasaki & Meju, 2006; Usui et al., 2017; Yoshimura et al., 2018). For determining the best model, we test 7 different values of $\boldsymbol{\alpha^2}$ (100, 10, 3.16, 1, 0.562, 0.316, 0.1). The previously observed data was computed by the inversion program "FEMTIC" and obtained the best model with $\boldsymbol{\alpha^2}$=1 by L-curve method (i.e., finding the maximum curvature in a plot of the data misfit versus model roughness with different trade-off parameters) (Hansen & O'Leary, 1993). With the preferred trade-off parameters ($\boldsymbol{\alpha^2}$=1 and $\boldsymbol{\beta^2}$=0.01), the model converged at 29th iteration while the changes were less than 1% from previous iteration value. From the initial model to the final

model, the root-mean-square (RMS) misfit decreased from 32.2 to 1.2. The best model computed from the previously observed MT/AMT data in the period between 2001 to 2005 was named "model P" in this article.

By considering the difference of the observation sites between the previous (2001-2005) and new (2017-2018) observation, "model P" was utilized as the initial model for the newly observed data. The model of newly observed data was then computed with the same setting ($\boldsymbol{\alpha^2}$=1 and $\boldsymbol{\beta^2}$=0.01) for consistency, and obtained the final model at 14th-iteration. It should be noted that the RMS value of the newly observed data decreased to less than 1.0 at the 8th-iteration, which denoted the probability of over-fitting issues (Chave & Jones, 2012). To prevent the over-fitting, the 7th-iteration was then be decided to be the final model. The best model computed from the newly observed MT/AMT data in the period between 2017 to 2018 was named "model N" in this article.

3.4 Inversed Modeling Result with Previously Observed Data (2001-2005)

The previously observed data (2001-2005) and newly observed data (2017-2018) had a marked difference in their numbers of the observation sites. A broader and denser distribution has a better position to provide a more reliable result, while the RMS value is close. Moreover, "model N" was computed from "model P" that the information from the latter should be further robust than the former. The previously observed data with more numbers of the MT/AMT stations had a better position to interpret the subsurface structures. Therefore, "model P" was chosen for

discussing its implication in this section. Meanwhile, “model N” will be employed to discuss the temporal differences.

For the comparison between observed and calculated data, a phase tensor (Caldwell et al., 2004) analysis was employed for examining the result. The phase tensor ellipses of the previously observed data were drawn in Figure 3.6. The phase tensor ellipse plot was focused on the core region of Mt.Shirane (Figure 3.4) for the hydrothermal system around the Yugama crater lake. Figure 3.6 represents the phase tensor ellipses of observed and calculated data. The ellipses were filled by Φ_2, the geometric mean of the maximum phase $\Phi_{\max}$ and minimum phase $\Phi_{\min}$ (i.e., phase tensor determinant phase), which is rotational invariants and indicate electrical conductivity changes with depth (Booker, 2014). In Figure 3.6, the observed and calculated data had a proper fitting in the majority of the sites from high to low frequencies. At the west of Yugama crater lake, the Φ_2 increased from 40° to 60°. In the eastern area of the Yugama crater, the Φ_2 had a higher value (>60°) than at the western (<60°) within the frequency range 70.0-4.4 Hz. This feature reversed in 1.1-0.3 Hz. In Figure 3.6, the induction arrows (Parkinson, 1962) were further added for a graphical representation of the anomalous geomagnetic variation. Figure 3.6 shows the induction arrows directing to Yugama crater lake at frequencies 70.0-17.5 Hz and directing to southwestward at frequencies 4.4-1.1 Hz.

By considering with the benefit in clarifying the preferred orientation of regional structure and the unaffectedness by local structure distortion (Booker, 2014), phase tensor is an essential tool of MT data analysis particularly in volcanic structure research in demonstrating the continuous

change in space and period (e.g., Heise et al., 2008; Hill et al., 2009). A smooth variation of phase tensor ellipse indicates the consistency which represents data quality. Furthermore, the ellipse rotation can provide a preliminary understanding of the subsurface structure before the modeling computation. The direction of the steepest electrical conductivity gradient was represented by the direction of phase tensor ellipses. In 2-D cases, the direction of axis points to the strike of structure; in 3-D cases, the semi-major axis and semi-minor axis point to the direction of greatest and least inductive response, respectively (Booker, 2014).

Moreover, the phase tensor analysis also provides resistivity-frequency-relevant information by the value of its components. A determinant phase that is higher than 45° indicates the increase of electrical conductivity with increasing depth. In Figure 3.6, both the phase tensor ellipses and determinant phase value showed good agreement between the observed and the calculated data. At the northeast of Yugama crater lake, the change of determinant phase angle denoted that the subsurface structures were changing from mainly resistive downward (70-4.4 Hz) to conductive downward (1.1 Hz). It indicated a resistor overlaying a conductor. At the east of Yugama crater lake, the change denoted that the subsurface structures were changing from strongly conductive downward (70-4.4 Hz) to mainly resistive downward (1.1 Hz). It indicated a conductor overlaying a resistor. In the long period, the high determinant phase indicated a regional deep resistivity structure beneath the Yugama crater lake (0.3Hz). The direction of real induction arrows indicated the position of the subsurface conductive structure (Gregorri & Lanzerotti, 1980; Weaver & Agarwal, 1991). The different directions of the real induction arrows between 70.0-17.5 Hz and 4.4-1-1 Hz might indicate the changes in the conductor position from the center of Mt. Shirane to the southeast of Mt. Shirane. However, the induction arrows could

potentially be affected by steeply elevated topography, which is common in volcano studies (e.g., Kanda et al., 2013; Müller & Haak, 2004). Thus, the explanation of the induction arrows direction should be interpreted by considering the other information.

For representing the inverted result with the previously observed data, the best-fit modeling result could be demonstrated by a combination of a plan view resistivity structure map, a north-south (NS), and an east-west (EW) cross-section profiles. For examining the hydrothermal fluid reservoir at the location where was inferred by the previous researches (e.g., Kumagai et al., 2002; Nakano et al., 2003; Nakano & Kumagai, 2005; Ogawa et al., 2016; Ohba et al., 2008; Ohba et al., 2019), the altitude in the resistivity structure maps was firstly set at 1400m ASL. To demonstrating the visualized features underlying the Yugama crater lake, the resistivity structure map with two crosssections through the Yugama crater lake is represented in Figure 3.7. To verify the potential hydrothermal fluid path, a microseismic data set from November 2001 to March 2003 (Mori et al., 2006; Nurhasan et al., 2006) and from September 2013 to January 2019, and the locations of demagnetization/magnetization dipoles from October 1996 to September 2012 were combined in the final model representation. The microseismic swarm hypocenters were separated into three groups: before, during and after the volcanic unrest (March-May 2014). The microseismic swarm hypocenters and the location of observation sites were plotted with a 200-meter-wide projection clipper. The three-dimensional locations of the geomagnetic dipole sources, which included two demagnetization periods and four magnetization periods (Takahashi & Fuji, 2014), were projected on the maps and cross-sections of the model. An inflation source during 2014 unrest was employed in the representation (Ogawa et al., 2016).

Two primary conductors are represented in “model P” (Figure 3.7). One of the conductors, C1, was located slightly east of Yugama crater lake with 1-10 ohm-meters resistivity. This conductor represented a bell-shape in the crossed vertical profiles (Figure 3.8). Another deep conductor, C2, was beneath the summit of Mt. Shirane that the resistivity is down to 0.1 ohm-meters. These two conductors were connected at the west of Yugama crater lake. Temporarily, this connection was described as an individual conductor, C3, before the interpretation. A resistor, R1, was underlying the conductor C1. The hypocenters of microseismic swarm distributed along the edge of conductor C3 and resistor R1, beneath the magnetic dipole source.

For evaluating the reliability of the electrical conductivity structures and their robustness in “model P”, two modified models “model P_M1” and “model P_M2”, with respectively replacing the deep conductor C2 and the connecting conductor C3, were utilized in the forwarded computation as a sensitivity test. In the first modified model “model P_M1”, the tetrahedral elements which the gravity center is in a cuboid range: [-600m < northing < 2000m; -1300m < easting < 700m; -2000 < altitude (ASL) < 900] (i.e. the deep conductor C2) had a fixed resistivity value to 50 ohm-meter (i.e. make this structure resistance). This modification represented removing the deep conductor beneath the summit of Mt. Shirane. The final RMS increased from 1.2 to 1.4. In the second modified model “model P_M2”, the elements in another cuboid range: [-500m < northing < 500m; -800m < easting < 4m; 900m < altitude (ASL) < 1500m] (i.e. the connecting conductor) were selected and had a fixed resistivity value to 100 ohm-meter (i.e. make this structure resistance). This modification represented removing the connection between the deep conductor and the bell-shaped conductor. The final RMS increased

from 1.2 to 1.32. The modified ranges are shown in Figure 3.9. The phase tensor analysis was utilized to clarify the changes between “model P” and the modified “model P_M1”, “model P_M2” (Figure 3.9). In Figure 3.9, “model P_M1” demonstrated ellipses with a smaller determinant phase (less than 45°) at the northwest of the modified region than in the best-fit final model at 4.4 Hz. At 1.1 and 0.3 Hz, it represents a smaller determinant phase and shape changes of ellipses even outside of the modified region. “model P_M2” demonstrates visibly smaller determinant phase at a few sites at 4.4 Hz and disarray difference of determinant phase at 1.1 Hz. The differences between “model P” and “model P_M1”, “model P_M2” in the phase tensor analysis indicate the two tested features (removing deep conductors C2 in “model P_M1” and removing vertical conductor C3 in “model P_M2”) are sensitive in the modification. The major features of the subsurface electrical conductors beneath the Yugama crater were clarified due to the sensitivity test, which indicates the reliability of the modeling result for further interpretation.

The gradual changes in the primary features of the electrical conductors with depth are additionally represented by eight resistivity structure maps in Figure 3.10. At -1400 and -1200 meters depth, a resistor with 100 ohm-meter resistivity represented in the south of Yugama crater. This resistor was consistent with the location of previous eruption craters as an open slot of the shallow conductor C1. The slice view of east-west and north-south profiles are represented in Figure 3.11 and Figure 3.12, respectively. With the slice view of profiles, it is not difficult to figure out that the conductor C1 only represents its bell-shape surrounding the Yugama crater lake. Its connection with conductor C2 disappears at north and east of Yugama crater lake. Those conductors and resistors demonstrated the feature of 3-D structures, which also represented in

Figure 3.8. Due to the appearance of 3-D structures, the necessity of 3-D inversion is also verified.

3.5 The Implication of the 3-D MT Modeling with Previously Observed Data (2001-2005)

According to the previous researches, the conductors in the volcanic hydrothermal system usually indicate either clay minerals deposits, hydrothermal fluid or molten magma; the resistor usually indicate gas reservoirs or solidified magma (e.g., Ogawa et al., 1998; Nurhasan et al., 2006; Aizawa et al., 2009; Yamaya et al., 2013; Usui et al., 2016). The two major conductive bodies: the shallow bell-shaped conductor C1 and the deep conductor C2 have been demonstrated in the previously published resistivity models (Nurhasan, 2006; Nurhasan et al., 2006; Ogawa et al., 2016), but their connection, the vertical conductor C3 is a newly represented feature in 3D modeling. The sensitivity of this vertical conductor has been examined in the phase tensor analysis with the modified model 2, that the potential of its existence is trustable.

The 2-D model introduced by Nurhasan et al. (2006) did not represent a bell-shape of C1 on account of the modeling profile offset and the dimensional related distortion (i.e., a 3-D structure occurs misinterpreting in the 2-D model) (Ledo, 2005). The appearance of C1 in this article is closer to the represented on in the 3-D model introduced by Ogawa et al. (2016). A borehole drilling information from a well at the east of Yugama crater was introduced by Yokoyama et al. (2010). The borehole sample denoted the appearance of a smectite reach structure at 1800m ASL. This depth is the top of C1 in “model P” (Figure 3.7). Therefore, conductor C1 can be interpreted as a smectite rich zone owing to its resistivity value (Logsdon & Laird, 2004). The

smectite deposits can be a impermeable cap structure that obstruct the fluid path due to its low porosity which is common in the volcano (e.g., Asaue et al., 2006; Newman et al., 2008; Piña-Varas et al., 2014; Seki et al., 2015; Yamaya et al., 2013). The appearance of the fluid path can be evidenced by the microseismic swarm. When the overpressurized fluid invades the rock body through its fracture system, the effective normal stress will be dropped, and microseismicity will be induced. (Benson et al., 2014; Kurz et al., 2004; Terakawa, 2017). The distribution of the seismic swarm indicates the direction of the overpressurized fluid path. In Figure 3.7, the east-west profile represented the underlying cumulate seismic swarm beneath the conductor C1 that can be interpreted as the overpressurized fluid path, which is sealed by the impermeable smectite layer.

The sensitivity test model "model P_M1" by removing the conductor C2 reduces determinant phases in that area, which indicates the downward conductive feature disappears (Figure 3.9). The regional effect of determinant phases and ellipses by removing C2 at 1.1 and 0.3 Hz indicates the clarity of C2 existence and justifies the feasibility of interpreting C2. In all the previous studies of Mt. Shirane (Kumagai et al., 2002; Nakano et al., 2003; Nakano & Kumagai, 2005; Nurhasan et al., 2006; Ohba et al., 2000, 2008; Ohba et al., 2019), a deep magmatic structure was claimed to supports the hydrothermal system. The geochemical analysis in the previous studies (Ohba et al., 1994, 2000, 2008; Ohba et al., 2019; Sano et al., 1994; Takano et al.,1994) demonstrated the fluid in the shallow hydrothermal system which is related to the invades fluid and the discharged fluid from the deep sealed magma. In the further deeper region, such fluid within the high-pressure and high-temperature then becomes the supercritical fluid (Aizawa et al., 2011; Hattori, 1993; Ogawa et al., 2014; Yamaya et al., 2013). The conductor C2

can be interpreted to the top of the sealed supercritical fluid. Such a supercritical state model of the saline brine was introduced by Afanasyev et al. (2018) for interpreting the volcanic hydrothermal systems. The sealing zone is breached that allows the fluid releases upward. The composition of this sealing zone could be quartz, gypsum, alunite, and other secondary minerals (Ohba et al., 2008; Ohba et al., 2019). The deep feature of this supercritical fluid is represented in Figure 3.13 by an N53°W profile. The deep resistor in Figure 3.7 is related to a much deeper feature in Figure 3.13, which can be traced to 7 km depth below the sea level (9 km depth from the surface). The structure with the lowest resistivity is represented above 0 m ASL, as in Figure 3.7. This supercritical fluid migration composed of magmatic gas from the deep degassing magma and the heated water. It provides high-temperature and high-pressure fluid injecting to the bottom of the shallow hydrothermal system of a volcano is one of the major types of phreatic eruption system (Stix & Maarten de Moor, 2018) (Figure 3.14).

The connecting vertical conductor C3 and its nearby resistor R1 are newly introduced features in this study, which are very critical because its position is highly related to the spatial distribution of micro-seismic swarm hypocenters (Figure 3.7). In the sensitivity test with “model P_M2”, removing C3 changes phase tensor distribution at 4.4 Hz only around the Yugama crater. The vanished sub-vertical conductive feature leads to a smaller determinant phase. The changes in the determinant phase at 1.1 Hz are affected by the overlaying modified complicated structures that demonstrate disarray differences. The connecting area at the west of Yugama crater lakes, therefore, could be interpreted due to the clarified existence. The upper part of C3 can be related to the conductor C1 that interpreted as the extension of C1, which is part of the smectite clay cap. The temperature of this smectite increase with depth and the approach to conductor C2 that has

much high-temperature. During the temperature increasing, the smectite-to-illite conversion is induced. The smectite starts reacting at 100°C, converses to illite, and form mixed-layer clay in 300-400°C, which is a typical hydrothermal reactivity (Eberl et al., 1978; Inoue et al., 1992). During the transformation, the porosity and permeability decrease with the increasing illite proportion and illite/smectite ratio that the mixed layer generally becomes further impermeable (Liu et al., 2016). However, this transformation could also probably generate a fracture zone in the structure that, instead, increases the permeability of the structure (Vidal et al., 2018). Furthermore, when this mixed-layer clay goes deeper, approach to the sealing magma, the euhedral illite, and berthierine could be produced with relatively high porosity (Yau et al., 1987). With those situations, the pore-contained mineral could be a potential path of hydrothermal fluid. Thus, we then interpret C3 and R1 as a part of the mixed-layer clay with a smectite-to-illite conversion. While the highly pressured magmatic gas from C1 flow through the path between C3 and R1, it leads to micro-seismic swarms.

Therefore, the phreatic eruption system of Mt. Shirane can be comprehended by the electrical resistivity model interpretation (Figure 3.15). Beneath the summit of Mt. Shirane, below 600m (ASL) is the top of the supercritical state brine conduits, which provided from the deeper degassing magma. The brine conduit is sealed by breach sealing zone composed of quartz, gypsum, alunite, and other secondary minerals. The fluid is released from the breach and flows upward through the fracture zone within the mixed-layer clay. This activity creates micro-seismic swarms beneath the Yugama crater lake at 600-1400 m ASL. This hydrothermal fluid flow is blocked by an impermeable, bell-shaped smectite clay cap at 1400m ASL. The local meteoric water flows through unrecognized fractures then mix with crater lake water and

magmatic gas in this space. By heating with the high-temperature magmatic gas, this space becomes a liquid/vapor reservoir. The phase change in this two-phase-reservoir leads the cycle of magnetization-demagnetization (Takahashi & Fuji, 2014). Thus, the location of the geomagnetic dipole sources indicates the two-phase-reservoir. The invasion of the hydrothermal fluid flow through the fracture zone within the clay cap to Yugama crater lake is evidenced by the seismicity there during the 2014 unrest event.

3.6 Robustness test of the model feature by separating the dataset into two

An example in Figure 3.16 demonstrates different features in the two resistivity models, "model P_S1" and "model P_S2", with the data from separated data sets, S1 and S2, respectively. The data sets S1 and S2 were randomly selected from the previously observed data with half numbers of the sites. All the parameters in the computation were consistently set as when "model P" was computed. The RMS value of "model P_S1" and "model P_S2" are 1.18 and 1.36 when they were converged at 16^{th} and 20^{th} iteration, respectively. The low RMS value indicates both models are well-fitted with the observed data. However, the demonstrated features in the two models are dissimilar. The complicated subsurface structures could induce such a result. The existence of primary features (two primary conductors C1 and C2 and their connection C3, the resistor R1 underlying the shallow conductor C1) are consistent that indicates the robustness of their existence. The minor features (e.g., the shape of structures) are different that indicate the selection of the sites' location, and their data could influence the appearance of the representing features.

3.7 Robustness test of the model feature by changing the beta

In section 3.3, the regularization function $\phi_D(\boldsymbol{m}_D)$ was controlled by trade-off parameter $\boldsymbol{\beta^2}$ to reduce the galvanic distortion effect. The extent of galvanic distortion effect reduction can be adjusted by choosing different $\boldsymbol{\beta^2}$. This study chose $\boldsymbol{\beta^2}$=0.01 by referring to the previous studies and computed the final model, "model P". In this section, a robustness test of the model feature by changing the $\boldsymbol{\beta^2}$ was operated to verify the sensitivity of the modeling result to this parameter. Besides "model P" with chosen $\boldsymbol{\beta^2} = 0.01$, three testing models were computed with different $\boldsymbol{\beta^2}$=0.1, $\boldsymbol{\beta^2}$=1.0 and $\boldsymbol{\beta^2}$=10.0 and named as "model P_B0.1", "model P_B1" and "model P_B10", respectively. The RMS value of those three models was 1.28, 1.42, and 1.26, respectively. Figure 3.7 demonstrates the value of four components of the galvanic distortion matrix D_{xx}, D_{xy}, D_{yx}, and D_{yy}.(Equation 3.36). With $\boldsymbol{\beta^2}$=10.0, the diagonal components of the galvanic distortion D_{xx} and D_{yy} are close to 1 in most of the sites, and the off-diagonal components D_{xy} and D_{yx} are close to 0 in most of the sites. With the definition in Equation 3.25a, this result indicates that the observed data represents the regional features, and the galvanic distortion effect was not considered in "model P_B10". The components of the galvanic distortion matrix were generally increasing with the decreasing $\boldsymbol{\beta^2}$. That indicates the observed response was further regarded as the distorted response when $\boldsymbol{\beta^2}$ was smaller. There was the extreme value of distortion parameters at four of the sites when $\boldsymbol{\beta^2} = 0.01$. Such value indicates that the observed data from those sites was taken by the program as seriously distorted data. This special situation should be carefully discussed in the next paragraph.

To verify the effect of the distortion matrix, the modeling result and the phase tensor were compared within different models. The models that computed with different trade-off parameter $\boldsymbol{\beta^2}$ are demonstrated in Figure 3.18. The region away from the observation sites at least 100m was masked in the profiles for representing how the result with different $\boldsymbol{\beta^2}$ were changed in the strongly controlled and the weakly controlled feature. The primary features (e.g., the conductors C1, C2, and the resistor R1) are similar in different models. All these primary features were in the strongly controlled region that denoted the $\boldsymbol{\beta^2}$ did not intensely affect those features. Conversely, the models demonstrated some dissimilarities of the features at the place where out of the strongly controlled region. Another comparison with phase tensor analysis is demonstrated in Figure 3.19. The data from observation and different calculated models represented similar features at 70 Hz and 8.8 Hz in the phase tensor plot but partly dissimilar features at 1.1 Hz. According to the sensitivity test with "model P_M1" (Figure 3.9), the data at that frequency represented the feature at the depth where conductor C2 existed. This difference has been represented in the resistivity model (Figure 3.18) at 1km east of Yugama. The sites with extreme values that were represented in Figure 3.17 was marked in Figure 3.19. The four sites represented the locally affected differences at 1.1 Hz, but most of the other sites represented similar features. This result denotes that the extreme value did not affect the model as much as it represented in the distortion component plot.

3.8 The Inversed Model with Newly Observed Data and the Discussion

This study utilized two sets of MT/AMT data for a time-lapse interpretation to comprehend the probability of temporal changes in the volcanic hydrothermal system beneath Mt. Shirane. One

data set is from the previous observation from 2001 to 2005, and another one is from the new observation from 2017 to 2018.

The phase tensor analysis for the observed data versus the calculated model represents a proper fitting at higher frequencies (17.5-4.4 Hz) and a fair fitting at a lower frequency (1.1 Hz) (Figure 3.20). The analysis result indicates that the shallow features in the calculation product are credible. According to the reported volcano activity and frequent seismic events, there could be changes in the subsurface features that may be represented in the models with different data sets. A comparison of the modeling result with previously observed and newly observed data is represented in Figure 3.21 and Figure 3.22 within the same east-west and north-south cross-sections, respectively. In the east-west section (Figure 3.21), the major features, the two primary conductors and the connecting vertical conductor, have no significant changes with the comparison to the previously observed data. The notable difference is that the underlying resistor beneath the bell-shaped conductor in the model with newly observed data is more conductive (from 100 ohm-m to 10 ohm-m). Another difference is the surface at [Easting=800m] significantly resistive (>1000 ohm-m), which was not represented in “model P” from all 91 sites (Figure 3.8) but was represented in the two models with separated data sets (Figure 3.16). In the north-south section (Figure 3.22), the notable difference is that the shallow conductor occurs a discontinuous part that replaced by a relatively resistive gap. Above that gap is a more resistive zone (>100 ohm-m), which does not represent in the model with previously observed data. The resistivity and the shape of the deep conductor are also different within the two models.

Instead of hastily interpreting the differences between two models as the temporal changes due to the different cycling volcanic activity periods, which has been described in the previous studies of Kusatsu-Shirane volcano (Kumagai et al., 2002; Nakano & Kumagai, 2005; Ohba et al., 2008; Ohba et al., 2019), the difference between two data sets should be firstly considered. It must be mentioned that the numbers of observation sites between the two data sets have a large difference. There are 91 sites in the previously observed data, but only ten sites in the newly observed data. Therefore, a model that is calculated with the data from much fewer sites could be further influenced by the numbers and locations of the sites, as the demonstrated example in Figure 3.16. Although the probability of the influence from site allocation can not be ignored, the comparison of the phase tensor plot between the data from previous observation and new observation positively represents the observed differences (Figure 3.23). The observed data represents relatively similar features in the shallow structure (17.5 Hz) but different features in the deeper structure (1.1 Hz). That the temporal changes probably exists. The probability can be further enhanced if the site's location in two data sets is further closer.

This study demonstrates that interpreting temporal changes in the previously and newly observed data sets has difficulty when the number of sites has a massive difference. The difference in two testing models with separated data sets satisfies the importance of the serried allocation of the observation sites. When the subsurface structure is complicated, a time-lapse monitoring system requires consistent observing locations and a close number of sites. In this study, the time-lapse monitoring with only MT data could not robustly verify the temporal changes due to the difference in the sites' conditions between the previous and new observations. Interpreting the demonstrated differences between the two models (Figure 3.21 & Figure 3.22) is not as reliable

as interpreting “model P” (Figure 3.15). The interpretation of model N is temporarily held here before justifying the existence of changed features. For this objective, this study utilizes an alternative examination with CSEM observation data, which will be introduced in the next chapter for clarifying the credibility of the difference in the time-lapse monitoring.

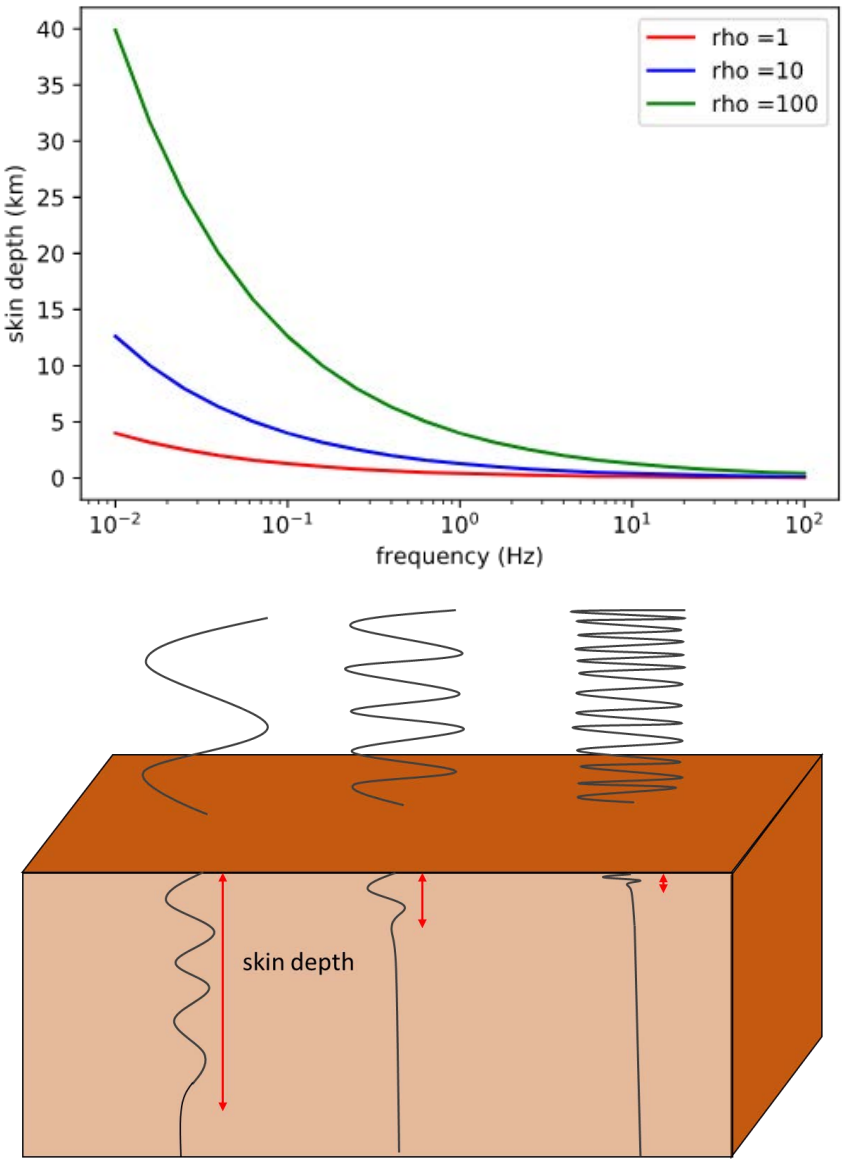

Figure 3.1

The frequency-space relationship represented by skin depth with its schematic.

The upper subfigure plots the skin depth in the homogeneous earth with different resistivity. The lower subfigure presents a schematic of the skin depth at different frequencies.

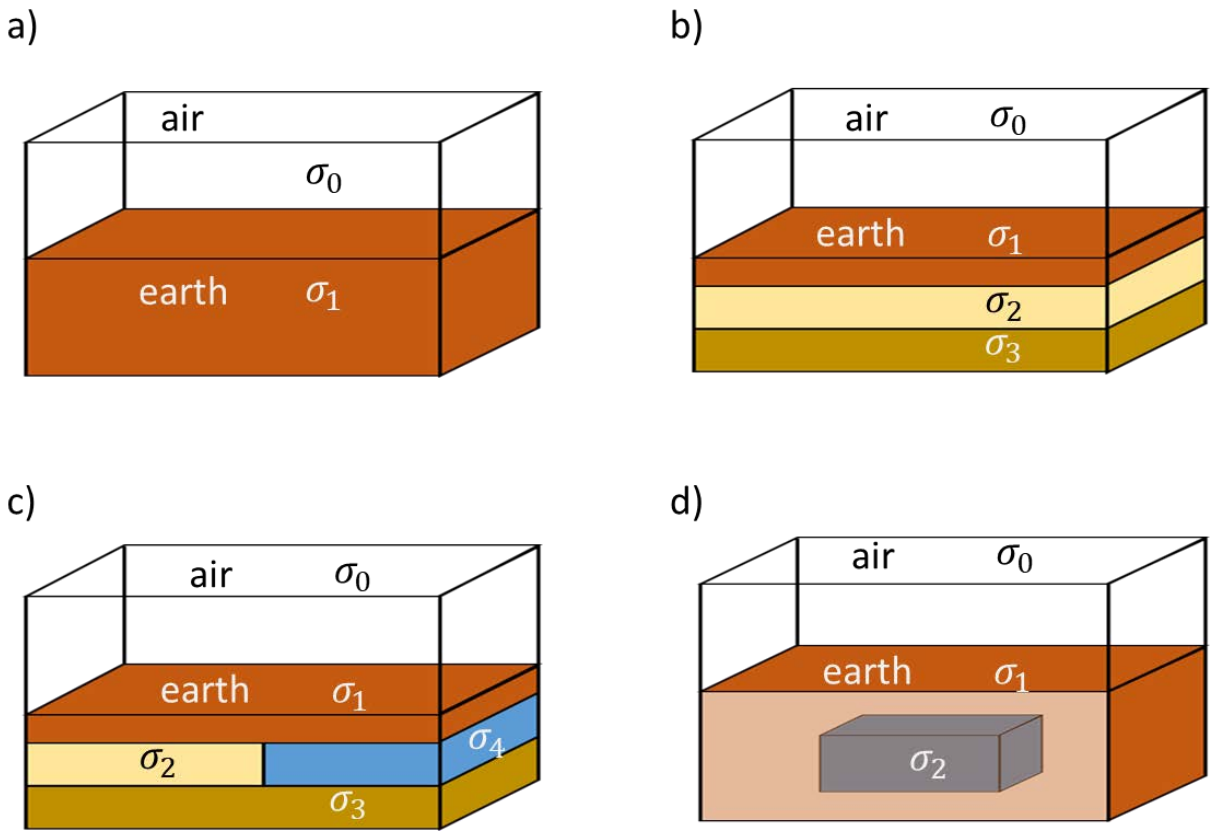

Figure 3.2

Schematic diagrams of different dimension subsurface structures.

The type of dimensions for subsurface structure can be simplified to (a) a uniform half-space; (b) 1-D layered earth with horizontal conductivity differences; (c) 2-D structure; (d) 3-D structure.

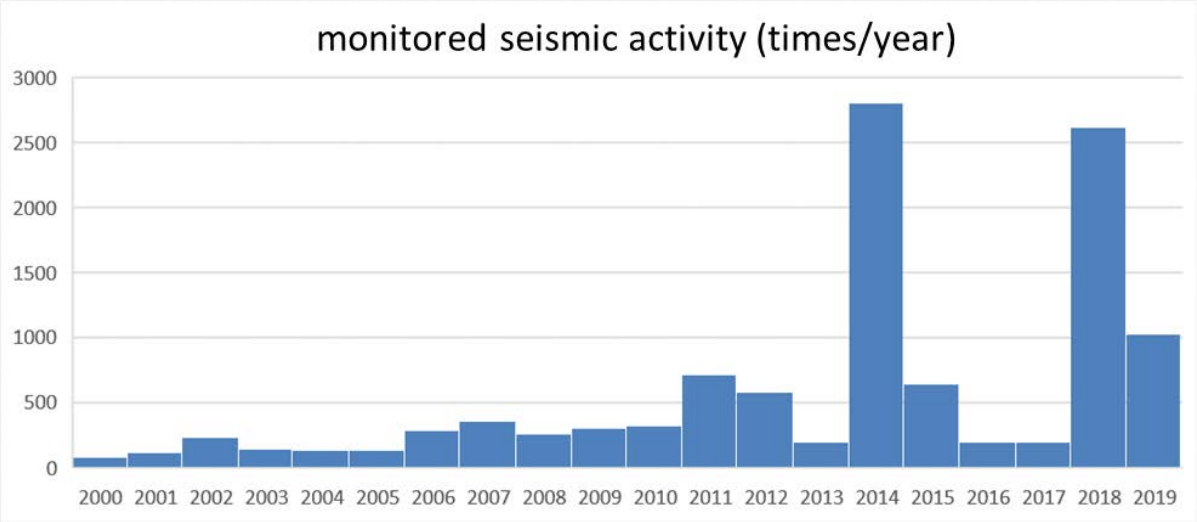

Figure 3.3

Monitored seismic activities from 2000 to 2019 surrounding the Kusatsu-Shirane volcano.

This chart is based on the monitored data from Japan Meteorological Agency which recorded the detected seismic activities from 2000 to 2019 surrounding the Kusatsu-Shirane volcano.

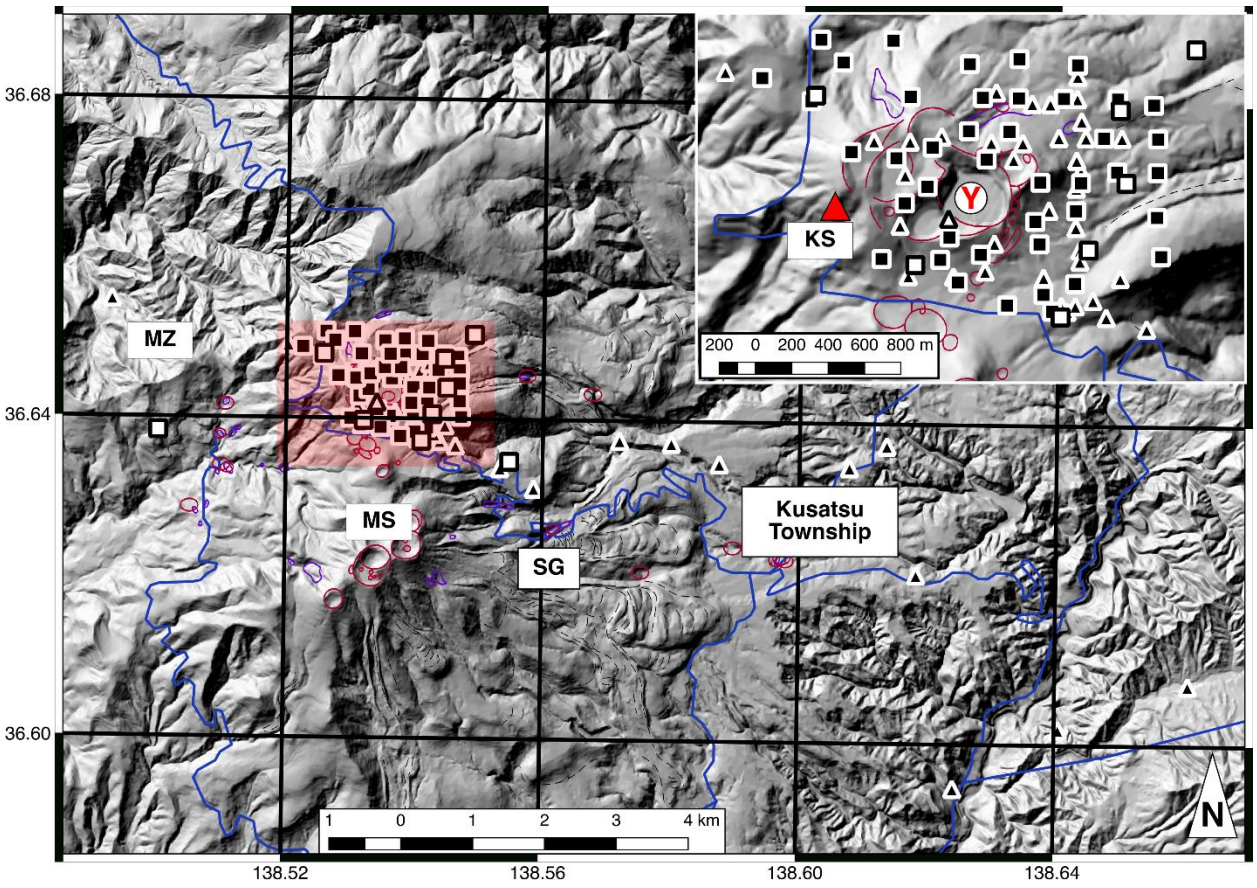

Figure 3.4

A regional-scale and a local-scale map of Kusatsu-Shirane Volcano with previously observed and newly observed MT/AMT stations.

The base map is the topographic map with grayscale shaded relief. The square and triangle symbols denote the MT and AMT stations, respectively. The black-filled and white-filled polygon symbols and triangle symbols denote the previously observed and newly observed stations, respectively. The red circles and open curves show the craters of past eruptions. The purple closed curves show the fumarole zones. The blue curves show the local highway as a reference item on the map. The abbreviation symbol “SG”, “MS” and “MZ” denotes the location of Sesshougawara fumarolic area, Mt. Motoshirane, and

Manza hot spring field, respectively. The area of the local-scale map is masked by a red rectangle. In the local-scale map, additionally, the abbreviation symbol “KS” denotes Mt. Shirane and the red triangle denotes its mountain peak. The white circle with symbol “Y” denotes the center of Yugama crater lake.

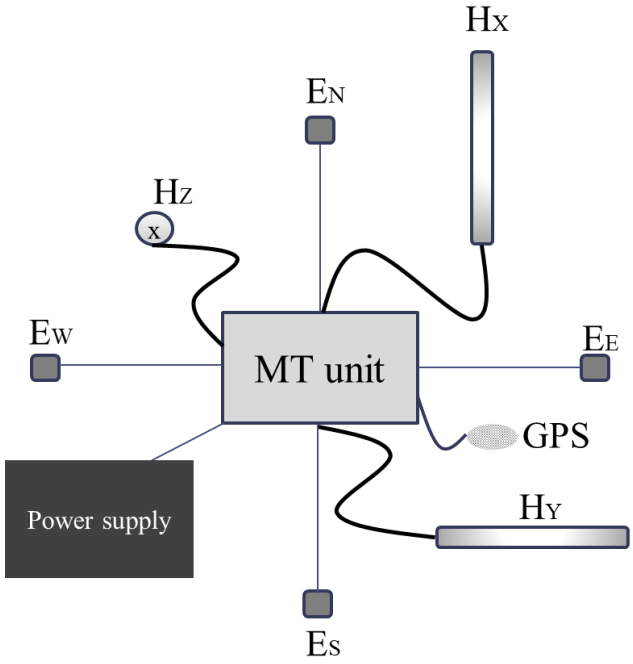

Figure 3.5

A schematic diagram of a 2E3H MT receiver.

The two sets of electrodes are installed to align with the ground surface. Hx and Hy magnetic coil sensors are horizontally installed and Hz magnetic coil sensor is vertically installed overlaying in the ground. The MT unit synchronizes with the GPS signal in full of the measurement.

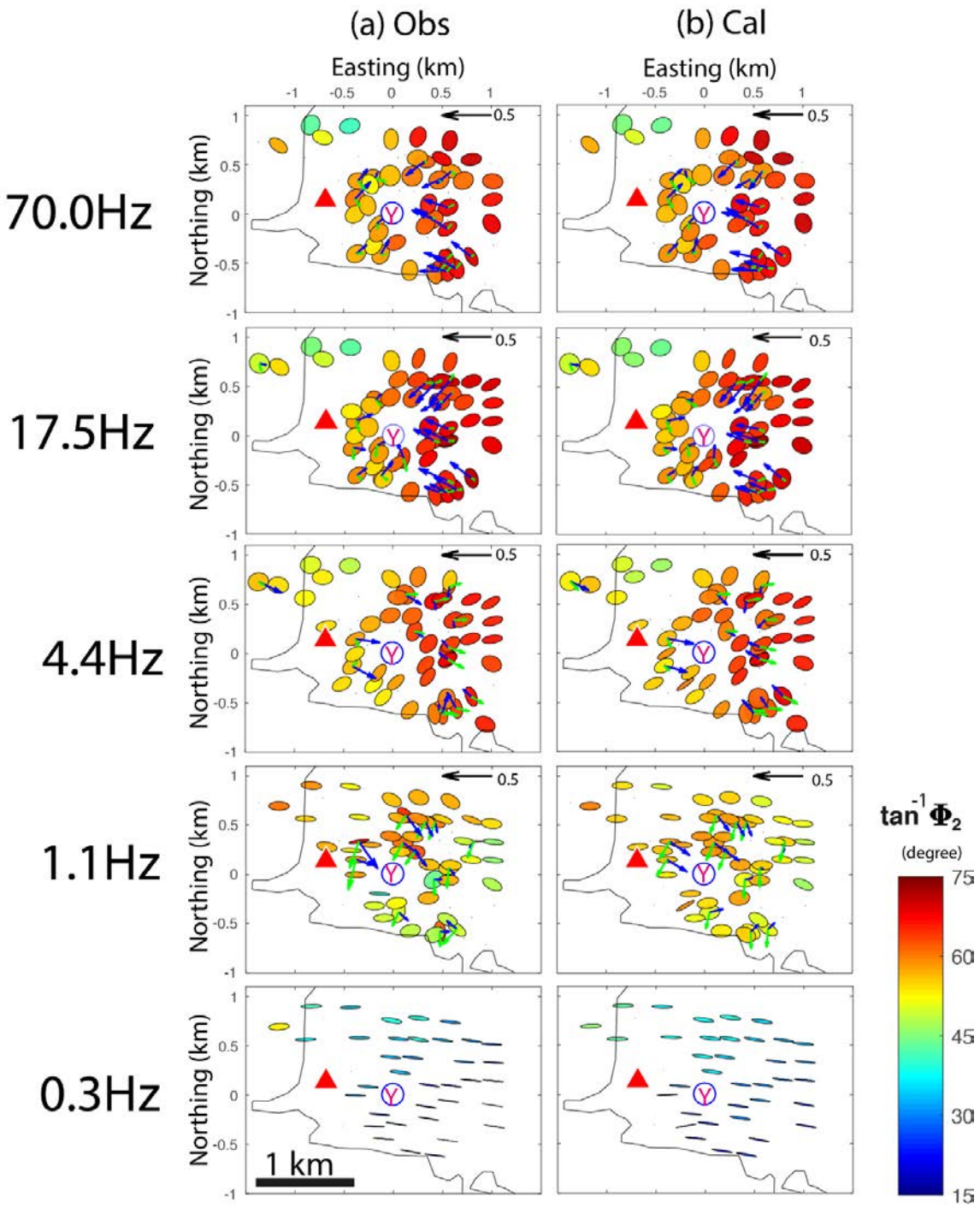

Figure 3.6

Comparison of phase tensor ellipses of the previously observed MT data between (a) the observed result (Obs) and (b) the best-fitted final model (Cal).

The observed data and the calculated data is represented in the left and right column, respectively. The chosen frequencies for all the four data sets are 70 Hz, 17.5 Hz, 4.4 Hz, 1.1 Hz, and 0.3 Hz, from top to bottom. The phase tensor ellipses are filled by the angle of the determinant phase Φ_2, which is the geometric mean value of maximum and minimum of phase tensor. The black strike arrow represents a unit Parkinson's induction vector with a tipper value 0.5. The blue and green strike arrows represent the real and imaginary Parkinson's induction vector, respectively. The black curve, red triangle and blue circle with symbol "Y" denote local highway, the mountain peak of Mt. Shirane and center of Yugama crater lake, respectively.

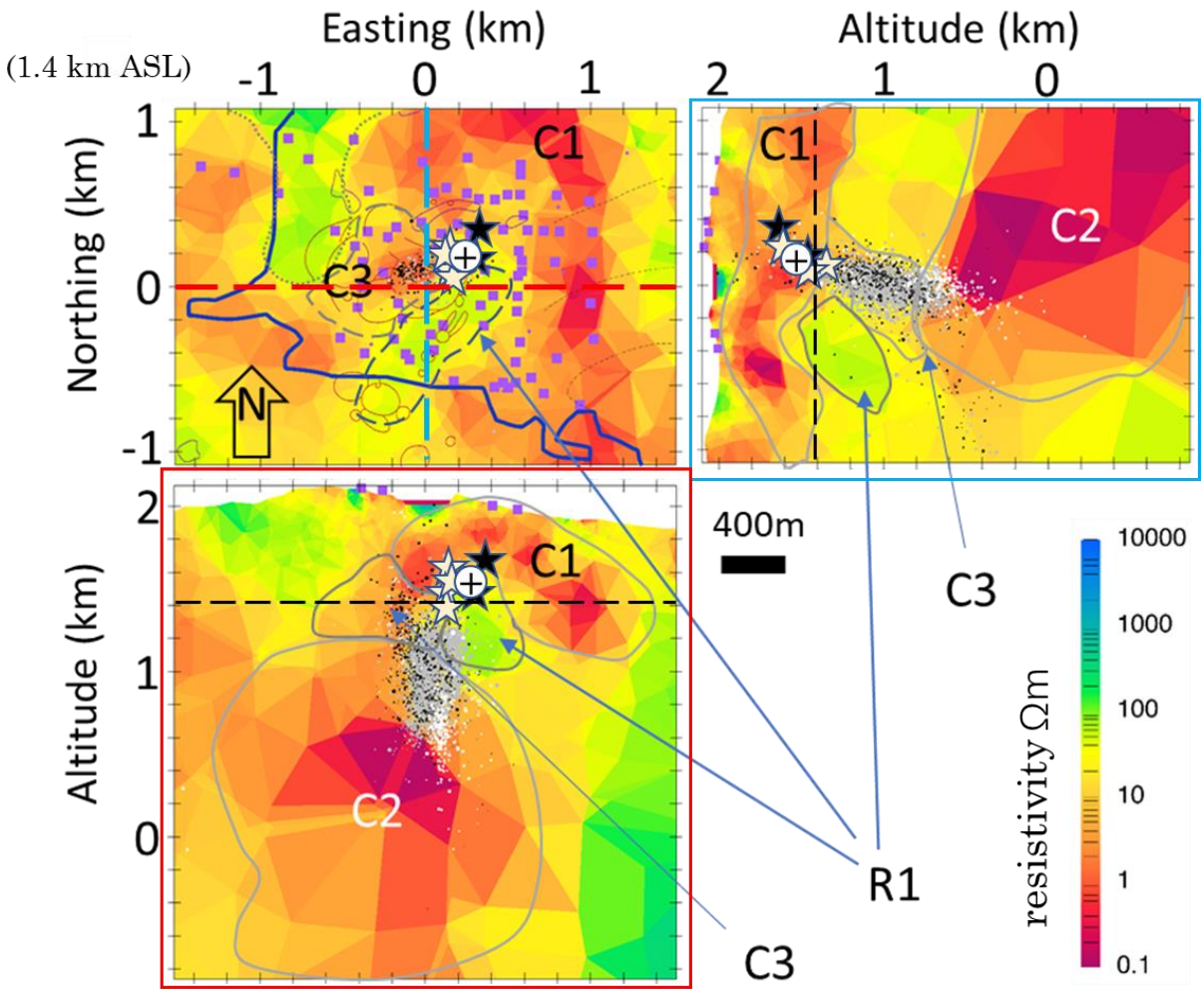

Figure 3.7

The multiview projection of the best final model from previously observed MT/AMT data.

The upper-left subfigure is the plan view map at 1400 m height (ASL). The red and blue lines in the plan view map denote the east-west and north-south sections cutting through Yugama crater lake, respectively. The lower-left subfigure is the east-west direction profile. The upper-right subfigure is the north-south direction profile. In all the subfigures, the purple squares denote the location of MT/AMT stations. The cross denotes the inflation source. The light and dark stars denote the past magnetization and

demagnetization centers, respectively. The white, gray and black dots denote the micro-seismic hypocenters before, after and during the recorded high seismic activity period in March-May 2014, respectively. All the MT/AMT stations and micro-seismic hypocenters are clipped with a 200-meter-boundary along with either the map or profiles. The blue curve denotes the local highway. In the plan view map, the red circles and open curves show the craters of past eruptions; the purple closed curves show the fumarole zones, and the dash lines denote the Aoba lava flow.

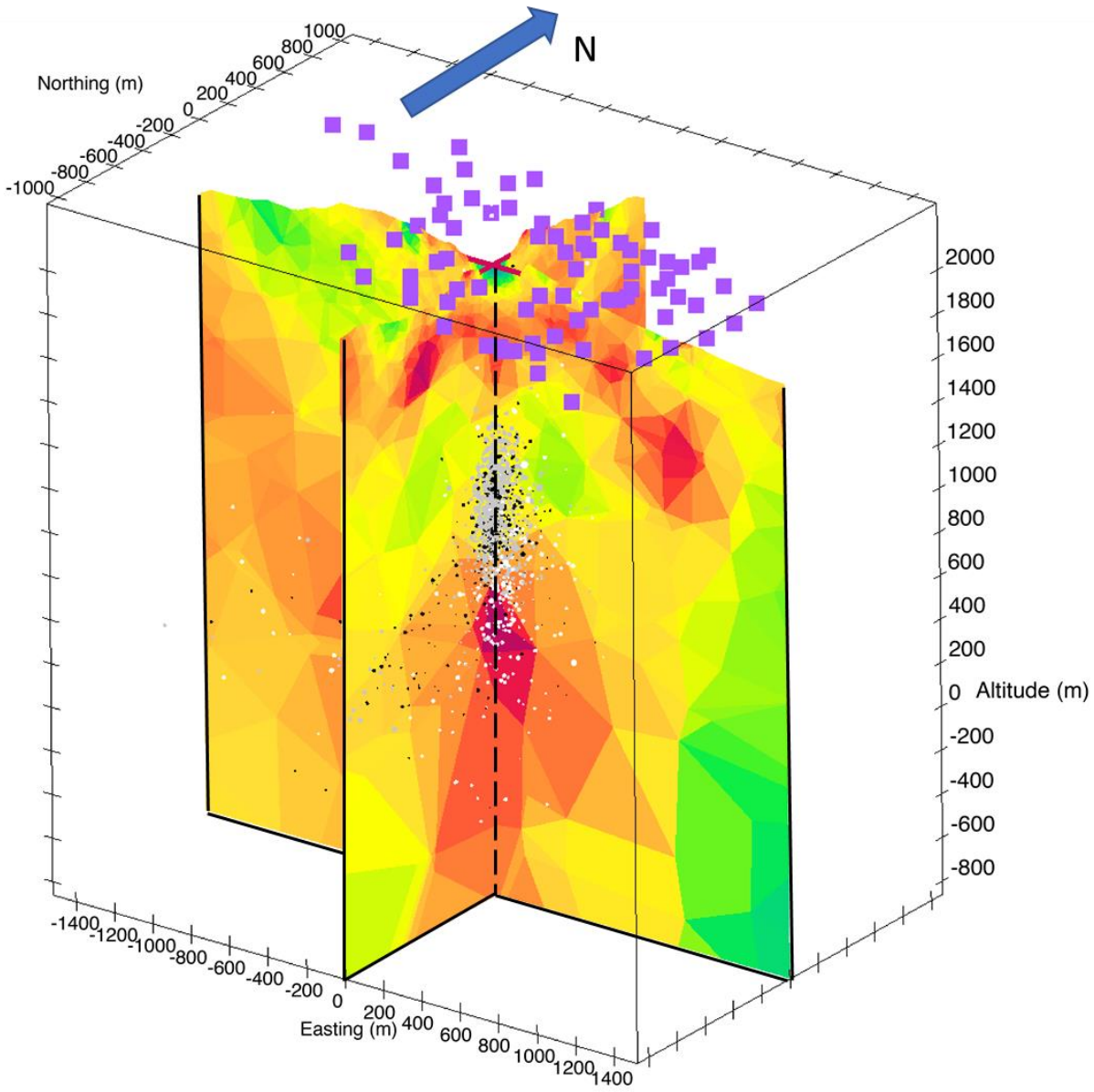

Figure 3.8

The crossed vertical profiles of the best final model “model P”.

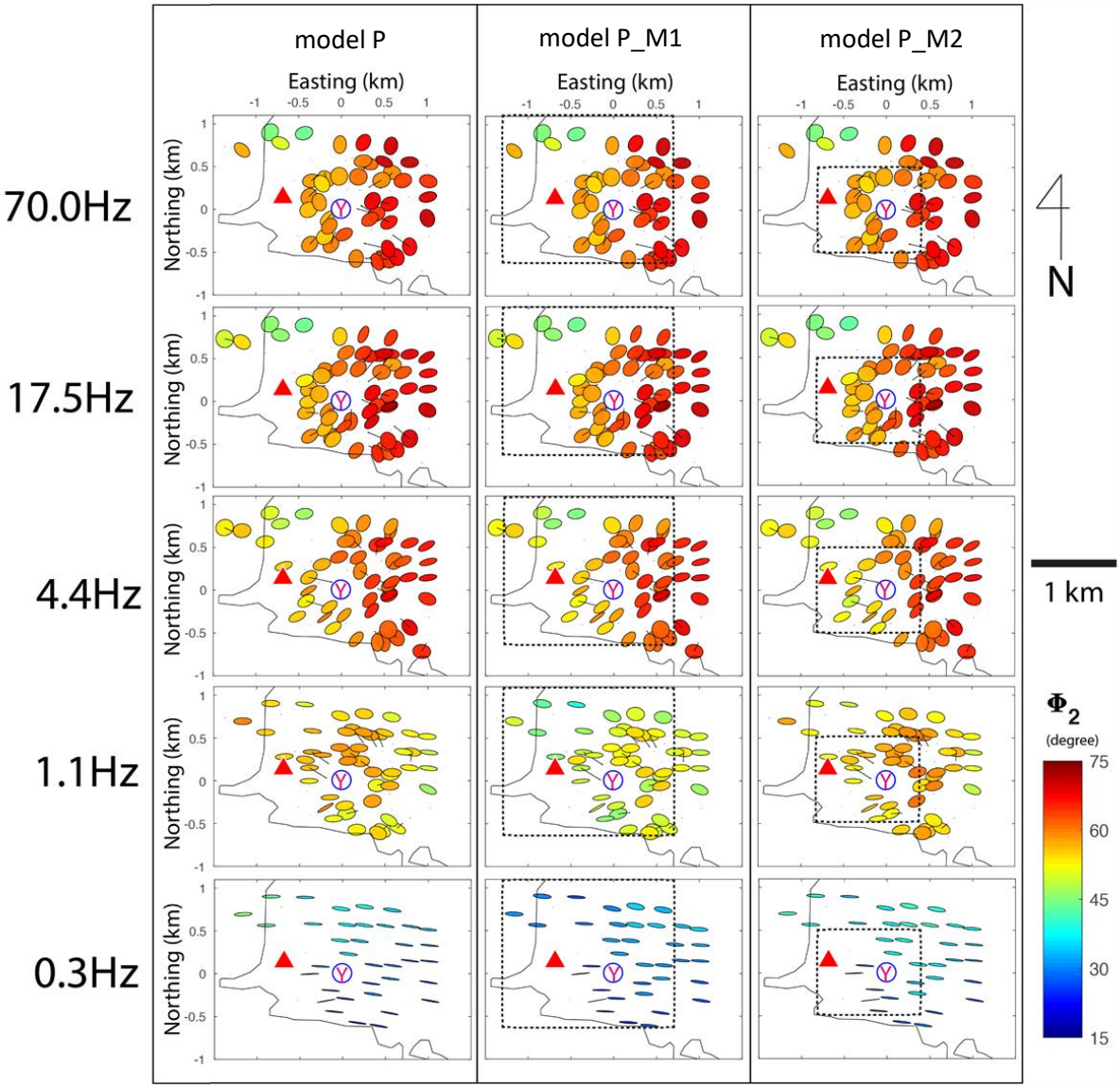

Figure 3.9

Comparison of the phase tensor ellipses between the data from “model P”, “model P_M1” and “model P_M2”.

The calculated data from the best-fitted final model “model P”, the modified model “model P_M1” and modified model “model P_M1” is represented from the left to the right columns, respectively. The chosen frequencies for all the four data sets are 70 Hz, 17.5 Hz, 4.4 Hz, 1.1 Hz, and 0.3 Hz, from top to bottom. The phase tensor ellipses are

filled by the angle of the determinant phase Φ_2, which is the geometric mean value of maximum and minimum of phase tensor. The horizontal direction areas of modified model 1 and model 2 are separately marked with dashed rectangles. The black strike arrows show the direction of Parkinson's induction vectors. The black curve, red triangle and blue circle with symbol "Y" denote local highway, the mountain peak of Mt. Shirane and center of Yugama crater lake, respectively.

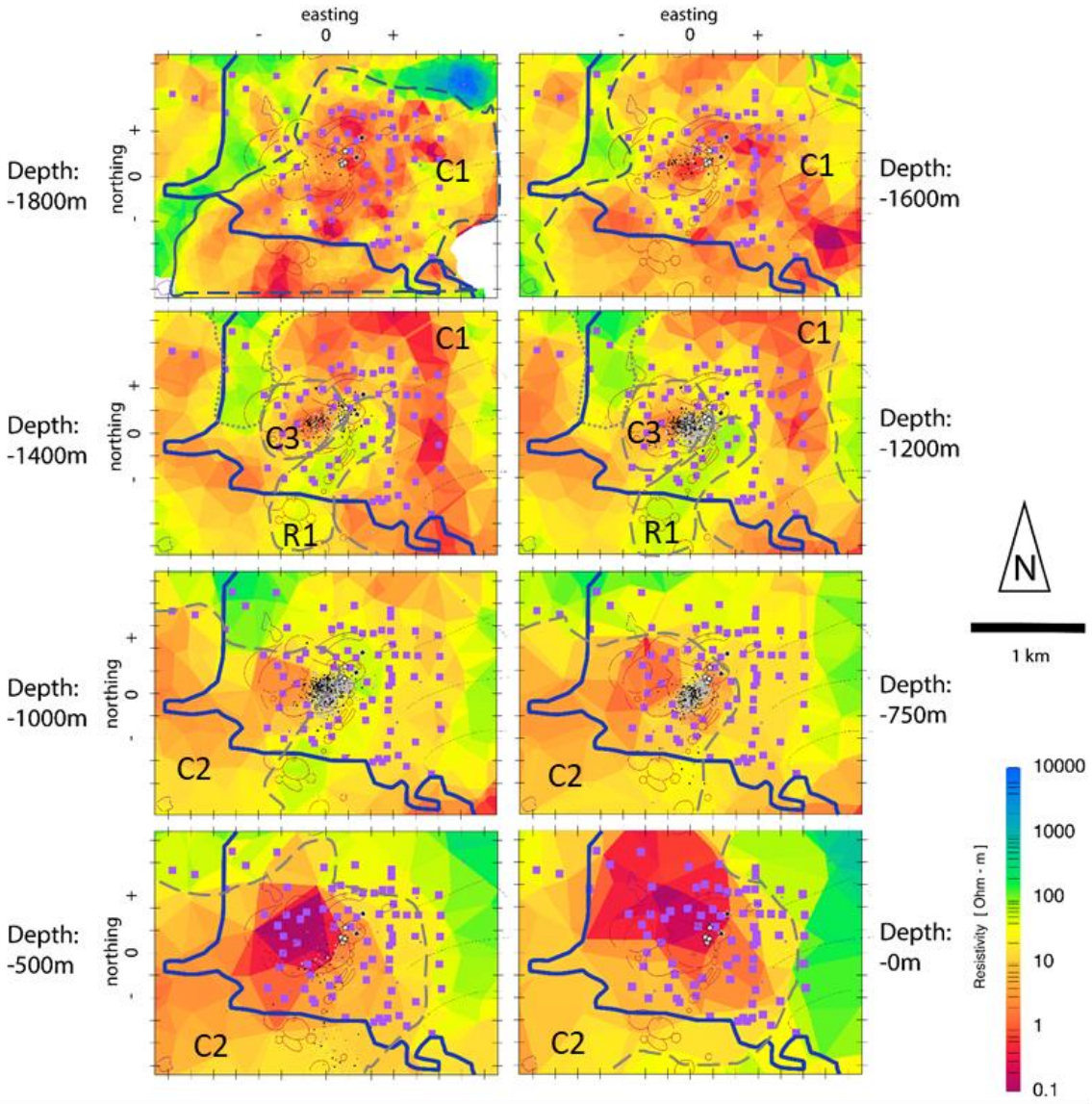

Figure 3.10

The plan view map of the “model P” in different depth.

The purple squares denote the location of MT/AMT stations. The cyan cross denotes the inflation source. The white and black stars denote the past magnetization and demagnetization centers, respectively. The white, gray and black dots denote the micro-seismic hypocenters before, after and during the recorded high seismic activity period in

March-May 2014, respectively. All the MT/AMT stations and micro-seismic hypocenters are clipped with a 200-meter-boundary along with either the map or profiles. The blue curve denotes the local highway. The red circles and open curves show the craters of past eruptions. The purple closed curves show the fumarole zones. The dash lines denote the Kagusa lava flow.

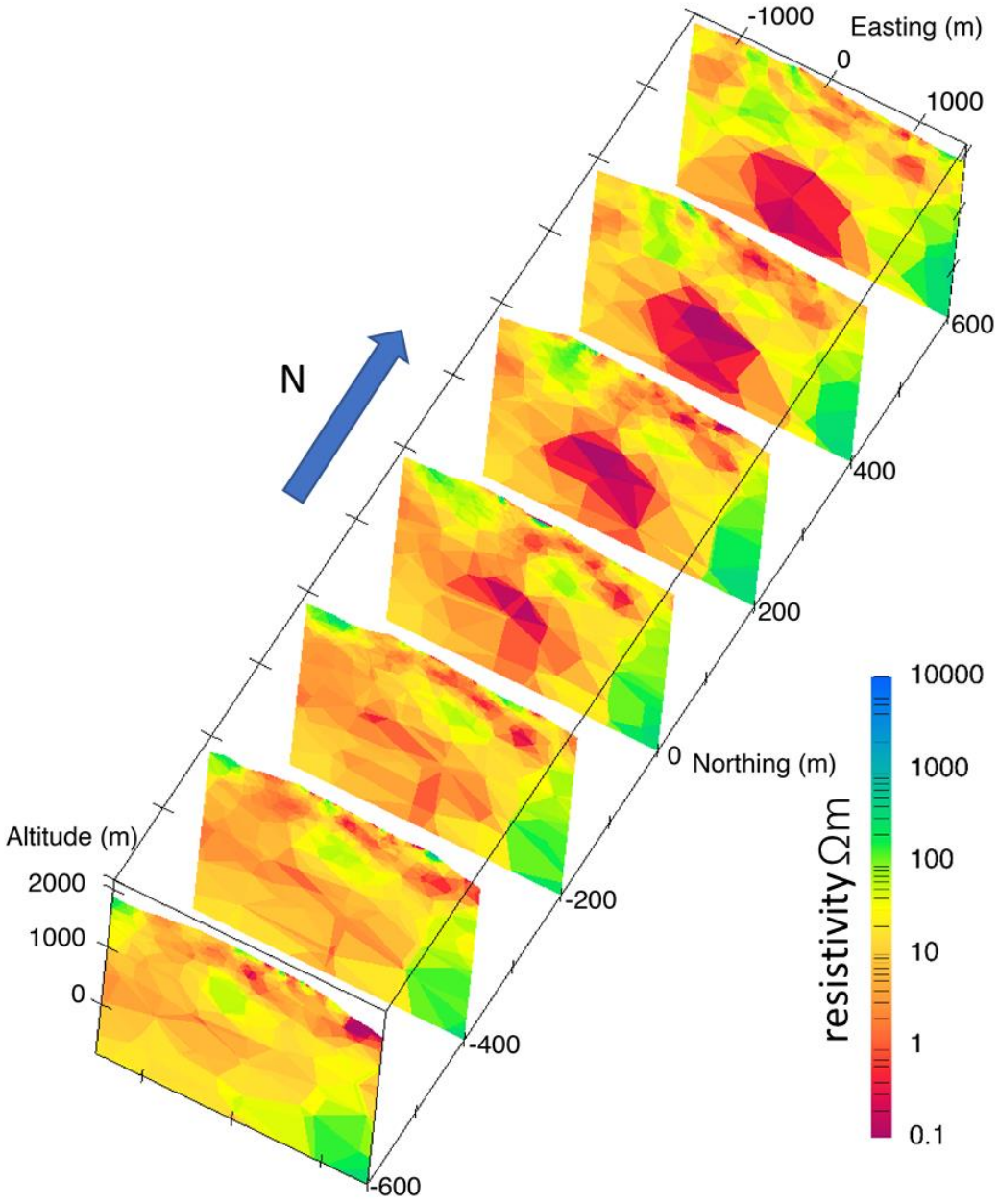

Figure 3.11

The slice view of east-west profiles from the “model P”.

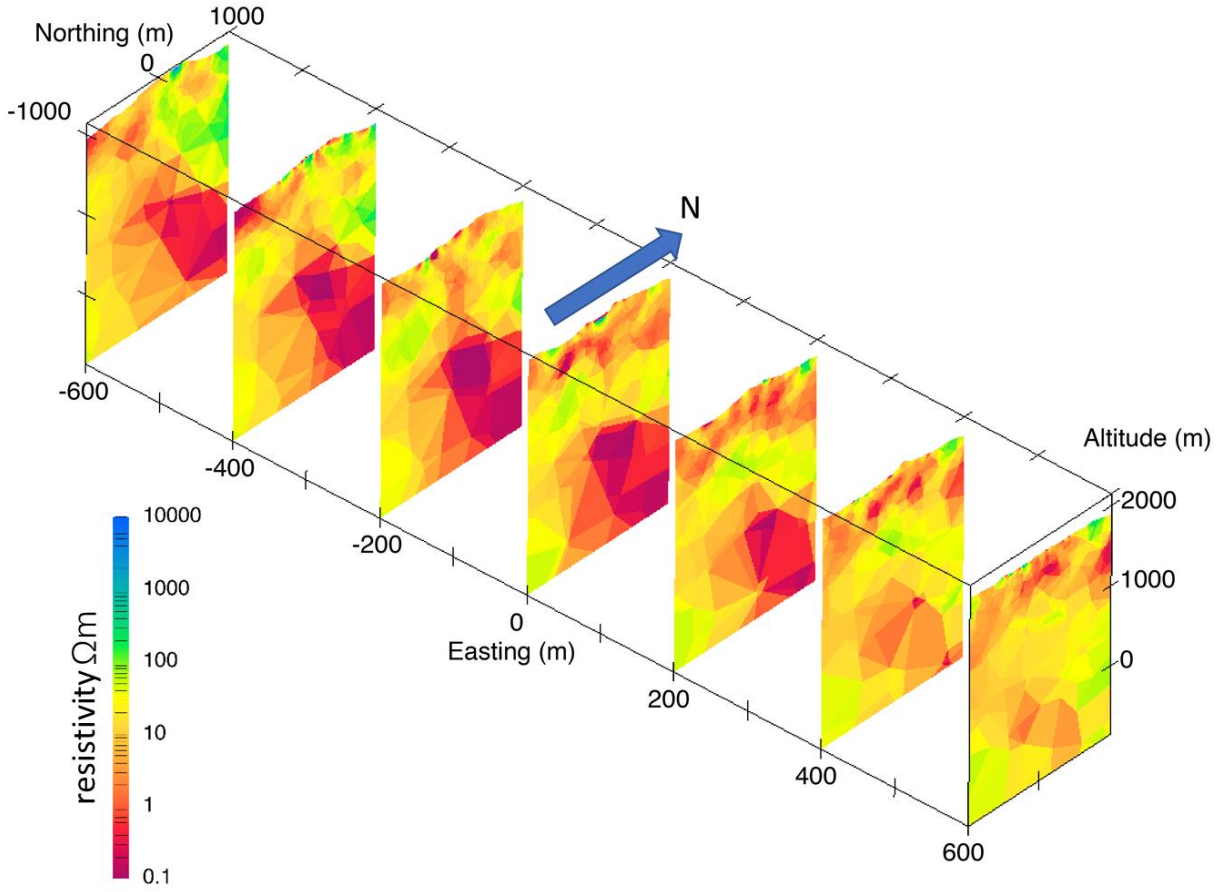

Figure 3.12

The slice view of north-south profiles in the “model P”.

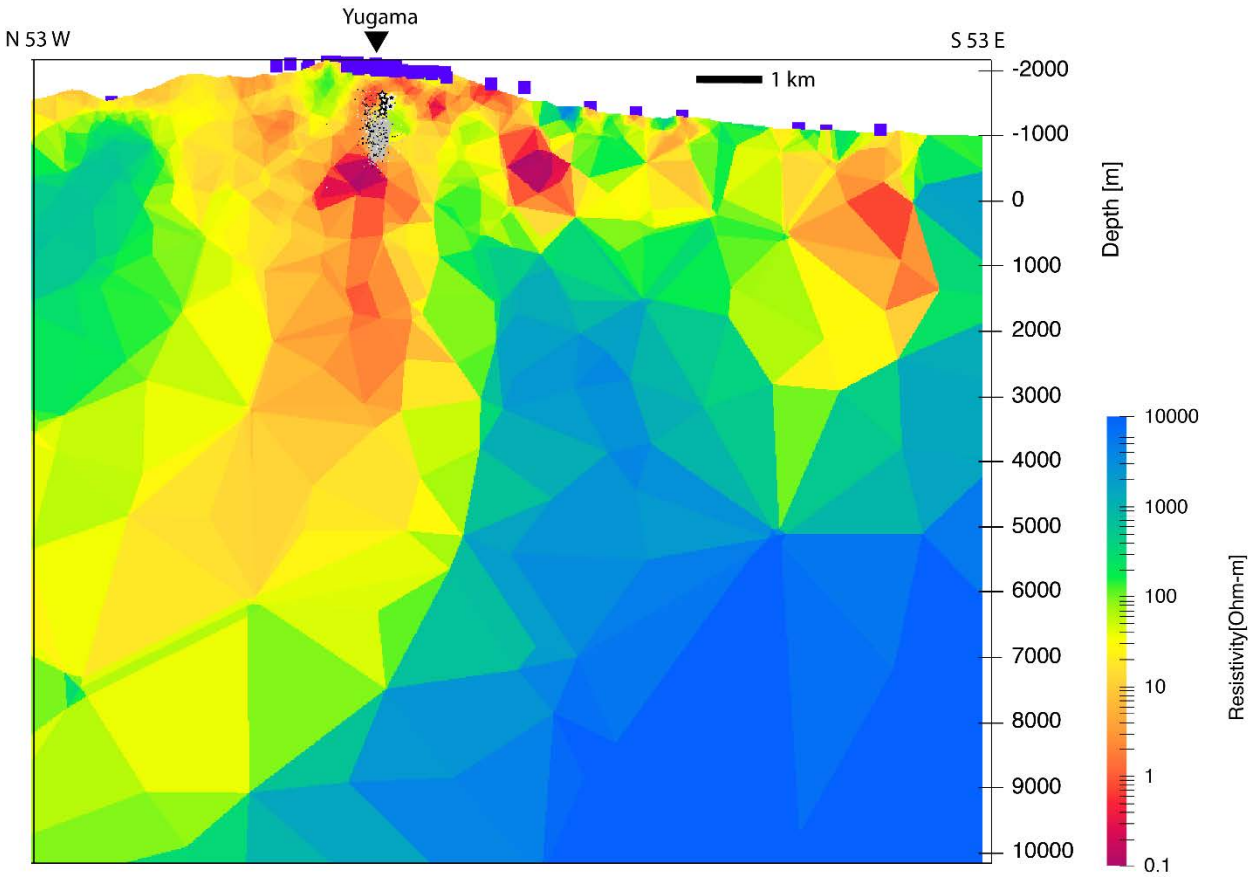

Figure 3.13

The oblique profile of the resistivity model “model P”.

This profile aligns with N 53°W direction and represents the further deeper features or the model. The upper black bold line denotes the scale bar of 1 km length.

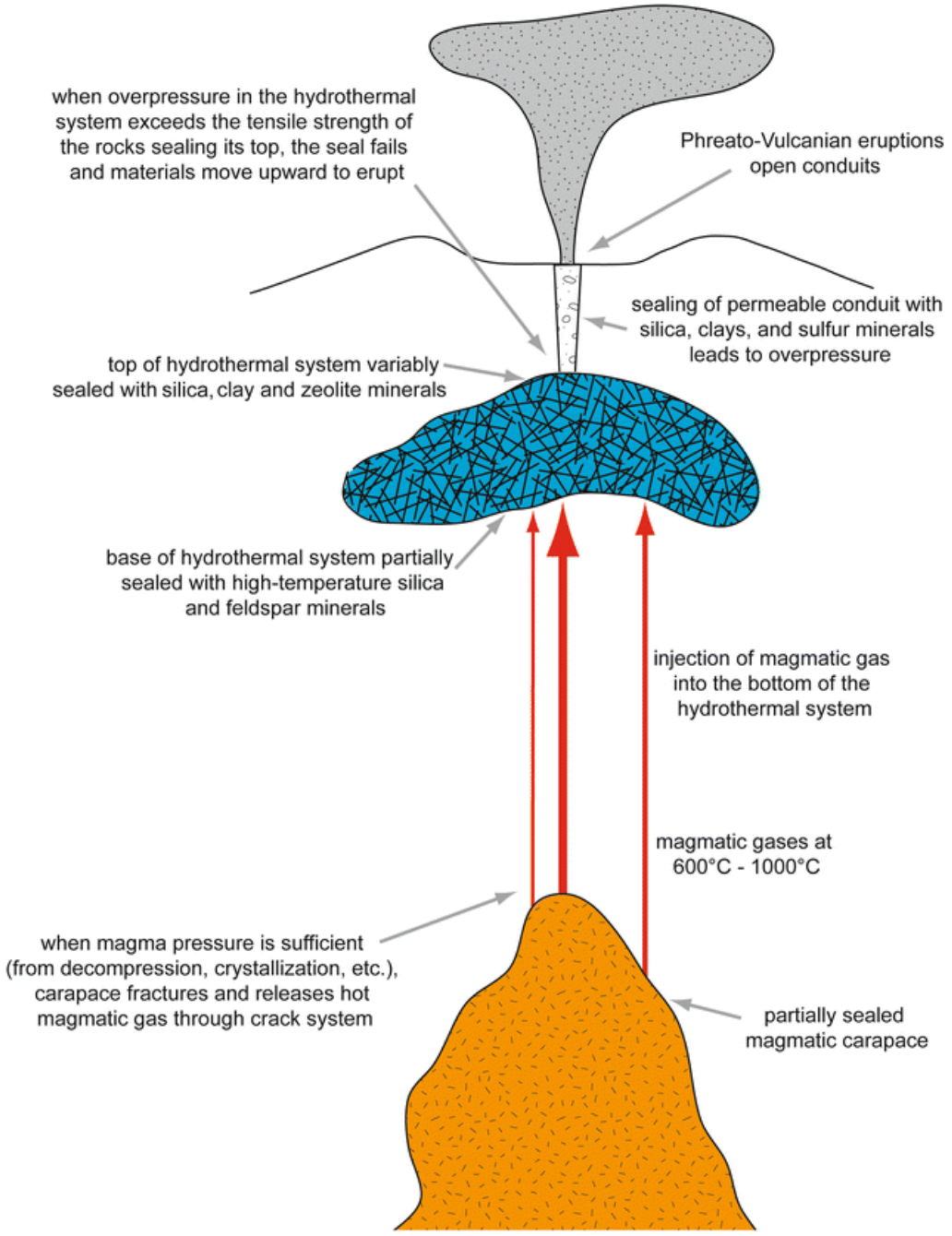

Figure 3.14

The schematic diagram for the underlying hydrothermal systems beneath the Yugama crater. (Stix & Maarten de Moor, 2018)

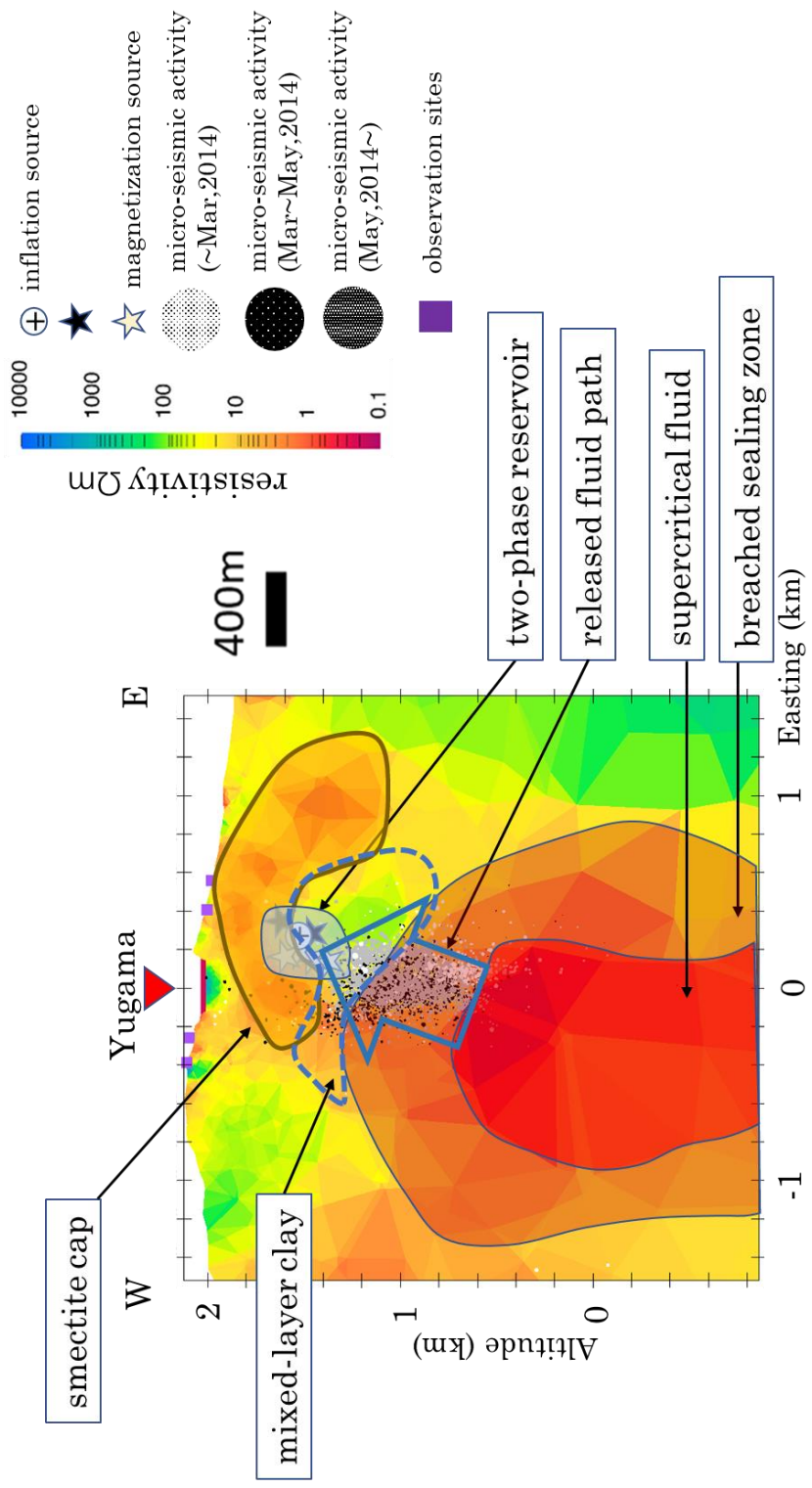

Figure 3.15

Interpretation of inversed modeling result with previously observed MT/AMT data.

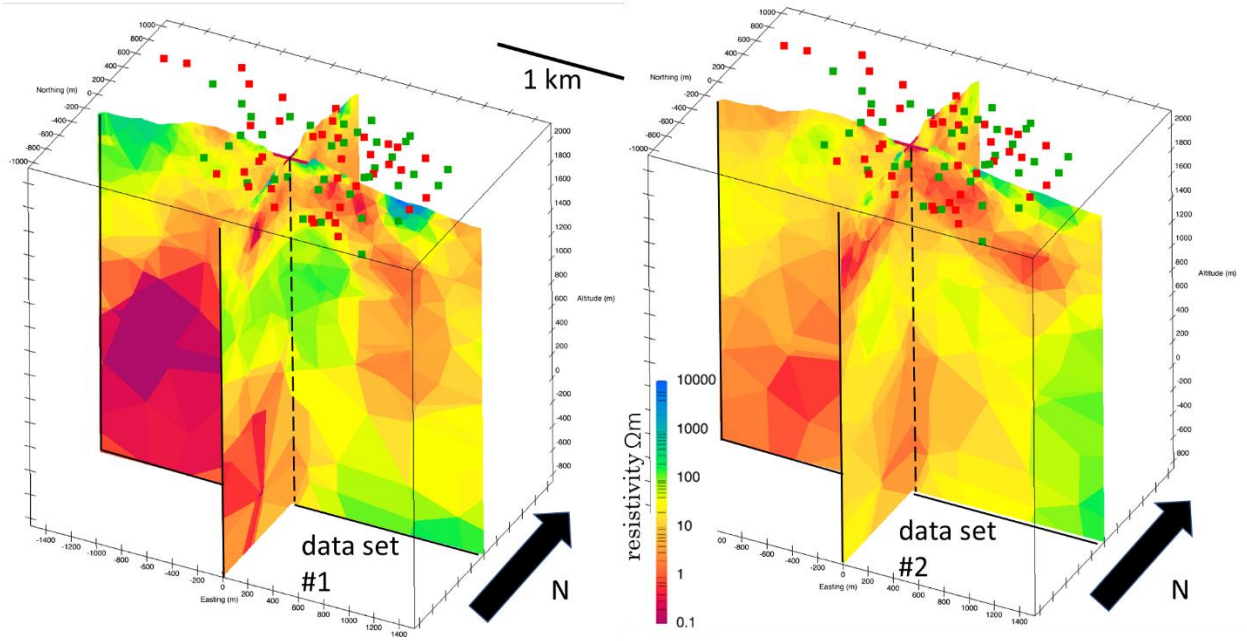

Figure 3.16

Resistivity models “model P_S1” and “model P_S2”.

The models were computed with the data from two randomly separated data sets S1 and S2. The red and green squares denote the sites in data set S1 and S2, respectively.

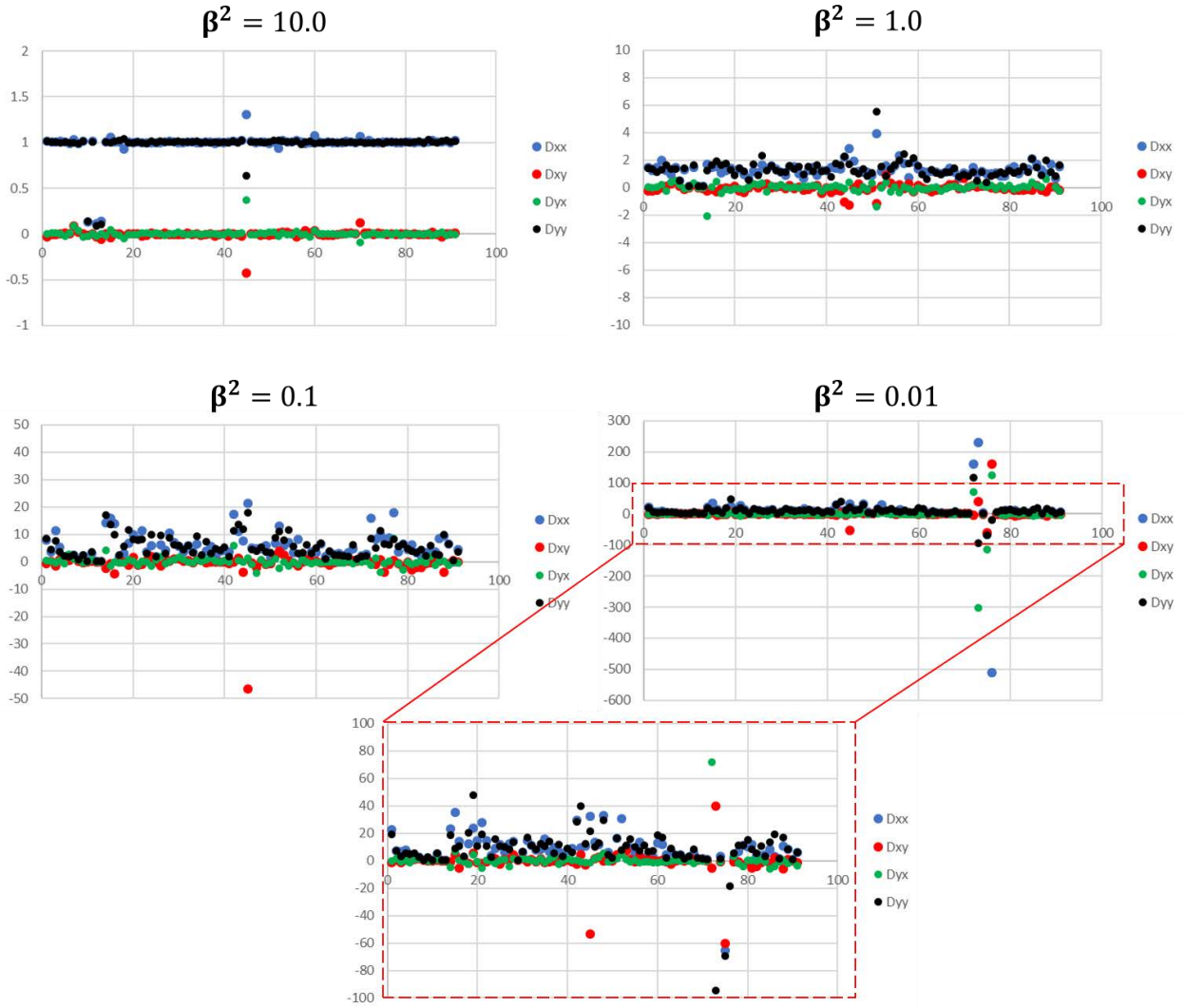

Figure 3.17

Comparison of galvanic distortion components from the modeling computation with different β^2.

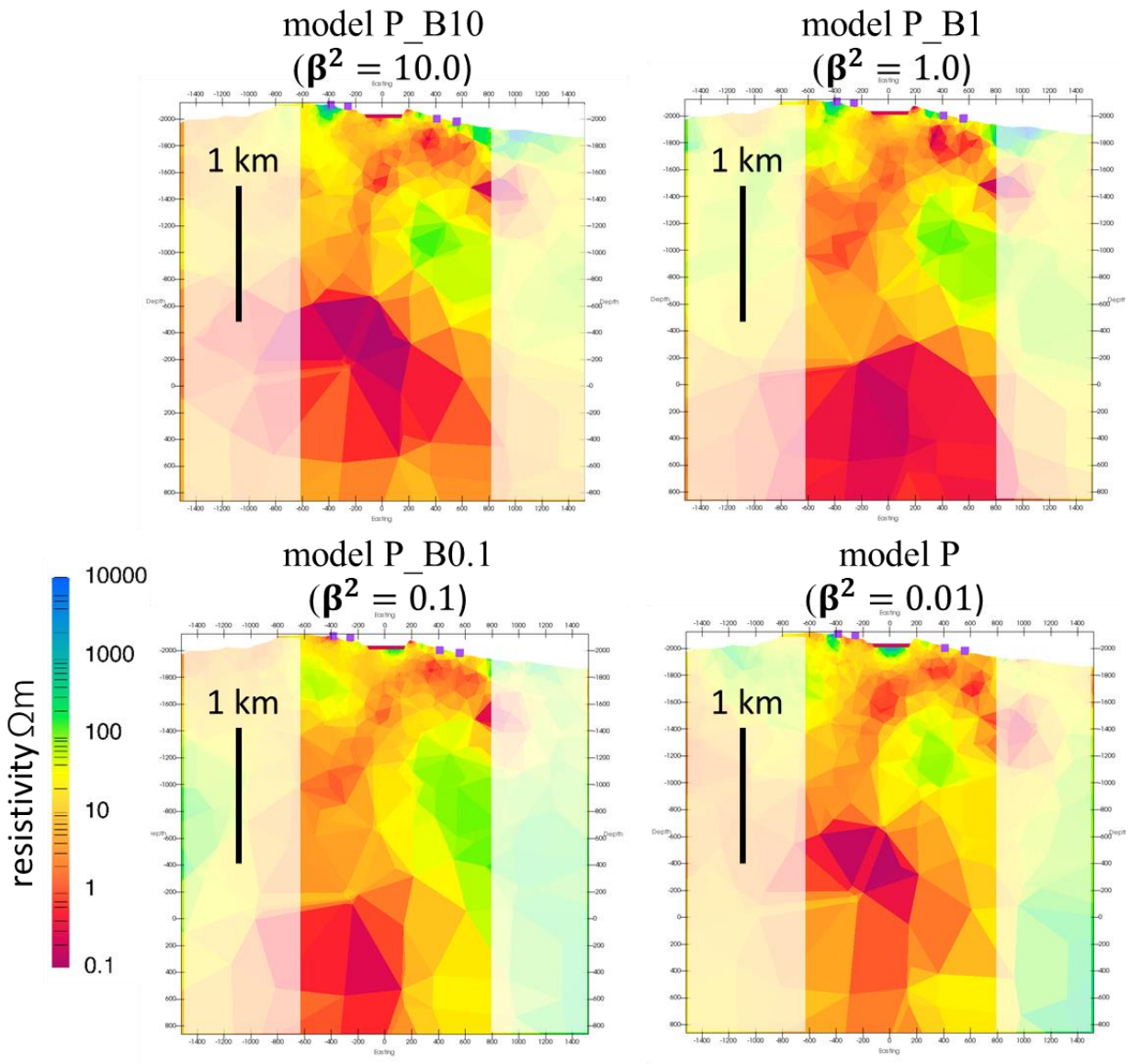

Figure 3.18

Comparison of modeling result from the computation with different $\boldsymbol{\beta^2}$.

The figures represent the east-west profiles of different resistivity models with the changing $\boldsymbol{\beta^2}$. The region where away from the observation sites at least 100m was masked by white color.

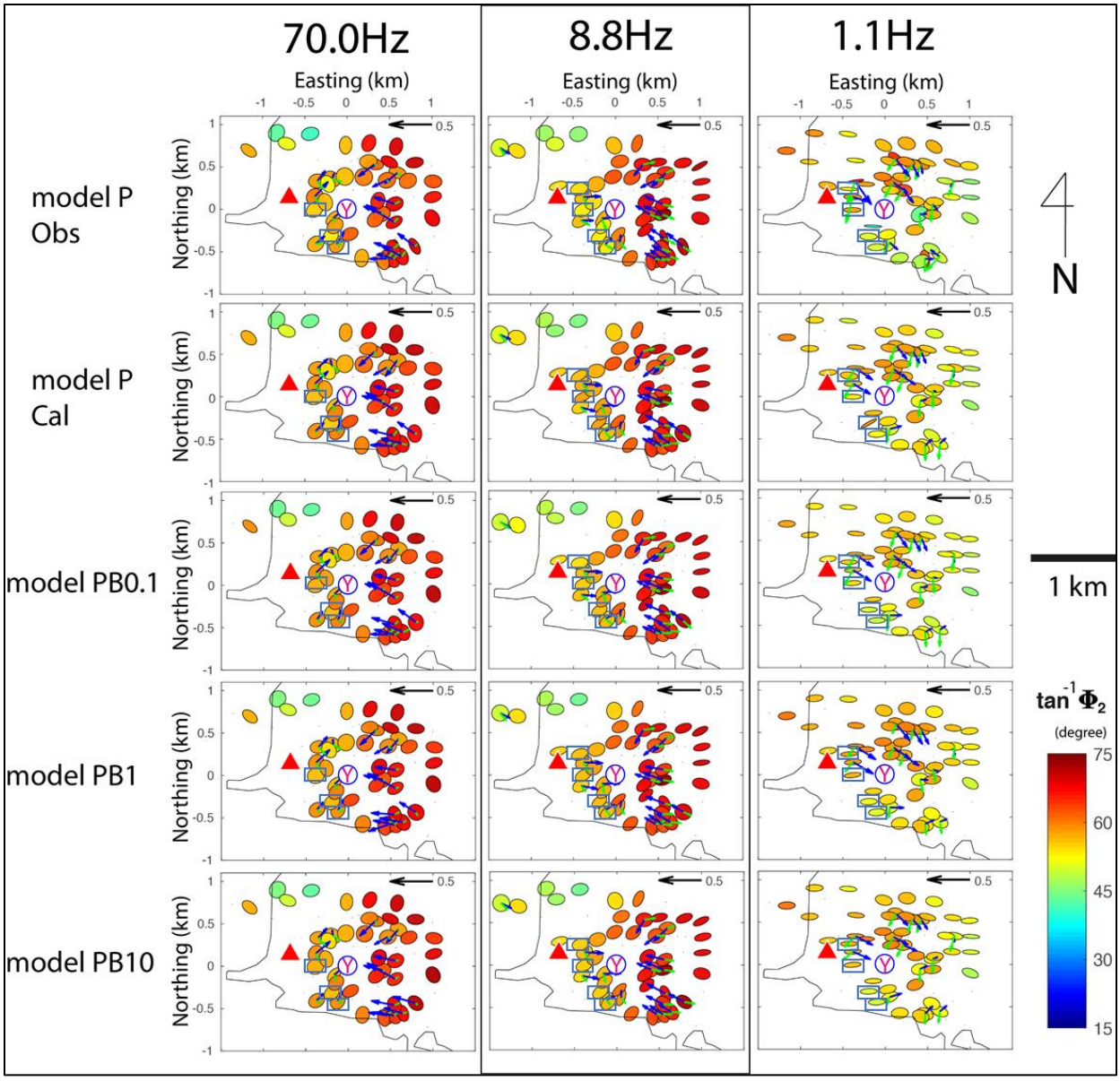

Figure 3.19

Phase tensor analysis of different models with changing $\boldsymbol{\beta^2}$.

The "model P Obs", "model P Cal", "model PB0.1", "model PB1", and "model PB10" represents the observed data, the computed model with $\boldsymbol{\beta^2}$=0.01, $\boldsymbol{\beta^2}$=0.1, $\boldsymbol{\beta^2}$=1 and $\boldsymbol{\beta^2}$=10, respectively. The sites with extreme distortion value when $\boldsymbol{\beta^2}$=0.01 are marked by blue squares.

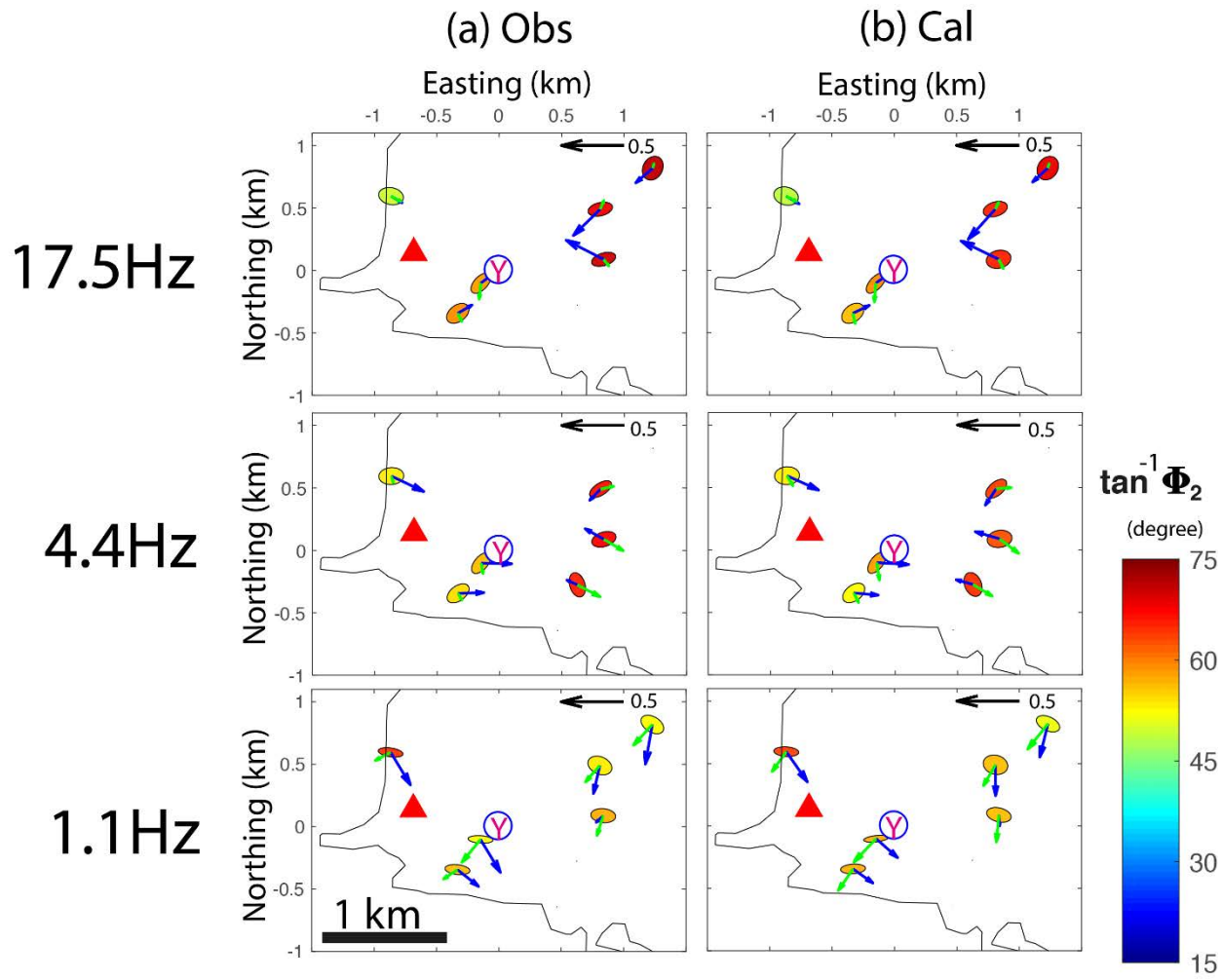

Figure 3.20

Comparison of phase tensor ellipses of the newly observed MT data between (a) the observed result (Obs) and (b) the best-fitted final model "model N" (Cal).

The observed data and the calculated data is represented in the left and right column, respectively. The chosen frequencies for all the four data sets are 17.5 Hz, 4.4 Hz, and 1.1 Hz, from top to bottom. The phase tensor ellipses are filled by the angle of the determinant phase Φ_2, which is the geometric mean value of maximum and minimum of phase tensor. The black strike arrow represents a unit Parkinson's induction vector with a tipper value 0.5. The blue and green strike arrows represent the real and imaginary

Parkinson's induction vector, respectively. The black curve, red triangle and blue circle with symbol "Y" denote local highway, the mountain peak of Mt. Shirane and center of Yugama crater lake, respectively.

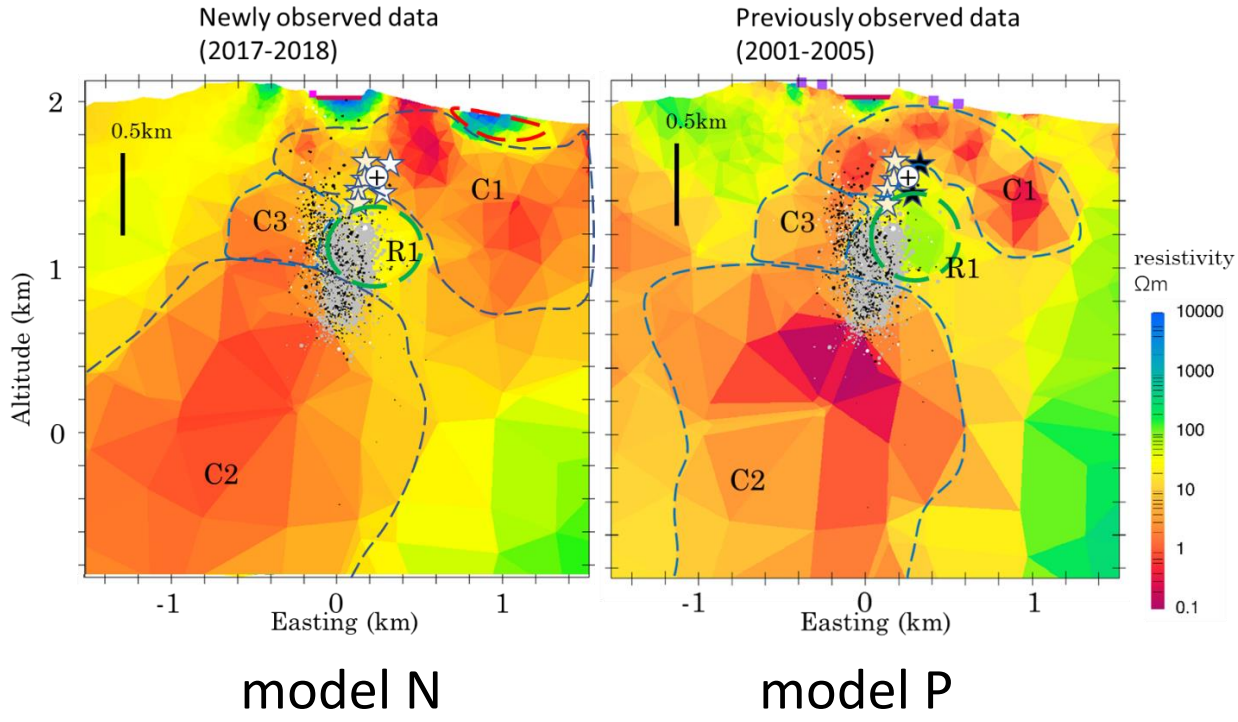

Figure 3.21

Comparison of the resistivity model between the previously observed and newly observed MT/AMT data, east-west profiles.

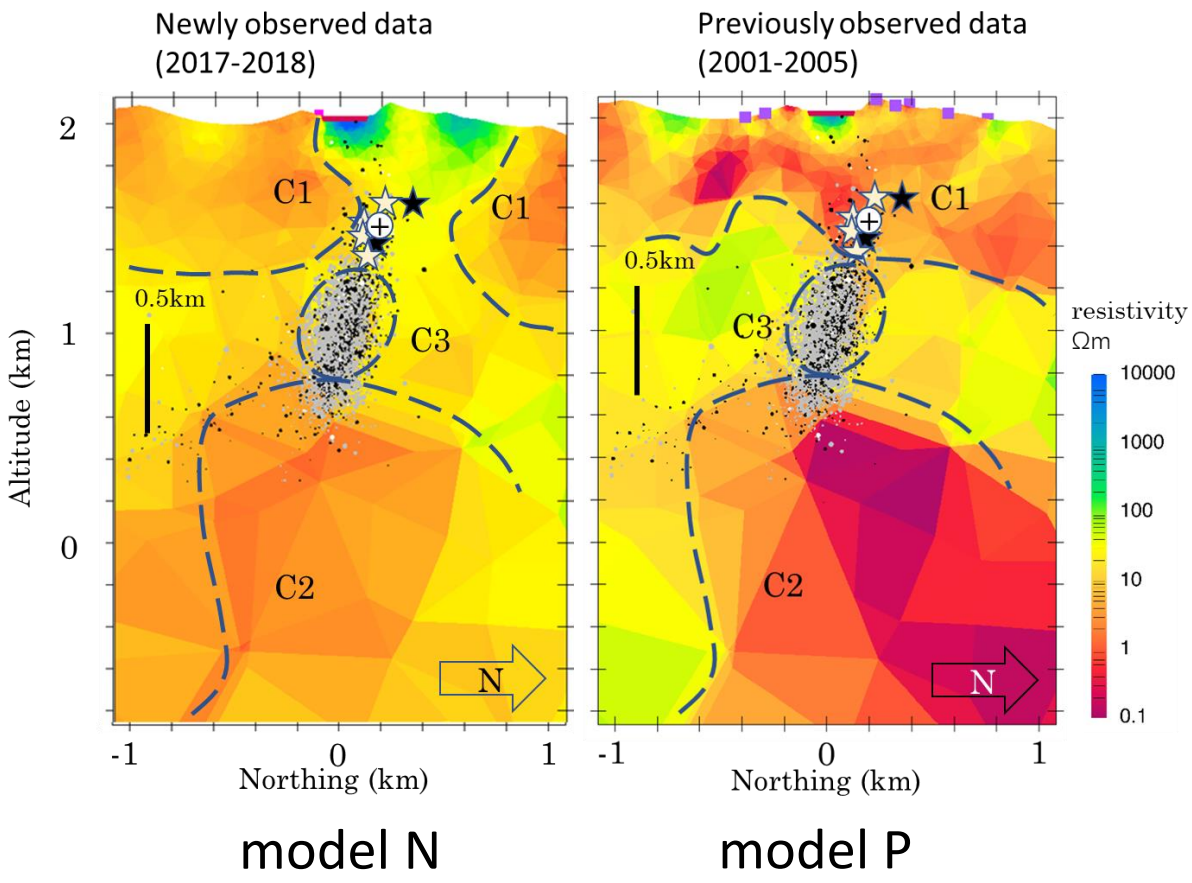

Figure 3.22

Comparison of the resistivity model between the previously observed and newly observed MT/AMT data, north-south profiles.

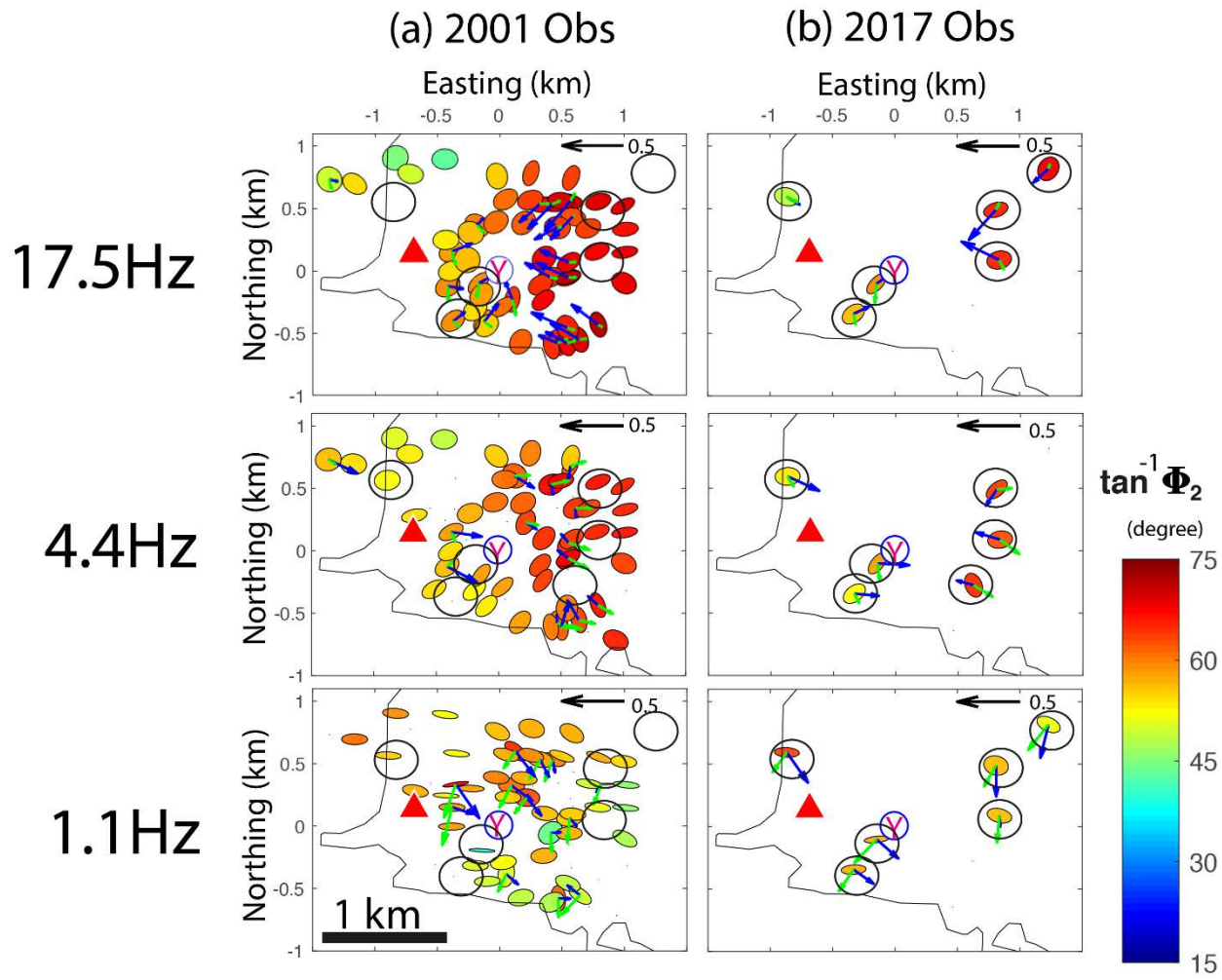

Figure 3.23

Comparison of phase tensor ellipses between (a) the previously observed result (2001 Obs) and (b) the newly observed data (2017 Obs).

The observed data and the calculated data is represented in the left and right column, respectively. The chosen frequencies for all the four data sets are 17.5 Hz, 4.4 Hz, and 1.1 Hz, from top to bottom. The phase tensor ellipses are filled by the angle of the determinant phase Φ_2, which is the geometric mean value of maximum and minimum of phase tensor. The black strike arrow represents a unit Parkinson's induction vector with a tipper value 0.5. The blue and green strike arrows represent the real and imaginary

Parkinson's induction vector, respectively. The black curve, red triangle and blue circle with symbol "Y" denote local highway, the mountain peak of Mt. Shirane and center of Yugama crater lake, respectively.

Chapter 4. Electromagnetic Accurately Controlled Routinely Operated Signal System (EM-ACROSS)

In this chapter, the theory of the controlled-source electromagnetic method is reviewed at first, and the newly developed controlled-source system "EM-ACROSS" is described with its hardware design and the data processing scheme. A new definition of response function and numerical calculation of induction responses is introduced to utilize the product of EM-ACROSS. The method was applied to Kusatsu-Shirane volcano for monitoring purposes of its geothermal system.

4.1 The Fundamentals of Controlled-Source Electromagnetic (CSEM) Method

The introduced Maxwell equation in Chapter 3 was considered for the cases with natural source, the current density is only considered as generated by the electric field (Equation 3.9). With a source existed case, the current density should be divided into two terms:

$$\mathbf{J} = \sigma\mathbf{E} + \mathbf{J_s} \tag{4.1}$$

where $\mathbf{J_s}$ is the current density from artificial sources.

With substituting the current density term by Equation 4.1 and considering the following usage in the frequency domain, Equation 3.1 and 3.2 can be represented as:

$$\nabla \times \mathbf{E} = -\partial_t \mathbf{B} = -\mathrm{i}\omega\mathbf{B} \tag{4.2}$$

$$\nabla \times \mathbf{H} = \sigma\mathbf{E} + \mathbf{J_s} + \partial_t \mathbf{D} = \sigma\mathbf{E} + \mathbf{J_s} + \partial_t \varepsilon\mathbf{E} = \sigma\mathbf{E} + \mathbf{J_s} + \mathrm{i}\omega\varepsilon\mathbf{E} \tag{4.3}$$

Equation 4.2 and 4.3 in the CSEM method have different representation due to the variant source types. Ward & Hohmann (1988) introduced several types of source, including:

(1) vertical magnetic dipole, which is usually a large horizontal rectangular or circular loop laying on the surface of the Earth, and measuring inside or outside the loop;

(2) horizontal magnetic dipole, which is a usual tool in airborne electromagnetic for a long distance between the measurement place and the loop;

(3) horizontal electric dipole, which is a grounded wire with current injection.

In this article, only the horizontal electric dipole is discussed. With substituting Equation 3.2 in Equation 4.2, the rotation of the electric field can be represented as:

$$\nabla \times \mathbf{E} = -i\omega\mu_0\mathbf{H} \tag{4.4}$$

then substituting Equation 4.4 in Equation 4.3:

$$\nabla \times \nabla \times \mathbf{E} = -i\omega\mu_0\nabla \times \mathbf{H} = -i\omega\mu_0\sigma\mathbf{E} - i\omega\mu_0\mathbf{J_s} + \mathrm{i}\omega^2\varepsilon\mu_0\mathbf{E} \tag{4.5}$$

In the geophysical investigation case, the $\mathrm{i}\omega^2\varepsilon\mu_0\mathbf{E}$ can be neglected due to the frequency is usually much lower that $\omega^2\varepsilon\mu_0$ is relatively too small ($\varepsilon\mu_0 = 8.85 \times 10^{-12} \times 4\pi \times 10^{-7} \approx 1.1 \times 10^{-17}$). Then Equation 4.5 can be rewritten as a diffusion equation of the electric field:

$$\nabla \times \nabla \times \mathbf{E} + i\omega\mu_0\sigma\mathbf{E} = -i\omega\mu_0\mathbf{J_s} \tag{4.6}$$

Equation 4.6 provides an advantage that the unknown of the equation is restricted into only the electric field due to a known source term in the CSEM. That Equation 4.6 can be regarded as a response function of the source.

A benefit of the CSEM case is that the electromagnetic field response can be represented with spatial distribution by analytical solution with known source parameters. The simplest case is the assumption of a horizontal infinitesimal electric dipole in laying on the surface of a uniform medium. Kaufman & Keller (1983) introduce an analytical solution by neglecting the electric displacement and the current density turms in Equation 4.3. An assumption of a horizontal infinitesimal electric dipole situated in a uniform medium with the moment:

$$\mathbf{p} = \frac{Idl}{4\pi\sigma} e^{i\omega t} \boldsymbol{\eta} \tag{4.7}$$

where $\mathbf{p}$ is the dipole moment, I is the current amplitude, dl is the dipole length, and $\boldsymbol{\eta}$ is dipole direction.

In the spherical coordinates (R, θ, φ) with zero-frequency, the electromagnetic field at an arbitrary location in the space is:

$$E_R = \frac{Idl}{2\pi\sigma R^3} \cos\theta \tag{4.8a}$$

$$E_\theta = \frac{Idl}{4\pi\sigma R^3} \sin\theta \tag{4.8b}$$

$$E_\varphi \equiv 0 \tag{4.8c}$$

$$H_\varphi = \frac{Idl}{4\pi R^2} \sin\theta \tag{4.8d}$$

Such analytical solutions can be moreover interpreted to a uniform half-space by applying the vector potential with considering the case of the quasi-stationary field. Based on the fact from Equation 3.3 and 3.6, that $\nabla \cdot \mathbf{H} = 0$**,** a vector potential **A** of the electrical type can be defined as:

$$\mathbf{H} = \boldsymbol{\nabla} \times \mathbf{A} \tag{4.9}$$

then

$$\mathbf{E} = i\omega\mu\mathbf{A} + \frac{\nabla\nabla\cdot\mathbf{A}}{\sigma} \tag{4.10}$$

An analytical solution of the electric field in Cartesian coordinates (x, y, z) generated by a η-direction finite dipole source with uniform half-space case is described by Ward & Hohmann (1988) with applying the vector potential:

$$E_{\boldsymbol{\eta}\|} = \frac{Idl}{2\pi\sigma R^3}\left[-2 + (ikR+1)e^{-ikR} + \frac{3{\eta_\|}^2}{R^3}\right] \tag{4.11a}$$

$$E_{\boldsymbol{\eta}\perp} = \frac{3Idl}{2\pi\sigma R^5}[\eta_\|\eta_\perp] \tag{4.11b}$$

where

$$R = \sqrt{{\eta_\|}^2 + {\eta_\perp}^2} \tag{4.11c}$$

$$k = \sqrt{\mu\varepsilon\omega^2 - i\mu\omega\sigma} \tag{4.11d}$$

which σ is the electrical conductivity, μ is the magnetic permeability of the half-space medium, η is the x- or y- direction and $\eta_\|$, $\eta_\perp$ are the distance at parallel and perpendicular directions, respectively.

The analytical solution in Equation 4.8a-4.8d is only with a case that the transmitter (current dipole source) and the receiver are both located on the surface of homogeneous earth with a low-enough frequency (most of the geophysical applications conform with this condition) to apply the quasi-static approximation. Those analytical solutions can be utilized in verifying the numerical computation results. Figure 4.1 presents an example result of the analytical solution in Equation 4.11a-4.11d. In some CSEM cases with simple subsurface structures, such as the tectonic features covered by heavy sediment in marine CSEM observation, with considering the seabed topography versus the investigation scale, the seabed could be assumed as a flat surface

with 1-D layered structures. In that case, if the conductive anomaly target is assumed with a simple shape (disc or spheres), the analytical solution can be utilized for an approximate solution (Constable & Srnka, 2007). However, in most of the onshore investigation, the structures are too complicated to be represented by the analytical solution, that the numerical computation is yet required for such cases. It must be noted that the electric field could be affected by the galvanic distortion in the real case, particularly in such a case as in this study: a hydrothermal system beneath the pyroclastic cone that has a 3-D structure with complicated shallow and local conductive anomalies (Chave & Smith, 1994; Groom and Bailey 1989). That the response function should also be considered as distorted. To minimize the effect of the galvanic distortion, a solution will be introduced in the following sections to address the distorted response.

4.2 Distorted CSEM Response and its Solution

The fundamental of the galvanic distortion has been described in Chapter 3. This real, dimensionless, frequency-independent tensor is generated by the near-surface inhomogeneities in the local structure and will strongly affect the modeling computation and interpretation which assuming the observed electromagnetic field features are regional (Smith, 1997). Although the relationship between the regional and local electric field can be described by a distortion tensor (Equation 3.22), neither the distortion tensor components nor the regional electric field can be directly solved from the observed local electric field because both the regional electric field and the distortion tensor have unknown parameters.

To solve the galvanic distortion effect under the premise that bypass how to obtain the distortion parameters, this study borrows the purpose in the phase tensor (Caldwell et al., 2004) and introduce a distortionless response. If we consider two independently responded electric fields from different sources with unit current, the distorted electric fields observed at one place can be represented from Equation 3.22 as:

$$\begin{pmatrix} E1_{x-local} & E2_{x-local} \\ E1_{y-local} & E2_{y-local} \end{pmatrix} = \begin{pmatrix} D_{xx} & D_{xy} \\ D_{yx} & D_{yy} \end{pmatrix} \begin{pmatrix} E1_{x-regional} & E2_{x-regional} \\ E1_{y-regional} & E2_{y-regional} \end{pmatrix} \tag{4.12}$$

where the $E1$ and $E2$ are the observed electric field, relate to the signals from different source moments.

If we defined the tensor of the distortion and the local electric field, the regional electric field, at frequency f as:

$$\boldsymbol{E}(f)^{\mathbf{12}}_{local} = \begin{pmatrix} E1(f)_{x-local} & E2(f)_{x-local} \\ E1(f)_{y-local} & E2(f)_{y-local} \end{pmatrix} \tag{4.13a}$$

$$\boldsymbol{D} = \begin{pmatrix} D_{xx} & D_{xy} \\ D_{yx} & D_{yy} \end{pmatrix} \tag{4.13b}$$

$$\boldsymbol{E}(f)^{\mathbf{12}}_{regional} = \begin{pmatrix} E1(f)_{x-regional} & E2(f)_{x-regional} \\ E1(f)_{y-regional} & E2(f)_{y-regional} \end{pmatrix} \tag{4.13c}$$

then Equation 4.12 could be simplified with substituting Equation 4.13a-c:

$$\boldsymbol{E}(f)^{\mathbf{12}}_{local} = \boldsymbol{D}\boldsymbol{E}(f)^{\mathbf{12}}_{regional} \tag{4.14}$$

If we multiply an inverse matrix of $\boldsymbol{E}(f)^{\mathbf{12}}_{local}$ at a different frequency at the left-hand side of itself, Equation 4.14 becomes

$$\begin{aligned}\boldsymbol{E}(f_2)^{\mathbf{12}}_{local}{}^{-1}\boldsymbol{E}(f_1)^{\mathbf{12}}_{local} &= \left(\boldsymbol{D}\boldsymbol{E}(f_2)^{\mathbf{12}}_{regional}\right)^{-1}\boldsymbol{D}\boldsymbol{E}(f_1)^{\mathbf{12}}_{regional} \\ &= \boldsymbol{E}(f_2)^{\mathbf{12}}_{regional}{}^{-1}\boldsymbol{D}^{-1}\boldsymbol{D}\boldsymbol{E}(f_1)^{\mathbf{12}}_{regional} = \boldsymbol{E}(f_2)^{\mathbf{12}}_{regional}{}^{-1}\boldsymbol{E}(f_1)^{\mathbf{12}}_{regional}\end{aligned} \tag{4.15}$$

The distortion tensor $\boldsymbol{D}$ then is vanished in Equation 4.15. This article defines an electric field response tensor $\boldsymbol{\varphi}$ where

$$\boldsymbol{\varphi}(f_1, f_2) = \begin{bmatrix}\varphi_{\mathbf{11}} & \varphi_{\mathbf{12}} \\ \varphi_{\mathbf{21}} & \varphi_{\mathbf{22}}\end{bmatrix} = \boldsymbol{E}(f_2)^{\mathbf{12}^{-1}}\boldsymbol{E}(f_1)^{\mathbf{12}} \tag{4.16}$$

that $\boldsymbol{\varphi}$ can be regarded as a distortionless response tensor:

$$\begin{aligned}\boldsymbol{\varphi}(f_1, f_2)_{local} &= \boldsymbol{E}(f_2)^{\mathbf{12}}_{local}{}^{-1}\boldsymbol{E}(f_1)^{\mathbf{12}}_{local} = \boldsymbol{E}(f_2)^{\mathbf{12}}_{regional}{}^{-1}\boldsymbol{E}(f_1)^{\mathbf{12}}_{regional} \\ &= \boldsymbol{\varphi}(f_1, f_2)_{regional}\end{aligned} \tag{4.17}$$

For utilizing this distortionless response tensor in the CSEM method, there are three essentials should be satisfied. The first essential is the regional electric field $\boldsymbol{E}(f)^{\mathbf{12}}_{regional}$. In the real case observation, the regional electric field is originally unknown due to its distorted feature. This study utilized the assumption that the electric field represents the regional features when it is calculated from a model that contains the regional features. For instance, if an inverted model is calculated by an algorithm that considers and deals with the distortion effect, such as using the phase tensor as the modeling parameters (e.g., Patro et al., 2012; Tietze et al., 2015) or computing with a weighted distortion tensor (e.g., Usui, 2015), then the model can be regarded as representing the regional features. When the electric field is calculated from the forward modeling with the parameters from that model (e.g., electrical resistivity), it also represents the regional features. With this assumption, the regional electric field can be reached by the

modeling computation, and the local electric field can be reached by the observation. Then Equation 4.17 can be modified to

$$\boldsymbol{E}(f_2)_{obs}^{\mathbf{12}\ -1}\boldsymbol{E}(f_1)_{obs}^{\mathbf{12}} = \boldsymbol{E}(f_2)_{cal}^{\mathbf{12}\ -1}\boldsymbol{E}(f_1)_{cal}^{\mathbf{12}} \tag{4.18}$$

where $\boldsymbol{E}(f)_{obs}^{\mathbf{12}}$ is the distortion contained observed electric field and $\boldsymbol{E}(f)_{cal}^{\mathbf{12}}$ is the calculated electric field from a prior model, which is assumed to be distortionless. This equation, therefore, neglects the distortion effect.

The second essential is two independent electric fields with the same frequency. In Equation 4.13a and 4.13c, the electric field tensor $\boldsymbol{E}(f)^{\mathbf{12}}$ is calculated from two independent electric fields $E1$ and $E2$ with the same frequency f. However, in a real case, distinguishing the composed electric field generated from different sources at a single frequency is difficult. This study utilized an assumption that when two frequencies are mutually close enough, we can regard that two different frequencies as the same one due to they represented the features from the same subsurface structure. The measurements of close frequency pairs can be realized using the tensor EM-ACROSS system, which will be described later.

The third essential is that the observed data must have small errors for enabling the removal of distortion. Equation 4.15 is only meaningful when E field data have small errors. The typical noise issue in the CSEM observation will be introduced in the next section.

4.3 The Noise Issue in CSEM Observation

For a reliable and accurate comprehension of the responses in terms of subsurface features, obtaining data with high accuracy and high precision is essential. However, there are various kinds of the source of electromagnetic noises in the survey environment, and their related signal may be present in CSEM responses. Ward (1983) summarized the noise-related problems in the CSEM investigation, which includes natural field noise, cultural noise, instrumental noise, and geological (terrain) noise. The geological (terrain) noise occurs during the electromagnetic fields transmitting through the discontinuity with massive electrical conductivity difference. McCracken et al. (1986) described as “overburden effect”. This noise can be considered as topographic distortion effects. The instrumental noise should be handled before the main observation by the initial experiment that is not the object here. Only the natural field noise and cultural noise will be discussed in the following content.

In the passive electromagnetic methods, such as the MT method, the natural signal from solar wind plasma and globally propagated lightning storm events are necessary to a successful observation. The data quality is often improved during a period with stronger solar activity. In contrast to the passive electromagnetic method, the generated signal from those natural sources becomes a class of noise according to the irrelevance of natural sources with the controlled source. Different from the perpetually and constantly existed noise from the natural source, the cultural noise is gradually rising with the progressively increasing with the progress of civilization. Nowadays, the consumption of electric energy has already exponentially increased by comparing it to decades ago. Concomitantly, the increasing cultural noise is the consequence of widespread locally propagated signals from modern products. Szarka (1988) described the problems of cultural noise with two major types: the passive noise and the active noise. The

passive noise is generated by the unnatural conductive (e.g., buried pipelines, grounded cable) or resistive (e.g., ditched, asphalt) materials in the observation environment. Those materials affect as compact or elongated shallow resistivity inhomogeneities. Fortunately, the effects of passive noise can be omitted with an advanced understanding of the observation area. The major problem comes from the active noise: AC or DC electric power transmission lines, rectifier, DC traffic substations, AC railway lines, electric fence, and the rest kinds of electric power-related instruments. Those immovable active sources produce either regular or irregular parasitic electromagnetic fields then disturbing the observation. Besides that, the moving vehicles cause magnetic effects is also a popular problem in many observation areas.

Throughout a long period of the past, discovering a method for reducing the noise is a significant objective for the CSEM method. The methodology of noise reduction can be classified into two parts: the instrument related solution and the process related solution. Theoretically, the most immediate solution for reducing the noise is enlarging the source moment at the transmitter. It can be either extending the length of the source (e.g., Barannik et al., 2013; Sternberg, 1979; Van Zijl & Joubert, 1975; Velikhov et al., 2001) or increasing the power of transmitter output (e.g., Keller et al., 1984) or applying both of them as a combination (e.g., Velikhov et al. 1987; Zhdanov, 2010). Then the noise effects decrease with the increase of signal-to-noise ratio (SNR). Although many researchers successfully utilized this solution in their cases, however, it is not always practicable for all kinds of investigations. For example, the CSEM method in Keller et al. (1984) is time-domain sounding with the designed signal that amplitude up to 2000 A. That can be feasible in time-domain sounding but is almost not applicable to frequency-domain CSEM, particularly for an investigation of a deeper structure with a signal at low frequency. Figure 4.2

represents a schematic frequency spectrum of the horizontal magnetic field in the environment (Macnae et al., 1984). With consideration of the skin depth (Equation 2.10b) and penetration function (Equation 2.11), an observation for deeper structures requires a signal at lower frequencies. The geomagnetic signal exponentially increases in the low-frequency band, and it is obvious that we could not unlimitedly enlarge the output of the transmitter with an exponent to compete with the natural signal. Thus, the methods of noise reduction with an instrument related solution should be more considered within the operation. One of the examples was introduced by Streich et al. (2011): a transmitter system design that developed for land-based CSEM case in a CO_2 injection test. The widely spread three-phase transmitters take effect with short transmitter-to-receiver distance. Based on the different conditions of the instruments and environment in a survey, the hardware system should be separately designed.

Unlike the particular conditions of different surveys in the instrument related solution, the process related solution is more general-purpose for various cases. One of the standard solutions is the digital high-pass filter, which can substantially facilitate the noise above 0.1 Hz in the frequency domain processing (SanFilipo & Hohmann, 1982) has been extensively used in many kinds of instruments but has its limitation at lower frequencies. Even though such a standard method is not applicable due to its limitation, there are still many developed methods introduced in past studies, that will be further introduced in the following section.

4.4 The Electromagnetic Accurately-Controlled, Routinely-Operated Signal System (EM-ACROSS)

A solution for the noise reduction object was introduced as a combination of the instrument related method and the process related method in the CSEM investigation, which is called an electromagnetic accurately controlled routinely operated signal system (EM-ACROSS). The prototype of EM-ACROSS was a seismic accurately-controlled, routinely-operated signal system (ACROSS) proposed and developed in the 1990s (Kumazawa, 1998a,b) for monitoring the seismic wave transmission with a repeated artificial vibration source (Yokoyama et al., 2002) and then be utilized in CSEM method (Nakajima et al., 1998; Nakajima et al., 2000). The purpose of EM-ACROSS, whose schematic diagram is representing in Figure 4.3, begins with the assumption that the environmental noise is Gaussian white noise. A probability density of general normal distribution can be represented as:

$$f(x \mid d^2) = \frac{1}{\sqrt{2\pi d^2}} e^{-\frac{(x-\bar{x})^2}{2d^2}} \tag{4.19}$$

where $f(x \mid d^2)$ is the probability density of value x, in signal processing case, x is the signal amplitude and $\bar{x}$ is its mean value, d is its standard deviation.

A Gaussian white noise has a finite standard deviation and a mean value equal to zero. In the theory of CSEM method, the transmitted signal from the controlled source and the observed signal at the receivers should be completely relevant, and its electromagnetic field can be described with a response function F_R:

$$S_\eta^R(f) = F_R(f) S_\eta^T(f) \tag{4.20}$$

where $S_\eta^R(f)$ and $S_\eta^T(f)$ are the observed electromagnetic field at the receivers, and transmitted electromagnetic field, respectively, with their η-component (e.g., x-, y-, or z-component in Cartesian coordinates), at a specific frequency f. Here the response function $F_R(f)$ is a function which related to the resistivity structure, the transmitter-receiver distance, and other factors.

Understandably, the noise exists in most of the real cases, that the observed electromagnetic field becomes:

$$S_\eta^R(f) = F_R(f)S_\eta^T(f) + N_\eta^R(f) \tag{4.21}$$

where $N_\eta^R(f)$ is the environmental noise around the receivers.

Considering the situation described in Equation 4.21, if (1) a signal is transmitted with high accuracy and high precision, the standard deviation of the transmitted signal d_T will be relatively further smaller than the standard deviation of the noise d_N ($d_T \ll d_N$). Furthermore, (2) when a white noise-contained signal with time length T and spectral density γ is repeated for *n* times, its standard deviation after discrete processing is:

$$d_{out} = \frac{\gamma_{in}}{\sqrt{T \times n}} = \frac{\gamma_S + \gamma_N}{\sqrt{T \times n}} \tag{4.22}$$

where the γ_{in} is the spectral density of the noise-contained signal, γ_S is the spectral density of the received signal which is transferred from the transmitter site, γ_N is the spectral density of the noise and d_{out} is the standard deviation of the output signal (McCracken et al., 1986).

The purpose of EM-ACROSS is then can be introduced as a combination of (1) and (2): with consistently transmitting a signal (a routinely-operated signal) with high accuracy and precision (an accurately-controlled signal), both the transmitted signal and the processed received signal has a lower error. Additionally, considering the assumption of Gaussian white noise, if a signal is repeated for *n* times, the represented transfer function in Equation 4.21 for the i^{th}-repeat becomes:

$$S_{\eta\,i}^R(f) = F_R(f)S_{\eta\,i}^T(f) + N_{\eta\,i}^R(f) \tag{4.23a}$$

and the mean value of all the repetition becomes:

$$\overline{S_\eta^R}(f) = F_R(f)\overline{S_\eta^T}(f) + \overline{N_\eta^R} = F_R(f)\overline{S_\eta^T}(f) \tag{4.24b}$$

because the mean value of Gaussian white noise is zero. Thus, the noise effect is neglected, and the received electromagnetic field is directly relevant to the transmitted signal $\overline{S_\eta^T}(f)$ from the transmitter site:

$$S_{\eta\,i}^T(f) = I_{\eta\,i}^T(f) + N_i^T(f) \tag{4.25a}$$

where the $I_{\eta\,i}^T$ is the i^{th}-repeat injecting current at the transmitter and $N_i^T(f)$ is the noise at the transmitter site (e.g., instrument noise).

Due to the noise is relatively small when the system is actually controlled, the noise term $N_i^T(f)$ can be neglected and Equation 4.25a becomes:

$$S_{\eta\,i}^T(f) = I_{\eta\,i}^T(f) \tag{4.25b}$$

Substitute Equation 4.25b into 4.24b, the final response function of the received electromagnetic field and the signal-contained current can be described:

$$\overline{S_\eta^R}(f) = F_R(f)\overline{I_\eta^T}(f) \tag{4.26}$$

With a stable long-term observation, the system could achieve a high SNR by stacking the repeated signal and provides correct response function which contains electrical conductivity information of the subsurface structures.

The purpose of the EM-ACROSS is same as of the original ACROSS with a source which generates elastic wave (Ikuta et al 2002; Ikuta and Yamaoka 2004; Tsuji et al 2018) but has more advantages. Due to the rotating speed of the seismic vibrator was gradually changing in the

transmission, the coverage and resolution of a signal in the frequency spectrum are limited with the elastic wave. The waveform of a signal is also limited. Unlikely, the EM-ACROSS has further higher flexibility in the transmission that various waveforms could be used with wide band-coverage and high resolution.

The ACROSS and EM-ACROSS prototypes (Kumazawa, 1998a,b) introduced four features in the system: (1) a exact simultaneity in transmission and observation activity; (2) the signal which is accurately controlled during the transmission; (3) the high obtainable SNR at receiver; and (4) the fully recorded transmission activity (Nakajima et al. 2000). It should be noted that the repeated transmission with high accuracy and precision should be directly related to the design of the instrument itself. It means the instrument noise must be entirely eliminated, and the effect of environmental conditions changes must be reduced by calibrating the temporal variations in a long operation routine (Yamaoka et al. 2008). In the previous studies (Nakajima et al. 2000; Yamaoka et al. 2002), the EM-ACROSS prototypes obtained the signals with acceptably high SNR when the power of transmitted signal was smaller than conventional land-based CSEM survey with a similar transmitter-to-receiver distance (e.g., Boerner 1993; Streich et al. 2013). An improved EM-ACROSS was demonstrated by Kumazawa et al. (2007) with a more extended operation test. The SNR significantly increased with the same culture noise conditions. The long transmission routine retained the received EM-ACROSS signal to be sufficiently robust in comparison to the aperiodic noise in the data stacking and the anti-noise performance is provided without enlarging the source moment. Then EM-ACROSS presented its benefit in the economic concern of instruments as a solution to the noise reduction.

Owing to the beneficial features of EM-ACROSS, this system was permitted in the long-term volcanic activity monitoring. In the following content of this article, an improved edition will be introduced with following the scheme of EM-ACROSS prototype and additionally promoted in the development, operation, and data processing for obtaining the volcano monitoring data.

4.5 The System Design and Signal Design of EM-ACROSS

An efficient design of the system should be directly relevant to the observation conditions and targets. Three essential subitems in EM-ACROSS, the transmitter, the receiver, and the signal, should be individually concerned to efficaciously achieve an enhancement in the anti-noise performance and signal stability. The distinguishing feature in this study is utilizing two independent sets of the grounded wire sources for obtaining the electric field tensor. The purpose of this feature is established with the consideration of a 2x2 galvanic distortion tensor with real and frequency-independent components, which has been described in Equation 4.12.

In the assumption of the EM-ACROSS prototype, the noise type is Gaussian white noise and could be canceled out in its mean value. However, the environmental noise in the real case is more complicated and will remain. To make the noise-contained observed signal becomes coherent in the processing, we then firstly applied the simultaneous EM-ACROSS transmission with two current dipole components.

4.5.1 The Signal Design of EM-ACROSS

The signal of this system was designed specifically for simultaneous transmission. In the frequency-domain CSEM method, the sinusoid signal is prevalent due to its harmonic-free feature (e.g., Nakajima et al., 2020; Streich et al., 2011). The waveform of a superimposed wave from an appropriate set of continuous sinusoidal waves with multiple frequencies and arbitrary phase can be represented as:

$$I(t) = \sum_{i=1}^{n} A_i[sin(2\pi f_i t + \phi_i)], t = [0, T] \quad (4.27)$$

where I is the waveform with time-variant amplitude, A_i is the amplitude factor, ϕ_i is the arbitrary phase shift, f_i is the frequency, T is the time-length of a superposed signal, n is the number of superposed signals, and t is the time variable in an interval $\{t \in \mathbb{R} | 0 \leq t \leq T\}$.

To minimize the maximum instantaneous amplitude of the pulse from constructive interference in the superposition, ϕ_i should be selected by different values. For competing with the natural noise at lower frequencies which related to the exponentially increased geomagnetic signal (Macnae et al., 1984), the amplitude factor should be enlarged with the period ($\frac{1}{f_i}$) as increased exponentially. Although the amplitudes could not match with an approximate pink noise floor for representing the geomagnetic noise (Hipkin, 2001; Wardinski & Holme, 2011; Nichols et al., 1988) due to the reality of instrument limitation, this still can profitably allocate the power of transmitter output into individual waves. In this study, two source moments were employed in the system with different signals. Their coefficients were individually adjusted inasmuch as the identifiability in the simultaneous transmission.

At the survey region, Kusatsu-Shirane volcano, the primary targets are beneath the summit in less than 10 km depth. Considering the skin depth (Equation 2.10a & 2.10b), a wave with a frequency above 10^{-2}Hz is reasonable within some conductive structure with 10 Ωm resistivities. With the consideration of the lower bound of frequencies, the time-length of a superposed signal was set to 100 seconds. There were 16 superposed waves employed in the 2018 Kusatsu-Shirane volcano EM-ACROSS investigation. These 16 superposed waves with different waveform coefficients were assigned to two sources (grounded dipole). The frequency coefficients were chosen from a set of prime numbers to avoid the harmonic effect during simultaneous transmission. Even though the sinusoidal signal has, theoretically, no harmonic effect, but the harmonic still could occur from the finite impulse response filter that applied in the receiver beforehand. It is obvious that those frequency coefficients should be individually chosen for different source moments (i.e., the source moments have no repetitive frequency coefficients), but should also be set as close as possible to respond to the subsurface features at a close depth. The arbitrary phase shift of each sinusoidal wave was randomly selected in a range between [-180~180] degrees. The amplitude factor for each wave was slightly enlarged approximately with following an imaginary noise level $1/f$ (i.e., the larger amplitudes were set for the sinusoidal waves with lower frequencies). All the employed coefficients for Equation 4.27 in the 2018 full operation are represented in Table 4.1. The waveforms of two designed signals are represented in Figure 4.4.

4.5.2 The instrument design of EM-ACROSS

The instruments of this system were, in addition, specially designed for the simultaneous transmission. A schematic diagram represents the design of the EM-ACROSS transmitter instrument in Figure 4.5. The waveforms generated by Equation 4.27 were stored in a two-channel function generator with 512 kB 16-bit data points. The function generator was synchronized with a 10 MHz signal from a GPS clock. Thus, the designed signals could be accurately controlled during the entire operation (Kumazawa et al. 2007). After a trigger signal from the GPS clock, two channels output the signal with 9 Volt-peak-to-peak to two amplifiers. The amplifiers enlarged the voltage in 80 times and injected into two sets of grounded wire, diple_{NS} & diple_{EW}. During a long-term operation, the environmental conditions may have various changes, owing to significant seasonal component effects (Abdelfettah et al. 2018). Therefore, the injecting current in each grounded wire source was recorded by a multi-channel digital data logger as the reference in the data processing. In the electromagnetic diffusion equation (Equation 4.6), the most variant coefficient during a long-time transmission is the electrical conductivity σ of the earth. Then Equation 4.25b can be rewritten to a form contains the change of electrical conductivity σ.

$$S^T_{\eta\,i}(f) = I^T_{\eta\,i}(f, \bar{\sigma} + \Delta\sigma) \tag{4.28}$$

where $\bar{\sigma}$ is the mean electrical conductivity in entire transmission and $\Delta\sigma$ is the electrical conductivity change during the transmission.

For minimizing the effects of this additional variance, the signal output for the current injection was set under a constant voltage mode (i.e., fixed the voltage of output signal by tuning the current value). Then Equation 4.28 becomes:

$$S^T_{\eta\,i}(f) = I^T_{\eta\,i}(f, \sigma) \tag{4.29}$$

which the electrical conductivity change during the transmission can be substituted to the variance of recorded current. In the CSEM method, a long grounded wire has a source moment that equal to the multiplication of the loaded current and the length of the wire. From the conventional Ohm's law, the strength of the source moment related to the length of the dipole if the current is fixed then the dipole length becomes a variance. When we try to utilize two dipoles with similar source moments, a constant voltage output also provided regularized current-length moments for different grounded wire sources. The grounded wire sources are independent and approximately orthogonal for maximumly cover the propagation angle of electromagnetic fields. Each end of the dipoles was a grounded electrode array for reducing the effect of not-exactly-homogeneous soil (i.e., the resistivity in a dipole array is the average of in all the electrodes). The receiver of EM-ACROSS requires, identically, high accuracy during the observation. The instrument used in MT investigation, the satellite-synchronized data acquisition units MTU-5 series, also provides such features that were chosen as the receiver.

4.5.3. Data Processing of EM-ACROSS

The EM-ACROSS stabilized the signal by reducing the environmental effects during a long time transmission. That the data processing should properly utilize this feature. With the consideration in the purpose of EM-ACROSS, that the observed electromagnetic fields have higher relevance to the transmitted signal than to the environmental noise (Equation 4.26), the processing flow of observed data should correlate with the recorded transmitted signal.

In a CESM investigation with a simultaneous transmission EM-ACROSS, two components of electric fields (E_X, E_Y) and three components of magnetic fields (H_X, H_Y, H_Z) in the received signal, and two components of transmitted current (I_{NS} and I_{EW}) in the transmitted signal, are measured as the data content. At the outset of the processing flow, these different data sets are represented as a symbol S_η , where η is the component for electromagnetic fields and the name of the grounded wires for the transmitted current, to simplify the representation format. A processing flow for enhancing the data quality is represented with its schematic flow diagram in Figure 4.6.

According to Equation 4.27, entire time-series data $S_\eta(t)$ has a time length L which

$$L = T \times n \times f_s \tag{4.30}$$

where T is the signal time-length in Equation 4.27, n is the number of signal repetition and f_s is the instrument sampling rate. In MTU-5 series, the sampling rate $f_s = 15$ Hz for the continuous recording band.

$S(t)$ will be processed in the frequency domain after discrete processing, such as discrete-time Fourier transform (DTFT):

$$S_\eta(k) = \mathcal{F}\left(S_\eta(t)\right) = \sum_{t=0}^{L-1} e^{-i\frac{2\pi tk}{L}} S_\eta(t)\,, \qquad k = [0, L-1] \tag{4.31}$$

where $S_\eta(t)$ is the time-series data and $S_\eta(k)$ is its DTFT with a frequency resolution $\frac{f_s}{L}$(Hz/bin).

It should be noted that $S_\eta(t)$ contains the information from both CSEM response signal $S_\eta^R(t)$ or $S_\eta^T(t)$ and noise $N_\eta(t)$ which:

$$S_\eta(t) = S_\eta^R(t) + N_\eta(t) \quad \text{or} \quad S_\eta(t) = S_\eta^T(t) + N_\eta(t) \tag{4.32}$$

It is not difficult to know that $N_\eta(t)$ is variant in time, with the assumption that the aperiodic noise dominates the environmental noise, and the Gaussian white noise can be canceled out in mean value (Equation 4.23b). Therefore, a data stacking process can be applied in this case with starting from a step calls "data frame division"(Figure 4.6 [A]):

The entire time-series data $S_\eta(t)$ with time length L can be divided into numbers of "data frames" ${S_\eta}^f(t)$ with time length L^f which:

$$S_\eta(t) = \left\{{S_\eta}_1^f(t), {S_\eta}_2^f(t), \dots, {S_\eta}_i^f(t)\right\}, i = \left[1,2, \dots, \left(\frac{L}{L^f}\right)\right], \text{and } L = \sum L^f \tag{4.33}$$

With frame division, the frequency resolution changes from $\frac{f_s}{L}$ to $\frac{f_s}{L^f}$ in Equation 4.33. The frequency resolution denotes the width of the spectral components in the frequency spectrum which can define how clear the information can be presented. When the value of a frequency resolution is decreasing, the data quality in the frequency domain is reduced by mixing the information from nearby spectral components. However, there is not only disadvantages in the frame division, but also a benefit that the noise condition can be finely individualized in the processing. Here is a trade-off between the improve the data by a better frequency resolution and by a finer noise individuality. In this study, L^f was set to 1000 seconds as 10 repeats of the signal. For increasing the number of samples as well as prevent the occurrence of the missing portion of the signal (Trethewey, 2000), a resampling window with L^f length is shifting with $\frac{L^f}{10}$

distance in the frame division (Figure 4.6 [B]), then the resampled data frame ${S_\eta}_i^{fr}$ can be represented as:

$$ {S_\eta}_{i+1}^{fr}(t) = {S_\eta}_i^{fr}\left(t + \frac{L^f}{10}\right), i = \left[1,2,\dots,\#{S_\eta}_i^{fr}(t)\right]|_{\#{S_\eta}_i^{fr}(t)=10\left(\frac{L}{Lf}\right)-9} \tag{4.34} $$

where $\#S_i^{fr}(t)$ is a simplified symbol for representing the total number of the resampled data frames.

It should be mentioned that the shifting windows sampling will enlarge the fake harmonics in the frequency spectra, thus the frequency of each waveform should not be others' divisors. This will not be an issue while choosing the prime number frequency factors in the signal design.

The relevance of the transmitted signal and received electromagnetic fields has been described in Section 4.4 (Equation 4.26) that a completeness check (Figure 4.6 [C]) of transmitter data is necessary. Part of the transmitter data can be missing, due to the battery issue of the digital data logger, the power failure problem, or other unexpected issues that can even exist in a very short period. The process of completeness check can be represented like a delta function:

$$ {S_\eta}_i^{fr}(t) = \begin{cases} {S_\eta}_i^{fr}(t), & {I_\eta}_i^{fr}(t) \text{ is fine} \\ NaN, & {I_\eta}_i^{fr}(t) \text{ is missing} \end{cases} \tag{4.35} $$

especially here, ${S_\eta}_i^{fr}(t)$ represents only ${E_\eta}_i^{fr}(t)$ or ${H_\eta}_i^{fr}(t)$ but not ${I_\eta}_i^{fr}$.

The DTFT of $S_i^{fr}(t)$ can be computed using a fast Fourier transform (FFT) algorithm by the MATLAB "fft" function, which can be represented as:

$$S_{\eta_i}^{fr}(k) = \text{fft}\left(S_{\eta_i}^{fr}(t)\right) = \sum_{t=1}^{L^f} e^{\frac{-2\pi i(t-1)(k-1)}{L^f}} S_{\eta_i}^{fr}(t), k \in \left[1, \#S_{\eta_i}^{fr}(t)\right] \quad (4.36)$$

It must be noted that the results of conventional DTFT will not be accurate if a signal is discontinuous (i.e., the first point and the last point in a signal is not equal) (Fan & Liu, 2004). Thus each data frame $S_{\eta_i}^{f}(t)$ requires modifications to avoid the endpoint discontinuity issue (Figure 4.6 [D]). A detrend function (Figure 4.6 [D1]) is applied to each data frame $S_{\eta_i}^{f}(t)$ to remove the very-long-period fluctuation, which can be occurred by the very-low-frequency noise or by instrument issue during the observation (e.g., cable connection). Then a window function must be employed to the data frame $S_{\eta_i}^{f}(t)$ (Figure 4.6 [D2]). With trial-and-error testing, a Tukey window $w(t)$ (also known as tapered cosine window) with 1% taper length was chosen to modify the value of the endpoint as well as preserve more information:

$$w_{1\%}(t) = \begin{cases} \frac{1}{2}\left\{1 + \cos\left(\frac{2\pi}{0.99}\left[t - \frac{0.99}{2}\right]\right)\right\}, & 0 \le t < \frac{0.99}{2} \\ 1, & \frac{0.99}{2} \le t < 1 - \frac{0.99}{2} \\ \frac{1}{2}\left\{1 + \cos\left(\frac{2\pi}{0.99}\left[t - 1 + \frac{0.99}{2}\right]\right)\right\}, & 1 - \frac{0.99}{2} \le t < 1 \end{cases} \quad (4.37)$$

where $w_{1\%}(t)$ is a Tukey window with a 1% taper length.

After computing the DTFT for a data fram S_i^{fr} (Figure 4.6 [E]), its information in frequency domain at frequency f is:

$$S_{\eta_i}^{fr}(f) = S_{\eta_i}^{fr}\left(\frac{kf_s}{L^f}\right) \quad (4.38)$$

For eliminating the effect from noise, a distance-based outlier detection method (Knorr 2000; Orair 2010) is utilized in the frequency domain data. The outlier was, however, defined by mean absolute deviation (MAD) and median value instead of by standard deviation and mean value.

Inasmuch as the receiver data distribution was not a normal distribution, which was comprehensible by considering the colored noise and persistent culture noise, the combination of MAD and median was much appropriate (Leys et al. 2013; Chai & Draxler 2014). With defining an outlier threshold as double of MAD and a breakpoint $k\%$ where $k\% \in [0,1]$, we conducted a routine for eliminating the outliers (Figure 4.6 [F]):

(a) calculate MAD and the median of data frames at each chosen frequency ω_j to obtain $S_{\eta}^{fr}{}_{MAD}(f_j)$ and $S_{\eta}^{fr}{}_{median}(f_j)$;

(b) calculate the distance between the median $S_{\eta}^{fr}{}_{median}(f_i)$ to each frame $S_{\eta_i}^{fr}(f_j)$ on the complex plane to obtain $\left|S_{\eta}^{fr}{}_{median}(f_j) - S_{\eta_i}^{fr}(f_j)\right|$;

(c) eliminate the i^{th}-data frame $S_{\eta_i}^{fr}(f_j)$ if its $\left|S_{\eta}^{fr}{}_{median}(f_j) - S_{\eta_i}^{fr}(f_j)\right| > 2S_{\eta}^{fr}{}_{MAD}(f_j)$ at any frequency f_j;

(d) inspect the number of remaining frames, if the percentage of remaining frames is less than $k\%$ of total frames, then stop the outlier elimination routine, otherwise, apply the remaining frames to (a) and do the second elimination.

This routine eliminates the high-noise-contained frames by assuming the noise is not sinusoidal that its frequency spectra are not fully independent between different frequencies. Therefore, one of the frequency spectra with a significant error may indicate that other frequency spectra have been affected even though it is not "economic" in the utilization.

The final step of the data processing is data stacking (Figure 4.6 [G]) for removing the Gaussian white noise (Equation 4.23b). In this study, we employed the frequency-dependent conventional

equal-weight stacking, which is equivalent to averaging the remaining data frames $\overline{S_\eta{}^{fr}}(f_j)$ at frequency f_j. After that, the magnitude $\left|S_\eta{}^{fr}(f)\right|$ and phase $\varphi_{S_\eta{}^{fr}}(f)$ of $\overline{S_\eta{}^{fr}}(f_j)$ can be obtained with their standard deviation error $S_\eta{}^{fr}{}_{err}(f)$ and $\varphi_{S_\eta{}^{fr}{}_{err}}(f)$:

$$\left|S_\eta{}^{fr}(f)\right| = \frac{\left|\overline{S_\eta{}^{fr}}(f_j)\right|}{2L^f} \tag{4.39a}$$

$$\phi_{S_\eta{}^{fr}}(f) = \tan\left(\frac{\Re\overline{S_\eta{}^{fr}}(f_j)}{\Im\overline{S_\eta{}^{fr}}(f_j)}\right) \tag{4.39b}$$

$$S_\eta{}^{fr}{}_{err}(f) = \sqrt{\frac{1}{2L^f \times \#S_{\eta_i}{}^{fr}(t)}\sum\left(\left|S_\eta{}^{fr}(f)\right| - S_{\eta_i}{}^{fr}(f_j)\right)^2} \tag{4.39c}$$

$$\phi_{S_\eta{}^{fr}{}_{err}}(f) = \sin^{-1}\frac{S_\eta{}^{fr}{}_{err}(f)}{\left|S_\eta{}^{fr}(f)\right|} \tag{4.39d}$$

The electromagnetic field in the discrete frequency domain can be obtained from this processing flow. Note that the outlier elimination routine would not, especially, be applied in processing the transmitter (i.e., $I_{NS}(f_j)$ and $I_{EW}(f_j)$) due to the transmitter data has been accurately controlled. Additionally, a combined data set of the received electric data and transmitted signal data (e.g., $\frac{E_x(f)}{I_{NS}(f)}$) can also substitute $S_\eta(f)$ in the outlier elimination and stacking process that the result demonstrates the CSEM field (unit:$\frac{V}{Am^2}$) in the frequency domain as the commonly obtained parameters in the CSEM studies (i.e., normalized electric field).

4.6 Data acquisition and result

Since the significant property of the EM-ACROSS relates to the ability of noise reduction, the enhancement in noise removal should be firstly verified. In this subsection, the main objective is inspecting the result and verifying the performance of noise reduction by the simultaneously transmitted EM-ACROSS.

For verifying the purpose of the system design and the data processing flow, an initial experiment was operated in 2017. A map in Figure 4.7 represents the location of the observation sites and the grounded wire at the transmitter site. In this experiment, both the instrument design and the signal design was simplified. The system was operated with the alternate transmission (i.e., alternated the transmission between two dipole sources) instead of simultaneous transmission. The frequency coefficients were chosen to be simple variables (Table 4.2) (e.g., the same amplitude factor, ten binary frequencies factor 0.01 Hz to 5.12 Hz). Moreover, the operation time was shorter (less than 24 hours per alternation). Figure 4.8 demonstrates the obtained result from the initial experiment by the magnitude-frequency spectra from one of the observation sites, KS004. The five components of the observed electromagnetic field with the EM-ACROSS signal from grounded dipole source "EW" was represented in the figure, the outlier elimination routine was stopped after the 3nd-loop. An additional Ex component with the EM-ACROSS signal from another grounded dipole source "NS" was also represented for comparison.

The magnitude-frequency spectra represent both the pre-processing data (i.e., the DTFT result from the entire time-series data $S_\eta(t)$) and the post-processing data (i.e., the processed result

$\overline{S_\eta{}^{fr}(f_j)}$). In the result with the EM-ACROSS signal from EW dipole, the noise floor markedly decreases in all of the five electromagnetic components. A twice-to-ten-times decrease in the noise floor indicates a part of the noise was successfully removed in the data processing. The Ey, Hx, Hy, and Hz components (Figure 4.8 “B”, “D”, “E” and “F”) demonstrate the small error at higher frequencies (e.g., above 0.64 Hz) that indicates the high SNR and low noise effects. Different from the other four components observing the same EM-ACROSS signal, the Ex component (Figure 4.8 “A”) has no improved result. The noise floor is exponentially increasing with the period as mentioned in the previous studies (Macnae et al., 1984), that the EM-ACROSS signal spectra are overlayed by the noise floor at the lower frequency part.

In comparison with the magnitude-frequency spectrum of Ey component (Figure 4.8 “B”), the magnitude of the observed signal in Ex component (Figure 4.8 “A”) is ten-times-lower than in Ey. In another comparison with the Ex component with the EM-ACROSS signal from another grounded dipole source NS (Figure 4.8 “C”), the latter one is demonstrating a smaller error than the former. These differences can be explained by the characteristics due to the radiation pattern of the dipole source (Goldstein & Strangway, 1975; Liu et al., 2017). Thus, utilizing two orthogonally placed sources is strongly recommended for solving this issue. The characteristic of the different error at high frequencies and low frequencies can be explained by (1) the numbers of repetitions for a waveform is related to its frequencies and remarkably affect the noise reduction (i.e., a waveform with higher frequency repeated more times in the superposed wave, which occurs more data sample in the DTFT and has more efficiency in the data stacking than the one with lower frequency) and (2) the exponentially increased noise floor that is generated from the natural noise. By discussing this issue, the first explanation indicates that a longer

operation should improve the result of noise reduction; the second explanation indicates that an enlargement of the amplitude in the superposed waveforms may provide an ability to compete with the natural noise floor.

With the obtained verification and experience from the initial experiment, a full operation was utilized in 2018, at the same location in the Kusatsu-Shirane volcano region (KS001 had no CSEM survey in 2018) (Figure 4.7). The same location also had an MT observation described in Chapter 3. In this full operation, the transmitter simultaneously transmitted two different signals. The operation was from July to November 2018. The results from a one-month-continual transmission (September 27 to October 27) are represented and discussed in this section. A monitored current load record (Figure 4.9) represented the minimal error (0.2 %) that indicates the transmitted signal was accurately controlled and had high accuracy and precision in the full operation.

For the consistency in the representation, site KS004 is chosen again for demonstrating the results in frequency spectra. Figure 4.10 demonstrates a result of the observed electric field with its horizontal components, and the outlier elimination routine was stopped after the 5^{th}-loop. It is evident that the error is further reduced within this operation, particularly at low frequencies. The amplitude changes of the noise within the data processing can not be simply distinguished on the chosen frequencies spectra but can be conjectured in nearby spectra by their amplitude decline. In this result, some spectra with a large magnitude, which are more significant than the EM-ACROSS signal, are vanished after the processing. The frequency spectra of the electric field

represent the trends of the observed signals that are smooth but gradually change. Moreover, two signals generated different responses in the received electric field.

The results represented in Figure 4.10 further justify the ability of noise reduction within a more extended operation. The gradually enlarged amplitude of the superposed waveform presented its benefit in the competition with the natural noise floor. The trends of the observed signals demonstrate a change from far-intermediate field to near field in the phase plot, which conforms to the fundamental of skin depth. The different responses generated by two signals indicate the probability of local inductive distortion on x(north-south)-direction (Constable, 2010) that the source with different polarization is essential to discover this feature. The vanished noise in many spectra indicates that Gaussian white noise is in the majority of the environmental noise. However, the remained noise floor also indicates a proportion of the non-Gaussian noise that could not be simply removed in the data stacking. Moreover, the Gaussian white noise may contain a significant variance that could not be removed by only the data stacking and represents a significant error, although its stacking value has been minimized. These features of the noise require the outlier elimination routine for obtaining a discriminate final result.

For verifying the efficiency of the outlier elimination routine, Figure 4.11 represents a comparative result of the x-component electric field between stacking the 0^{th}-loop (i.e., contains all the data for stacking, no outliers were eliminated) and 5^{th}-loop outlier elimination products. The noise floor has declined in the 0^{th}-loop routine and has only a few changes in 5^{th}-loop. That indicates the dropped amplitude of the Gaussian white noise. Even though the amplitude of the

noise has declined, its variance still remains that is represented by the large error in the 0^{th}-loop stacking result. It is not difficult to discern that the amplitude has only a few changes between the two results at high frequencies, which means the effect of the noise has decreased. However, the noise still dominates the amplitude of stacking results at low frequencies that should be removed. Moreover, a large error disturbs the comprehension of the result and influence our interpretation. Thus, the outlier elimination routine has its advantages in clarifying the final product.

The features of utilizing the signal from simultaneously transmitted EM-ACROSS has been described in this section. The signal is robust in the data processing to counteract the noise that becomes reliable for noise reduction. For further examining the observation result and utilizing the features in this system, a forward model should be prepared that will be described in the following sections.

4.7 The Fundamental of Finite Element Method (FEM)

The observed CSEM data for the utilization of distortionless response tensor has been obtained. As the mentioned essentials in section 4.2, the forward modeling to represent the regional electric field then should be processed. In some simple cases, the analytical solution could provide a schematic view of the electromagnetic wave propagation with simple postulates and could be an approximate solution. However, unlike the probability of an assumption of 1-D layered earth in the marine CSEM cases, the land CSEM cases usually require the numerical computation for the relevant results. In the cases of CSEM study, three classes of the numerical

computation are commonly employed in the CSEM modeling: (1) the integral equation method (IEM), (2) the finite-difference method (FDM) and (3) the finite-element method (FEM) (Avdeev, 2005).

The IEM can be considered as the derivative of the analytical solution with extending conditions. A typical example is a long grounded wire as an assumed superposition of the electric dipoles. The analytical solution of a finite-length dipole is approached to an infinitesimal electric dipole that the error will occur when the transmitter-receiver distance is too small. For an available approach, the long grounded wire should be divided into many short segments and superposition the electromagnetic fields transmitted by each segment with integral equations. This basic IEM was introduced by Kaufman & Keller (1983) and Ward & Hohmann (1988) with Bassel function. Include but not limited to the long-wire approximation; furthermore, the IEM can also apply to 3-D cases with simple structure. Wannamaker et al. (1984) introduced an algorism for a 3-D conductive anomaly body in the 1-D layered earth by the integration of the Green's function at nodes on the cuboid gridded elements. The IEM can also be used for identifying the real case problem in a simple model. Andréis & MacGregor (2008) used 1-D IEM for tackling the airwave problem in shallow water CSEM sounding. The IEM is straight forward in representing with functions of the computational result terms. However, it is only utilizable in a simple case when the model can be described by equations, such as cuboid gridded elements with a simple shaped target in a uniform half-space or 1-D layered earth. It also confronts with the heavy load of computation when the domain is enlarging (Xiong, 1992). With consideration of the topographic effects, which should be represented by small elements, and commonly 3-D

structures with complicated shapes underlying the volcano, the IEM is not, therefore, an applicable method in this study.

The FDM is a, possibly the most, standard method in CSEM forward modeling, particularly in time domain CSEM. The method has an early and widely spread since the 1970s (Yee, 1966) due to its simplicity and fast computation speed. In this method, the electromagnetic equation (e.g., Helmholtz equation or Maxwell's differential equation) (e.g., Abubakar et al., 2008) or the conductivity (e.g., Commer & Newman, 2008) is discretized on a staggered grid. The components of the electromagnetic field are located at the center of a cuboid element and slightly be offset (half of the element size in each component) to its connecting elements. All the averaged discretized components then become an equation system to be solved (Fomenko & Mogi, 2002). A substantive advantage of FDM is its high accommodation of arbitrary media types (e.g., inhomogeneous, anisotropic, or frequency-dependent dispersive) to Maxwell's equation (Gedney, 2011; Weiss & Newman, 2002). Besides the familiar finite-difference time-domain (FDTD) method, the FDM is also utilized in the frequency domain problem for the land-based CSEM survey (Grayver et al., 2014; Streich, 2009; Streich et al., 2011). Due to the method is assigning the cuboid gridded elements, in the 3-D problems the meshes which have to be filled in the full 3-D space lead to the cubically grown degrees of freedom while the size of the computational domain is increasing linearly. This situation can occur in a low-frequency land-based CSEM case, in which the skin depth is relatively large. Moreover, in a sharp topography situation, as most of the survey at volcanoes, the cuboid elements are required to be much finner to represent the altitude variances by small stair steps. Then the equation system could become extremely large (Avdeev, 2005; Gedney, 2011; Newman & Alumbaugh, 1995; Smith & Booker,

1991). Therefore, the FDM is inadequate with this topic with the consideration of such disadvantages.

The FEM that permits the unstructured meshes is then appointed as the final option for this topic. Recently, the method has gained popularity in electromagnetic studies with the increasing demand for modeling with unstructured elements (e.g., Key & Weiss, 2006; Mitsuhata, 2000; Wannamaker et al., 1986). By employing the unstructured elements in the model, a complicated geological structure can be efficiently represented. A model with structural girds provides an unambiguous understanding in the linear equation system with its straightforwardness and can be simply post-process (e.g., Siripunvaraporn et al., 2005). However, a smaller amount of unknows in the linear equation system leads to economizing usages of memory, and CPU clock has more benefits while solving a problem model with finer meshes.

The procedure of establishing the formulations of a frequency domain FEM has been described with Maxwell's equations (Equation 4.2 and 4.3) and rewrote as a diffusion equation (Equation 4.6). That reduces the total number of the parameters in the equations which have to be solved. For the numerical calculation, a weak formulation via Garlerkin's method is introduced by Jin (2002) by applying the weighted residual integral for element:

$$R_i^m = \iiint_{V^m} N_i^m r \, dV \tag{4.40}$$

where R_i^m is the weighted residual integral for element m on its i^{th}-component (node, edge or shape), N_i^m is the basis function (or, as known as the shape function) of the i^{th}-component

(node, edge or shape) in element *m,* V^m is the element volume, and r is the residual error associated with a boundary-value problem. Formulate Equation 4.6 via Garlerkin's method, then the weak formulation of the diffusion equation is resulting in:

$$\iiint_{V^m} \mathbf{N}^m \cdot (\nabla \times \nabla \times \mathbf{E}^{\boldsymbol{m}} + i\omega\mu_0\sigma^m\mathbf{E}^m + i\omega\mu_0\mathbf{J}_{\boldsymbol{s}})dV = 0 \tag{4.41}$$

with

$$\mathbf{N}^m = \sum_{i=1}^{\max i} N_i^m \tag{4.42}$$

The basis function is variant due to the element type (line, triangle, rectangle, tetrahedron, or cubic), the based type (node-based, edge-based, or surface-based) in the FEM. That the final representation of Equation 4.42 will be relatively different. The details of the procedure of generating the basis function and the utilization of FEM in this article will be further detailedly described in the following relative chapter by describing the CSEM modeling procedure.

4.8 Element-Based CSEM Forward Modeling with Tetrahedral Elements

Based on different methods, depends on computing the value on the element node or edge, in representing the electromagnetic field in an element (e.g., tetrahedron, cuboid, or hexahedron), the basis function could be represented by either a node-based shape function or an edge-based shape function. According to the shape of elements, the mesh types can be separated into unstructured meshes, structured meshes, and hybrid meshes that combine both of them. The unstructured meshes, such as triangle elements in 2D and tetrahedral elements in 3D, have intermittent connectivity between the connecting elements that provide any possible elements to

unrestrictedly represent the structure but with high space inefficiency during the computation, because of the unexpected location of the related element components. The structured meshes, such as quadrilateral elements in 2D and cuboidal elements, hexahedral elements in 3D, have regular connectivity with the neighborhoods, and the model has, therefore, high space efficiency in the storage. The tetrahedral-, cuboidal-, and hexahedral-elements are all commonly used in the modeling computation of electromagnetic investigation. The cuboidal element is the most straightforward mesh type that the spatial relationship of all the element components can be represented with their coordinate information. It is simple in the case that does not consider the topography (e.g., Hu et al., 2015). However, if the topography information has to be employed in the model, it requires additional adjustments such as element subdivision (e.g., Qiang et al., 2007) or stair-like placement (e.g., Müller & Haak, 2004; Matsunaga et al., 2019). The hexahedral element then is the more efficient unstructured mesh in representing the topography (e.g., Nam et al., 2007). Although those efficient unstructured meshes are simply comprehensible either in the coordinate information or functions system, however, the number of the element components is higher (8 nodes, 12 edges and 6 surfaces per element) than the tetrahedral element (4 nodes, 6 edges and 4 surfaces per element). This difference is not apparent if the model contains a few elements. However, in CSEM cases, the computational domain usually is farther than the distance between the transmitter and the receiver considering the skin depth (Equation 3.10) and efficient penetration equation (Equation 3.11). Then the number of elements exponentially increases with enlarging the computational domain in three dimensions, although there are numbers of the elements not interested in the problem. With the consideration of such issues, the tetrahedral element that can represent the topography information and ample model space with fewer element components is utilized in this topic.

The degree of freedom in edge-based FEM is defined on the edges, that the tangential component of the electromagnetic field has an enforced continuity. Therefore, the spurious solutions from the imposed continuity condition in node-based FEM are precluded. This advantage makes the usage of edge-based FEM far more than of node-based FEM in solving the electromagnetic problems. The discussion of node-bases FEM in mathematical theories is more than in real-world applications (e.g., Andersen & Volakis, 1998; Wang & Ida, 1991). In this topic, the edge-based method is selected with following most of the CSEM modeling studies (e.g., Cai et al., 2014; Cai et al., 2015; Cai et al., 2017; Chung et al., 2014; Mukherjee & Everett, 2011).

Moreover, the basis function of edge-based method can be modified with different polynomial degrees (which is called the p-version FEM)(e.g., Carnevali et al., 1993), or variable refined element size (which is called the h-version FEM)(e.g., Fish, 1994), or employing both methods together (which is called the hp-version FEM)(e.g., Krause & Rank, 2003), to improve the computational result. A method that detailedly representing the elements can further explicitly represent an element in mathematics; however, it also increases the complexity of equations (e.g., Badea et al., 2001; Pardo et al., 2010; Savage & Peterson, 1996). Furthermore, there have also been many results from the previous research that demonstrate the success in the CSEM method with simpler representation (e.g., Chung et al., 2014; Hu et al., 2015; Mukherjee & Everett, 2011) that an uncomplicated representation is also acceptable with its efficiency of time and speed.

The way of representing the element and its components have been reviewed with their features, included advantages and disadvantages. Considering with the topography information, the larger skin depth at lower frequencies, and the efficiency of time, the first order edge-based FEM with tetrahedral elements method is utilized for computing the electromagnetic propagated electric field from grounded wires.

4.8.1. Formulation of vector basis function

Since the vector components of the electromagnetic field have been decided to be represented on first-order (linear) edges of a tetrahedral element, the basis function (Equation 4.42) can be formulated by starting with the domain discretization. In this subsection, the flow of formulating the FEM linear equations systems follows the introduction from Jin (2002). In the formulation, all the element components (nodes or edges) can be arranged by either a global numbering system or a local numbering system. The global numbering system denotes the identifier of an element component in the whole modeling space, and the local numbering system denotes the identifier of an element component in its relative elements (i.e., the elements which store that component). In the local numbering system of a tetrahedral element, the stored nodes can be denoted by $n_L(i,m)$, where $i = 1,2,3,4$ and $m = 1,2,3,\dots,M$ is the order of tetrahedral elements where M is the total number of tetrahedral elements in the modeling space. Then the local number system of nodes becomes a $4 \times M$ integer array. In the global numbering system, the nodes can be denoted by $n_G(i)$, where the maximum of i is not in proportion to the number of tetrahedral elements but depending on the algorithm in the mesh generation. Similarly, the stored edges in a tetrahedral element can be denoted by $e_L(i,m)$, where $i = 1,2,3,\dots,6$ and $m = 1,2,3,\dots,M$ where M is the number of tetrahedral elements, same as in n_L and e_L is a $6 \times M$

integer array. That is obvious that the size of the global edges list $e_G(i)$ is also not in proportion to the number of tetrahedral elements (Figure 4.12).

After the domain has been discretized, the next step of formulating the basis function is applying the edge shape function. Jin (2002) represented a formulating process to obtain the edge shape function from the nodal shape function. In a tetrahedral element which is composed of four nodes $[n_1, n_2, n_3, n_4] \in n_L(i, m)$, an unknown value can be represented as a spatial-variant function φ_m, where:

$$\varphi^m(x, y, z) = a^m + b^m x + c^m y + d^m z \tag{4.43}$$

With enforcing Equation 4.43 at $n_i(x_i, y_i, z_i)$, the decomposed function φ_i can be written into:

$$\varphi_i^m(x, y, z) = a_i^m + b_i^m x_i + c_i^m y_i + d_i^m z_i \tag{4.44}$$

or representing with a linear interpreted node shape function $L_i^m(x, y, z)$:

$$\varphi^m(x, y, z) = \sum_{i=1}^{4} L_i^m \varphi_i^m \tag{4.45}$$

Here the node shape function possesses the unknown properties at any location (x, y, z) in the element m from the properties on four nodes n_i^m. It is a linear combination of the coefficients in the decomposed spatial-variant unknown function φ_i :

$$L_i^m(x, y, z) = \frac{1}{6V^m}(a_i^m + b_i^m x_i + c_i^m y_i + d_i^m z_i) \tag{4.46}$$

where V^m is the volume of element m and also can be represented as a determinant of the local nodes' coordinates:

$$V^m = \frac{1}{6}\begin{vmatrix} 1 & 1 & 1 & 1 \\ x_1^m & x_2^m & x_3^m & x_4^m \\ y_1^m & y_2^m & y_3^m & y_4^m \\ z_1^m & z_2^m & z_3^m & z_4^m \end{vmatrix} \tag{4.47}$$

In Equation 2.25, the node shape function has a property that

$$L_i^m = \delta_{ij} = \begin{cases} 1, & i = j \\ 0, & i \neq j \end{cases} \tag{4.48}$$

which denotes the interpolation function between two nodes n_i and n_j.

As the existence of interpolation function between two nodes, the interpolation between two node shape function L_i^m and L_j^m is also exist and can be represented as:

$$W_{ij}^m = L_i^m \nabla L_j^m - L_j^m \nabla L_i^m \tag{4.49}$$

which possesses all the properties for an edge field which is composed of n_i^m and n_j^m. By following the node-edge relationship that defined by Jin (2002) (Table 4.3), the edge shape function can be formulated as:

$$N_i^m = W_{i_1 i_2}^m l_i^m = \left(L_{i_1}^m \nabla L_{i_2}^m - L_{i_2}^m \nabla L_{i_1}^m\right) l_i^m \tag{4.50}$$

By substituting equation 4.50 into 4.49, and assume the electric field on edge components is the unknown function, then a shape function represented the electric field in the element m can be written as:

$$\boldsymbol{E^m}(x, y, z) = \sum_{i=1}^{6} N_i^m E_i^m \tag{4.51}$$

Before employing Equation 4.50 into Equation 4.41 and 4.42, we firstly rewrite Equation 4.41 by following the vector calculus identities:

$$(\nabla \times \nabla \times \mathbf{A} + \mathbf{A}) \cdot \mathbf{B} = \big((\nabla \times \mathbf{A}) \cdot (\nabla \times \mathbf{B}) + \mathbf{A} \cdot \mathbf{B}\big) \tag{4.52}$$

then substituting Equation 4.42 and 4.51 into 4.41:

$$\iiint_{V^m} \left[(\nabla \times N_i^m) \cdot \left(\nabla \times N_j^m\right) + i\omega\mu_0\sigma^m N_i^m \cdot N_j^m\right] E_j^m dV = i\omega\mu_0 N_i^m \cdot J_i^m \tag{4.53}$$

It must be noted that Equation 4.53 is currently still employed with the local numbering system. Therefore, the global numbering system should be projected into the local system in each element. In this topic, a processor program "GiD" (CIMIN, 2019) was used for the mesh generation process. The program provides node ID and element ID but no edge ID. This technical issue can be solved by utilizing a paring function for uniquely encoding two node IDs into one edge ID. In mathematical consideration, this function should be bijective and invertible; in computational consideration, this function should be primitive recursive (Robinson, 1995) (i.e., can be computed in a program with all "for" loops). For these requirements, the Cantor pairing function is an option that matches all of the requirements (Lisi, 2007; Szudzik, 2006). For any normal number N_1 and N_2, a one-to-one projected object N_0 can be obtained by the Cantor pairing function π as:

$$N_0 = \pi(N_1, N_2) = \frac{1}{2}(N_1 + N_2)(N_1 + N_2 + 1) + N_2 \tag{4.54}$$

with its inversion

$$N_2 = N_0 - \frac{w^2 + w}{2}, \qquad \text{and } N_1 = w - N_2, \qquad w = floor\left(\frac{\sqrt{8N_0 + 1} - 1}{2}\right) \tag{4.55}$$

In this case, N_1 should be limited that always smaller than N_2 to avoid the over-paring issue (i. e. , $\pi(N_1, N_2)$ and $\pi(N_2, N_1)$ are different but denotes the same edge, which will cause difficulty in distinguishment during programming). This paring function is efficient to clarify the

connection between node IDs and edge ID in both local and global numbering system (Figure 4.12).

Therefore, for four nodes in an element m with their global numbering ID: $n_G(o)$, $n_G(p)$, $n_G(q)$, $n_G(r)$, their local number is defined n_1, n_2, n_3, and n_4 respectively if $o < p < q < r$. Moreover, any two nodes will define an edge identifier from the Cantor pairing function and their global numbering ID (e.g., $\pi(n_G(o), n_G(p))$. With sorting the edge identifiers, the global edge number $e_G(i)$ then can be obtained by their ordinals (e.g., if an edge is connecting by $n_G(1)$ and $n_G(2)$, its global number $e_G(i)$ is 1 because of $\pi(1,2) = 8$ is the minimum number).

4.8.2. The sparse linear equations system

Since the global edge number has been defined, the weak form electromagnetic diffusion equation (Equation 4.53) can, therefore, be utilized in a global numbering system and be solved as a linear equations system:

$$[\mathbf{K}]\{\mathbf{E}\} = \{\mathbf{I}\} \tag{4.56}$$

where

$$[\mathbf{K}] = \begin{bmatrix} K_{11} & \cdots & K_{1j} \\ \vdots & \ddots & \vdots \\ K_{i1} & \cdots & K_{ij} \end{bmatrix} \quad | \quad i, \mathrm{j} \in [1, \max(e_G)] \tag{4.57}$$

is a $\max(e_G) \times \max(e_G)$ size matrix with vector components K_{ij}:

$$K_{ij} = \iiint_{V^m} \left[(\nabla \times N_i^m) \cdot (\nabla \times N_j^m) + i\omega\mu_0\sigma^m N_i^m \cdot N_j^m \right] dV \tag{4.58}$$

$$\{\mathbf{E}\} = \begin{Bmatrix} E_1^m \\ \vdots \\ E_j^m \end{Bmatrix} | \quad \mathrm{j} \in [1, \max(e_G)] \tag{4.59}$$

is a $\max(e_G) \times 1$ size vector with the unknown electric field on the edge $e_G(j)$, and

$$\{\mathbf{I}\} = \begin{Bmatrix} I_1^m \\ \vdots \\ I_i^m \end{Bmatrix} | \quad i \in [1, \max(e_G)] \tag{4.60}$$

is a $\max(e_G) \times 1$ size vector with components I_i^m:

$$I_i^m = -i\omega\mu_0 \iiint_{V^m} N_i^m \cdot J_s \, dV = -i\omega\mu_0 \int N_i^m \cdot I_s \, dl \tag{4.61}$$

on edge $e_G(i)$, where I_s is the current amplitude on the edge $e_G(i)$.

In this study, the current is assumed flowing through edge $e_G(i)$, that the basis function N_i^m in Equation 4.61 can be simply represented as a delta function as in Equation 4.48, and its integral is the length of the edge $e_G(i)$. With this assumption, Equation 4.61 can be modified as:

$$I_i^m = -i\omega\mu_0 \int \delta_i^m \cdot I_s \, dl = \begin{cases} -i\omega\mu_0 I_s \, l_i, & e_G(i) \; is \; on \; the \; wire \\ 0, & e_G(i) \; is \; not \; on \; the \; wire \end{cases} \tag{4.62}$$

where l_i is the length of an edge $e_G(i)$.

According to the previous researches in CSEM modeling using FEM, the boundary condition in this model is considered to be a homogeneous Dirichlet boundary condition:

$$\mathbf{E}_{|\partial\Omega} = 0 \tag{4.63}$$

which denotes the tangential components of the electric field is vanish at the computational boundaries. A technical approach for employing the homogeneous Dirichlet boundary condition

in the linear equations system is enforcing the diagonal components K_{ii} in the matrix [**K**] to be a substantial value when the edge $e_G(i)$ locates on the computational boundary:

$$K_{ii} = \begin{cases} 10^{70}, & e_G(i)|\partial\Omega \\ \iiint_{V^m} \left[(\nabla \times N_i^m) \cdot (\nabla \times N_j^m) + i\omega\mu_0\sigma^m N_i^m \cdot N_j^m \right] dV, & else \end{cases} \quad (4.64)$$

It is not difficult to understand that $e_G(i)|\partial\Omega$ is far away from the CSEM source and obviously, have no current load that $I_i^m = 0$ (Equation 4.62). In solving the linear equations, the relative electric field edge component E_i^m on edge $e_G(i)|\partial\Omega$ will be forced to an extremely small value which can be approximately denoted as zero a tangential electric field.

In this linear equations system, matrix [**K**] is sparse, complex, symmetric, but not Hermitian. Furthermore, vector {**I**} is also sparse. Such a linear equations system can be simply solved by utilizing a sparse linear system dedicated direct solver (e.g., "spsolve" under the numerical computation library "SciPy" in Python language (Jones et al., 2001); UMFPACK in C language (David, 2004)).

The electric field in the solution of the linear equations system (Equation 4.56) denotes the strength on the edge vectors $e_G(j)$. Those values have to be composed to an arbitrary point in the element by utilizing Equation 4.51 for interpreted in the coordinate system (e.g., Ex, Ey, and Ez). Besides the interpolated edge shape function (Equation 4.50), an alternative expression for the basis function N_i^m in Equation 4.51 was introduced by Barton & Cendes (1987). For an arbitrary

point $\boldsymbol{n}(\boldsymbol{x},\boldsymbol{y},\boldsymbol{z})$ within the element m, the factor shape function N_i^m at that location $(\boldsymbol{x},\boldsymbol{y},\boldsymbol{z})$ can be represented as:

$$N_i^m = \frac{l_i^m}{6V^m}\left[\left(\boldsymbol{n_L}\left(i1',m\right)\times\boldsymbol{n_L}\left(i2',m\right)\right)+\left(\boldsymbol{n_L}\left(i2',m\right)-\boldsymbol{n_L}\left(i1',m\right)\right)\times\boldsymbol{n}\right] \tag{4.65}$$

where l_i^m is the length of edge $e_L(i,m)$, $\boldsymbol{n_L}\left(i1',m\right)$ and $\boldsymbol{n_L}\left(i2',m\right)$ is the location $(\boldsymbol{x},\boldsymbol{y},\boldsymbol{z})$ of the diagonal nodes $n_L\left(i1',m\right)$ and $n_L\left(i2',m\right)$ of edge $e_L(i,m)$ that is defined in Table 4.3. The result of Equation 4.65 is a vector with x-, y-, and z-direction components. Substituting Equation 4.65 into 4.51, the x-, y-, and z-direction components of the electric field $\boldsymbol{E^m}(x,y,z)$ then can be obtained. The FEM forward model can be examined by the analytical solution of a homogeneous halfspace (Equation 4.11a-d). Figure 4.13 represented a comparison of the analytical solution result and the numerical result from a roughly simplified testing model. The distance at 1-4 km away from the transmitter fits the analytical result that a model with a more detailed design can be employed in the computation.

4.9 New Introduction of the Distortionless Response with EM-ACROSS Signal

With the introduced methodologies in previous sections, the distortionless response can be utilized because its three essentials, the noise reduced observed data, two sets of the independent received signals, and the forward modeling to calculate the regional electric field, have been satisfied. In this section, the distortionless response tensor is utilized to examine the inversed model in Chapter 3.

Owing to the ability of noise reduction with EM-ACROSS signal, that has been verified and represented the data with high precision and stable value with small error, the received data which represents the local electric field can be assumed that highly relevant to the distorted regional electric field. Then Equation 4.17 can be represented as

$$\begin{aligned}\Delta\boldsymbol{\varphi} = \begin{bmatrix}\Delta\varphi_{\mathbf{11}} & \Delta\varphi_{\mathbf{12}}\\ \Delta\varphi_{\mathbf{21}} & \Delta\varphi_{\mathbf{22}}\end{bmatrix} &= \boldsymbol{\varphi}(f_1, f_2)_{local} - \boldsymbol{\varphi}(f_1, f_2)_{regional}\\ &= \boldsymbol{E}(f_2)^{\mathbf{12}}_{local}{}^{-1}\boldsymbol{E}(f_1)^{\mathbf{12}}_{local} - \boldsymbol{E}(f_2)^{\mathbf{12}}_{regional}{}^{-1}\boldsymbol{E}(f_1)^{\mathbf{12}}_{regional}\\ &\rightarrow minimum\end{aligned} \tag{4.66}$$

where $\Delta\boldsymbol{\varphi}$ is defined as a differential response tensor that indicates the dissimilarity of the distortion-removed local electric field response and the regional electric field response.

Furthermore, because the signal source in MT observation and in CSEM observation are independent, the correlation between two obtained data is only the response that relevant to the resistivity. Therefore, Equation 4.66 can be utilized for examining the inversed model and indicating the accuracy of the model when the observed electric field data has high precision. It should be mentioned that the f in $\boldsymbol{E}(f)^{\mathbf{12}}$ should be carefully chosen from the EM-ACROSS frequencies because that will strongly affect the result. In this study, the f in Equation 4.66 is chosen to be one based frequency for the multiplier $\boldsymbol{E}(f)^{\mathbf{12}}_{obs}$, $\boldsymbol{E}(f)^{\mathbf{12}}_{cal}$ and one variable frequency for the multiplicand $\boldsymbol{E}(f)^{\mathbf{12}}_{obs}{}^{-1}$, $\boldsymbol{E}(f)^{\mathbf{12}}_{cal}{}^{-1}$ then Equation 4.66 can be modified to

$$\Delta\boldsymbol{\varphi} = \boldsymbol{E}(f_i)^{\mathbf{12}}_{obs}{}^{-1}\boldsymbol{E}(f_0)^{\mathbf{12}}_{obs} - \boldsymbol{E}(f_i)^{\mathbf{12}}_{cal}{}^{-1}\boldsymbol{E}(f_0)^{\mathbf{12}}_{cal} \rightarrow minimum \tag{4.67}$$

4.9.1 Examination of the MT models

In Chapter 3, two models with different data sets were demonstrated with their dissimilarity. Here we can utilize Equation 4.67 to examine two models with the CSEM data. The $\boldsymbol{E}(f)_{cal}^{\mathbf{12}}$ is calculated by the edge-based FEM algorithm, which introduced in section 4.8. For utilizing that algorithm, the resistivity value from two different inversed models was employed as the input parameter σ^m in the forward modeling. In the MT modeling, the mesh was generated by a Delaunay-based quality tetrahedral mesh generator "TetGen" (Si, 2015). In the CSEM forward modeling, the mesh was generated by a mesh generator program "GiD" with its algorithm. Therefore, the produced meshes between the two models were quite different. In the CSEM forward modeling, the resistivity of an element was borrowed from the element in the MT model, which the one has the closest gravity center. The computing program language was written in Python 3.7. Generating the sparse stiffness matrix with computing the resistivity information on TSUBAME3 (the supercomputer portal operated by Tokyo Institute of Technology) took 6.5 hours for the first time and a 492452x492452 size sparse matrix. A sparse linear system dedicated direct solver "spsolve" under the numerical computation library "SciPy" was utilized to solve the sparse linear equations system (Equation 4.56). There were 16 frequencies (Table 4.1) employed in the solver. The sparse linear equations system was solved for 3 hours by individual computation.

A comparable plot of the observed data and calculated data is represented in Figure 4.14. The data is from site KS007 (Figure 4.7), which was located close to the summit of Yugama crater. Both the models with previously observed data and with newly observed data have a lousy fitting with the observed CSEM data on the frequency spectra. It is not unexpected when we try to fit a distortionless data with a distortion influenced data. With only the direct comparison, examining

the modeling result becomes mean less. Thus, a comparison in the distortionless response tensor is more practicable. With utilizing Equation 4.66, the $E1$ and $E2$ in Equation 4.13a and 4.13c represented the electric field related to the grounded sources dipole_{NS} and dipole_{EW}, respectively. The base frequency f_0 was set to the highest two frequencies, 4.61 and 4.63 Hz due to its smallest error in most of the sites. The differential electric field response tensor is represented in Figure 4.15 with plotting the real part and imaginary part of each component. The result in the differential response tensor (Equation 4.66) represented an apparent difference between the data from two models. By employing the model with previously observed data ("model P") in the regional electric field computation, the differential response tensor represented a significant value. A kind of such result indicates a significant difference between the distortion-removed observed data and the distortionless calculated data on this site. In contrast, the model with newly observed data (model N) represented a much smaller differential response tensor, which indicates the calculated data further close to the observed data.

To utilize this method in the modeling interpretation for the differences between two models which were represented in Chapter 3 (Figure 3.17 & 3.18), data from the sites which align at the east of Yugama crater (i.e., from KS002, KS003, KS004, and KS005) (Figure 4.7) was employed. The results with the previously observed data and the newly observed data are represented in Figure 4.16 and 5.16, respectively, by plotting the real part and imaginary part of the differential response tensor components. The "model N" (Figure 4.17) represents a vertically denser plot on the different components of the differential response tensor. In contrast, the "model P" (Figure 4.16) represents a relatively scattered plot. That indicates the forward modeling computation with the resistivity parameters from "model N" has a closer result to the

distortionless observed data. The independent signal sources between MT and CSEM methods signify this result is robust that “model N” is credible. Thus, the dissimilarity of the two models can be interpreted to the temporal changes.

4.9.2 Examination of the test models with imaginary resistor

The previous research of Kusatsu-Shirane volcano demonstrated the existence of a sealing zone beneath Yugama crater lake (Ohba et al., 2008; Ohba et al., 2019) with probable composed of quartz, gypsum, alunite, or similar secondary hydrothermal. Those probable minerals are further resistive than the sealed fluid and overlaying clay cap (e.g., Caselle et al., 2019; Dong Wook Shin & Tomozawa, 1993). When a thin resistor is encased by conductors, it will be difficultly detected in the MT sounding method because the induced electric fields from the plan wave natural signal are mainly horizontal. Those horizontal electric fields are less sensitive to the horizontal thin resistor (Constable & Weiss, 2006). In the CSEM case, the penetrating vertical component of the electric current can be interrupted by such a thin resistor and represent its feature in the response (Hordt et al., 2000).

For examining the sensitivity of the CSEM sounding method to the thin resistive structure in this study, two test models were modified by adding a thin resistor into “model N”. In the first test model “model N_R1”, a resistor with 10^6 Ohm-meter resistivity and [1.2 km x 1.2 km x 0.6 km (north-south, east-west, vertical)] volume was added at [0, -0.4, 0.9 km (northing, easting, altitude)] overlying the conductor C2. This resistor represents the top of the silica sealing zone that caps the supercritical fluid (Dong Wook Shin & Tomozawa, 1993). According to the

sensitivity test in Chapter 3 for the deep conductor C2, this change should represent its feature at a frequency range between 8.8-2.2 Hz.

The test model "model N_R1" is examined by differential electric field response with CSEM data after the forward modeling. Figure 4.18 firstly demonstrates the plot of the electric field at one site in the testing area, KS07, and one site out of the testing area, KS02. Both two sites represent the affected features in both components of the electric field. The relative change in the differential electric field response is demonstrated in Figure 4.19. The actual difference in the differential electric field response $\boldsymbol{\Delta\varphi}$ is the change in test model TR1 references to the original model. The affected features from an added strong resistor are obvious in this analysis as in the amplitude and phase plot of the electric fields. The change of both the electric fields and the response at lower frequencies indicates the penetrating radiation pattern of the electric current at near-field is interrupted. These results demonstrate the sensitivity of the CSEM method response in the resistive structure, regardless of inside or outside of the changing area.

The MT data is also utilized for examining this model. Besides the phase tensor analysis introduced in Chapter 3, an imitative method from differential electric field response is utilized here. By substituting the impedance tensor from Equation 3.25a in Equation 4.15 and 4.66 by replacing the electric field, a distortionless response of the impedance tensor φ_Z then can be obtained. To verify its sensitivity to the changing features, the relative change in φ_Z at the same sites is demonstrated in Figure 4.20. The impedance is also affected by the added resistor. Compare to the CSEM data demonstrating the change of penetrating electric current at near-field

(the lower frequencies, < 1Hz), the impedance demonstrating larger change at the frequencies where the added resistor located (0.5-4.4 Hz). The phase tensor plot is demonstrated in Figure 4.21. Considering the high resistivity of the added resistor, the changes in the phase tensor plot is relatively not obvious. Only a distinguishable change at KS07 and a slight visible change at KS09 at 4.4-2.2 Hz are represented. At sites out of the modified area, the features of phase tensor are unchanged between the two models.

In the second test model TR2, the resistor R1 that discovered in the MT model (Figure 3.10 and 3.17) was modified by 10^6 Ohm-meter resistivity from "model N". This resistor represents a situation that the overpressured gas is released from the sealed supercritical fluid and fills the space, underlies the clay cap as a time-variable changing feature. The plot of the electric field at site KS07 and KS02 are represented in Figure 4.22. The change in electric fields is relatively smaller in test model TR2, so as the relative change in the differential electric field response (Figure 4.23). The site KS07, which right above the resistor, represents less difference than site KS02, which is out of the changing area. This feature is due to the overlying conductor C1 and the underlying conductor C2, which fully envelope the resistor R1. Therefore, the electric current has less potential to penetrate this resistor, particularly with its tube-shape. The response of the impedance tensor φ_Z from MT data is even more sensitive to this feature (Figure 4.24). Similar to test model TR1, the changes in the phase tensor plot is relatively not noticeable. Only a distinguishable change at KS07 2.2 Hz is represented.

The examination of two testing models with imaginary resistors demonstrates the ability and disability of the CSEM method. The resistor can be distinguished, even its thickness is less than the locating depth. However, when a resistor is fully enveloped by conductors and the horizontal area is not wide enough, investigating this resistor will be difficult. For the case of Kusatsu-Shirane volcano, the CSEM method can determine the appearance of the thin resistive sealing zone in the inverse modeling but might be challenging to determine the temporal changes in resistor R1 due to its tube shape. In the sensitivity test of MT data, the response of the impedance tensor φ_Z could probably provide a better comprehension of the changed structure than the phase tensor analysis. That becomes a feasible option for examining a model at specific sites.

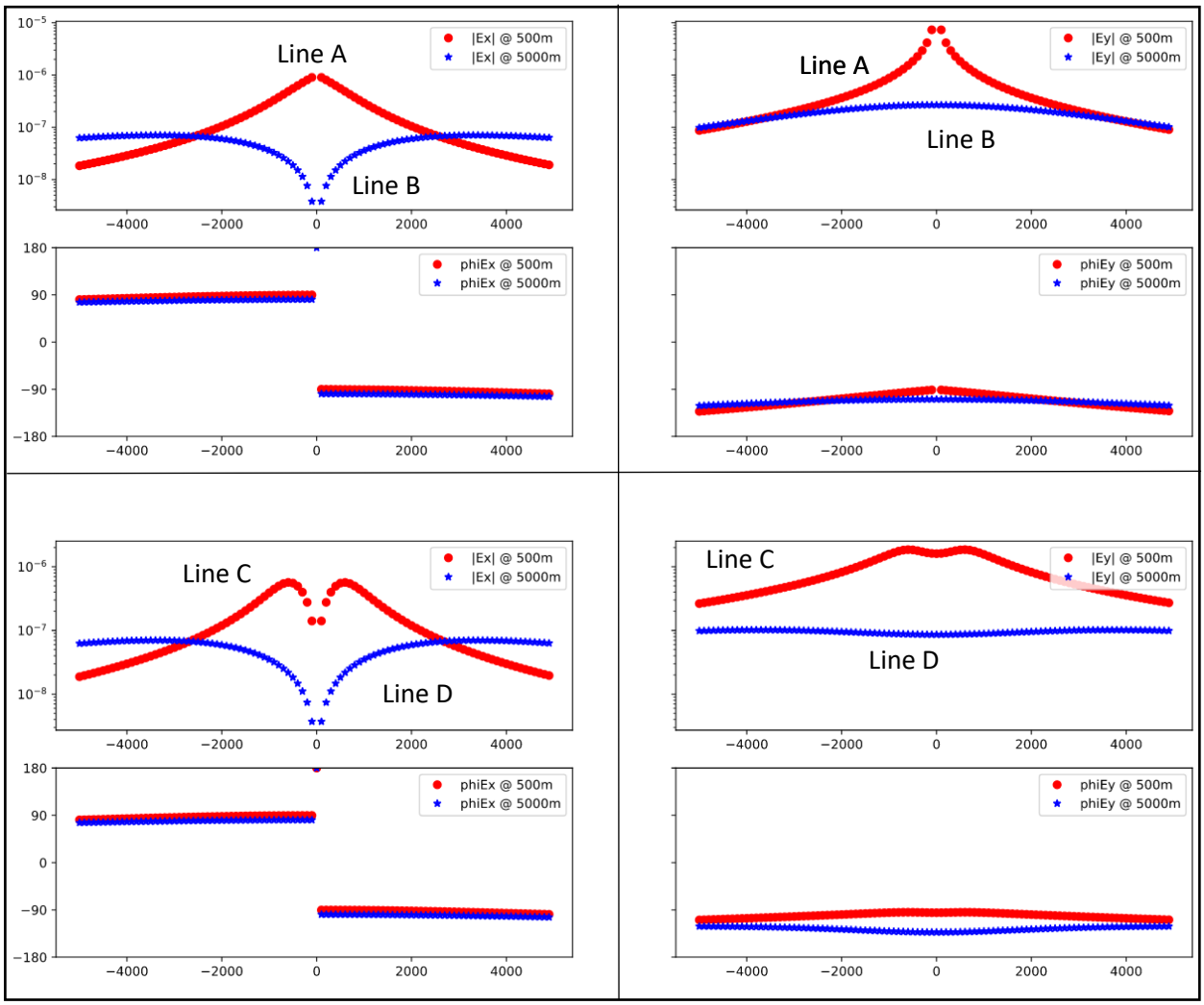
Line A
Line B
|Ex| @ 500m
|Ex| @ 5000m
phiEx @ 500m
phiEx @ 5000m
|Ey| @ 500m
|Ey| @ 5000m
phiEy @ 500m
phiEy @ 5000m
Line C
Line D

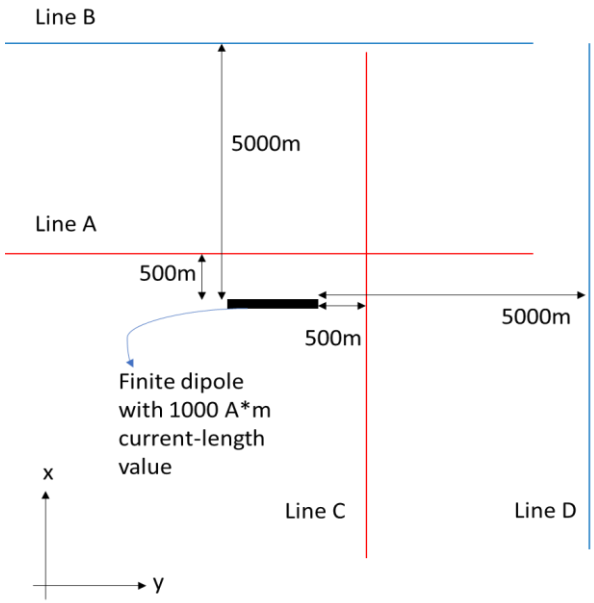
Line B
5000m
Line A
500m
500m
5000m
Finite dipole
with 1000 A*m
current-length
value
x
y
Line C
Line D

Figure 4.1

Analytical solution result of grounded electric dipole.

This example presents the amplitude (upper subfigures) and phase (lower subfigures) of electromagnetic fields in Ex and Ey components, which are results of the analytical solution in Equation 2.40a-2.40d. A y-directed finite electric dipole source with a current*length value=1000 A-m is placed at (0,0,0)m. Line A is an x-directed observation profile at (0,500,0)m; Line B is an x-directed observation profile at (0,5000,0)m; Line C is a y-directed observation profile at (500,0,0)m and Line D is a y-directed observation profile at (5000,0,0)m.

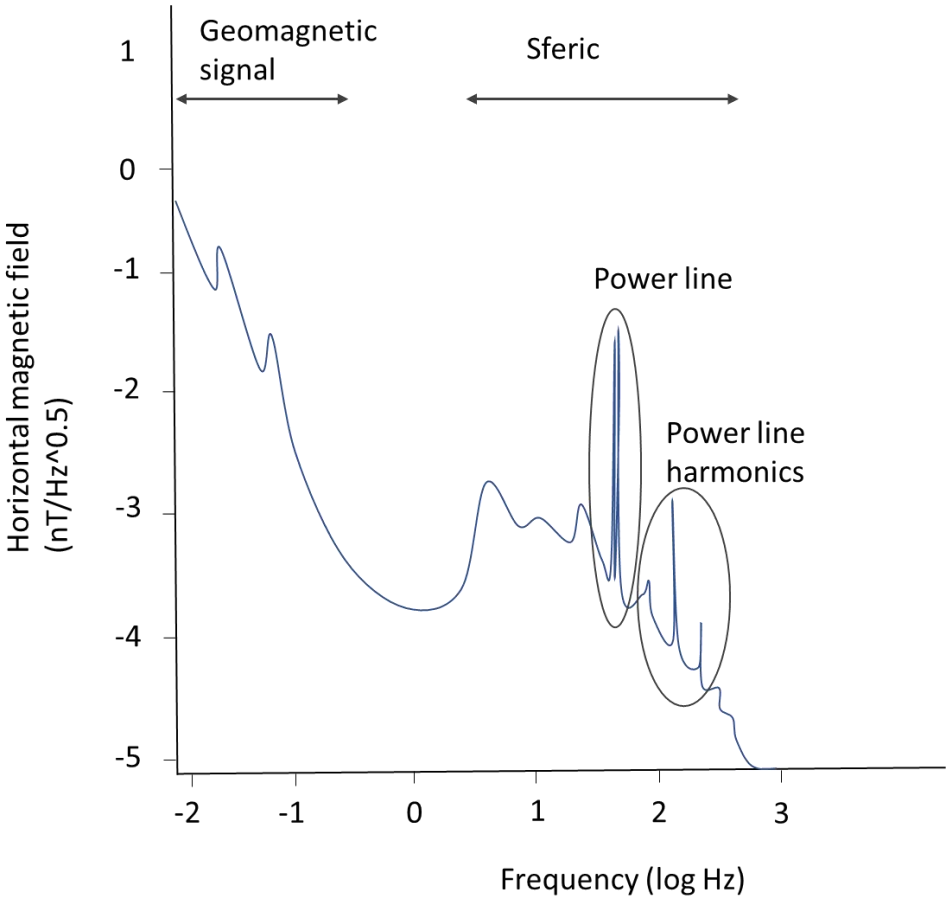

Figure 4.2

The schematic frequency spectrum of the horizontal magnetic field in the environment.

This schematic diagram was modified based on the result of Macnae et al. (1984).

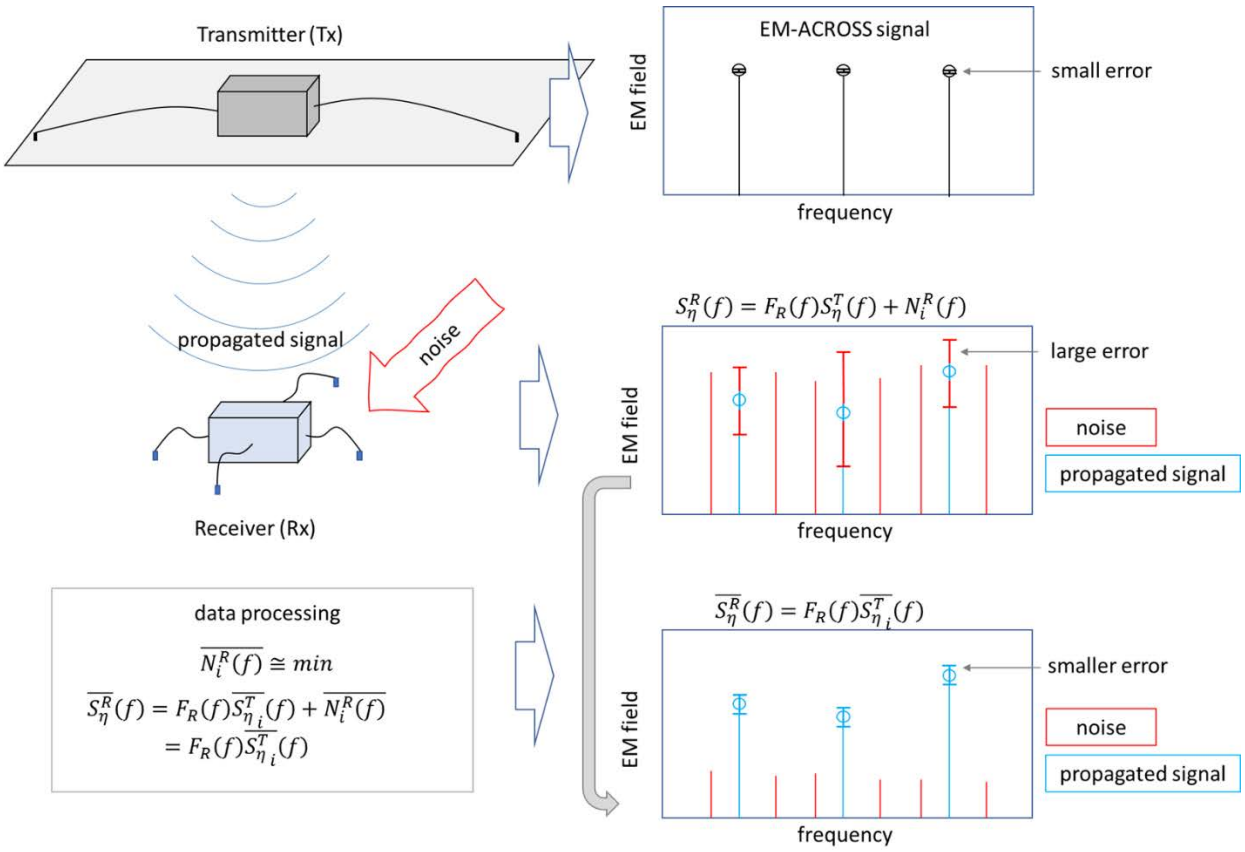

Figure 4.3

The schematic diagram of the EM-ACROSS proposition.

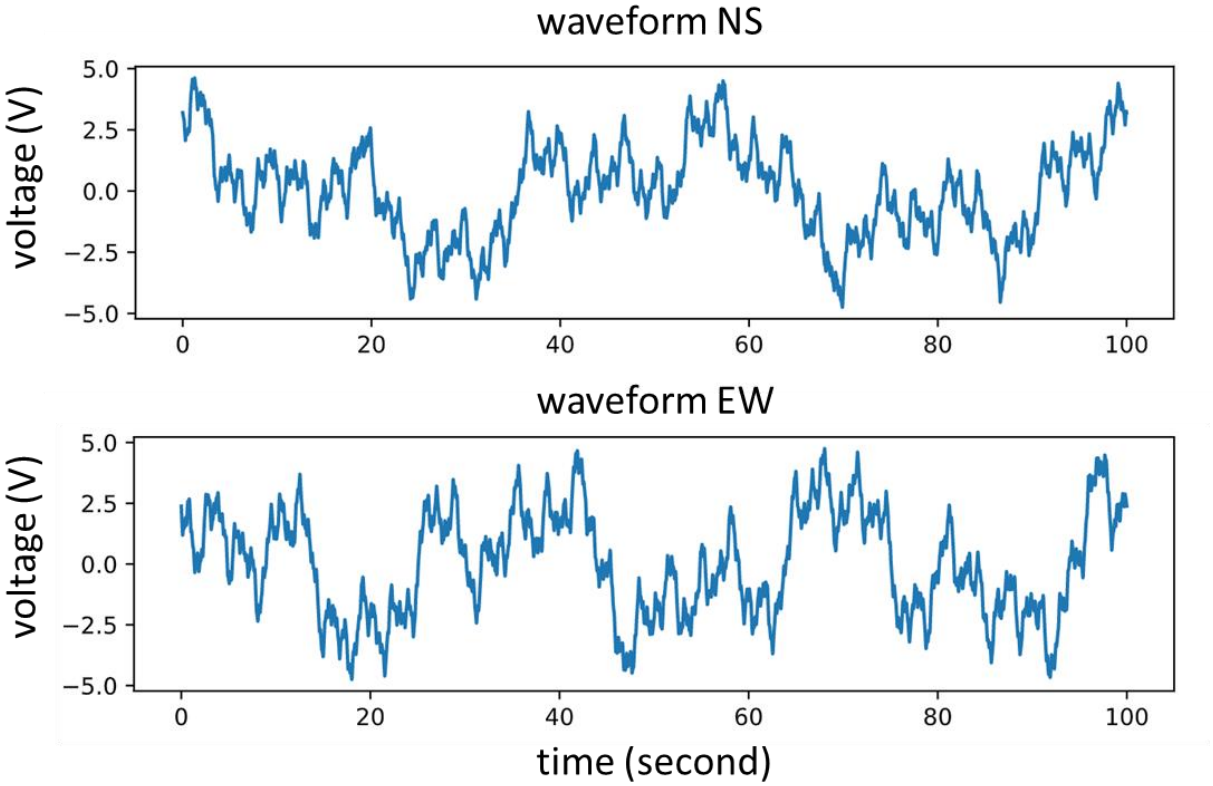

Figure 4.4

The stored waveforms in two-channels of the function generator.

The amplitude of these graphs has been converted from digits to the output voltage. The output voltage value is from the investigation record in 2018, at Kusatsu-Shirane volcano, Japan.

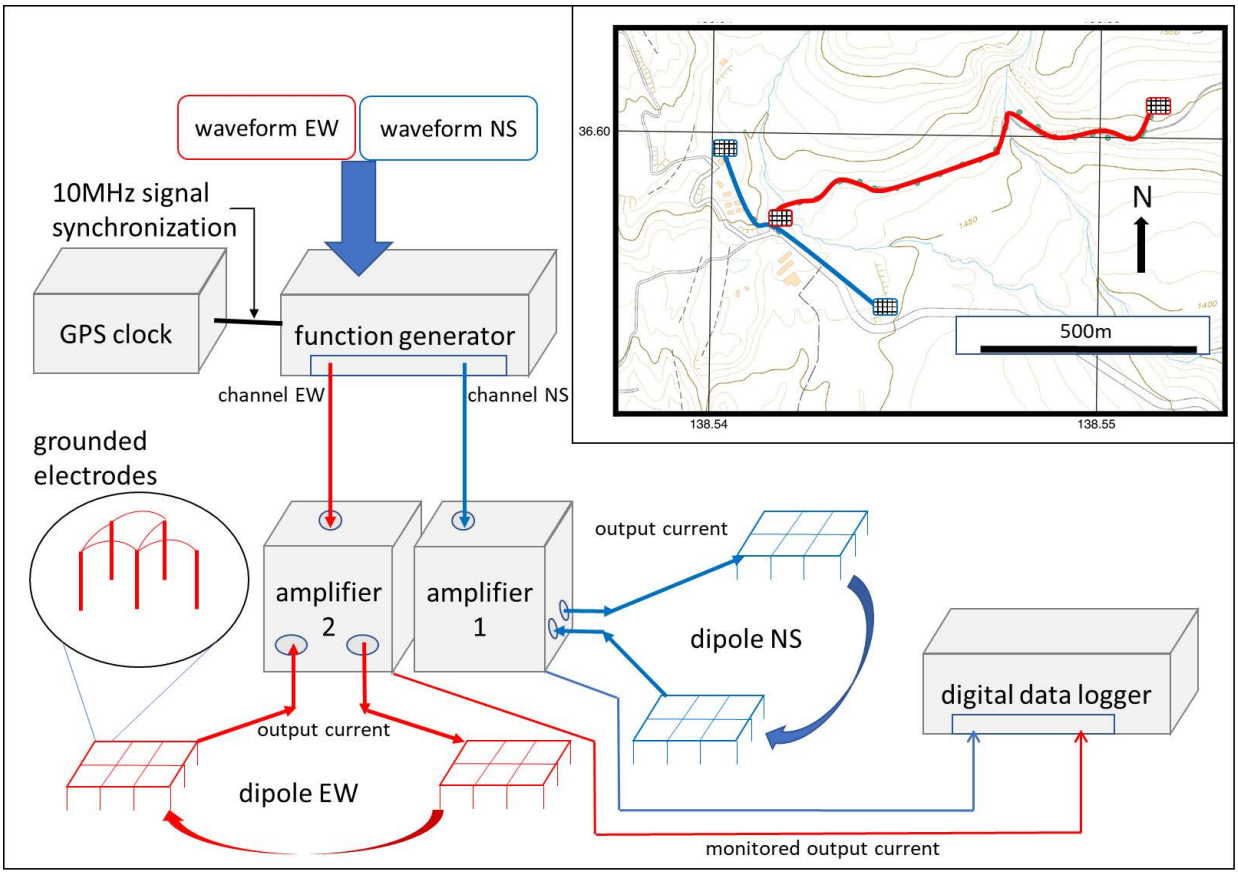

Figure 4.5

The schematic diagram of the instrument design of a simultaneously transmitting EM-ACROSS.

The two waveform EW and NS are represented in Figure 4.4. The function generator sends the signals by independent channels. The two amplifiers enlarged these signals and inject to the ground by two sets of the dipoles. The dipoles are quasi-orthogonal for the most efficient propagation coverages. At each end of the dipoles is a grounded electrodes array to minimize the inhomogeneous resistivity from the surface soil. A digital data logger continually records the monitored output current during the transmission.

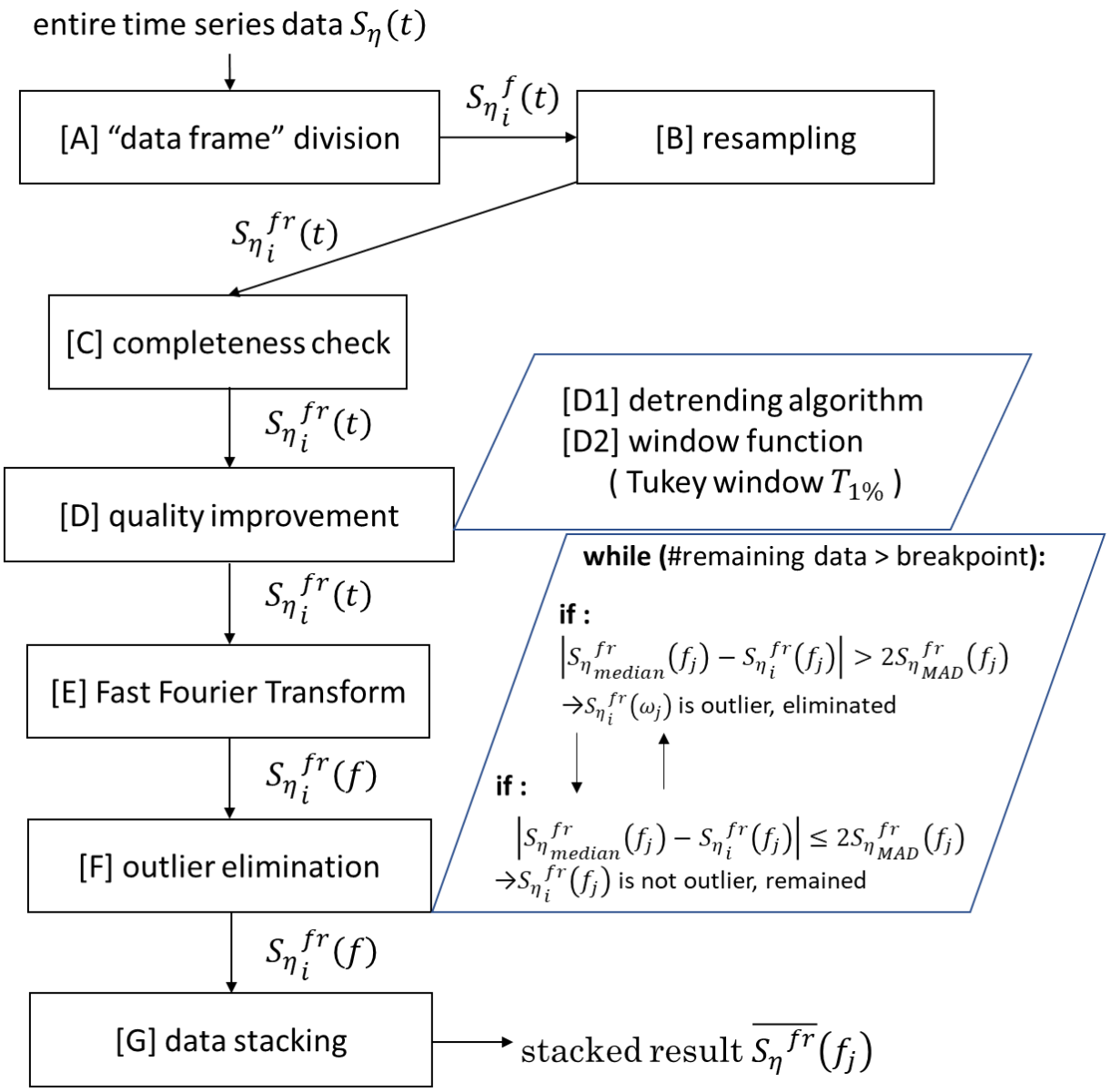

Figure 4.6

The schematic flow diagram of the data processing for the observed data with CSEM signal from EM-ACROSS.

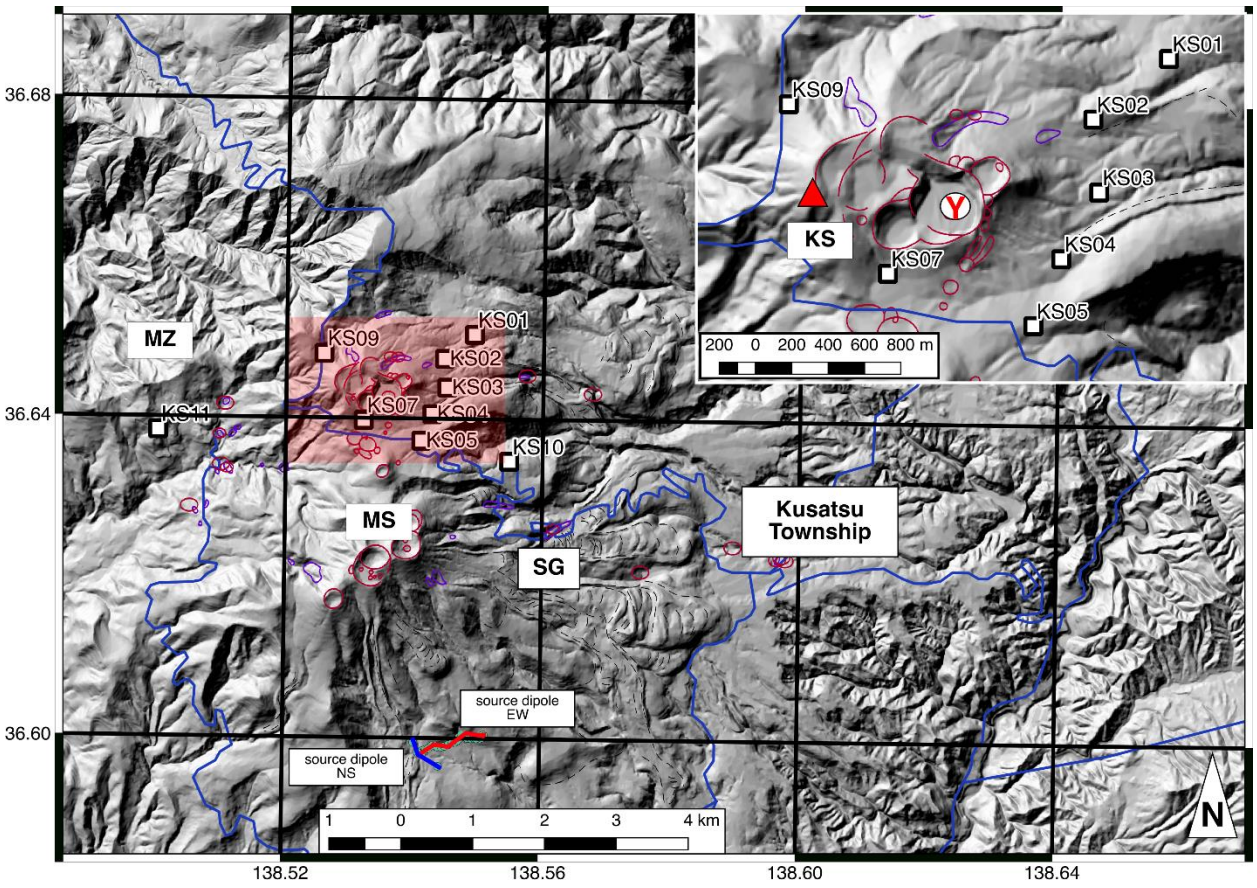

Figure 4.7

A regional-scale and a local-scale map of Kusatsu-Shirane Volcano with receivers and source dipoles of EM-ACROSS.

The base map is the topographic map with grayscale shaded relief. The square and triangle symbols denote the receivers in EM-ACROSS. The red circles and open curves show the craters of past eruptions. The purple closed curves show the fumarole zones. The blue curves show the local highway as a reference item on the map. The abbreviation symbol “SG”, “MS” and “MZ” denotes the location of Sesshougawara fumarolic area, Mt. Motoshirane, and Manza hot spring field, respectively. The area of the local-scale map is masked by a red rectangle. In the local-scale map, additionally, the abbreviation

symbol “KS” denotes Mt. Shirane and the red triangle denotes its mountain peak. The white circle with symbol “Y” denotes the center of Yugama crater lake. The bold red and blue line at the bottom of the figure with “source dipole EW” and “source dipole NS” markers denotes the grounded wire and dipole sets of the EM-ACROSS transmitter in east-wast direction and in the north-south direction, respectively.

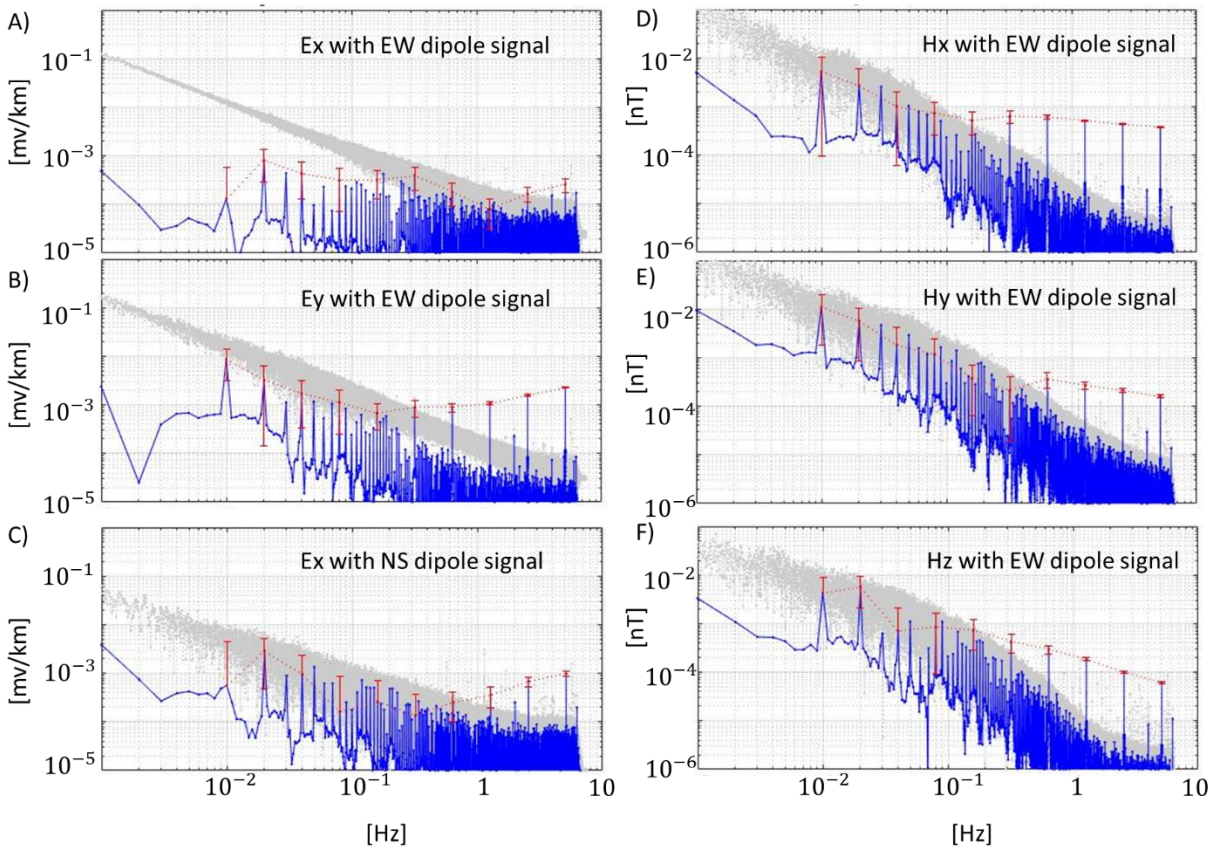

Figure 4.8

The magnitude-frequency spectra of observed electromagnetic components from the 2017 initial experiment.

The gray lines denote the pre-processing data and the blue lines denote the post-processing data. The red bars denote the standard deviation error at the located frequencies.

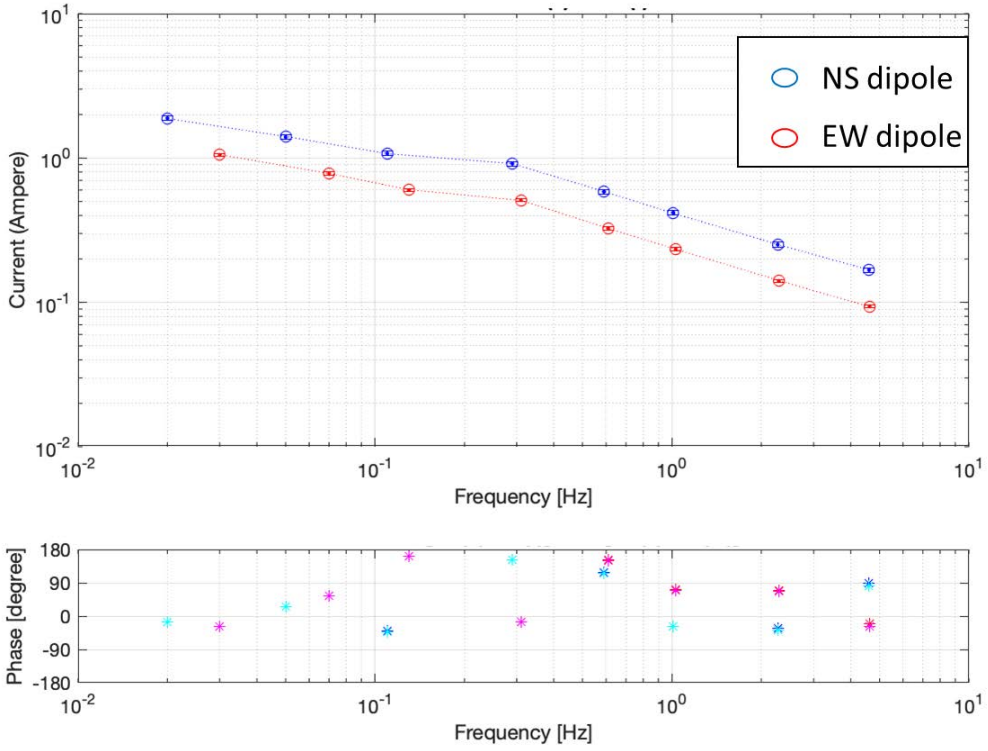

Figure 4.9

The frequency spectra of monitored current load in the full EM-ACROSS operation in 2018.

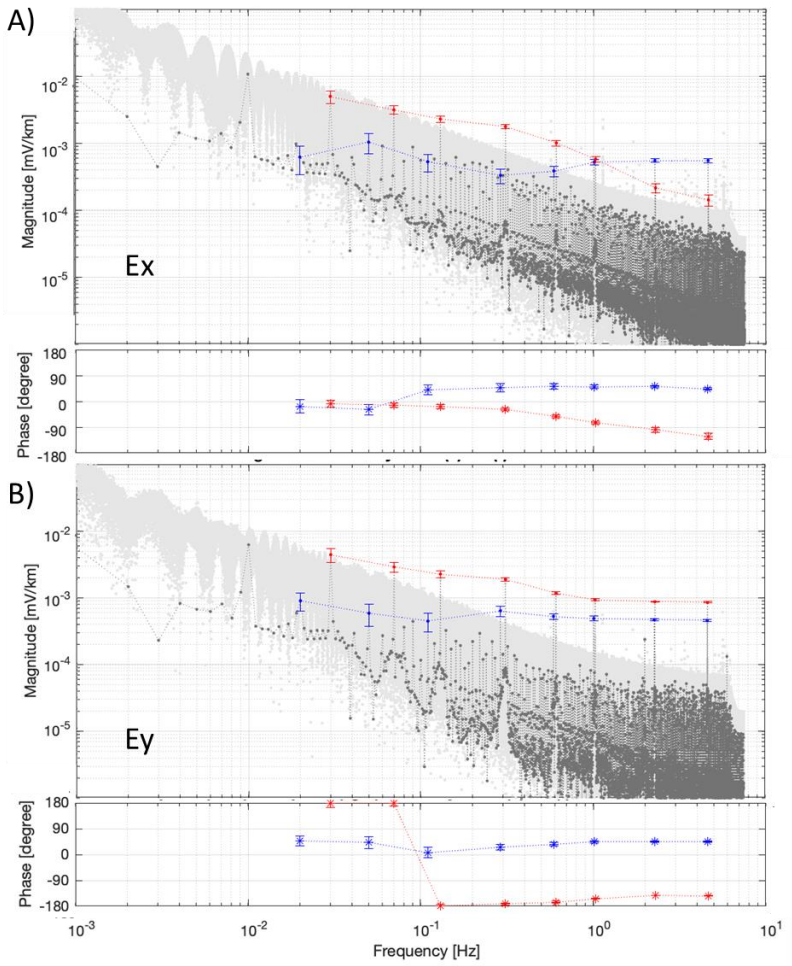

Figure 4.10

The frequency spectra of observed x-component (A, upper) and y-component (B, lower) electric field from the 2018 full operation.

The light and dark gray lines denote the pre-processing and the post-processing data, respectively. The blue and red bars denote the error of "NS-dipole signal related" and "EW-dipole signal related" electric fields' amplitude and phase, respectively. The blue and red dot line denotes the trend of the changes in frequency. The phase value has been normalized with the value of the randomly selected phase shift in the signal design (Table 4.1).

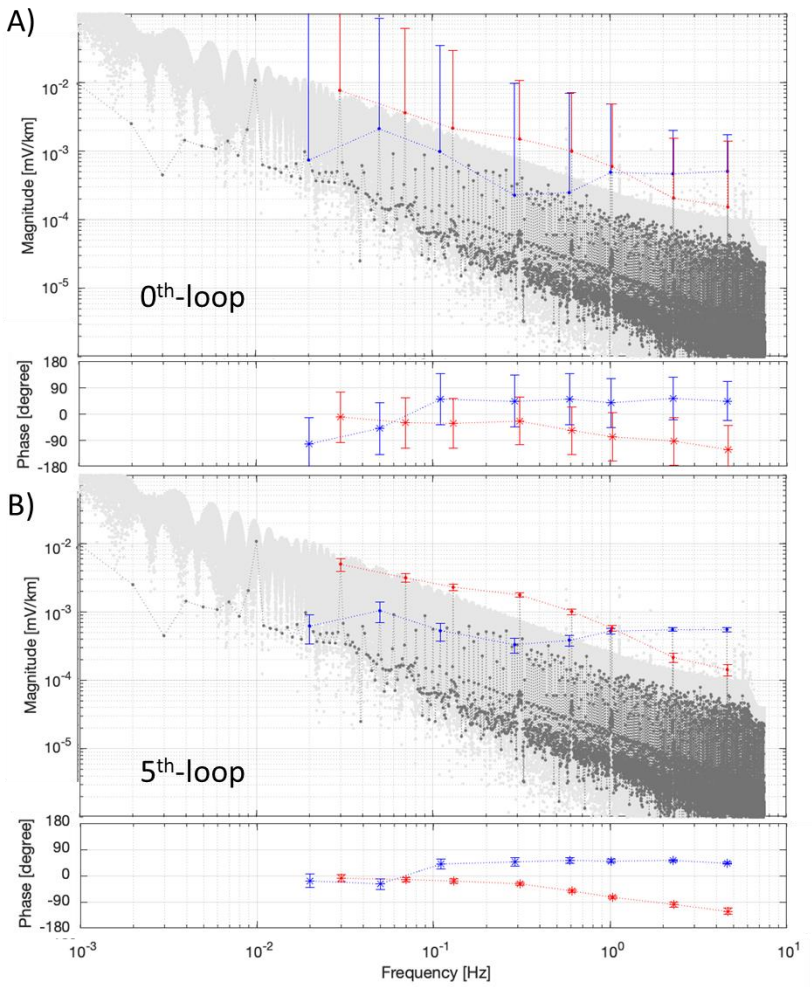

Figure 4.11

The comparative result of the x-component electric field stacking between applying the 0^{th}-loop (A, upper) and the 5^{th}-loop (B, lower) outlier elimination products.

The light gray lines denote the pre-processing data and the dark gray lines denote the post-processing data. The blue and red bars denote the error of "NS-dipole signal related" and "EW-dipole signal related" electric fields' amplitude and phase. The blue and red dot line denotes the trend of the changes in frequency. The phase value has been normalized with the value of the randomly selected phase shift in the signal design (Table 4.1).

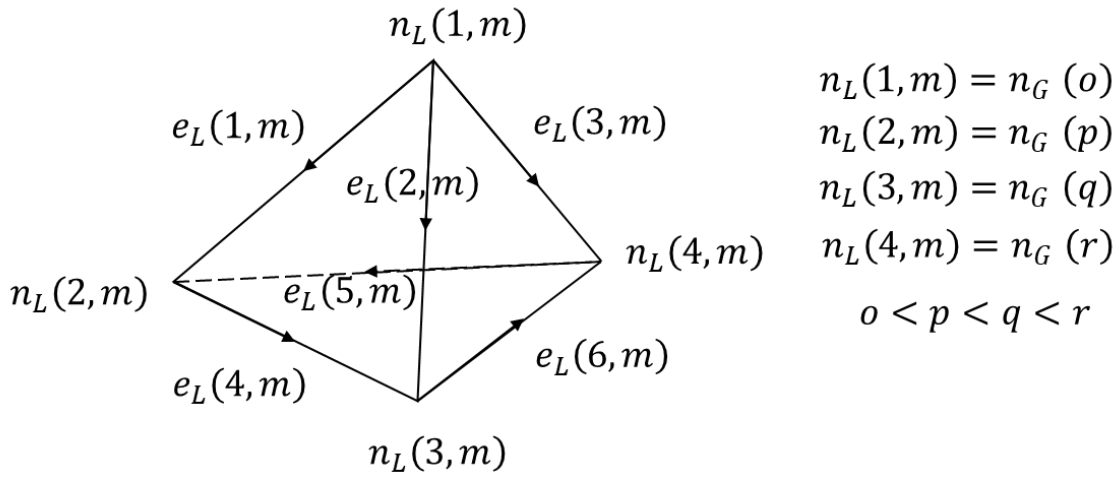

Figure 4.12

The schematic diagram of a global-local numbering system for a tetrahedral element *m*.

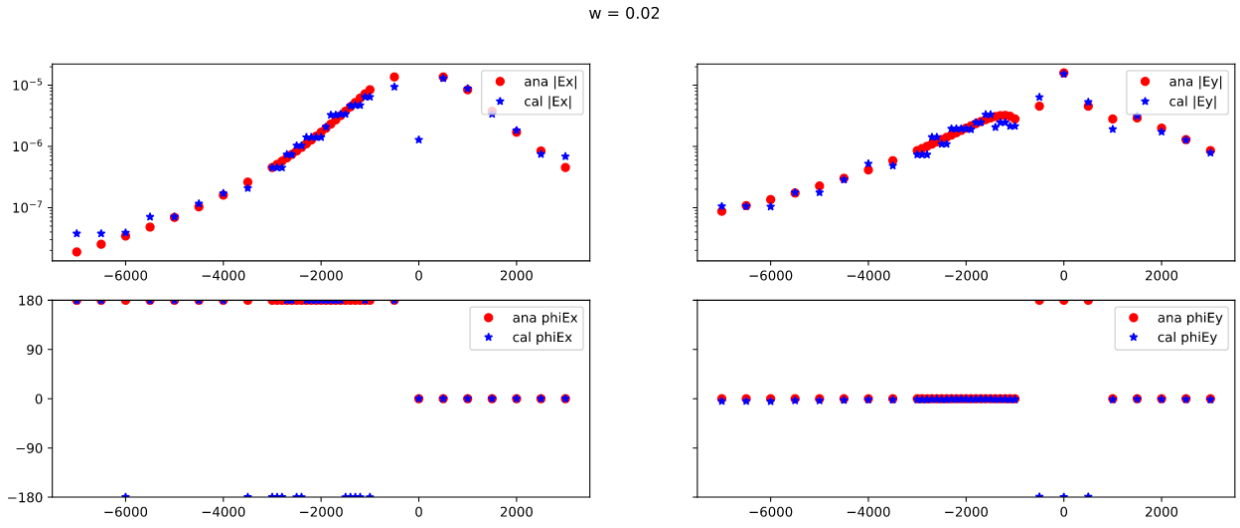

Figure 4.13

The comparison of the computed electric field from the analytical solution and forward modeling.

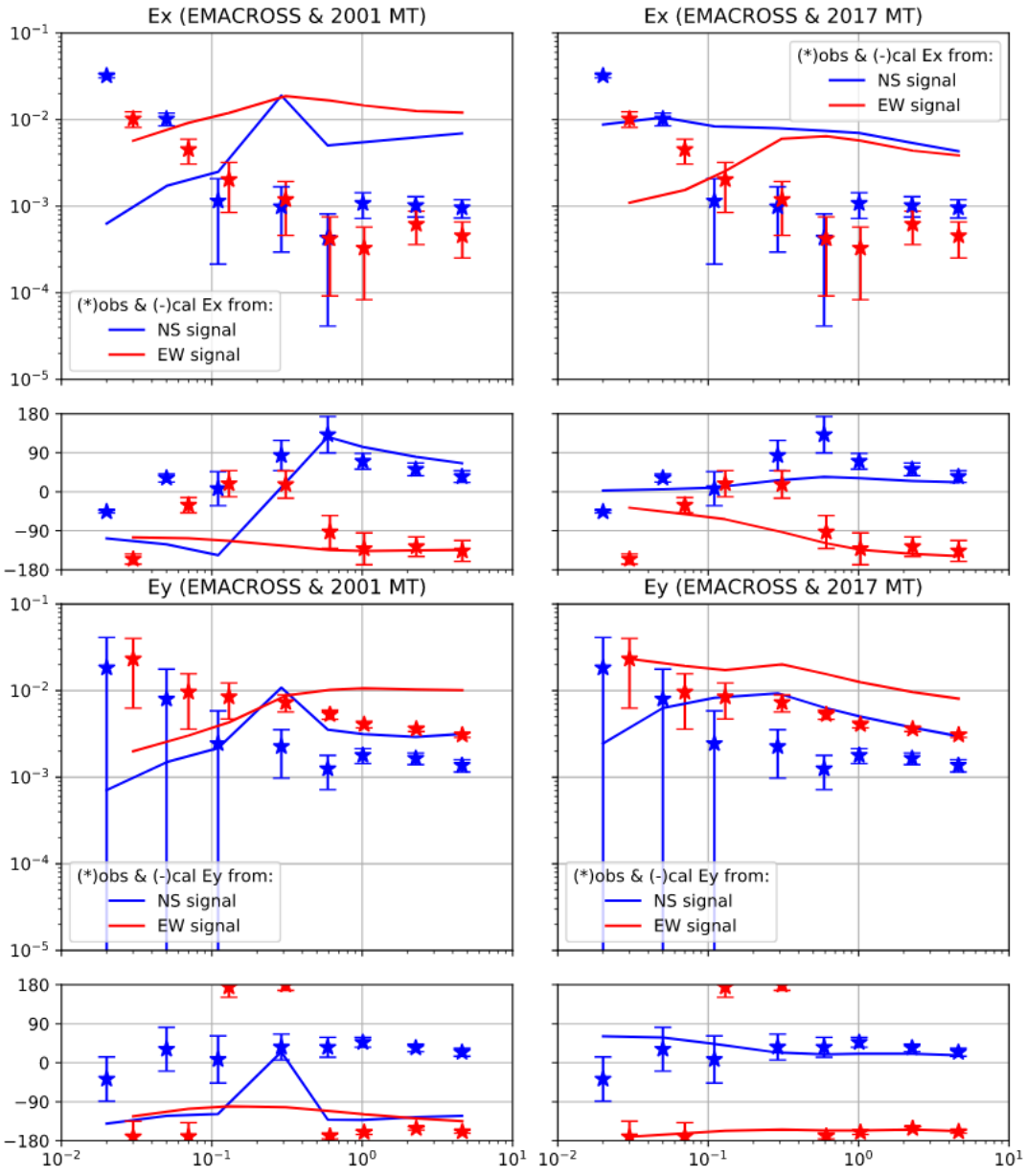

Figure 4.14

The comparative result of the observed electric field and the calculated electric field from two different models with previously observed data and newly observed data.

The subfigures with a subtitle (EMACROSS & 2001 MT) represented the electric field components of the observed data (star symbols and error bars) and the calculated result

(dash lines) from previously observed data. The subfigures with a subtitle (EMACROSS & 2017 MT) represented the electric field components of the observed data and the calculated result from newly observed data.

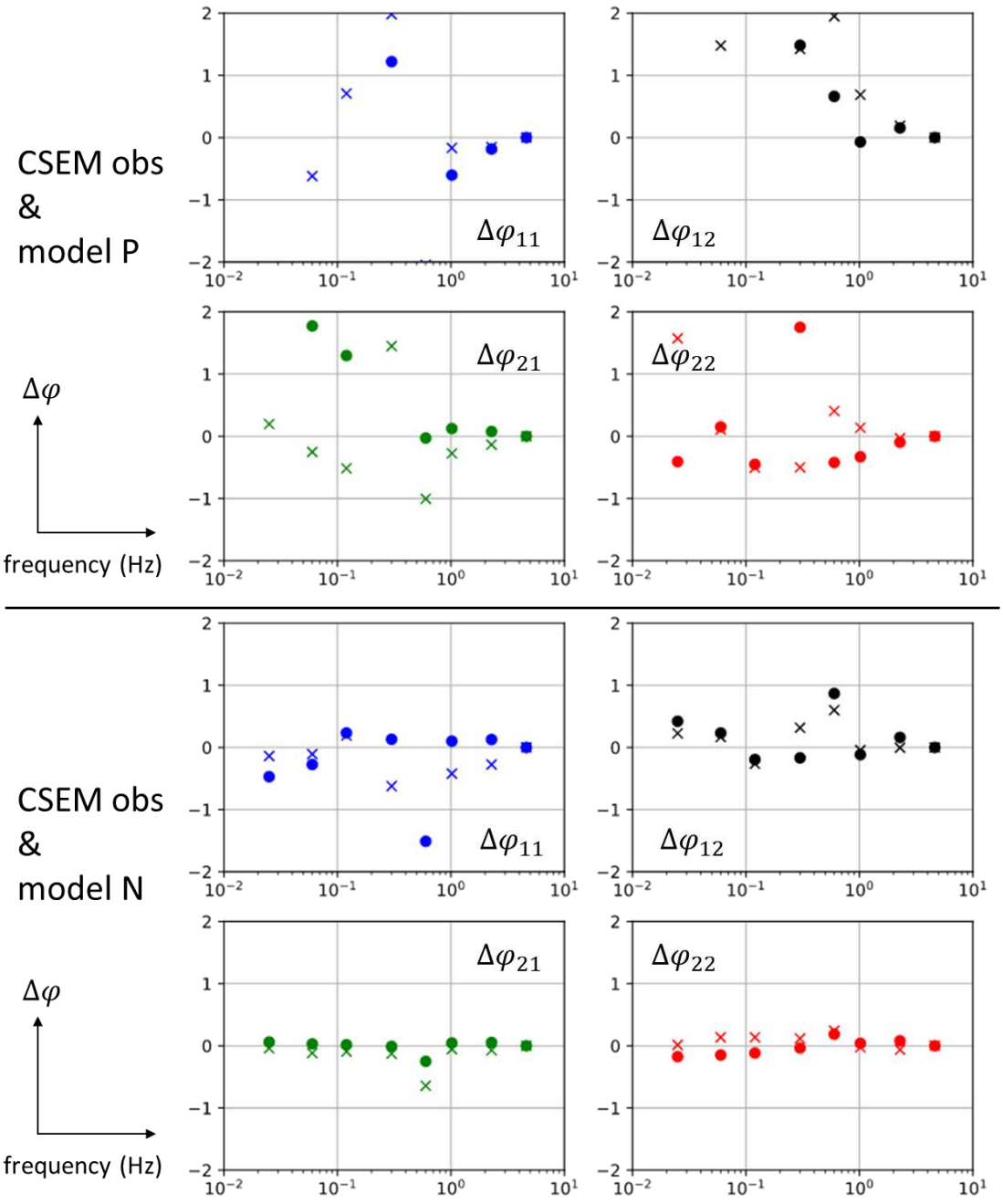

Figure 4.15

The comparative result of the differential response tensor from two different models.

The comparative result of the differential response tensor from two different models, one with previously observed data ("model P") and one with newly observed data (model N)

from site KS007. The real part and imaginary part of the differential response tensor components are plotted by dots and cross, respectively.

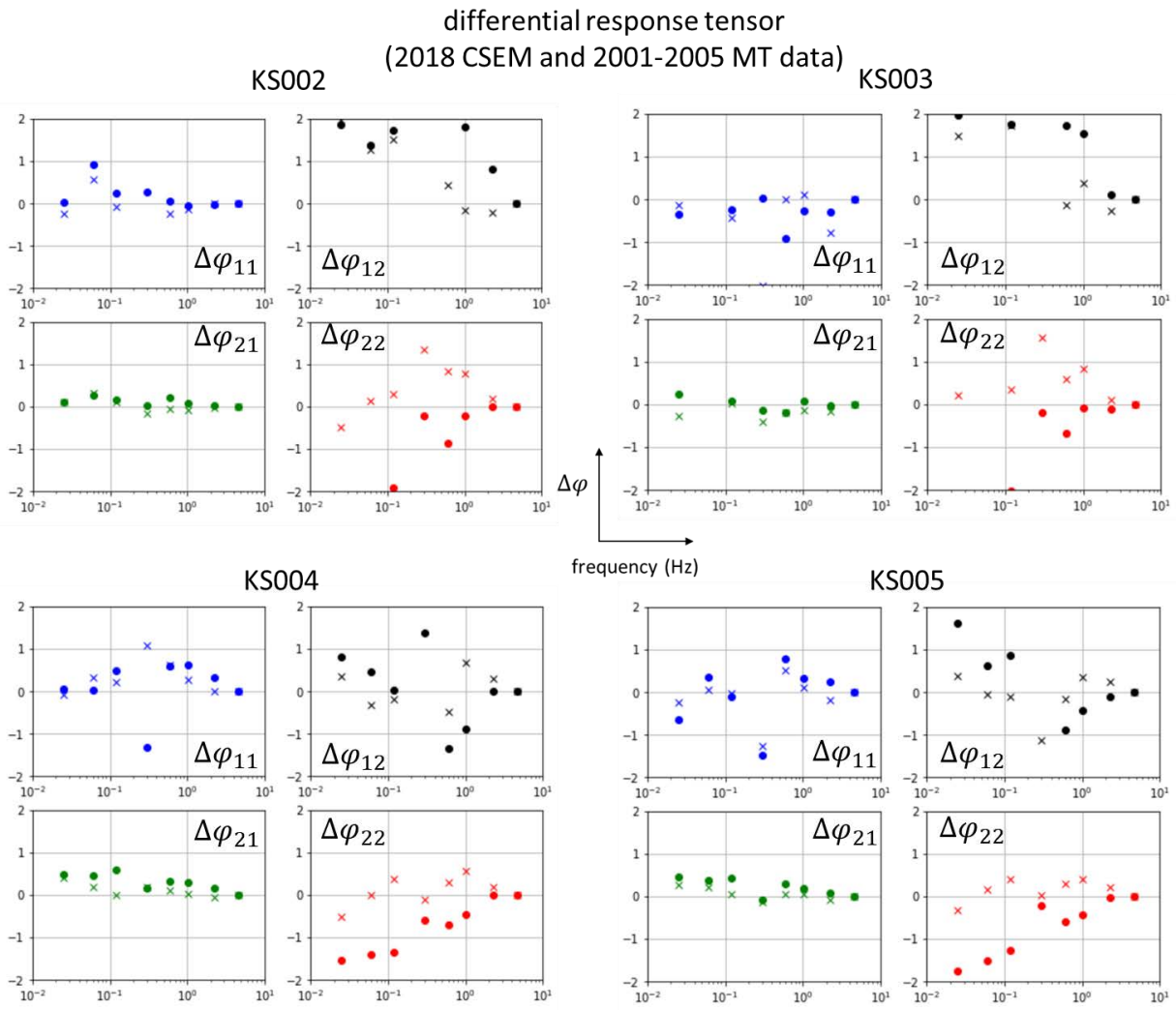

Figure 4.16

The comparative result of the differential response tensor from the observed data and "model P" from site KS002, KS003, KS004, and KS005.

The real part and imaginary part of the differential response tensor components are plotted by dots and cross, respectively.

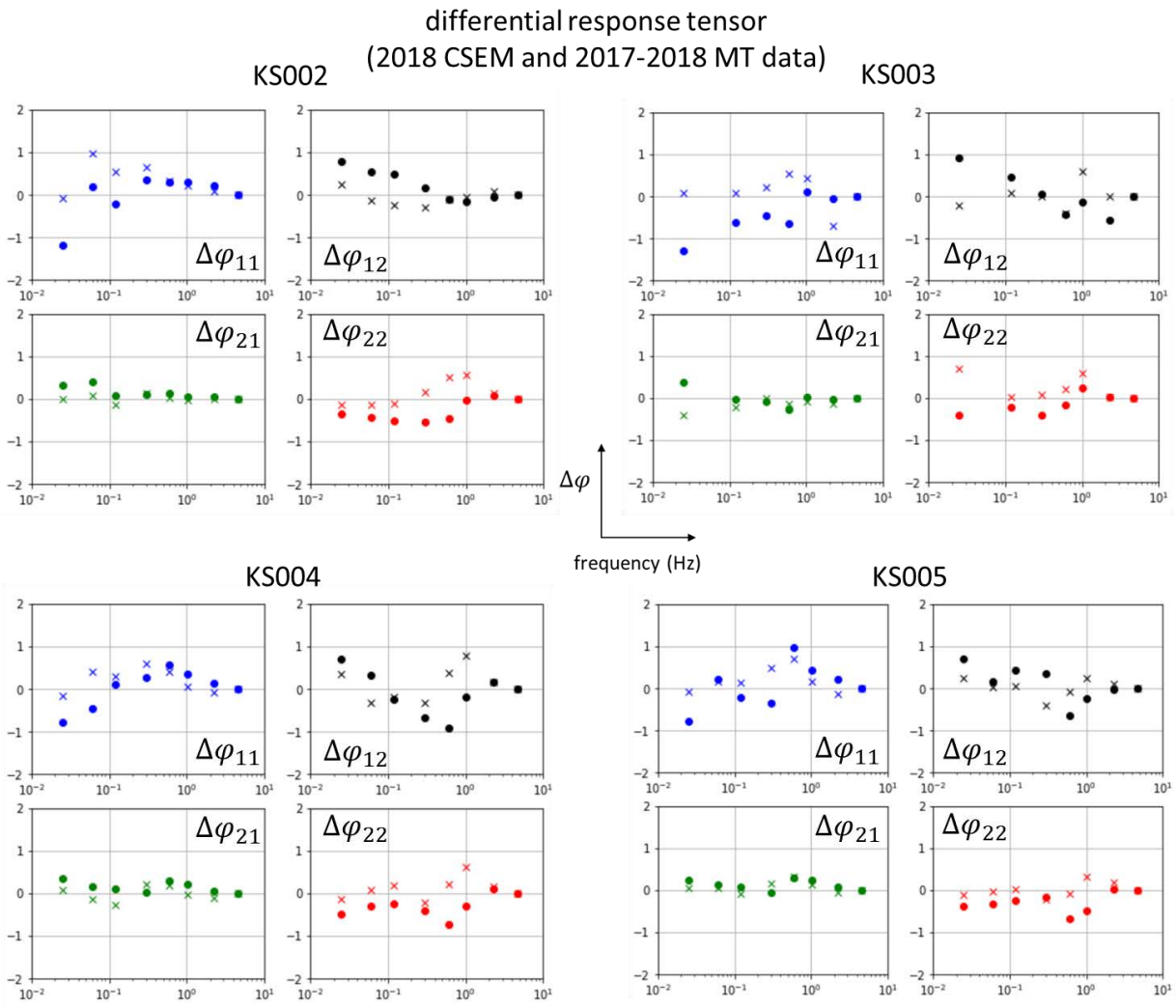

Figure 4.17

The comparative result of the differential response tensor from observed data and "model N" from site KS002, KS003, KS004, and KS005.

The real part and imaginary part of the differential response tensor components are plotted by dots and cross, respectively.

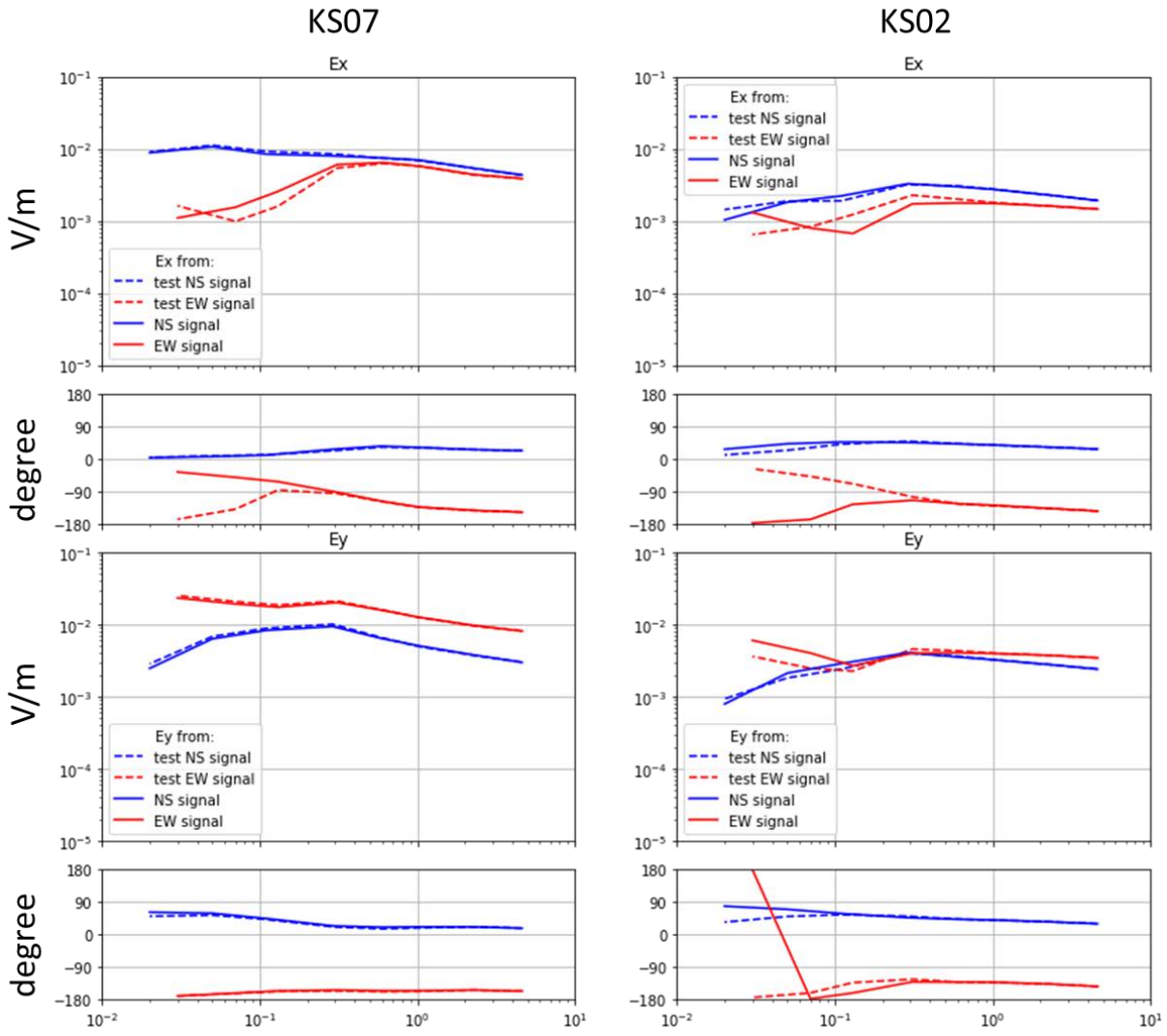

Figure 4.18

Calculated electric field from the original model and test model TR1 with the newly observed data.

The location of KS07 and KS02 is represented in Figure 4.7. The blue and red lines represent the electric field at receivers from source dipole NS and dipole EW, respectively. The solid and dash line denotes the forward model from the original model and test model TR1, respectively.

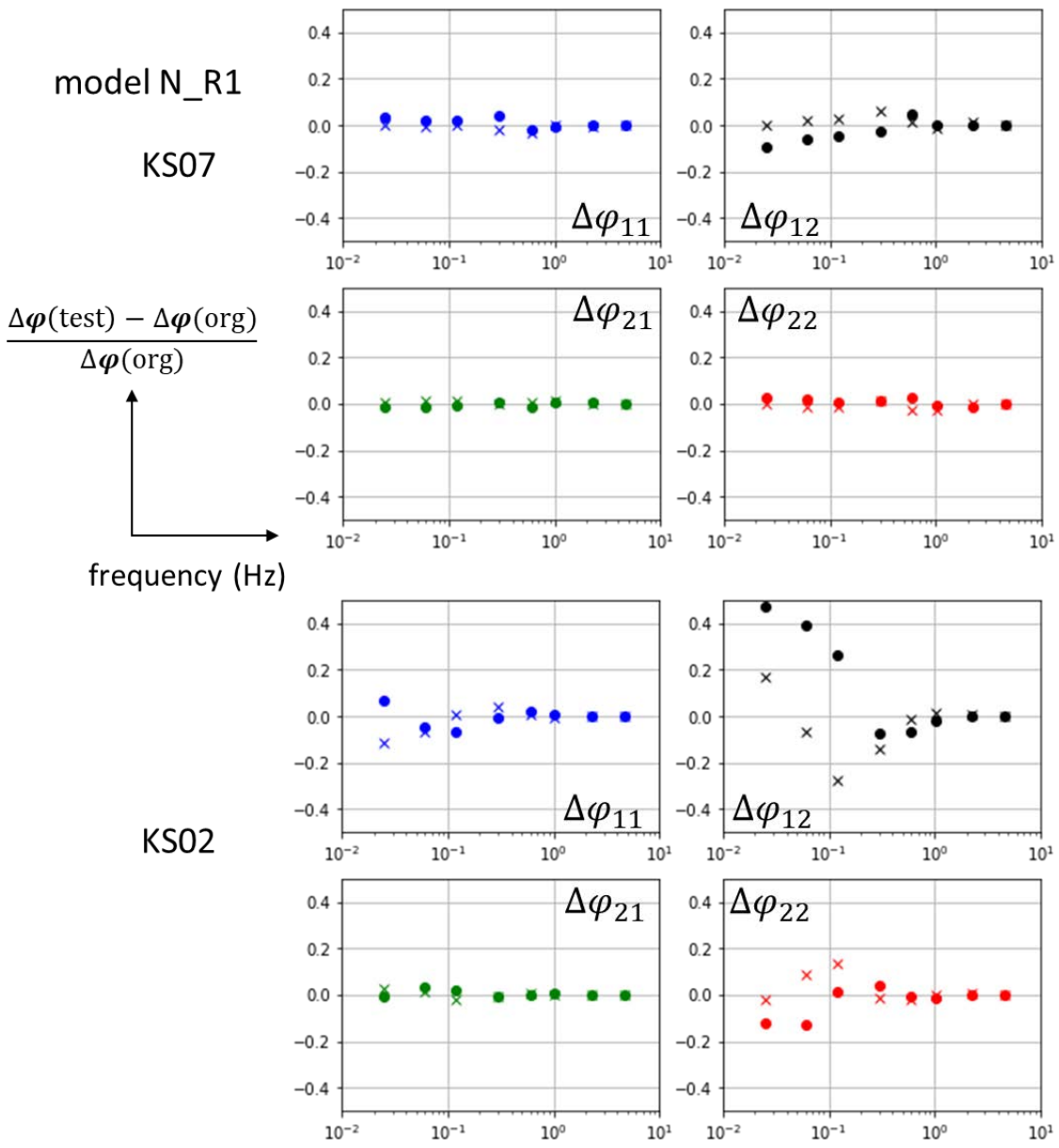

Figure 4.19

The comparative result of the differential response tensor from the original model (model N) and the test model (model N_R1).

The horizontal axis is the frequency and the vertical axis is the relative change of the differential response tensor $\Delta\boldsymbol{\varphi}$ in test model TR1 and original model".

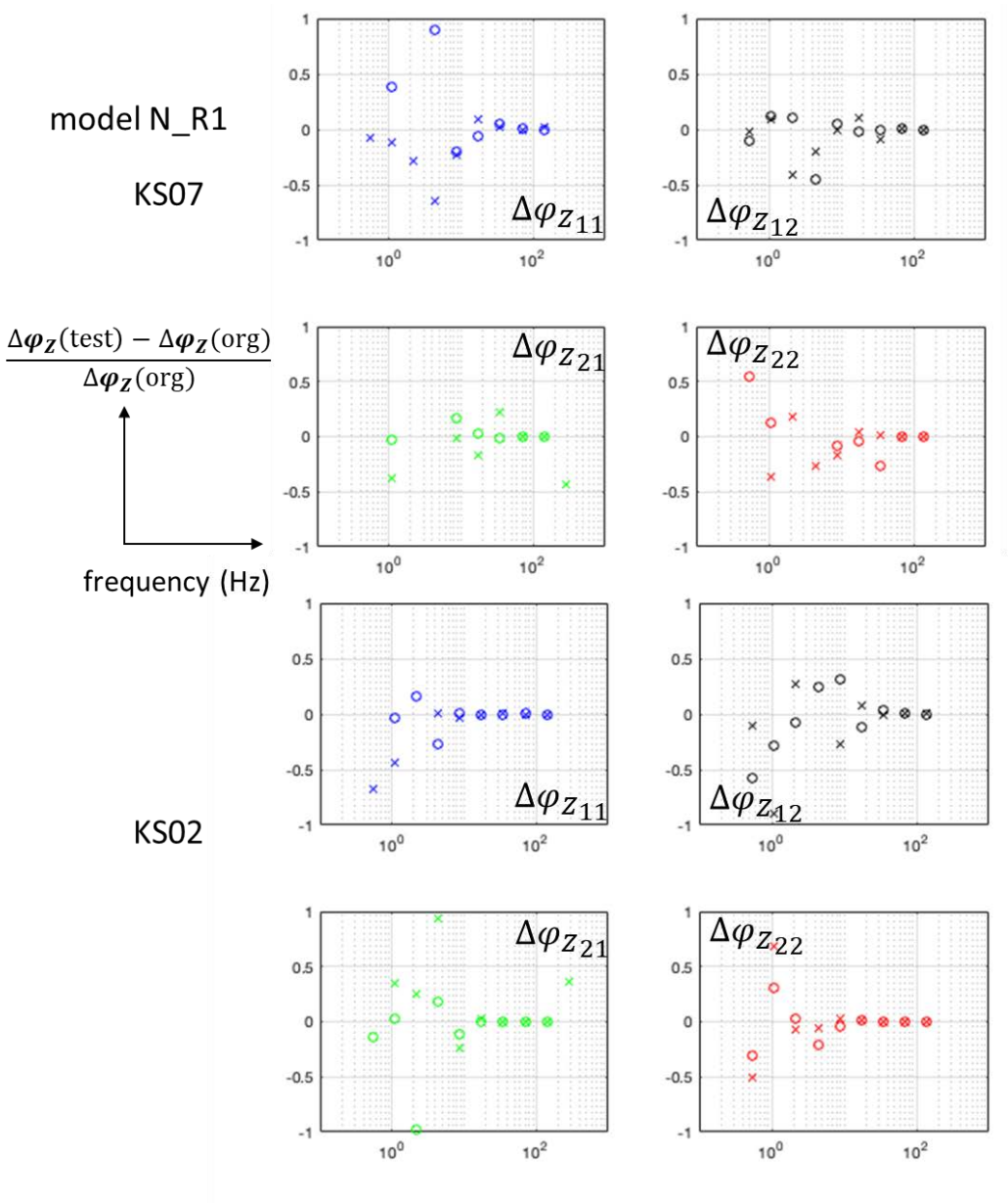

Figure 4.20

The comparative result of the differential response tensor of impedance tensor from the original model (model N) and the test model (model N_R1).

The horizontal axis is the frequency and the vertical axis is the relative change of the differential response tensor of impedance $\Delta\boldsymbol{\varphi_Z}$ in test model TR1 and original model".

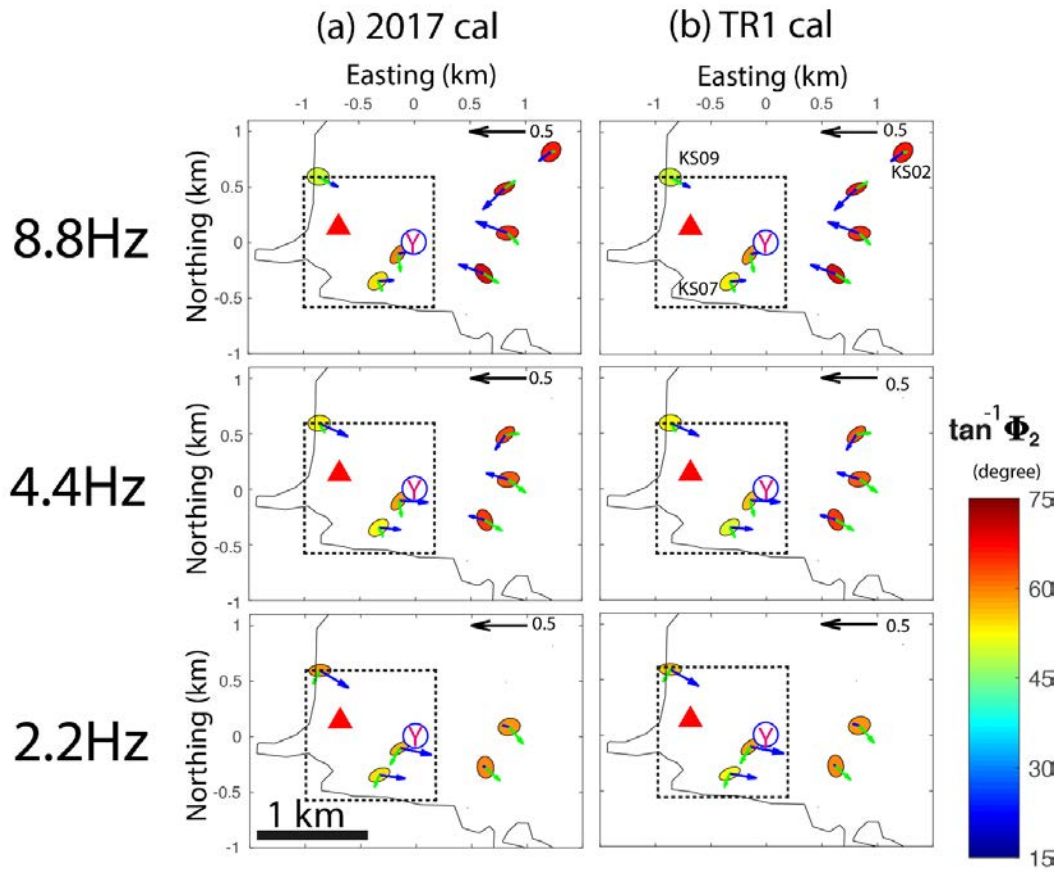

Figure 4.21

Comparison of the phase tensor ellipses between the data from (a) “model N” (2017 cal) and the test model “model N_R1” (TR1 cal) with the newly observed data.

The phase tensor ellipses are filled by the angle of the determinant phase Φ_2, which is the geometric mean value of maximum and minimum of phase tensor. The area of a modified resistor is marked with dashed rectangles. The black strike arrow represents a unit Parkinson’s induction vector with a tipper value 0.5. The blue and green strike arrows represent the real and imaginary Parkinson’s induction vector, respectively. The black curve, red triangle and blue circle with symbol “Y” denote local highway, the mountain peak of Mt. Shirane and center of Yugama crater lake, respectively.

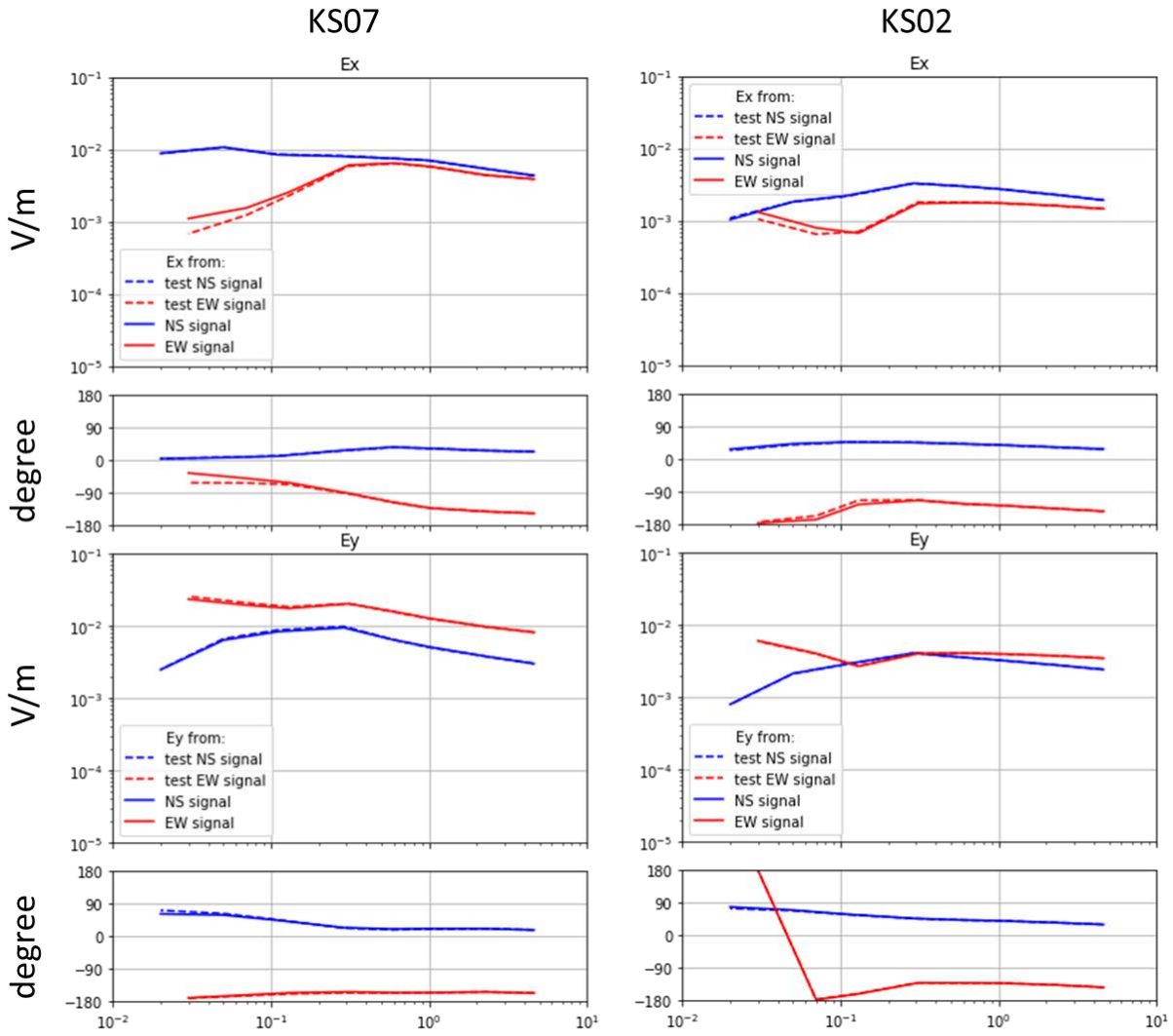

Figure 4.22

Calculated electric field from the original model and test model TR2 with the newly observed data.

The location of KS07 and KS02 is represented in Figure 4.7. The blue and red lines represent the electric field at receivers from source dipole NS and dipole EW, respectively. The solid and dash line denotes the forward model from the original model "model N" and test model "model N_R2", respectively.

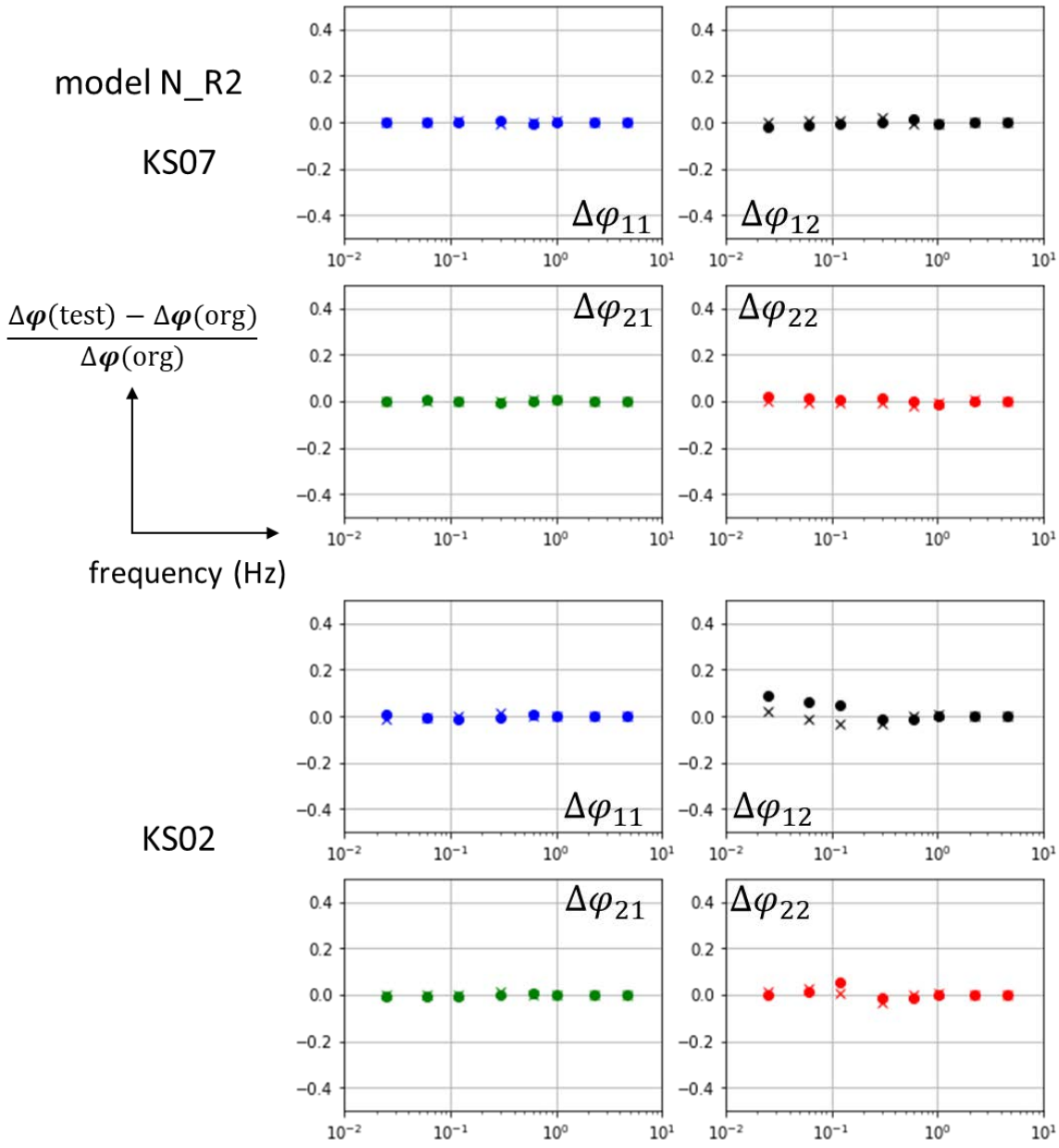

Figure 4.23

The comparative result of the differential response tensor from the original model (model N) and the test model (model N_R2).

The horizontal axis is the frequency and the vertical axis is the relative change of the differential response tensor $\Delta\boldsymbol{\varphi}$.

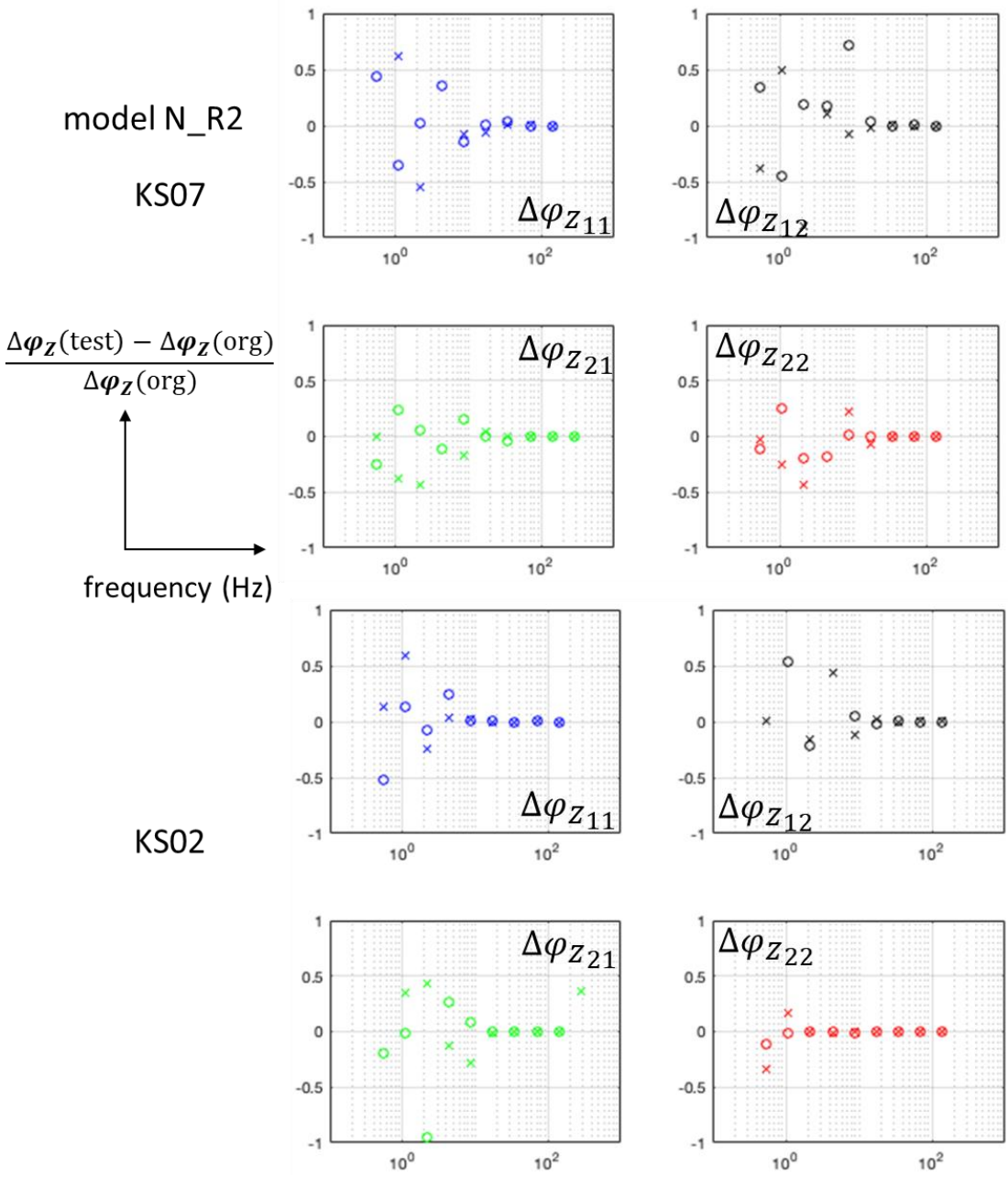

Figure 4.24

The comparative result of the differential response tensor of impedance tensor from the original model (model N) and the test model (model N_R2).

The horizontal axis is the frequency and the vertical axis is the relative change of the differential response tensor of impedance $\Delta\boldsymbol{\varphi_Z}$.

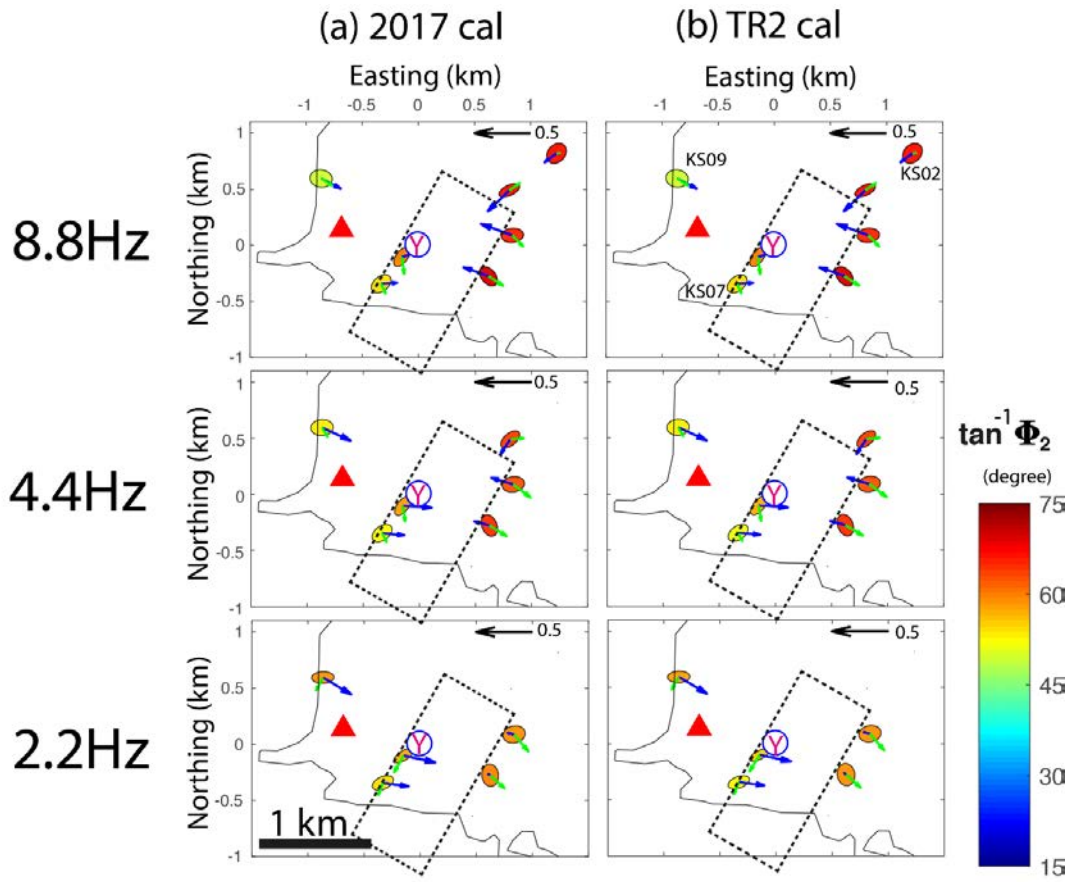

Figure 4.25

Comparison of the phase tensor ellipses between the data from (a) “model N” (2017 cal) and the test model “model N_R2” (TR2 cal) with the newly observed data.

The phase tensor ellipses are filled by the angle of the determinant phase Φ_2, which is the geometric mean value of maximum and minimum of phase tensor. The area of a modified resistor is marked with dashed rectangles. The black strike arrow represents a unit Parkinson’s induction vector with a tipper value 0.5. The blue and green strike arrows represent the real and imaginary Parkinson’s induction vector, respectively. The black curve, red triangle and blue circle with symbol “Y” denote local highway, the mountain peak of Mt. Shirane and center of Yugama crater lake, respectively.

		Dipole NS		Dipole EW	
i	A_i	f_i (Hz)	ϕ_i (deg)	f_i (Hz)	ϕ_i (deg)
1	2.3	0.02	-15.3	0.03	-28.5
2	1.7	0.05	24.5	0.07	53.7
3	1.3	0.11	-41.8	0.13	161.2
4	1.1	0.29	151.7	0.31	-16.8
5	0.7	0.59	115.6	0.61	149.9
6	0.5	1.01	-28.9	1.03	69.5
7	0.3	2.27	-36.8	2.29	66.0
8	0.2	4.63	81.4	4.61	-26.9

Table 4.1

Coefficients of the superimposed sinusoidal waves in Equation (5.9) for the full operation in 2018.

i	A_i	f_i (Hz)	
1	1.0	0.01	ϕ_i (deg)
2	1.0	0.02	179.5
3	1.0	0.04	104.5
4	1.0	0.08	-107.7
5	1.0	0.16	-140.8
6	1.0	0.32	-75.0
7	1.0	0.64	145.7
8	1.0	1.28	130.8
9	1.0	2.56	-147.6
10	1.0	5.12	-46.7

Table 4.2

Coefficients of the superimposed sinusoidal waves in Equation (5.9) for the initial experiment in 2017.

Local Edge $e_L(i,m)$	Local node $n_L(i1,m)$	Local node $n_L(i2,m)$	Local node $n_L\left(i1',m\right)$	Local node $n_L\left(i2',m\right)$
$e_L(1,m)$	$n_L(1,m)$	$n_L(2,m)$	$n_L(3,m)$	$n_L(4,m)$
$e_L(2,m)$	$n_L(1,m)$	$n_L(3,m)$	$n_L(4,m)$	$n_L(2,m)$
$e_L(3,m)$	$n_L(1,m)$	$n_L(4,m)$	$n_L(2,m)$	$n_L(3,m)$
$e_L(4,m)$	$n_L(2,m)$	$n_L(3,m)$	$n_L(1,m)$	$n_L(4,m)$
$e_L(5,m)$	$n_L(4,m)$	$n_L(2,m)$	$n_L(1,m)$	$n_L(3,m)$
$e_L(6,m)$	$n_L(3,m)$	$n_L(4,m)$	$n_L(1,m)$	$n_L(2,m)$

Table 4.3

The local numbering system definition for a tetrahedral elements m.

The symbol $e_L(i,m)$ denotes the local ID of $e_L(i,m)$, that is defined from its first composed node $n_L(i1,m)$ and the second composed node $n_L(i2,m)$. The diagonal local nodes of $e_L(i,m)$ are defined with symbol $n_L\left(i1',m\right)$ and $n_L\left(i2',m\right)$.

The local ID of a node $n_L(i)$ is defined from its order in the global numbering system $n_G(i)$, where $n_G\big(n_L(1,m)\big) < n_G\big(n_L(2,m)\big) < n_G\big(n_L(3,m)\big) < n_G\big(n_L(4,m)\big)$.

Chapter 5. Conclusion

In this thesis, the magnetotelluric method and EM-ACROSS method were applied to Kusatsu-Shirane volcano to image the hydrothermal system in three-dimensions. Those methods were also utilized to image the temporal change of the resistivity structure between the volcanic inactive and active periods. The MT data was utilized to compute the resistivity model due to its well-developed methodologies in solving the galvanic distortion effect, topography effect, and noise issues. For interpreting temporal changes in the time-lapse MT monitoring, the location, and the number of observation sites could influence the modeling result that should be carefully considered. This study introduced a method to interpret the time-lapse MT monitoring data with fewer sites and sparser distribution. The distortionless electric field response tensor is introduced and utilized in this study to examine the models with time-lapse MT monitoring data and joint CSEM data.

In Chapter 3, the magnetotelluric data observed around the Yugama crater at Kusatsu-Shirane volcano, which obtained during an inactive (2001-2005) and an active (2017-2018) period of the volcano, was utilized in the data analysis and modeling:

Firstly, the magnetotelluric data in a period between 2001-2005 from the observation sites, that covered the summit region of 2 km x 2km with a typical site spacing of 200 m, was inverted by utilizing an unstructured tetrahedral finite element algorithm with handling the topographic effect. The interpretation of the represented features describes the implication of those features in

this credible resistivity model. The final model demonstrated the following features in the observation region:

(1) an impermeable clay cap (C1) as the near-surface conductor

(2) the brine reservoir (C2) as a deep conductor at a depth of 1.5 km from the surface

(3) a vertical conductor (C3) connecting the deep conductor (C2) to the clay cap (C1) associated with the seismicity, which implies a fluid and gas path from the brine reservoir toward the underlying space of the clay cap

(4) the resistive zone below the clay cap which has an elongated direction in the NE to SW and following the locations of the past phreatic eruption

The past magnetization/demagnetization sources and the inflation source of the 2014 unrest are located just below the clay-cap, consistent with the clay capped geothermal model. The major conductive and resistive structures represent a noticeable 3-D feature that can only be interpreted in a 3-D model.

Secondly, to verify the robustness of the significant features in the resistivity model, those features were tested by different methods. The first test was operated by forwarding the modified model by removing significant features. The test models showed significantly worse fit to the observed data, as evidenced by the increase of RMS misfit and also by plotting the phase tensor ellipse. Another test for the robustness was carried out by randomly splitting the MT data into two sub-datasets. The inversed models with two separate datasets were compared and afterward confirmed that the significant features in the model were robust. Moreover, the other robustness test with changing the trade-off parameter of the distortion strength was examined then

confirmed the existence of the major features in all of the distortion strengths. Those examinations verified the credibility of the major features for the interpretation.

Finally, the obtained magnetotelluric dataset during the active volcanic period (2017-2018) was inverted by utilizing the same three-dimensional inversion code. Because of the limited number of sites in 2017-2018, the final model with the 2001-2005 dataset was utilized as an initial model. The new model during the high volcanic activity has more conductive features below the clay cap. The newly observed data represents changing features in the phase tensor analysis that initially indicates the temporal change of the hydrothermal system beneath Mt. Shirane exists. That model was examined afterward by utilizing an alternative method with CSEM data.

In Chapter 4, a distortionless electric field response tensor was introduced at first. The electric field response tensor requires a set of the electromagnetic tensor field from the CSEM observation. To achieve this objective, a signal system, simultaneously transmitted EM-ACROSS, is developed in this study.

Firstly, the system design references the purpose of the EM-ACROSS prototype in the previous research and is enhanced for the two motivations in this study: solving the galvanic distortion effect and reduce the influence of noise. The purpose of the EM-ACROSS is consistently transmitting a specially designed signal with high accuracy and precision to obtain a robust signal in the data processing. With an assumption that the environmental noise is dominated by Gaussian white noise, a robust signal can remain in the data stacking, and then a noise-free response function can be obtained. The signal and the instrument from the prototype were

redesigned with considering the electric tensor field. A serial data processing flow is specially developed for the simultaneously transmitted EM-ACROSS to promote the efficiency of noise reduction. With operating the simultaneously transmitted EM-ACROSS, the processed data from the receivers represented a strong performance in the noise elimination by competing with geomagnetic noise and efficiently removing the aperiodic noise. The error of the observed result was small enough to be utilized in the modeling computation.

Secondly, a forward modeling algorithm was regenerated in this article by referencing the previous researches. The forward model applied the edge-based frequency-domain FEM with unstructured tetrahedral meshes. Both the computed inversed models with MT data were utilized as the base model in the forward modeling. A local-to-global numbering system was additionally defined in this article to solve the technical issues. The algorithm generated a sparse linear equations system and solved the solution by a sparse linear direct solver “Scipy.SPsolve” in python language. The calculated electric field in the forward modeling result is assumed to be distortionless. The resistivity information from the inversed models has been treated for the distortion effect; therefore, the distortion contained observed data, and the distortionless calculated data had an apparent mismatch as in the expectation. Thus, the direct comparison between the two data could not be interpreted. Therefore, the distortionless response tensor for examination is necessary for this article.

Finally, the differential electric field response utilizing the data from simultaneously transmitted EM-ACROSS and MT observation was applied to verify the existence of changing features between the previously observed MT data and the recently observed MT data. The differential electric field response represented its feasibility in the modeling result examination. The results

represented significant dissimilarities from different models that support the reliability of the interpretation.

Since the robustness of the temporal changing features was justified, the data from two sets of MT observations hold its credibility for a joint interpretation as a result of the time-lapse monitoring.

Figure 3.22 demonstrates the conductor C2 representing less conductive in “model N”. Since the conductor C2 has been interpreted to the top of the supercritical state saline brine reservoir, this decreasing conductivity can be interpreted to the reducing volume of fluid, implying the fluid has been released from the breached sealing zone. Figures 5.1 and 5.2 represent the scatter plot of the altitude of monitored microseismic hypocenters versus their monitored time, as evidence of time-variable change. In an active period of the volcano since March 2014, the microseismic events were monitored in the deeper structures. The intrusion of releasing fluid in the surrounding structures could occur such microseismic events. After the high conductivity saline brine released, the meteoric water could invade this reservoir through the breached sealing zone and lead to the reducing conductivity. Ohba et al. (2008) have demonstrated a model for previous temporal change in the deep fluid reservoir over the period 1966 to 2005 and claimed the meteoric water invaded in 1990-1995. This mechanism of the deep fluid exchange and transportation could be indicated on the change of the resistivity structure model.

Figure 3.22 also demonstrates the conductor C1 representing a gap at 400 meters north to the Yugama crater in “model N”. Since the conductor C1 has been interpreted to the impermeable

smectite contained clay cap, this gap can be interpreted to the crack in the smectite filled by releasing gas. The monitored inflation activity can induce the appearance of the expanded crack in the smectite cap (Terada et al., 2018). The increasing resistivity can be interpreted as the temporally increasing invasion of the fumarolic gas (Ohba et al., 2019). The gas released upward to the surface at the fumarole zone (Figure 3.4). The shallow structure above this cap is more resistive than in model P, which might be due to the higher volume of the released gas but needs more information such as gas flux monitoring data to be convinced.

Figure 3.21 demonstrates the underlying resistor R1 beneath conductor C1 representing more conductive in “model N”. Since the resistor R1 has been interpreted to the mixed-layer clay with fracture as a two-phase reservoir, the changing resistivity in this structure can be considered as the change of the saturated fluid. The drying process of fluid in this reservoir has been introduced with its relevant changes in the overlying structure between cracks expand and collapse in Kumagai et al. (2002) by monitored long-period seismicity events. Such a change of the composition was not unidirectional but a repeated cycle caused by water supply, which has been introduced in Nakano & Kumagai (2005). Therefore, a more conductive feature in “model N” can be interpreted to the two-phase reservoir filling with conductive fluid. This presumption could be supported by the overlapping hypocenters of the microseismic swarm, which has been interpreted to the fluid path, and this two-phase reservoir. It can also be supported by the monitored suspended magnetization (JMA, 2019) as a mechanism of thermal demagnetization. When the two-phase reservoir was filling with the conductive saline from the deeper supercritical fluid reservoir, the water/gas ratio changed in this region and the resistivity also decreased. This fluid intrusion caused the originally saturated fluid releasing upward, which

could be indicated by the rising hypocenters with time in Figures 5.1 and 5.2. While the heated volcanic hydrothermal fluid releasing at the surface, like the Yugama crater lake or the fumarole zone at the north of Yugama crater, it can be monitored in the geochemical analysis by temperature and chemical concentrations changes (Terada et al. 2018).

Therefore, the temporal changes of the hydrothermal system beneath Mt. Shirane during a period between 2001 to 2018 can be interpreted with the time-lapse monitoring MT data and joint CSEM data. In the 2014 volcanic activity at Mt. Shirane, the supercritical fluid reservoir released overpressured fluid upward through the breached sealing zone. The released overpressured flow through the fracture in the overlying mixed-layer clay structure that led the monitored microseismic activity. The released fluid filled the two-phase reservoir in the mixed-layer clay structure and caused the thermal demagnetization. The filled fluid also increased the liquid/gas ratio in the two-phase reservoir. It represented a relatively conductive feature in the resistivity model "model N". The filled two-phase reservoir released more gas upward to the surface through the expended crack in the clay cap and turn the structure resistive in "model N". The filled two-phase reservoir also released more water upward to the Yugama crater lake, which has been monitored and analyzed in Ohba et al. (2019). The path and time of releasing water upward to the Yugama can be indicated by the microseismic hypocenters (Figure 5.1 and 5.2). A conceptual model for the temporal changes in the hydrothermal system beneath Mt. Shirane is demonstrated in Figure 5.3.

The conceptual model with credible spatial information for the temporal changes in the hydrothermal system beneath Mt. Shirane is first demonstrated in this study. Credible spatial information is indicated by the change in the resistivity model. The research in this article solved the environmental noise issue and distortion effect by joint the passive and active electromagnetic sounding method that provided a new conception in future exploration.

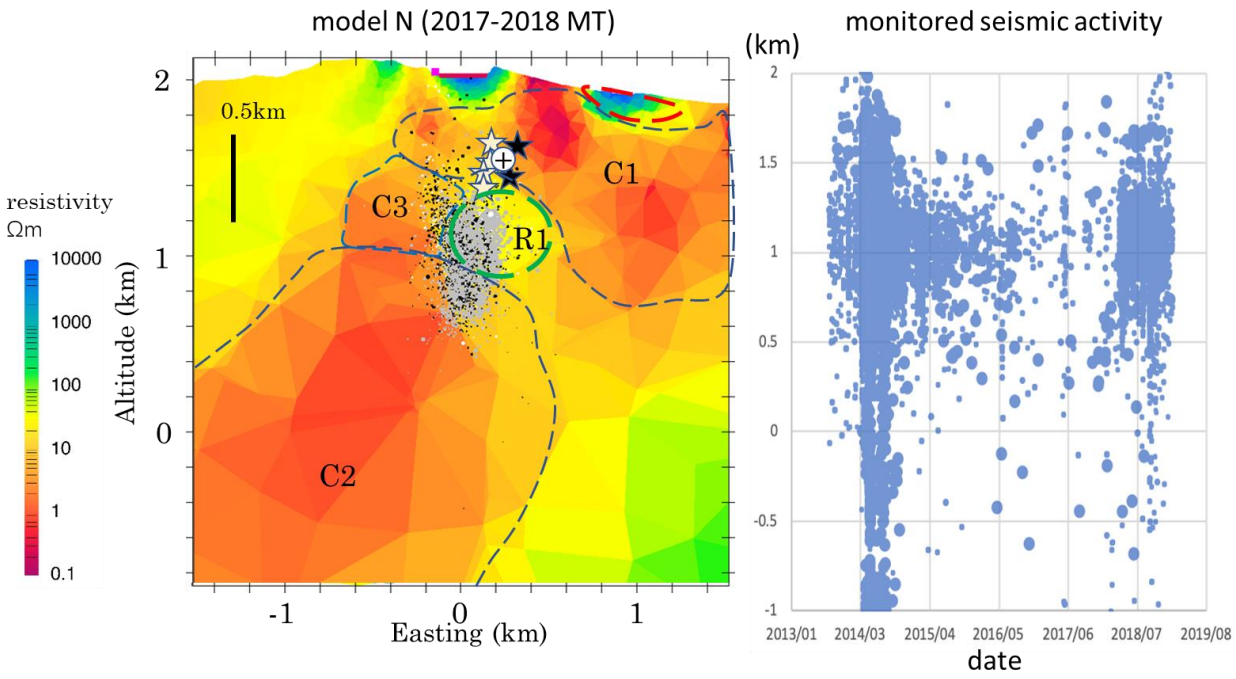

Figure 5.1

The scatter plot of altitude of microseismic hypocenter versus monitored date and the east-west profile of resistivity model N.

The data of microseismic is monitored during a period between Sep 2013-Feb 2019. The size of circles denotes the relative magnitude of seismic activity. It must be noted that the plotted hypocenter in the profile is filtering by a 200-meter-wide projection clipper that does not represent all the microseismic data as in the scatter plot.

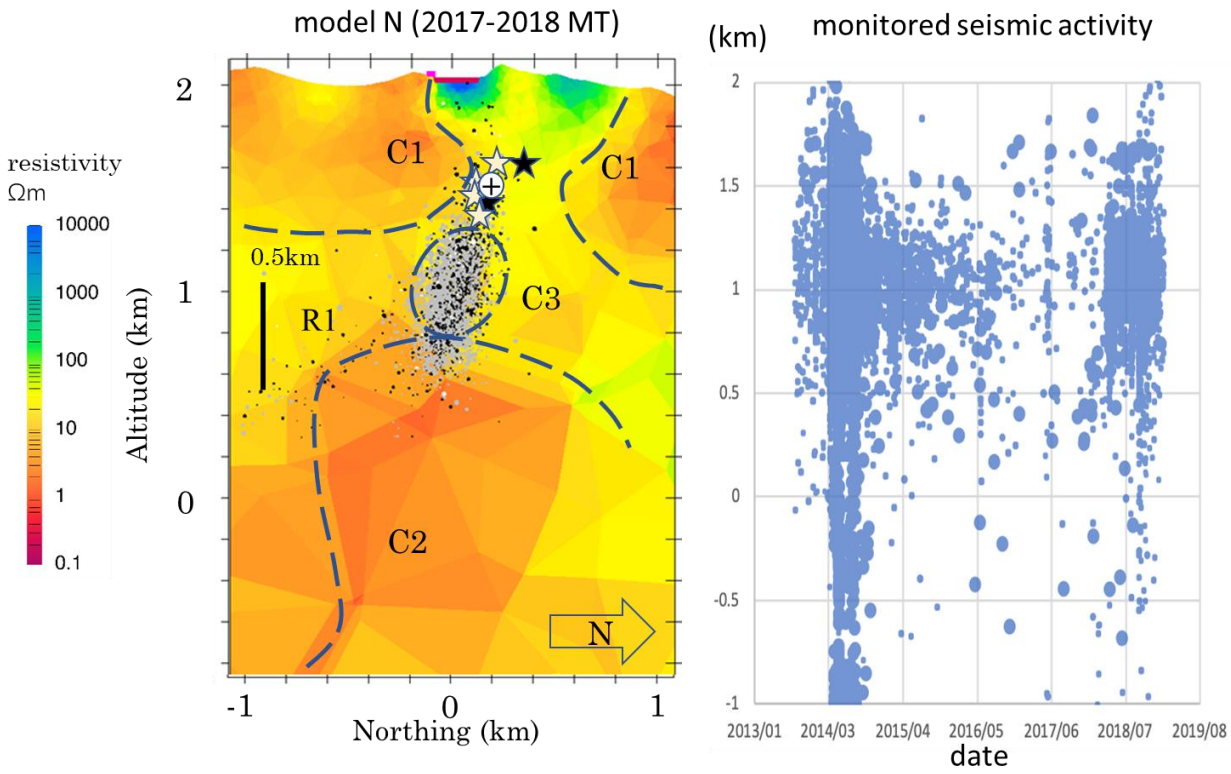

Figure 5.2

The scatter plot of altitude of microseismic hypocenter versus monitored date and the north-south profile of resistivity model N.

The data of microseismic is monitored during a period between Sep 2013-Feb 2019. The size of circles denotes the relative magnitude of seismic activity. It must be noted that the plotted hypocenter in the profile is filtering by a 200-meter-wide projection clipper that does not represent all the microseismic data as in the scatter plot.

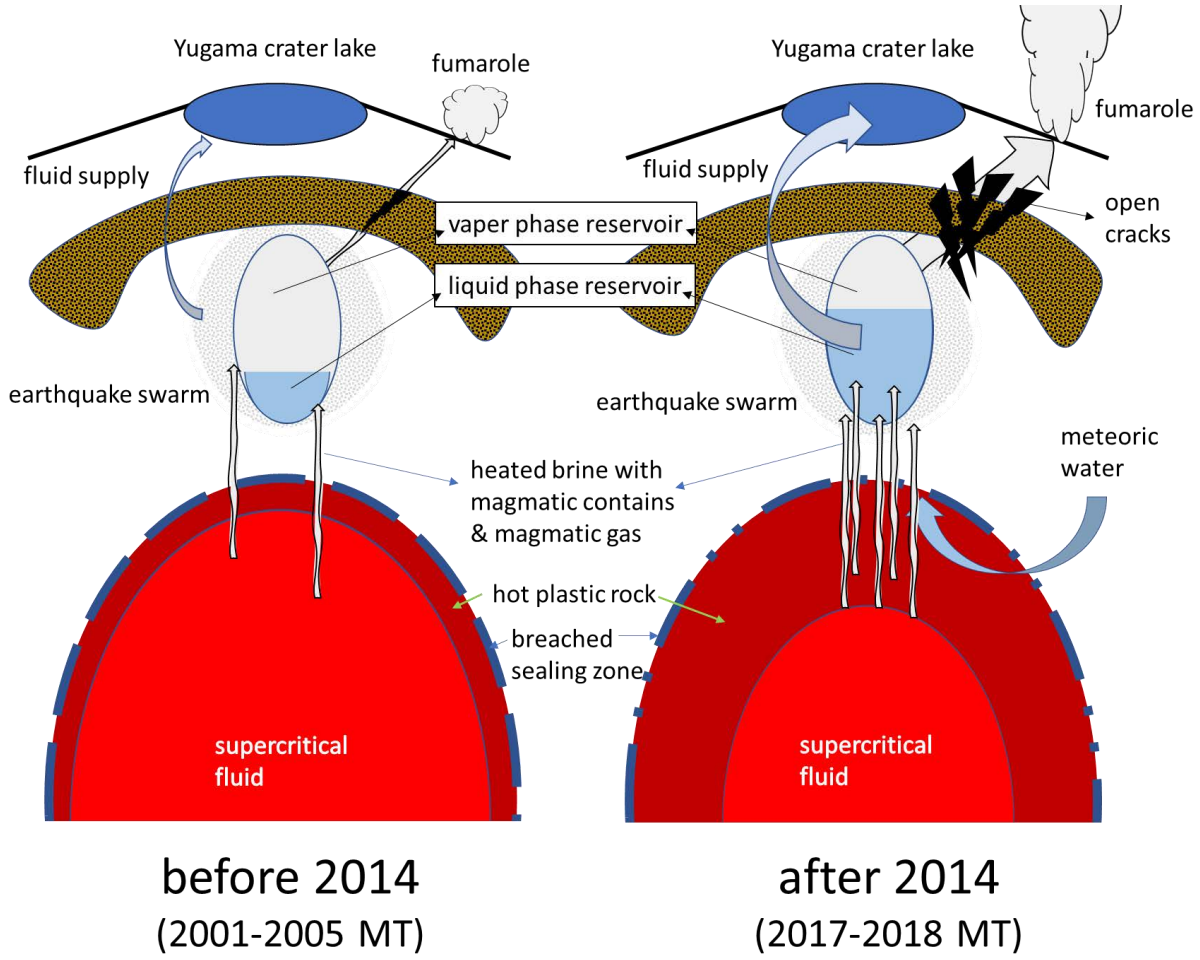

Figure 5.3

The conceptual model for the temporal changes in the hydrothermal system beneath Mt. Shirane between 2001 and 2018.

REFERENCES

Abdelfettah Y, Sailhac P, Larnier H, et al. (2018) Geothermics Continuous and time-lapse magnetotelluric monitoring of low volume injection at Rittershoffen geothermal project, northern Alsace – France. *Geothermics 71*:1–11 . doi: 10.1016/j.geothermics.2017.08.004

Abubakar, A., Habashy, T. M., Druskin, V. L., Knizhnerman, L., & Alumbaugh, D. (2008). *2.5D forward and inverse modeling for interpreting low-frequency electromagnetic measurements. GEOPHYSICS, 73*(4), F165–F177. doi:10.1190/1.2937466

Afanasyev, A., Blundy, J., Melnik, O., & Sparks, S. (2018). Formation of magmatic brine lenses via focussed fluid-flow beneath volcanoes. *Earth and Planetary Science Letters, 486,* 119–128. doi:10.1016/j.epsl.2018.01.013

Aizawa, K., Kanda, W., Ogawa, Y., Iguchi, M., Yokoo, A., Yakiwara, H., & Sugano, T. (2011). Temporal changes in electrical resistivity at Sakurajima volcano from continuous magnetotelluric observations. *Journal of Volcanology and Geothermal Research, 199*(1-2), 165–175. doi:10.1016/j.jvolgeores.2010.11.003

Aizawa, K., Ogawa, Y., & Ishido, T. (2009). Groundwater flow and hydrothermal systems within volcanic edifices: Delineation by electric self-potential and magnetotellurics. *Journal of Geophysical Research: Solid Earth*, *114*(1), 1–12. doi: 10.1029/2008JB005910

Aizawa K, Koyama T, Hase H, et al. (2013a) Three-dimensional resistivity structure and magma plumbing system of the Kirishima Volcanoes as inferred from broadband magnetotelluric data. *J Geophys Res Solid Earth* 1–18 . doi: 10.1002/2013JB010682.Received

Aizawa K, Koyama T, Uyeshima M, et al. (2013b) Magnetotelluric and temperature monitoring after the 2011 sub-Plinian eruptions of Shinmoe-dake volcano. *Earth Planets Space 65:*539–550 . doi: 10.5047/eps.2013.05.008

Aizawa, K., Yoshimura, R., Oshiman, N., Yamazaki, K., Uto, T., Ogawa, Y., … Furukawa, Y. (2005). Hydrothermal system beneath Mt. Fuji volcano inferred from magnetotellurics and electric self-potential. *Earth and Planetary Science Letters, 235*(1-2), 343–355. doi:10.1016/j.epsl.2005.03.023

Andréis, D., & MacGregor, L. (2008). *Controlled-source electromagnetic sounding in shallow water: Principles and applications. GEOPHYSICS, 73*(1), F21–F32. doi:10.1190/1.2815721

Andersen, L. S., & Volakis, J. L. (1998). Hierarchical tangential vector finite elements for tetrahedra. *IEEE Microwave and Guided Wave Letters, 8*(3), 127–129. doi:10.1109/75.661137

Archie, G. E. (1942). The Electrical Resistivity Log as an Aid in Determining Some Reservoir Characteristics. *Transactions of the AIME, 146*(01), 54–62. doi:10.2118/942054-g

Asaue, H., Koike, K., Yoshinaga, T., & Takakura, S. (2006). Magnetotelluric resistivity modeling for 3D characterization of geothermal reservoirs in the Western side of Mt. Aso, SW Japan. *Journal of Applied Geophysics*, *58*(4 SPEC. ISS.), 296–312. https://doi.org/10.1016/j.jappgeo.2005.05.006

Avdeev, D. B. (2005). *Three-Dimensional Electromagnetic Modelling and Inversion from Theory to Application. Surveys in Geophysics, 26*(6), 767–799. doi:10.1007/s10712-005-1836-x

Baba, K., & Chave, A. D. (2005). Correction of seafloor magnetotelluric data for topographic effects during inversion. *Journal of Geophysical Research: Solid Earth*, *110*(12), 1–16. https://doi.org/10.1029/2004JB003463

Barannik, M. B., Kolobov, V. V., Selivanov, V. N., Kuklin, D. V., Zhamaletdinov, A. A., & Shevtsov, A. N. (2013). Portable generator for deep electromagnetic soundings and monitoring of seismically active zones with the use of industrial power transmission lines. *Seismic Instruments, 49*(3), 275–284. doi:10.3103/s0747923913030031

Badea, E. A., Everett, M. E., Newman, G. A., & Biro, O. (2001). Finite-element analysis of controlled-source electromagnetic induction using Coulomb-gauged potentials. *GEOPHYSICS, 66*(3), 786–799. doi:10.1190/1.1444968

Barton, M. L., & Cendes, Z. J. (1987). New vector finite elements for three-dimensional magnetic field computation. *Journal of Applied Physics, 61*(8), 3919–3921. doi:10.1063/1.338584

Benson, P. M., Vinciguerra, S., Nasseri, M. H. B., & Young, R. P. (2014). Laboratory simulations of fluid/gas induced micro-earthquakes: Application to volcano seismology. *Frontiers in Earth Science*, *2*(November), 1–6. https://doi.org/10.3389/feart.2014.00032

Boerner, D. E., Wright, J. A., Thurlow, J. G., & Reed, L. E. (1993). *Tensor CSAMT studies at the Buchans Mine in central Newfoundland. GEOPHYSICS, 58(1), 12–19.* doi:10.1190/1.1443342

Booker, J. R. (2012). Magnetotelluric phase tensor evolution. In *21st Electromagnetic (EM) Induction Workshop Darwin, Australia*.

Booker, J. R. (2014). The magnetotelluric phase tensor: a critical review. *Surveys in Geophysics*, *35*(1), 7-40. doi: 10.1007/s10712-013-9234-2

Cagniard, L. (1953). Basic theory of the magneto-telluric method of geophysical prospecting. *Geophysics, 18*(3), 605-635. doi:10.1190/1.1437915

Cai, H., Čuma, M., & Zhdanov, M. S. (2015). Three-dimensional parallel edge-based finite element modeling of electromagnetic data with field redatuming. *SEG Technical Program Expanded Abstracts 2015.* doi:10.1190/segam2015-5869468.1

Cai, H., Hu, X., Li, J., Endo, M., & Xiong, B. (2017). Parallelized 3D CSEM modeling using edge-based finite element with total field formulation and unstructured mesh. *Computers & Geosciences, 99*, 125–134. doi:10.1016/j.cageo.2016.11.009

Cai, H., Xiong, B., Han, M., & Zhdanov, M. (2014). 3D controlled-source electromagnetic modeling in anisotropic medium using edge-based finite element method. *Computers & Geosciences, 73,* 164–176. doi:10.1016/j.cageo.2014.09.008

Caldwell, T. G., Bibby, H. M., & Brown, C. (2004). The magnetotelluric phase tensor. *Geophysical Journal International, 158*(2), 457-469. doi: 10.1111/j.1365-246X.2004.02281.x

Carnevali, P., Morris, R. B., Tsuji, Y., & Taylor, G. (1993). New basis functions and computational procedures for p-version finite element analysis. *International Journal for Numerical Methods in Engineering, 36*(22), 3759–3779. doi:10.1002/nme.1620362202

Caselle, C., Bonetto, S., & Comina, C. (2019). Comparison of laboratory and field electrical resistivity measurements of a gypsum rock for mining prospection applications. *International Journal of Mining Science and Technology. 29* (6)*,* 841-849. doi:10.1016/j.ijmst.2019.09.002

Cegielski, P., & Richard, D. (2001). Decidability of the theory of the natural integers with the cantor pairing function and the successor. *Theoretical Computer Science, 257*(1-2), 51–77. doi:10.1016/s0304-3975(00)00109-2

Chai, T., & Draxler, R. R. (2014). Root mean square error (RMSE) or mean absolute error (MAE)? – Arguments against avoiding RMSE in the literature. *Geoscientific Model Development, 7*(3), 1247–1250. doi:10.5194/gmd-7-1247-2014

Chave, A. D., & Jones, A. G. (Eds.). (2012). The magnetotelluric method: Theory and practice. Cambridge University Press.

Chave, A. D., & Smith, J. T. (1994). On electric and magnetic galvanic distortion tensor decompositions. *Journal of Geophysical Research: Solid Earth, 99*(B3), 4669–4682. doi:10.1029/93jb03368

Chouet, B., Saccorotti, G., Dawson, P., Martini, M., Scarpa, R., De Luca, G., … Cattaneo, M. (1999). Broadband measurements of the sources of explosions at Stromboli Volcano, Italy. *Geophysical Research Letters, 26*(13), 1937–1940. doi:10.1029/1999gl900400

Chung, Y., Son, J.-S., Lee, T. J., Kim, H. J., & Shin, C. (2014). Three-dimensional modelling of controlled-source electromagnetic surveys using an edge finite-element method with a direct solver. *Geophysical Prospecting, 62*(6), 1468–1483. doi:10.1111/1365-2478.12132

CIMIN (2019). GiD [computer software]. Barcelona, Spain.

Commer, M., & Newman, G. A. (2008). *New advances in three-dimensional controlled-source electromagnetic inversion. Geophysical Journal International, 172*(2), 513–535. doi:10.1111/j.1365-246x.2007.03663.x

Constable, S. (2010). Ten years of marine CSEM for hydrocarbon exploration. *GEOPHYSICS, 75*(5), 75A67–75A81. doi:10.1190/1.3483451

Constable, S., & Srnka, L. J. (2007). An introduction to marine controlled-source electromagnetic methods for hydrocarbon exploration. *GEOPHYSICS, 72(2),* WA3–WA12. doi:10.1190/1.2432483

Constable, S., & Weiss, C. J. (2006). Mapping thin resistors and hydrocarbons with marine EM methods: Insights from 1D modeling. *GEOPHYSICS, 71*(2), G43–G51. doi:10.1190/1.2187748

Davis, T. A. (2004). Algorithm 832. *ACM Transactions on Mathematical Software, 30*(2), 196–199. doi:10.1145/992200.992206

Deen, J. A., Rye, R. O., Munoz, J. L., & Drexler, J. W. (1994). The magmatic hydrothermal system at Julcani, Peru; evidence from fluid inclusions and hydrogen and oxygen isotopes. *Economic Geology, 89*(8), 1924–1938. doi:10.2113/gsecongeo.89.8.1924

Dong Wook Shin, & Tomozawa, M. (1993). Electrical resistivity of silica glasses. *Journal of Non-Crystalline Solids, 163*(2), 203–210. doi:10.1016/0022-3093(93)90769-t

Eberl, D. (1978). Reaction Series for Dioctahedral Smectites. *Clays and Clay Minerals, 26*(5), 327–340. doi:10.1346/ccmn.1978.0260503

Egbert, G. D. (1997). Robust multiple-station magnetotelluric data processing. *Geophysical Journal International, 130*(2), 475–496. doi:10.1111/j.1365-246x.1997.tb05663.x

Egbert, G. D., & Booker, J. R. (1986). Robust estimation of geomagnetic transfer functions. *Geophysical Journal of the Royal Astronomical Society*, *87*(1), 173–194. https://doi.org/10.1111/j.1365-246X.1986.tb04552.x

Fan, G.-X., & Liu, Q. H. (2004). Fast Fourier Transform for Discontinuous Functions. *IEEE Transactions on Antennas and Propagation, 52*(2), 461–465. doi:10.1109/tap.2004.823965

Feynman, R. P., Leighton, R. B., & Sands, M. (1965). The Feynman lectures on physics; vol. i. American Journal of Physics, 33(9), 750-752. doi: 10.1119/1.1972241

Fish, J., & Markolefas, S. (1994). Adaptive global-local refinement strategy based on the interior error estimates of the h-method. *International Journal for Numerical Methods in Engineering, 37*(5), 827–838. doi:10.1002/nme.1620370508

Flóvenz, Ó. G., Hersir, G. P., Sæmundsson, K., Ármannsson, H., & Friðriksson, Þ. (2012). Geothermal Energy Exploration Techniques. *Comprehensive Renewable Energy,* 51–95. doi:10.1016/b978-0-08-087872-0.00705-8

Fomenko, E. Y., & Mogi, T. (2002). *A new computation method for a staggered grid of 3D EM field conservative modeling. Earth, Planets and Space, 54*(5), 499–509. doi:10.1186/bf03353041

Fournier, R. O. (1999). Hydrothermal processes related to movement of fluid from plastic into brittle rock in the magmatic-epithermal environment. *Economic Geology, 94*(8), 1193–1211. doi:10.2113/gsecongeo.94.8.1193

Gamble, T. D., Goubau, W. M., & Clarke, J. (1979a). Magnetotellurics with a remote magnetic reference. *GEOPHYSICS, 44*(1), 53–68. doi:10.1190/1.1440923

Gamble, T. D., Goubau, W. M., & Clarke, J. (1979b). Error analysis for remote reference magnetotellurics. *Geophysics*, *44*(5), 959-968. doi: 10.1190/1.1440988

Garcia, X., & Jones, A. G. (2002). *Atmospheric sources for audio-magnetotelluric (AMT) sounding. GEOPHYSICS, 67(2), 448–458.* doi:10.1190/1.1468604

Gedney, S. D. (2011). *Introduction to the Finite-Difference Time-Domain (FDTD) Method for Electromagnetics. Synthesis Lectures on Computational Electromagnetics, 6*(1), 1–250. doi:10.2200/s00316ed1v01y201012cem027

Glover, P. W. J., Hole, M. J., & Pous, J. (2000). A modified Archie's law for two conducting phases. *Earth and Planetary Science Letters, 180*(3-4), 369–383. doi:10.1016/s0012-821x(00)00168-0

Goldstein, M. A., & Strangway, D. W. (1975). Audio-frequency magnetotellurics with a grounded electric dipole source. *GEOPHYSICS, 40*(4), 669–683. doi:10.1190/1.1440558

Grayver, A. V., Streich, R., & Ritter, O. (2014). *3D inversion and resolution analysis of land-based CSEM data from the Ketzin CO2 storage formation. GEOPHYSICS, 79*(2), E101–E114. doi:10.1190/geo2013-0184.1

Gregori, G. P., & Lanzerotti, L. J. (1980). Geomagnetic depth sounding by induction arrow representation: A review. *Reviews of Geophysics*, *18*(1), 203–209. doi: 10.1029/RG018i001p00203

Groom, R. W., & Bailey, R. C. (1989). Decomposition of magnetotelluric impedance tensors in the presence of local three-dimensional galvanic distortion. *Journal of Geophysical Research, 94*(B2), 1913. doi:10.1029/jb094ib02p01913

Gunderson, R., Cumming, W., Astra, D., and Harvey, C. (2000). Analysis of smectite clays in geothermal drill cuttings by the methylene blue method: for well site geothermometry and resistivity sounding correlation. *Proceedings World Geothermal Congress 2000 Kyushu - Tohoku, Japan, May 28 - June 10, 2000,* 1175-1181.

Hansen, P. C., & O'Leary, D. P. (1993). The Use of the L-Curve in the Regularization of Discrete Ill-Posed Problems. *SIAM Journal on Scientific Computing*, *14*(6), 1487–1503. https://doi.org/10.1137/0914086

Hattori, K. (1993). High-sulfur magma, a product of fluid discharge from underlying mafic magma: Evidence from Mount Pinatubo, Philippines. *Geology, 21*(12), 1083. doi:10.1130/0091-7613(1993)021<1083:hsmapo>2.3.co;2

Hayakawa, Y., & Yui, M. (1989). Eruptive history of the Kusatsu Shirane volcano. *The Quaternary Research (Daiyonki-Kenkyu), 28*(1), 1–17. doi:10.4116/jaqua.28.1 (in Japanese)

Hayley K, Bentley LR, Gharibi M, Nightingale M (2007) Low temperature dependence of electrical resistivity: Implications for near surface geophysical monitoring. Geophys Res Lett 34:1–5 . doi: 10.1029/2007GL031124

Heise, W., Caldwell, T. G., Bibby, H. M., & Bannister, S. C., (2008). Three-dimensional modelling of magnetotelluric data from the Rotokawa geothermal field, Taupo Volcanic Zone, New Zealand. *Geophysical Journal International*, *173*(2), 740–750. https://doi.org/10.1111/j.1365-246X.2008.03737.x

Heise, W., Caldwell, T.G., Bibby, H.M., Bennie, S.L., (2010). Three-dimensional electrical resistivity image of magma beneath an active continental rift, Taupo Volcanic Zone, New Zealand. *Geophys Res Lett 37:*2–6 . doi: 10.1029/2010GL043110

Hill, G. J., Caldwell, T. G., Heise, W., Chertkoff, D. G., Bibby, H. M., Burgess, M. K., … Cas, R. A. F. (2009). Distribution of melt beneath Mount St Helens and Mount Adams inferred from magnetotelluric data. *Nature Geoscience, 2*(11), 785–789. doi:10.1038/ngeo661

Hipkin, R. G. (2001). The statistics of pink noise on a sphere: applications to mantle density anomalies. *Geophysical Journal International, 144*(2), 259–270. doi:10.1046/j.0956-540x.2000.01327.x

Hordt, Andrieux, Neubauer, Ruter, & Vozoff. (2000). A first attempt at monitoring underground gas storage by means of time-lapse multichannel transient electromagnetics. *Geophysical Prospecting, 48*(3), 489–509. doi:10.1046/j.1365-2478.2000.00192.x

Hu, Y.-C., Li, T.-L., Fan, C.-S., Wang, D.-Y., & Li, J.-P. (2015). Three-dimensional tensor controlled-source electromagnetic modeling based on the vector finite-element method. *Applied Geophysics, 12*(1), 35–46. doi:10.1007/s11770-014-0469-1

Ikuta, R. (2002). Continuous monitoring of propagation velocity of seismic wave using ACROSS. *Geophysical Research Letters, 29(13).* doi:10.1029/2001gl013974

Ikuta R, Yamaoka K (2004) Temporal variation in the shear wave anisotropy detected using the Accurately Controlled Routinely Operated Signal System (ACROSS). *J Geophys Res Solid Earth 109*:1–15 . doi: 10.1029/2003JB002901

Inoue, A., Utada, M., & Wakita, K. (1992). Smectite-to-illite conversion in natural hydrothermal systems. *Applied Clay Science, 7*(1-3), 131–145. doi:10.1016/0169-1317(92)90035-l

Iwamori, H., & Zhao, D. (2000). *Melting and seismic structure beneath the Northeast Japan Arc. Geophysical Research Letters, 27*(3), 425–428. doi:10.1029/1999gl010917

Jin, J. M. (2002). *The finite element method in electromagnetics*. John Wiley & Sons, New York, USA.

JMA. (2019). *Variation of Geomagnetic Total Intensity at Kusatsu-Shirane Volcano*. (Report No. 132). Tokyo, Japan.

Jones, E., Oliphant, T., & Peterson, P. (2001). SciPy: Open source scientific tools for Python.

Kamineni, D. C. (1983). Sulfur-isotope geochemistry of fracture-filling gypsum in an Archean granite near Atikokan, Ontario, Canada. *Chemical Geology, 39*(3-4), 263–272. doi:10.1016/0009-2541(83)90018-9

Kanda, W., Utsugi, M., Takakura, S., & Inoue, H. (2019). Hydrothermal system of the active crater of Aso volcano (Japan) inferred from a three-dimensional resistivity structure model. *Earth, Planets and Space*, *71*(1). https://doi.org/10.1186/s40623-019-1017-7

Kanda, W., Yamazaki, T., Ogawa, Y., Hashimoto, T., Sakanaka, S., Aizawa, K., et al. (2013). Shallow Resistivity Structure of Sakurajima Volcano Revealed by Audio-frequency

Magnetotellurics. *Bulletin of the Volcanological Society of Japan*, *58*(1), 251–267. https://doi.org/10.18940/kazan.58.1_251

Kaneko, T., Shimizu, S., and Itaya, T. (1991). K-Ar ages of the Quaternary volcanoes in the Shin-etsu highland area, central Japan, and their formation history. *Bull. Earthq. Res. Inst. Univ. Tokyo* 66, 299–332.

Kaufman, A. A., & Keller, G. V. (1983). Frequency and transient soundings. Chi-Yu King Roberto Scarpa, 207.

Keller, G. V., Pritchard, J. I., Jacobson, J. J., & Harthill, N. (1984). Megasource time-domain electromagnetic sounding methods. *GEOPHYSICS, 49*(7), 993–1009. doi:10.1190/1.1441743

Key, K., & Weiss, C. (2006). *Adaptive finite-element modeling using unstructured grids: The 2D magnetotelluric example. GEOPHYSICS, 71*(6), G291–G299. doi:10.1190/1.2348091

Knorr, E. M., Ng, R. T., & Tucakov, V. (2000). Distance-based outliers: algorithms and applications. *The VLDB Journal The International Journal on Very Large Data Bases, 8*(3-4), 237–253. doi:10.1007/s007780050006

Krause, R., & Rank, E. (2003). Multiscale computations with a combination of the h- and p-versions of the finite-element method. *Computer Methods in Applied Mechanics and Engineering, 192*(35-36), 3959–3983. doi:10.1016/s0045-7825(03)00395-5

Ku, C. C., Hsieh, M. S., & Lim, S. H. (1973). The Topographic Effect in Electromagnetic Fields. *Canadian Journal of Earth Sciences, 10*(5), 645–656. doi:10.1139/e73-065

Kumagai, H., & Chouet, B. A. (1999). *The complex frequencies of long-period seismic events as probes of fluid composition beneath volcanoes. Geophysical Journal International, 138(2), F7–F12.* doi:10.1046/j.1365-246x.1999.00911.x

Kumagai, H., Chouet, B. A., & Nakano, M. (2002). Temporal evolution of a hydrothermal system in Kusatsu-Shirane Volcano, Japan, inferred from the complex frequencies of long-period events. *Journal of Geophysical Research: Solid Earth*, *107*(B10), ESE 9-1-ESE 9-10. https://doi.org/10.1029/2001jb000653

Kumagai, H., Chouet, B. A., & Nakano, M. (2002*).* Temporal evolution of a hydrothermal system in Kusatsu-Shirane Volcano, Japan, inferred from the complex frequencies of long-period events. *Journal of Geophysical Research: Solid Earth, 107*(B10), ESE 9–1–ESE 9–10*.* doi:10.1029/2001jb000653

Kumazawa, M. (1998a). Theoretical basis, development and prospect of EM ACROSS—An approach unifying low frequency MT (magnetotellulic) and high frequency radar. *Abstracts of international workshop on frontiers in monitoring science and technology for earthquake environments*, A2-21.

Kumazawa, M. (1998b). A new light and new eye to look into the solid Earth and a potential monitoring methodology of geodynamics states—introduction to ACROSS*. Abstracts of international workshop on frontiers in monitoring science and technology for earthquake environments*, A-11.

Kumazawa M, Kunitomo T, Nakajima T, et al (2007). Development of ACROSS (Accurately Controlled, Routinely Operated, Signal System) to realize constant monitoring the

invisible Earth's interiors by means of stationary coherent elastic and electromagnetic waves, *JAEA-Research 2007-033*, p.1-150.

Kurz, J. H., Jahr, T., & Jentzsch, G. (2004). Earthquake swarm examples and a look at the generation mechanism of the Vogtland/Western Bohemia earthquake swarms. *Physics of the Earth and Planetary Interiors*, *142*(1–2), 75–88. doi:10.1016/j.pepi.2003.12.007

Ledo, J. (2005). 2-D versus 3-D magnetotelluric data interpretation. *Surveys in Geophysics*, *26*(5), 511–543. https://doi.org/10.1007/s10712-005-1757-8

Ledo, J., Queralt, P., & Pous, J. (1998). Effects of galvanic distortion on magnetotelluric data over a three-dimensional regional structure. *Geophysical Journal International, 132*(2), 295–301. doi:10.1046/j.1365-246x.1998.00417.x

Lévy L., Gibert B., Sigmundsson F., Flóvenz O.G., Hersir G.P., Briole P. and Pezard P.A. 2018. The role of smectites in the electrical conductivity of active hydrothermal systems: electrical properties of core samples from Krafla volcano, Iceland. *Geophysical Journal International* **215**, 1558–1582.

Leys, C., Ley, C., Klein, O., Bernard, P., & Licata, L. (2013). Detecting outliers: Do not use standard deviation around the mean, use absolute deviation around the median. *Journal of Experimental Social Psychology, 49*(4), 764–766. doi:10.1016/j.jesp.2013.03.013

Li, J. H., Zhu, Z. Q., Liu, S. C., & Zeng, S. H. (2011). *3D numerical simulation for the transient electromagnetic field excited by the central loop based on the vector finite-element method. Journal of Geophysics and Engineering, 8*(4), 560–567. doi:10.1088/1742-2132/8/4/008

Lisi, M. (2007). Some remarks on the Cantor pairing function, *Le Matematiche* ***62***(1), 55–65.

Liu, G., Li, S., Gu, D., Lu, Y., & Asamoah, E. (2016). Experimental study of petrophysical properties of a tight formation by considering the clay minerals and flow sensitivities. *Earth Sciences Research Journal, 20*(2), B1-B6. doi:10.15446/esrj.v20n2.54508

Liu, W., Lin, P., Lu, Q., Li, Y., & Li, J. (2017). Synthetic modelling and analysis of CSEM full-field apparent resistivity response combining EM induction and IP effect for 1D medium. *Exploration Geophysics.* doi:10.1071/eg17049

Logsdon, S. D., & Laird, D. A. (2004). Electrical conductivity spectra of smectites as influenced by saturating cation and humidity. *Clays and Clay Minerals*, *52*(4), 411–420. doi: 10.1346/CCMN.2004.0520402

Løseth, L.O., Amundsen L (2007) Removal of air-response by weighting inline and broadside CSEM / SBL data. In: SEG Technical Program Expanded Abstracts 2007. pp 529–533

Løseth, L.O., Amundsen, L., Jenssen, A.J. (2010) A solution to the airwave-removal problem in shallow-water marine EM. Geophysics 75:A37–A42 . doi: 10.1190/1.3475359

Macnae, J. C., Lamontagne, Y., & West, G. F. (1984). Noise processing techniques for time-domain EM systems. *GEOPHYSICS, 49*(7), 934–948. doi:10.1190/1.1441739

Madden, T., & Nelson, P. (1964). A defense of Cagniard's magnetotelluric method. Magnetotelluric methods, 89-102.

Markson, R., & Muir, M. (1980). *Solar Wind Control of the Earth's Electric Field. Science, 208*(4447), 979–990. doi:10.1126/science.208.4447.979

M. Meqbel, N., Egbert, G. D., Wannamaker, P. E., Kelbert, A., & Schultz, A. (2014). Deep electrical resistivity structure of the northwestern U.S. derived from 3-D inversion of USArray magnetotelluric data. *Earth and Planetary Science Letters, 402,* 290–304. doi:10.1016/j.epsl.2013.12.026

McCracken, K. G., Oristaglio, M. L., & Hohmann, G. W. (1986). Minimization of noise in electromagnetic exploration systems. *GEOPHYSICS, 51*(3), 819–832. doi:10.1190/1.1442134

Minami, T., Utsugi, M., Utada, H., et al. (2018) Temporal variation in the resistivity structure of the first Nakadake crater, Aso volcano, Japan, during the magmatic eruptions from November 2014 to May 2015, as inferred by the ACTIVE electromagnetic monitoring system. *Earth Planets Space* 70:1–10 . doi: 10.1186/s40623-018-0909-2

Mitsuhata, Y. (2000). *2-D electromagnetic modeling by finite-element method with a dipole source and topography. GEOPHYSICS, 65*(2), 465–475. doi:10.1190/1.1444740

Mogi, T., & Nakama, S. (1993). Magnetotelluric interpretation of the geothermal system of the Kuju volcano, southwest Japan. *Journal of Volcanology and Geothermal Research*, *56*(3), 297–308. https://doi.org/10.1016/0377-0273(93)90022-J

Mori, T., Hirabayashi, J., Nogami, K., & Onizawa. S. (2006). A new seismic observation system at the Kusatsu-Shirane volcano, *Bull. Volcanol. Soc. Japan*, Ser. 2, **51**, 41–47 (in Japanese with English abstract).

Mukherjee, S., & Everett, M. E. (2011). 3D controlled-source electromagnetic edge-based finite element modeling of conductive and permeable heterogeneities. *GEOPHYSICS, 76*(4), F215–F226. doi:10.1190/1.3571045

Müller, A., & Haak, V. (2004). 3-D modeling of the deep electrical conductivity of Merapi volcano (Central Java): integrating magnetotellurics, induction vectors and the effects of steep topography. *Journal of Volcanology and Geothermal Research, 138*(3-4), 205–222. doi:10.1016/j.jvolgeores.2004.05.023

Nabighian, M. N., & Macnae, J. C. (1991). Time-domain electromagnetic prospecting methods. Electromagnetic methods in applied geophysics, 2(part A), 427-509.

Nakajima, T., Kunitomo, T., Kumazawa, M., & Yokoyama, Y. (2000). Development of EM-ACROSS and its field test, *Bull. Earthq. Res. Inst. Univ. Tokyo*, **75**, 229–244 (in Japanese).

Nakajima, T., Kunitomo, T., Nagao, H. & Shigeta, N. (2020). Chapter 3.1 - Electromagnetic—accurately controlled routinely operated signal system and corresponding tensor transfer functions in diffusion field region. Elsevier Pub. 2010. In Kasahara, J., Zhdanov, M. S. & Mikada, H. (Ed) *Active Geophysical Monitoring (Second Edition),* Elsevier, Pages 167-181, ISBN 9780081026847, doi: 10.1016/B978-0-08-102684-7.00008-X.

Nakajima, T., Kumazawa, M., Kunitomo, T. & Tsuruga, K. (1998). Current approach and the preliminary results on the EM ACROSS utilizing the diffusional transmission of electromagnetic signals in the MT range. *Abstracts of international workshop on frontiers in monitoring science and technology for earthquake environments,* AP2-41.

Nakano, M., & Kumagai, H. (2005). Response of a hydrothermal system to magmatic heat inferred from temporal variations in the complex frequencies of long-period events at Kusatsu-Shirane Volcano, Japan. *Journal of Volcanology and Geothermal Research*, *147*(3–4), 233–244. https://doi.org/10.1016/j.jvolgeores.2005.04.003

Nakano, M., Kumagai, H., & Chouet, B. A. (2003). Source mechanism of long-period events at Kusatsu-Shirane Volcano, Japan, inferred from waveform inversion of the effective excitation functions. *Journal of Volcanology and Geothermal Research*, *122*(3–4), 149–164. https://doi.org/10.1016/S0377-0273(02)00499-7

Nam, M. J., Kim, H. J., Song, Y., Lee, T. J., Son, J.-S., & Suh, J. H. (2007). 3D magnetotelluric modelling including surface topography. *Geophysical Prospecting, 55*(2), 277–287. doi:10.1111/j.1365-2478.2007.00614.x

Nam, M. J., Kim, H. J., Song, Y., Lee, T. J., & Suh, J. H. (2008). Three-dimensional topography corrections of magnetotelluric data. *Geophysical Journal International*, *174*(2), 464–474. https://doi.org/10.1111/j.1365-246X.2008.03817.x

Nesbitt, B. E. (1993). Electrical resistivities of crustal fluids. *Journal of Geophysical Research: Solid Earth, 98*(B3), 4301–4310. doi:10.1029/92jb02576

Newman, G. A., & Alumbaugh, D. L. (1995). *Frequency-domain modelling of airborne electromagnetic responses using staggered finite differences1. Geophysical Prospecting, 43*(8), 1021–1042. doi:10.1111/j.1365-2478.1995.tb00294.x

Newman, G. A., Gasperikova, E., Hoversten, G. M., & Wannamaker, P. E. (2008). Three-dimensional magnetotelluric characterization of the Coso geothermal field. *Geothermics*, *37*(4), 369–399. https://doi.org/10.1016/j.geothermics.2008.02.006

Nichols, E. A., Morrison, H. F., & Clarke, J. (1988). Signals and Noise in Measurements of Low-Frequency Geomagnetic Fields. *Journal of Geophysical Research: Solid Earth, 93*(B11), 13743–13754. doi:10.1029/jb093ib11p13743

Nurhasan (2006). Electromagnetic imaging of Kusatsu-Shirane volcano and its implications for hydrothermal system. Tokyo Institute of Technology, Tokyo, Japan.

Nurhasan, Ogawa, Y., Ujihara, N., Tank, S. B., Honkura, Y., Onizawa, S., … Makino, M. (2006). Two electrical conductors beneath Kusatsu-Shirane volcano, Japan, imaged by audiomagnetotellurics, and their implications for the hydrothermal system. *Earth, Planets and Space, 58*(8), 1053–1059. doi:10.1186/bf03352610

Obara, K., & Sato, H. (1995). *Regional differences of random inhomogeneities around the volcanic front in the Kanto-Tokai area, Japan, revealed from the broadening of S-wave seismogram envelopes. Journal of Geophysical Research: Solid Earth, 100*(B2), 2103–2121. doi:10.1029/94jb02644

Ogawa, Y. (2002). On two-dimensional modeling of magnetotelluric field data. *Surveys in Geophysics*, *23*(2–3), 251–272. https://doi.org/10.1023/A:1015021006018

Ogawa Y, et al. (2018) Comprehensive survey of 2018 Kusatsu-Shirane eruption. In: Proc. Symp. on the natural disaster sciences. vol. 55, pp 25–30 (in Japanese)

Ogawa, Y., Ichiki, M., Kanda, W. *et al.* (2014). Three-dimensional magnetotelluric imaging of crustal fluids and seismicity around Naruko volcano, NE Japan. *Earth Planet Sp 66***, (**158), 1-13. doi:10.1186/s40623-014-0158-y

Ogawa, Y., Matsushima, N., Oshima, H., Takakura, S., Utsugi, M., Hirano, K., et al. (1998). A resistivity cross-section of Usu volcano, Hokkaido, Japan, by audio-magnetotelluric soundings. *Earth, Planets and Space*, *50*(4), 339–346. doi: 10.1186/BF03352120

Ogawa, Y.; Nurhasan, N.; Tank, B.; Terada, A.; Kanda, W.; Nogami, K. (2016). Three-dimensional magnetotelluric modeling of Kusatsu-Shirane volcano and its implications for recent volcanic unrest. American Geophysical Union, Fall Meeting 2016, abstract #GP42A-08.

Ohba, T., Hirabayashi, J., & Nogami, K. (1994). Water, heat Yugama and chloride budgets of the crater lake, at Kusatsu-Shirane volcano, Japan. *Geochemical Journal*, *28*, 217–231.

Ohba, T., Hirabayashi, J., & Nogami, K. (2000). D/H and 18O/16O ratios of water in the crater lake at Kusatsu-Shirane volcano, Japan. *Journal of Volcanology and Geothermal Research*, *97*(1–4), 329–346. https://doi.org/10.1016/S0377-0273(99)00169-9

Ohba, T., Hirabayashi, J., & Nogami, K. (2008). Temporal changes in the chemistry of lake water within Yugama Crater, Kusatsu-Shirane Volcano, Japan: Implications for the evolution of the magmatic hydrothermal system. *Journal of Volcanology and Geothermal Research*, *178*(2), 131–144. https://doi.org/10.1016/j.jvolgeores.2008.06.015

Ohba, T., Yaguchi, M., Nishino, K., Numanami, N., Tsunogai, U., Ito, M., & Shingubara, R. (2019). Time Variation in the Chemical and Isotopic Composition of Fumarolic Gasses at Kusatsu-Shirane Volcano, Japan. *Frontiers in Earth Science*, *7*(September), 1–17. https://doi.org/10.3389/feart.2019.00249

Orair, G.H., Teixeira, C.H.C., Meira, W., et al. (2010) Distance-Based Outlier Detection: Consolidation and Renewed Bearing. *The VLDB Journal The International Journal on Very Large Data Bases 3*:1469–1480

Pardo, D., Nam, M. J., Torres-Verdín, C., Hoversten, M. G., & Garay, I. (2010). Simulation of marine controlled source electromagnetic measurements using a parallel fourier hp-finite

element method. *Computational Geosciences, 15*(1), 53–67. doi:10.1007/s10596-010-9195-1

Parkinson, W. D., Miguel, S., Kuyper, K., & Darwin, D. (1962). The Infiuence of Continents and Oceans on Geomagnetic Variation & ssw s sw wsw. *Geophysical Journal of the Royal Astronomical Society*, *6*(4), 441–449.

Patro, P. K., & Egbert, G. D. (2011). Application of 3D inversion to magnetotelluric profile data from the Deccan Volcanic Province of Western India. *Physics of the Earth and Planetary Interiors*, *187*(1–2), 33–46. https://doi.org/10.1016/j.pepi.2011.04.005

Patro, P. K., Uyeshima, M., & Siripunvaraporn, W. (2012). Three-dimensional inversion of magnetotelluric phase tensor data. *Geophysical Journal International, 192*(1), 58–66. doi:10.1093/gji/ggs014

Piña-Varas, P., Ledo, J., Queralt, P., Marcuello, A., Bellmunt, F., Hidalgo, R., & Messeiller, M. (2014). 3-D Magnetotelluric Exploration of Tenerife Geothermal System (Canary Islands, Spain). *Surveys in Geophysics*, *35*(4), 1045–1064. https://doi.org/10.1007/s10712-014-9280-4

Qiang, J.-K., Shen, P., & Luo, Y.-Z. (2007). The Resistivity FEM Numerical Modeling on 3-D Undulating Topography. *Chinese Journal of Geophysics, 50*(5), 1378–1386. doi:10.1002/cjg2.1156

Rikitake, T., & Yokoyama, I. (1955). Volcanic activity and changes in geomagnetism. *Journal of Geophysical Research, 60*(2), 165–172. doi:10.1029/jz060i002p00165

Robinson, J. (1955). A Note on Primitive Recursive Functions. *Proceedings of the American Mathematical Society, 6*(4), 667. doi:10.2307/2033449

Sano, Y., Hirabayashi, J. I., Oba, T., & Gamo, T. (1994). Carbon and helium isotopic ratios at Kusatsu-Shirane Volcano, Japan. *Applied Geochemistry*, *9*(4), 371–377. https://doi.org/10.1016/0883-2927(94)90059-0

SanFilipo, W.A., & Hohmann, G.W. (1982). Computer simulation of low-frequency electromagnetic data acquisition. United States. doi:10.2172/5350452.

Sasai, Y., Zlotnicki, J., Nishida, Y., Yvetot, P., Morat, P., Murakami, H., … Sekiguchi, W. (1997). Electromagnetic Monitoring of Miyake-jima Volcano, Izu-Bonn Arc, Japan: A Preliminary Report. *Journal of Geomagnetism and Geoelectricity, 49*(11), 1293–1316. doi:10.5636/jgg.49.1293

Sasaki, Y., & Meju, M. A. (2006). Three-dimensional joint inversion for magnetotelluric resistivity and static shift distributions in complex media. *Journal of Geophysical Research: Solid Earth*, *111*(5), 1–11. https://doi.org/10.1029/2005JB004009

Savage, J. S., & Peterson, A. F. (1996). Higher-order vector finite elements for tetrahedral cells. *IEEE Transactions on Microwave Theory and Techniques, 44*(6), 874–879. doi:10.1109/22.506446

Schleicher, A. M., van der Pluijm, B. A., & Warr, L. N. (2012). Chlorite-smectite clay minerals and fault behavior: New evidence from the San Andreas Fault Observatory at Depth (SAFOD) core. *Lithosphere, 4(3), 209–220.* doi:10.1130/l158.1

Seki, K., Kanda, W., Ogawa, Y., Tanbo, T., Kobayashi, T., Hino, Y., & Hase, H. (2015). Imaging the hydrothermal system beneath the Jigokudani valley, Tateyama volcano, Japan: Implications for structures controlling repeated phreatic eruptions from an audio-frequency magnetotelluric survey. *Earth, Planets and Space*, *67*(1), 0–8. https://doi.org/10.1186/s40623-014-0169-8

Si, H. (2015). TetGen, a Delaunay-Based Quality Tetrahedral Mesh Generator. *ACM Transactions on Mathematical Software, 41*(2), 1–36. doi:10.1145/2629697

Siripunvaraporn, W., Egbert, G., Lenbury, Y., & Uyeshima, M. (2005). *Three-dimensional magnetotelluric inversion: data-space method. Physics of the Earth and Planetary Interiors, 150*(1-3), 3–14. doi:10.1016/j.pepi.2004.08.023

Smith, J. T. (1997). Estimating galvanic-distortion magnetic fields in magnetotellurics. *Geophysical Journal International, 130*(1), 65–72. doi:10.1111/j.1365-246x.1997.tb00988.x

Smith, J. T., & Booker, J. R. (1991). Rapid inversion of two- and three-dimensional magnetotelluric data. *Journal of Geophysical Research: Solid Earth, 96*(B3), 3905–3922. doi:10.1029/90jb02416

Spies, B. R. (1989). Depth of investigation in electromagnetic sounding methods. *Geophysics, 54*(7), 872-888. doi:10.1190/1.1442716

Spies, B. R., & Frischknecht, F. C. (1991). Electromagnetic sounding. *Electromagnetic methods in applied geophysics*, *2*(Part A), 285-426.

Streich, R. (2009). *3D finite-difference frequency-domain modeling of controlled-source electromagnetic data: Direct solution and optimization for high accuracy. GEOPHYSICS, 74*(5), F95–F105. doi:10.1190/1.3196241

Streich, R. (2016). Controlled-Source Electromagnetic Approaches for Hydrocarbon Exploration and Monitoring on Land. Surv Geophys 37:47–80 . doi: 10.1007/s10712-015-9336-0

Streich, R., Becken, M., Matzander, U., & Ritter, O. (2011). Strategies for land-based controlled-source electromagnetic surveying in high-noise regions. *The Leading Edge, 30*(10), 1174–1181. doi:10.1190/1.3657078

Streich, R., Becken, M., & Ritter, O. (2013). Robust processing of noisy land-based controlled-source electromagnetic data. *GEOPHYSICS, 78*(5), E237–E247. doi:10.1190/geo2013-0026.1

Streich, R., Becken, M., & Ritter, O. (2011). *2.5D controlled-source EM modeling with general 3D source geometries. GEOPHYSICS, 76*(6), F387–F393. doi:10.1190/geo2011-0111.1

Sternberg, B. K. (1979). Electrical resistivity structure of the crust in the southern extension of the Canadian Shield - Layered Earth Models. *Journal of Geophysical Research: Solid Earth, 84*(B1), 212–228. doi:10.1029/jb084ib01p00212

Stewart, M. T. (1982). Evaluation of Electromagnetic Methods for Rapid Mapping of Salt-Water Interfaces in Coastal Aquifers. *Ground Water, 20*(5), 538–545. doi:10.1111/j.1745-6584.1982.tb01367.x

Szarka, L. (1988). Geophysical aspects of man-made electromagnetic noise in the earth—A review. *Surveys in Geophysics, 9*(3-4), 287–318. doi:10.1007/bf01901627

Szudzik, M. (2006). An elegant pairing function. In NKS.

Takahashi, K., & Fujii, I. (2014). Long-term thermal activity revealed by magnetic measurements at Kusatsu-Shirane volcano, Japan. *Journal of Volcanology and Geothermal Research*, *285*, 180–194. https://doi.org/10.1016/j.jvolgeores.2014.08.014

Takano, B., Saitoh, H., & Takano, E. (1994). *Geochemical implications of subaqueous molten sulfur at Yugama crater lake, Kusatsu-Shirane volcano, Japan. GEOCHEMICAL JOURNAL, 28*(3), 199–216. doi:10.2343/geochemj.28.199

Takano, B., & Watanuki, K. (1990). *Monitoring of volcanic eruptions at Yugama crater lake by aqueous sulfur oxyanions. Journal of Volcanology and Geothermal Research, 40*(1), 71–87. doi:10.1016/0377-0273(90)90107-q

Terada, A., Morita, Y., Hashimoto, T., Mori, T., Ohba, T., Yaguchi, M., & Kanda, W. (2018). Water sampling using a drone at Yugama crater lake, Kusatsu-Shirane volcano, Japan. *Earth, Planets and Space*, *70*(1), 1–9. https://doi.org/10.1186/s40623-018-0835-3

Terakawa, T. (2017). Overpressurized fluids drive microseismic swarm activity around Mt. Ontake volcano, Japan Crustal Dynamics: Unified Understanding of Geodynamics Processes at Different Time and Length Scales Yoshihisa Iio, Richard H. Sibson, Toru Takeshita, Takeshi Sagiya, Bunichiro Shibazaki and Junichi Nakajima 4. Seismology. *Earth, Planets and Space*, *69*(1). https://doi.org/10.1186/s40623-017-0671-x

Thiel, S. (2008). Modelling and inversion of magnetotelluric data for 2-D and 3-D lithospheric structure, with application to obducted and subducted terranes (Doctoral dissertation).

Tietze, K., Ritter, O., & Egbert, G. D. (2015). 3-D joint inversion of the magnetotelluric phase tensor and vertical magnetic transfer functions. *Geophysical Journal International, 203*(2), 1128–1148. doi:10.1093/gji/ggv347

Trethewey MW (2000) Window and overlap processing effects on power estimates from spectra. *Mech Syst Signal Process, 14* :267–278 . doi: 10.1006/mssp.1999.1274

Tsuji S, Yamaoka K, Ikuta R, et al. (2018) Secular and coseismic changes in S-wave velocity detected using ACROSS in the Tokai region. *Earth, Planets and Space, 70:*(146) 1-10. doi: 10.1186/s40623-018-0917-2

Tsuya, H. (1933) Explosive activity of Volcano Kusatsu Shirane in October, 1932. *Bull. Earthq. Res. Inst. 11*, 82-113.

Uchida, T., Lee, T. J., Honda, M., Ashari, A., & Andan, A. (2002). 2-D and 3-D interpretation of magnetotelluric data in the Bajawa geothermal field, central Flores, Indonesia. *BULLETIN OF THE GEOLOGICAL SURVEY OF JAPAN*, *53*(2–3), 265–283.

Usui, Y. (2015). 3-D inversion of magnetotelluric data using unstructured tetrahedral elements: applicability to data affected by topography. *Geophysical Journal International*, *202*(2), 828–849. https://doi.org/10.1093/gji/ggv186

Usui, Y., Ogawa, Y., Aizawa, K., Kanda, W., Hashimoto, T., Koyama, T., et al. (2017). Three-dimensional resistivity structure of Asama Volcano revealed by data-space magnetotelluric inversion using unstructured tetrahedral elements. *Geophysical Journal International*, *208*(3), 1359–1372. https://doi.org/10.1093/gji/ggw459

Utada, H., Takahashi, Y., Morita, Y., et al. (2007) ACTIVE system for monitoring volcanic activity: A case study of the Izu-Oshima Volcano, Central Japan. *J Volcanol Geotherm Res* 164:217–243 . doi: 10.1016/j.jvolgeores.2007.05.010

Uto, K., Hayakawa, Y., Aramaki, S. & Ossaka, J. (1983) Geological map of Kusatsu-Shirane volcano, Geological Survey of Japan (in Japanese)

Uto, K., & Tatsumi, Y. (1996). *Quaternary volcanism of the Japanese Islands. The Island Arc, 5*(3), 250–261. doi:10.1111/j.1440-1738.1996.tb00030.x

Uyeshima, M. (2007). EM monitoring of crustal processes including the use of the Network-MT observations. In: Surveys in Geophysics. pp 199–237

Van Zijl, J. S. V., & Joubert, S. J. (1975). A crustal geoelectrical model for south african precambrian granitic terrains based on deep schlumberger soundings. *Geophysics, 40*(4), 657–663. doi:10.1190/1.1440556

Velikhov, E. P., Grigoriev, V. F., Zhdanov, M. S., Korotayev, S. M., Kruglyakov, M. S., Orekhova, D. A., … Schors, Y. G. (2011). Electromagnetic sounding of the Kola Peninsula with a powerful extremely low frequency source. *Doklady Earth Sciences, 438*(1), 711–716. doi:10.1134/s1028334x11050394

Velikhov, Y. P., Zhdanov, M. S., & Frenkel, M. A. (1987). Interpretation of MHD-sounding data from the Kola Peninsula by the electromagnetic migration method. *Physics of the Earth and Planetary Interiors, 45*(2), 149–160. doi:10.1016/0031-9201(87)90049-5

Vidal, J., Patrier, P., Genter, A., Beaufort, D., Dezayes, C., Glaas, C., … Sanjuan, B. (2018). Clay minerals related to the circulation of geothermal fluids in boreholes at

Rittershoffen (Alsace, France). *Journal of Volcanology and Geothermal Research, 349,* 192–204. doi:10.1016/j.jvolgeores.2017.10.019

Vozoff, K. (1991). The magnetotelluric method. In Electromagnetic Methods in Applied Geophysics: Volume 2, Application, Parts A and B (pp. 641-712). Society of Exploration Geophysicists.

Wada, I., & He, J. (2017). Thermal structure of the Kanto region, Japan. *Geophysical Research Letters, 44*(14), 7194–7202. doi:10.1002/2017gl073597

Waff, H. S. (1974). Theoretical considerations of electrical conductivity in a partially molten mantle and implications for geothermometry. *Journal of Geophysical Research, 79*(26), 4003–4010. doi:10.1029/jb079i026p04003

Wang, J.-S., & Ida, N. (1991). Eigenvalue analysis in electromagnetic cavities using divergence free finite elements. *IEEE Transactions on Magnetics, 27*(5), 3978–3981. doi:10.1109/20.104973

Wannamaker, P. E., Stodt, J. A., & Rijo, L. (1986). *Two-dimensional topographic responses in magnetotellurics modeled using finite elements. GEOPHYSICS,* 51(11), 2131–2144. doi:10.1190/1.1442065

Wannamaker, P. E., Hohmann, G. W., & SanFilipo, W. A. (1984). Electromagnetic modeling of three-dimensional bodies in layered earths using integral equations. *GEOPHYSICS, 49*(1), 60–74. doi:10.1190/1.1441562

Ward, S. H. (1983). Controlled source electrical methods for deep exploration. *Geophysical Surveys, 6*(1-2), 137–152. doi:10.1007/bf01453998

Ward, S. H., & Hohmann, G. W. (1988). Electromagnetic theory for geophysical applications. In *Electromagnetic Methods in Applied Geophysics: Voume 1, Theory* (pp. 130-311). Society of Exploration Geophysicists.

Wardinski, I., & Holme, R. (2011). Signal from noise in geomagnetic field modelling: denoising data for secular variation studies. *Geophysical Journal International, 185*(2), 653–662. doi:10.1111/j.1365-246x.2011.04988.x

Weaver, J. T., & Agarwal, A. K. (1991). Is addition of induction vectors meaningful? *Physics of the Earth and Planetary Interiors*, *65*(3–5), 267–275. https://doi.org/10.1016/0031-9201(91)90133-3

Weiss, C. J., & Newman, G. A. (2002). *Electromagnetic induction in a fully 3-D anisotropic earth. GEOPHYSICS, 67*(4), 1104–1114. doi:10.1190/1.1500371

Wirianto M, Mulder WA, Slob EC (2010) A feasibility study of land CSEM reservoir monitoring in a complex 3-D model. Geophys J Int 181:741–755 . doi: 10.1111/j.1365-246X.2010.04544.x

Wyss, M., Hasegawa, A., & Nakajima, J. (2001). Source and path of magma for volcanoes in the subduction zone of northeastern Japan. *Geophysical Research Letters, 28*(9), 1819–1822. doi:10.1029/2000gl012558

Xiong, Z. (1992). *Electromagnetic modeling of 3-D structures by the method of system iteration using integral equations. GEOPHYSICS, 57*(12), 1556–1561. doi:10.1190/1.1443223

Yamaoka K, Kunitomo T, Miyakawa K, et al. (2008) A trial for monitoring temporal variation of seismic velocity using an ACROSS system. Isl Arc 10:336–347 . doi: 10.1111/j.1440-1738.2001.00332.x

Yamaya, Y., Alanis, P. K. B., Takeuchi, A., Cordon, J. M., Mogi, T., Hashimoto, T., et al. (2013). A large hydrothermal reservoir beneath Taal Volcano (Philippines) revealed by magnetotelluric resistivity survey: 2D resistivity modeling. *Bulletin of Volcanology*, *75*(7), 1–13. https://doi.org/10.1007/s00445-013-0729-y

Yamaya, Y., Mogi, T., Hashimoto, T., & Ichihara, H. (2009). Hydrothermal system beneath the crater of Tarumai volcano, Japan: 3-D resistivity structure revealed using audio-magnetotellurics and induction vector. *Journal of Volcanology and Geothermal Research*, *187*(3–4), 193–202. https://doi.org/10.1016/j.jvolgeores.2009.09.008

Yau, Y. C., Peacor, D. R., Essene, E. J., Lee, J. H., Kuo, L. C., & Cosca, M. A. (1987). Hydrothermal treatment of smectite, illite, and basalt at 460°C: comparison of natural with hydrothermally formed clay minerals. *Clays & Clay Minerals*, *35*(4), 241–250. doi: 10.1346/ccmn.1987.0350401

Yee, K. (1966). Numerical solution of initial boundary value problems involving maxwell's equations in isotropic media. *IEEE Transactions on Antennas and Propagation, 14*(3), 302–307. doi:10.1109/tap.1966.1138693

Yokoyama Y, Kumazawa M, Nakajima T (2002) Transfer function measured by electromagnetic sounding with an accurately controlled signal. *Earth Planets Space 54,* 459–472 . doi: 10.1186/BF03353037

Yokoyama, T., Nogami, K., Ogawa, Y. (2010). Clay minerals in borehole core samples at Kusatsu-Shirane Volcano, Proc. *2010 Conductivity Anomaly Symp*., p.17. (in Japanese with English Abst.).

Yoshimura, R., Ogawa, Y., Yukutake, Y., Kanda, W., Komori, S., Hase, H., et al. (2018). Resistivity characterisation of Hakone volcano, Central Japan, by three-dimensional magnetotelluric inversion. *Earth, Planets and Space*, *70*(1), 1–10. https://doi.org/10.1186/s40623-018-0848-y

Zhang, P., Pedersen, L. B., Mareschal, M., & Chouteau, M. (1993). Channelling contribution to tipper vectors: a magnetic equivalent to electrical distortion. *Geophysical Journal International, 113*(3), 693–700. doi:10.1111/j.1365-246x.1993.tb04661.x

Zhdanov, M. S. (2010). Electromagnetic geophysics: Notes from the past and the road ahead. *Geophysics, 75*(5), 75A49–75A66. doi:10.1190/1.3483901

Zhdanov, M. S., & Keller, G. V. (1994). The geoelectrical methods in geophysical exploration (Vol. 31). Elsevier Science Limited.

Zlotnicki, J., & Nishida, Y. (2003). Review on Morphological Insights of Self-Potential Anomalies on Volcanoes. *Surveys in Geophysics, 24*(4), 291–338. doi:10.1023/b:geop.0000004188.67923.ac